

# INVESTIGATION OF THE IMAGING CAPABILITY OF MAGNETIC RESONANCE ANGIOGRAPHY SYSTEMS

Thesis presented for the degree of Master of  
Science (Med.Sci.) in the Faculty of Medicine,  
University of Glasgow,  
April 1995

Catherine Lacy MA  
Department of Clinical Physics and Bioengineering,  
22, Western Court,  
100, University Place,  
GLASGOW G12 8SQ

ProQuest Number: 13832085

All rights reserved

INFORMATION TO ALL USERS

The quality of this reproduction is dependent upon the quality of the copy submitted.

In the unlikely event that the author did not send a complete manuscript and there are missing pages, these will be noted. Also, if material had to be removed, a note will indicate the deletion.



ProQuest 13832085

Published by ProQuest LLC (2019). Copyright of the Dissertation is held by the Author.

All rights reserved.

This work is protected against unauthorized copying under Title 17, United States Code  
Microform Edition © ProQuest LLC.

ProQuest LLC.  
789 East Eisenhower Parkway  
P.O. Box 1346  
Ann Arbor, MI 48106 – 1346

Ther  
10449  
C071

GLASGOW  
UNIVERSITY  
LIBRARY

## ABSTRACT

The high incidence of heart disease, particularly on the West Coast of Scotland, makes any procedure which can enhance diagnostic performance in this area of high medical value. This study begins by comparing the known strengths and weaknesses of magnetic resonance angiography to those of conventional angiography and Duplex US. It describes in detail the theory firstly of magnetic resonance imaging, and secondly of the unique problems due to saturation and spin dephasing which arise when flowing spins are imaged. The rationale behind the design of commercially available pulse sequences specified for flow imaging is then described.

The study then moves into an account of the experimental work undertaken, using a rotating drum phantom containing a paramagnetically doped blood equivalent gel, to quantitatively compare the imaging performance of six angiographic sequences. First, a literature study is undertaken to critically establish the accepted normal blood flow rates in the major arteries. The rotating drum phantom and its mode of simulation of blood flow is next discussed. Acceptable relaxation times for in vivo blood are established by a thorough investigation of existing literature. Details are provided of the relaxation properties of the gel, and how these were reached, and a thorough discussion of the effect on the results of the study of discrepancies between these values and those obtained for in vivo blood flow follows.

The purpose of the study is to establish the effectiveness of six commercially available pulse sequences in imaging blood flow, and to

define the reasons for signal loss which detracts from their clinical effectiveness. Signal voids are known to arise when imaging clinical abnormalities such as stenoses, and this study seeks to establish the imaging conditions under which it can definitively be said that signal losses are due to vessel abnormalities, and not to 'blind spots' (i.e. insensitivities to flow) resulting from the inadequacy of sequence performance. Scans of the phantom using the six test sequences are used to evaluate under what imaging conditions the signal intensity will be reduced because of saturation and spin dephasing effects, giving the appearance of stenotic signal voids. Signal losses due purely to rotational phantom artefact effects are identified.

The study concludes by describing other areas of blood flow imaging to which the results of this study may be applicable. It also establishes some priorities for clinical magnetic resonance angiography imaging procedure.

## ACKNOWLEDGEMENTS

I would like to express my thanks to Dr. B.R. Condon and Professor A.T. Elliott who have supervised this project. Professor Elliott also arranged for laboratory facilities in the radiopharmacy at Western Infirmary to be available to me, for the preparation of the gel used in the rotating drum phantom. My thanks are also due to Dr. N. MacMillan for permission to use the MR scanner and SUN workstation at Western Infirmary, and for supplying the clinical images used in chapters one and nine, and to Dr. M. McJury for assistance during the performance of the scans of the rotating drum phantom.

I would also like to express my thanks to the staff of the Clydesdale Bank, and in particular to Richard Clow, Manager at Head Office, St. Vincent Place, Glasgow, without whose sound financial advice the completion of this thesis would have been impossible.

## CONTENTS

### CHAPTER ONE: INTRODUCTION

1.1	Introduction	1
1.2	MRA compared with conventional angiography.	2
1.2.1	Radiation risk associated with conventional angiography.	4
1.2.2	Procedural risk associated with conventional angiography.	6
1.3	MRA compared with Duplex US.	8
1.3.1	Resolution and bone penetration factors dictate the choice of MRA or ultrasound.	11
1.4	Rationale for the use of a rotating drum phantom to evaluate MRA sequences.	12
1.5	The aims and objectives of this project.	13

### CHAPTER TWO: PHYSICAL PRINCIPLES OF MRI

2.1	Introduction.	17
2.1.1	The RF signal.	17
2.2	The free induction decay.	19
2.3	Relaxation times.	20
2.3.1	T1 relaxation.	21
2.3.2	T2 relaxation.	21
2.3.3	T2* relaxation.	22
2.4	The spin echo.	22
2.5	Gradient echo refocussing.	24
2.6	Low angle fast imaging.	25
2.7	The use of compensating gradients.	27
2.8	Spatial information in the 2D slice.	27
2.8.1	Slice definition.	28
2.8.2	Frequency encoding.	29
2.8.3	Phase encoding.	30
2.9	3D volume data collection.	31
2.10.1	Two dimensional image reconstruction.	32
2.10.2	Three dimensional image reconstruction- MIP and MPR.	33
2.11	MRI hardware	34
2.11.1	The magnet.	34
2.11.2	Magnetic field gradients.	35
2.11.3	Duration and magnitude of gradient pulses.	35
2.11.4	Radio frequency systems.	36
2.11.5	Transmit and receive coil.	36
2.11.6	Receiver and detector system.	37
2.11.7	Computer hardware.	37
2.11.8	Computer software.	37
2.12	Conclusion	38

### CHAPTER THREE: PRINCIPLES OF MRA : TIME OF FLIGHT IMAGING

3.1	Spin saturation.	39
3.1.1	Effect of repeated RF pulses on static tissue spins.	39
3.1.2	Saturation effects in flowing spins.	42
3.1.3	Blood flow model.	42
3.1.4	Time of flight imaging.	43
3.2.1	Saturation effects in 3D TOF imaging.	44
3.2.2	Saturation effects in 2D TOF imaging.	46
3.3	Quantitative evaluation of blood flow rate effect on saturation.	47
3.4.1	Presaturation technique : the elimination of unwanted vessels.	48
3.4.2	Spatial misregistration due to flow.	49
3.5	Magnetisation transfer contrast effects.	49
3.6	Signal loss at high velocities- spin dephasing.	50
3.6.1	Motion-dependent transverse plane spin phase factor.	50
3.6.2	Mathematical analysis of spin dephasing.	52
3.6.3	The effect of spin dephasing due to velocity on image intensity.	53
3.7	Gradient moment nulling techniques.	54
3.7.1	Derivation of the profile of refocussing gradient lobes.	55
3.7.2	Effectiveness of gradient motion refocussing.	58
3.8	Conclusion	59

### CHAPTER 4 : PULSE SEQUENCES USED IN MRA

4.1	Introduction.	61
4.2	Time of flight fast imaging sequences.	61
4.2.1	The fast low angle single shot (FLASH) sequence.	61
4.2.2	Blood flow imaging using the FLASH sequence.	63
4.2.3	Steady State Free Precession in magnetic resonance	64
4.2.4	Free precession in the steady state (FISP) sequence	66
4.2.5	Blood flow imaging using the FISP sequence.	68
4.2.6	Behaviour of flowing spins in the FISP gradients.	68
4.3	Magnitude contrast sequences.	70
4.4	Conclusion	71

### CHAPTER 5 : BLOOD FLOW RATES IN THE HUMAN BODY- A CRITICAL REVIEW OF THE LITERATURE AND OF THE MRA PULSE SEQUENCES FOR PRODUCING VASCULAR VISIBILITY

5.1.1	Blood flow rates in the major arteries.	72
5.1.2	An equation for linear flow rate.	75
5.1.3	Survey of blood flow rates in the major arteries.	75

5.1.4	Blood flow rates adopted in this study.	80
5.1.5	Anomalies in flow rate values.	80
5.2	Pulsatile flow.	83
5.3	Application of standard MRA sequences to major vessels.	86
5.4	Conclusion.	88

## CHAPTER 6 : THE DESIGN OF THE ROTATING PHANTOM

6.1	Tube phantoms	90
6.2	Rotating drum phantoms	92
6.3	Blood flow velocity simulation by the rotating drum phantom.	94
6.4	Design details for the rotating drum phantom.	94
6.5	Conclusion	96

## CHAPTER 7 : PREPARATION OF A BLOOD EQUIVALENT GEL FOR MRA PURPOSES

7.1	Critical appraisal of previously published relaxation times for in vivo blood.	97
7.2	Critique of existing literature on blood relaxation time values.	97
7.3	Water as a blood mimicking medium for MRA purposes.	101
7.4	A paramagnetically doped rigid gel.	103
7.5	Preparation of phantom gel used in this study.	103
7.6	Gelatine as a substitute for agar as a setting agent.	108
7.7	Possible errors in phantom evaluation due to inaccurate gel relaxation times.	111

## CHAPTER 8 : THEORETICAL EVALUATION OF OPTIMUM PULSE SEQUENCE PARAMETERS AND COMPARISON WITH STANDARD CLINICAL VALUES

8.1	The mathematical definition of FISP and FLASH signals.	114
8.1.2	Estimation of T2* for a standard sample.	116
8.2.1	Calculation of T2.	116
8.2.2	Calculation of T2* for the rotating phantom gel.	117
8.3	Optimum flip angle for imaging in vivo blood using FISP sequences.	118
8.4	Optimum flip angle for imaging in vivo blood using the FLASH sequence.	119
8.5	Flip angle effects on saturation.	120
8.6	Effect on FISP signal strength of changing sequence parameters.	123

8.7	Effects on the FLASH sequence of changing the sequence parameters.	125
8.8	How closely should the relaxation times of the scanned gel mimic those of in vivo blood?	126
8.9	Conclusion	129

## CHAPTER 9 : QUALITATIVE EVALUATION OF ROTATING PHANTOM SCANS OBTAINED USING SIX MRA PULSE SEQUENCES

9.1	Introduction:clinical evaluation of pulse sequences.	134
9.1.1	FISP and FLASH sequences used in this study.	136
9.1.2	Factors which differentiate the chosen sequences.	138
9.1.3	Pulse sequence parameters used in the scans.	139
9.2	Evaluation of sequence performance:normalisation of the rotating drum image signal.	141
9.2.1	Discussion of image artefacts due to the gel in the drum.	142
9.2.1.1	Artefacts in FLASH 2D drum phantom images: bars of reduced signal intensity.	145
9.2.1.2	Artefacts in FISP 3D drum phantom images : zebra stripes.	148
9.3	QUALITATIVE OBSERVATIONS ON THE IMAGED SLICES	148
9.3.1	FISP 3D sequences imaged at 1T:	148
9.3.1.1	FISP 3D, FA = 40 <sup>0</sup> , TR = 36msec, TE = 10msec.	148
9.3.1.2	FISP 3D, FA = 20 <sup>0</sup> , TR = 36msec, TE = 10msec.	149
9.3.1.3	REPHASE-DEPHASE FISP 3D, FA=15 <sup>0</sup> , TR=50msec, TE=14/14msec.	149
9.3.2	FISP 3D sequences imaged at 1.5T:	151
9.3.2.1	FISP 3D, FA = 15 <sup>0</sup> , TR = 36msec, TE = 10msec.	151
9.3.3	FLASH 2D sequences imaged at 1T:	152
9.3.3.1	FLASH 2D, FA = 35 <sup>0</sup> , TR = 40msec, TE = 10msec.	152
9.3.3.2	FLASH 2D, FA = 40 <sup>0</sup> , TR = 39msec, TE = 10msec.	152
9.4	3D SURFACE COMPUTER RECONSTRUCTIONS OF NORMALISED IMAGE SLICE INTENSITY DATA.	153
	Sequences imaged at 1T:	
9.4.1	FISP 3D sequence designed for velocities up to 180cmsec <sup>-1</sup> .	154
9.4.2	FISP 3D sequence designed for velocities between 35 and 180cmsec <sup>-1</sup> .	155
9.4.3	FLASH 2D sequence designed to image velocities between 30 and 45cmsec <sup>-1</sup> .	155
9.4.4	FLASH 2D sequence designed to image velocities between 60 and 180cmsec <sup>-1</sup> .	156
9.4.5	REPHASE-DEPHASE FISP sequence designed for flow rates rates between 30 and 45cmsec <sup>-1</sup> .	156
	Sequence imaged at 1.5T:	

9.4.6	FISP 3D sequence designed to image flow between 30 and 45 cmsec <sup>-1</sup> .	157
9.5	Summary	157

## CHAPTER 10 : QUANTITATIVE COMPARISON OF IDEAL AND EXPERIMENTAL RESPONSE OF PULSE SEQUENCES IN THE IMAGING OF FLOWING SPINS

10.1	Introduction	160
10.2.1	Ideal slice signal intensity for rotating drum phantom scans.	163
10.2.2	Encoding gradients and velocity dephasing in the rotating drum phantom scans.	164
10.2.3	Positive detection of moving spins by the pulse sequence.	165
10.2.4	Observer evaluation of images.	166
10.3	Signal intensity obtained from FISP 3D scans.	167
10.3.1	Imaging capability of MRA pulse sequences.	168
10.3.2	Discrepancies observed between the ideal signal line and the experimental signal line for each imaged slice.	169
10.3.3	Saturation effects on the drum gel spins.	170
10.3.4	Signal degradation due to velocity dephasing effects.	173
10.4	Validation of the discussion of spin dephasing effects using Hahn's equation.	175
10.5	Imaging potential of other FISP 3D sequences at 1T.	177
10.5.1	FISP 3D sequence designed for velocities up to 180cmsec <sup>-1</sup> .	177
10.5.2	REPHASE-DEPHASE FISP 3D sequence designed for velocities in the range 30-45cmsec <sup>-1</sup> .	181
10.5.3	Imaging potential of FISP 3D sequence designed to image flow between 30 and 45cmsec <sup>-1</sup> at 1.5T.	183
10.6	Detected FISP signal approximates to a FLASH signal for moving spins.	185
10.7	FLASH 2D sequences.	189
10.7.1	FLASH 2D sequence designed to image flow in the range 30-45cmsec <sup>-1</sup> .	189
10.7.2	FLASH 2D sequence designed to image flow in the range 60-180cmsec <sup>-1</sup> .	191
10.8	Conclusion	193

## CHAPTER 11 : APPLICATION OF PHANTOM SCAN RESULTS TO PROBLEM AREAS OF DIAGNOSTIC IMAGING

11.1	Problems of imaging stenotic flow.	196
11.2	Problems associated with the imaging of aneurysms.	201
11.3	Problems of imaging tortuous vessels.	204

GLOSSARY OF TERMS

APPENDIX ONE : GRADIENT LOBE STRUCTURE OF ALL PULSE SEQUENCES MENTIONED

APPENDIX TWO : SLICE NORMALISED IMAGE INTENSITY PROFILES PRESENTED IN 2D GRAPHICAL FORM.

BIBLIOGRAPHY

## LIST OF FIGURES

- 1.1 Deaths due to diseases of the circulatory system, Scotland 1992.
- 1.2 Deaths by cause, Scotland 1992.
- 1.3 Conventional angiography versus magnetic resonance angiography.
- 1.4 Clinical versus phantom evaluation: carotid arteries.

- 2.1 Random orientation of proton spins.
- 2.2 Creation of net magnetic moment.
- 2.3. Generation of RF signal.
- 2.4. Characteristics of FID.
- 2.5. T1 relaxation.
- 2.6. T2 relaxation.
- 2.7. Behaviour of spins during spin echo sequence.
- 2.8. Behaviour of spins during gradient echo sequence.
- 2.9. Comparative signal from SE and fast sequences.
- 2.10. Plane selection in MRI.
- 2.11. Resistive coils in MR scanner.
- 2.12. Static field strength.

- 3.1 Spin vector saturation.
- 3.2 Loss in longitudinal magnetisation for repeated RF pulses.
- 3.3 Inflow and outflow for TOF.
- 3.4 Saturation effects in 3D acquisitions.
- 3.5 Spin velocity effect on saturation.
- 3.6 Saturation effects in 2D imaging.
- 3.7 Presaturation technique.
- 3.8 Use of presaturation pulse in phantom scans.
- 3.9 Ghosting.
- 3.10 Phase change due to spin motion in encoding gradients.
- 3.11 Phase differentials in laminar flow.
- 3.12 Effects on image intensity due to spin dephasing.
- 3.13 Laminar flow profile in major body vessels.
- 3.14 Effect of refocussing pulses on phase of spins.

- 4.1 Gradients applied during FLASH sequence.
- 4.2 Spin behaviour during FLASH sequence.
- 4.3 FLASH sequence imaging of flowing spins.
- 4.4 Effect of flip angle size in SSFP imaging.
- 4.5 Gradients applied during FISP sequence.
- 4.6 Effect of FISP gradients on stationary spins.
- 4.7 Behaviour of flowing spins in FISP gradients.
- 4.8 Computer simulation of transverse magnetisation with FISP.
- 4.9 Magnitude contrast sequences.

- 5.1 Cardiac cycle flow range.

- 6.1 Tube flow phantom.
- 6.2 Simulation of longitudinal flow by rotating drum phantom.
- 6.3 Rotating drum phantom
- 6.4 Details of phantom drums.

- 7.1a). Dependence of T1 on state of whole blood.
- 7.1b). Dependence of T2 on state of whole blood.

- 9.1 Normalisation procedure.
- 9.2 Normalised image intensity profile for six tested pulse sequences.
- 9.3 FLASH 2D FA = 40° image artefacts.
- 9.4 Artefacts in FISP 3D FA = 40° scans.
- 9.5 Measured locations of intensity minima in FLASH 2D FA = 40° scans.
- 9.6 Build-up of saturation effects in FLASH 2D FA = 40° scans.
- 9.7 Location of calculated minima with FLASH 2D v = 60-180cmsec<sup>-1</sup>.
- 9.8 Saturation effects in FISP 3D, FA = 40° scan.
- 9.9a) b) Formation of zebra stripes in FISP 3D imaging.
- 9.10 Clinical evidence of zebra stripes.
- 9.11 Console image slices of FISP 3D FA = 20° scans.
- 9.12 Console image slices of REPHASE-DEPHASE FISP 3D scan.
- 9.13 -9.15 Console image slices of FISP 3D at 1.5T with FA = 15°.
- 9.16 Console image slices of FLASH 2D FA = 35°.
- 9.17-9.18 Console image slices of FLASH 2D FA = 40°.

#### IMAGE INTENSITY SURFACE GRAPHS ACROSS SCANNED VOLUME OF ROTATING DRUM PHANTOM.

- 9.19a),b) FISP 3D, v<180cmsec<sup>-1</sup>.
  - 9.20a),b) FISP 3D, v = 35-180cmsec<sup>-1</sup>.
  - 9.21 FLASH 2D, v = 30-45cmsec<sup>-1</sup>.
  - 9.22 Normalised signal intensity profiles for FLASH 2D, v=60-180cmsec<sup>-1</sup>.
  - 9.23 REPHASE-DEPHASE FISP3D, v = 30-45cmsec<sup>-1</sup>.
  - 9.24 FISP 3D, v = 30-70cmsec<sup>-1</sup> at 1.5T.
- 10.1a) FLASH 2D encoding gradients relative to rotating drum.
  - 10.1b) FISP 3D encoding gradients relative to rotating drum.
  - 10.2 Vertical component of velocity profile for rotation rates 67, 114rpm.
  - 10.3 Signal to noise ratio in rotating drum phantom slices.
  - 10.4 FISP 3D v = 35-180cmsec<sup>-1</sup> 2D image intensity profiles.
  - 10.5 Saturation effects in FISP 3D v = 35-180cmsec<sup>-1</sup> scan.
  - 10.6 Signal loss across image volume for FISP 3D v = 35-180cmsec<sup>-1</sup>.
  - 10.7 Velocity and time dependent effects on spins for FISP 3D v=35-180cmsec<sup>-1</sup>.
  - 10.8 2D image intensity profiles for FISP 3D v<180cmsec<sup>-1</sup>.
  - 10.9 Saturation effects for FISP 3D v<180cmsec<sup>-1</sup>.
  - 10.10 Signal loss across image volume for FISP 3D v<180cmsec<sup>-1</sup>.
  - 10.11 Velocity and time dependent effects on spins for FISP 3D v<180cmsec<sup>-1</sup>.
  - 10.12 Observed signal loss in FISP 3D scan at 1.5T.
  - 10.13 FISP 3D detects like FLASH 2D under some scan conditions.
  - 10.14 Saturation effects in FLASH 2D v = 30-45cmsec<sup>-1</sup>.
  - 10.15 Signal loss across image volume for FLASH 2D v = 30-45cmsec<sup>-1</sup>.
  - 10.16 Signal loss across image volume for FLASH 2D, v = 60-180cmsec<sup>-1</sup>.
- 11.1 Rotating phantom drum face as a velocity vector phase map.

## LIST OF TABLES

- 5.1 Peak arterial flow rates.
- 5.2 Flow rates across the vessel lumen for major vessels, averaged for pulsatile flow.
- 5.3 Arterial flow rates across the vessel lumen used in this study, averaged for pulsatile flow.
- 5.4 Pulse sequences available for MRA and evaluated in this study.
- 7.1 Relaxation times of experimental gels.
- 8.1 Effect of changing sequence parameters on relative strength of FISP sequence signal.
- 8.2 Relative signal strengths in FISP 3D scans using a range of pulse sequence parameters.

# CHAPTER 1 : THE FRAMEWORK FOR THIS STUDY

## 1.1 INTRODUCTION

The potential importance of magnetic resonance angiography in medical provision in the late twentieth century is indicated by the data in the graphs in Figs. 1.1 and 1.2. These were obtained for the whole population of Scotland, both sexes and all ages, for the year 1992. (Report to the Registrar General for Scotland). It shows that diseases of the circulatory system accounted for 47% of all deaths in that year, and that only malignant neoplasms, which accounted for 22% of all deaths, in any way approached this as a source of major risk to the population. Any technique which can contribute to the early and safe diagnosis of arterial disease and thus aid its treatment, deserves particular study, so that its optimal use can be planned.

Similar concern has been voiced in the United States, to the extent that a National Trial was set up which examined the effectiveness of carotid endarterectomy in patients who had recently suffered an adverse cerebrovascular event, and who demonstrated carotid stenosis. This was the North American Symptomatic Carotid Endarterectomy Trial (NASCET). This study concluded that the percentage of stenosis is of supreme importance in elucidating who might benefit from endarterectomy (Bowen, 1994). This is indeed weight for the claim that any clinical imaging procedure which can enhance diagnosis of blood flow related disorders is of major importance at the present time.

MRA is not however the only medium by which blood flow can be imaged. It was preceded by conventional angiography, a technique

which uses X rays and film exposure, and images the flow of blood in vessels whose contrast has been enhanced by the introduction of an iodinated contrast agent, by intravenous or intra-arterial injection. By historical precedent in usage, by the clarity of the imaged vessels, and by its tested diagnostic efficacy, conventional angiograms are taken as the gold or reference standard against which other modalities are evaluated (Freiherr, 1994). CT angiography is a more recently developing technique (Jones-Bey 1994), whereby tomographic images are produced of contrast enhanced vessels rather than the projection of conventional X rays.

Apart from MRI applications, it is ultrasound techniques which have been found useful in investigating blood flow. Duplex Doppler with colour display can demonstrate flow direction, magnitude of velocity and flow patterns. Like MRA it is non-invasive, relying only on the signal reflected from the flowing blood stream to reconstruct the image.

## **1.2. MRA COMPARED WITH CONVENTIONAL ANGIOGRAPHY**

Since conventional angiography is the accepted technique, it is essential to evaluate other modalities against it when considering whether or not it can be superseded by them. If the diagnostic accuracy of other techniques does not approach that of conventional angiography, then other criteria, such as the cost of imaging, are secondary.

An extensive review of MR angiography as used in the diagnosis of occlusive diseases of the head and neck, and as compared with conventional angiography, has been undertaken by Bowen et al,

(1994). The conclusion of twelve surveys of work in this area, specifically the imaging of extra-cranial carotid stenosis, is collated by these authors. In all cases MR angiography findings are evaluated against parallel images of the same clinical situations produced by conventional angiography. This technique has precedent in time; it also has a good record when its imaged findings are compared with those of surgery, although 100% accuracy has not been achieved. Sensitivity and specificity of the images obtained using conventional angiography are however taken to be 100%, and sensitivity and specificity of other modalities are calculated by comparing their images with this gold standard. The report illustrates first of all that there is not as yet a consensus as to the factors which affect the quality of MRA images. The authors quote the specificity and sensitivity of the MRA images as evaluated against the conventional angiographic images, and in all cases these are less than 100%. What is there in the MRA imaging sequence which might produce this deficiency? The sequence type (2D or 3D Time-Of-Flight (TOF)) is given for each MRA examination, and also the echo time (TE) and the voxel size used in reconstruction. The authors do not quote the type of scanner used in each survey, nor do they say whether a spin echo or a fast imaging sequence is used, nor do they quote whether compensating pulses were used in the sequences. They do not give the pulse sequence repetition times (TR) or the flip angle (FA) imparted to the proton spins, both of which might be thought to have some bearing on the final results. Sensitivity for the MRA images ranges from 73% to 100%, and specificity from 59 to 99%, indicating that for the scan images used in this survey, there is quite a shortfall from the quality of the conventional angiographic images.

The conclusion of the authors of the carotid artery stenosis survey quoted here is that MR angiography has many potential applications in the evaluation of cerebrovascular disease, which can include cases of aneurysm, vascular malformation, neoplasm, arterial and venous occlusive disease, and the stenotic flow which arises at sites of atherosclerotic plaques. They find that although techniques have improved in sophistication since the first clinical trials in 1991, more work on sequence development is necessary before it can replace conventional angiography (figure 1.3).

Manning, Li and Edelman (1993), report that the availability of fast MRI techniques has eliminated artefacts due to cardiac and respiratory motion in coronary artery imaging. In evaluating the sensitivity and specificity of MR coronary angiography against contrast angiography, they found 90 and 92% respectively for moderately severe to severe stenoses. MR was found to give a high proportion of false negative results in the moderate stenosis range, and a high proportion of false positives in the mild stenosis range. The limitations of MRA were thought to be due to poor spatial resolution, the result of the use of relatively thick sections. They also noted that the relationship between the spatial extent of a stenosis, and its subsequent haemodynamic consequences, is not fully quantifiable. They do conclude, however, that the very ability of MRA to image abnormal blood flow may be diagnostically useful, for instance in the diagnosis of atherosclerosis.

#### **1.2.1 RADIATION RISK ASSOCIATED WITH CONVENTIONAL ANGIOGRAPHY**

A survey (Coulten and Readman, 1993) conducted to analyse radiographic practice for coronary angiography examinations in the

UK questioned superintendent radiographers in 48 NHS hospitals. The survey highlighted the variety of practice in that the range of projections used, and the number of times they were used, varied from centre to centre. Only five centres were able to provide an average patient radiation dose for the whole examination, and from these figures a calculated highest estimated radiation dose equivalent of 9.3mSv, and lowest dose of 2.4mSv, per examination, was obtained. The recommended dose limit quoted by the ICRP, (1990), is 1mSv in a year to the general public, and 20mSv per year, averaged over defined periods of 5 years, as the occupational dose limit. Combined figures for the eight most frequently used projections for the performance of a routine coronary angiogram gave a mean effective dose equivalent of 5.7mSv per examination. ICRP (1990) estimates a 2.5% per Sievert lifetime risk of fatal cancer for a population between the ages of 40 and 60 years. This is the age range most likely to encounter this type of examination. On this basis, the chances of fatal induced cancer arising from a conventional angiographic examination range from 1 in 4300 (highest dose) to 1 in 16000 (lowest dose).

A similar survey (Steele and Temperton, 1993) of patient doses received during digital subtraction angiography evaluates the risk of developing fatal cancer per million examinations as follows:

EXAMINATION	RISK/MILLION (RANGE)	MEAN RISK (%)
Carotid	0.02	50-600
Femoral	0.02	50-800
Hepatic	0.12	200-2400
Renal	0.08	300-1700

These risks of examination induced fatal cancer have to be evaluated against the fact that the patient is already diagnosed as having a condition which necessitates the examination for its alleviation.

### 1.2.2 PROCEDURAL RISK ASSOCIATED WITH CONVENTIONAL ANGIOGRAPHY

The use of an iodinated contrast agent in conventional angiography involves the introduction of the contrast agent into the arteriovenous system by an intravenous injection or by arterial catheterisation. The presence of the contrast agent may lead to complications, usually in the form of mild ischaemic strokes. A survey (Hankey and Warlow, 1990) of the risk of complications in conventional cerebral angiographic examinations looked at a total of eight prospective and seven retrospective studies, and found that the risks were due to the catheterisation procedure, rather than to the use of the contrast agent. For example, atherosclerotic plaque may be dislodged by the intravascular catheter

COMPLICATION	%RISK OF OCCURRENCE
Transient/reversible neurological damage	0 - 7.1
Permanent neurological damage	0 - 5.7
Death	0 - 0.7
Total risk of adverse complication	0 - 13.5

Ball (1985) noted the following as systemic complications: allergic phenomena (pruritis, periorbital edema), chest pain significant enough to terminate angiography, and acute shortness of breath. Neurological complications ranged through lightheadedness, headache, syncope, transient loss of vision, seizure, and progression of hemiparesis to complete stroke.

The percentage risk varied depending on the date of the study and thus the age and type of equipment, the age of the patient, the type of angiographic procedure performed, the type of contrast medium used, the experience of the angiographer, the period of time over which the neurologic and non-neurologic events subsequent to the examination are recorded, and the definition of reversible (persisting beyond 24 hours but less than one week), and permanent (to define this as anything greater than one week as the authors do does not seem to be adequate).

The same study gave comparable figures for complications arising from digital subtraction angiography as

<b>COMPLICATION</b>	<b>% RISK OF OCCURRENCE</b>
Transient/reversible neurological damage	0 - 5.9
Permanent neurological damage	0 - 1.0
Death	0
Total risk of adverse effect	0 - 6.9

A further survey (Lustgarten, 1994) estimates the risk of using preoperative angiography in conjunction with carotid endarterectomy as

Risk of minor neurological complication	1.3 - 4.5%
Risk of major sequelae	0.6 - 1.3%

It is clear that in conventional angiography complications arising from the use of the catheterisation procedure substantially outweigh those due to the radiation risk. It is also the case that although problems do exist in the case of MR, and specifically MRA imaging, such as claustrophobia in the patient, there are no known life-

threatening risks associated with the modality. Thus if means can be found to improve the diagnostic quality of MRA images, the advantages to the patient of its use rather than conventional angiography are immediately apparent. At the present time, the benefit to the patient of reliable imaging using conventional angiography is deemed to outweigh the disadvantages of procedural and radiation risks. To date, guidelines as to the acceptable limits on reduced specificity and sensitivity of MRA images as compared with those of conventional angiography, in the presence of proven advantage to the patient because no detrimental risk is involved in MRA, have not been developed.

### **1.3 .MRA COMPARED WITH DUPLEX ULTRASOUND**

Doppler ultrasound methods and MRA methods are both non-invasive techniques, and since neither of them involve radiation risks or contrast agent risks, there is value in making a comparison of what each of these methods can contribute to blood flow imaging.

A paper by Sitzer (1993) compares continuous wave Doppler ultrasonography, colour Doppler-assisted Duplex imaging, Systolic peak velocity flow measurement, magnetic resonance angiography and intra-arterial (DSA) angiography in their estimation of the degree of internal carotid stenosis. The value of this in clinical terms is that it has been found to be the most important predictor of ischaemic stroke in extra-cranial carotid artery disease.

The authors make it clear that the different Doppler methods are using different criteria to estimate the stenoses. Continuous wave Doppler ultrasonography does not image the vessel at all; it

produces a numerical value for the blood flow rate at the stenosis, which can then be compared with normal flow more distant in the vessel to find the degree of flow acceleration in the region of the stenosis. These use the acoustic signal from the blood, from which the degree of turbulence can also be assessed. The degree of stenosis can then be estimated on a seven point percentage scale by comparison with standard results. Systolic peak velocity flow measurement is also an acoustic Doppler method.

It is only colour Doppler-assisted Duplex imaging which can give a real-time display of anatomic detail, and hence reveal arterial flow in a manner comparable to that of MRA or conventional angiography. The dimensions of the vessel are presented in colour-coded form, and the degree of stenosis can be calculated after measurement on transverse views of the narrowest part of the tube. The degree of luminal reduction is obtained as the percentage area of cross-sectional area reduction  $(1 - A_S/A_N) \times 100\%$ , where  $A_S$  = minimum stenotic cross section, and  $A_N$  = normal cross section.

This latter method of stenotic evaluation is comparable to that used in MRA, where the severity of stenosis is determined as the percentage of diameter reduction on the view showing the greatest extent of luminal narrowing i.e. degree of stenosis =  $(1 - D_S/D_N) \times 100\%$ . This formulation was also used by the authors to calculate the degree of stenosis when digital subtraction angiograms were being evaluated.

The survey of Sitzer and Furst used the DSA's as the gold standard, and the sensitivities, specificities and predictive values of

continuous wave Doppler, colour Doppler, maximum systolic peak flow velocity and MRA were evaluated against this standard. The different methods were found to perform differently depending on the degree of stenosis present. Below 60% stenosis, continuous wave and colour Doppler both correlated poorly with invasive angiography, whilst MRA correlated best. In the 60-99% stenosis range, there was not much difference between either of the Doppler methods and MRA, all three correlating strongly with conventional angiography. The measurement of maximum systolic peak flow rate showed marked variability between subjects and did not accurately predict the degree of stenosis in this range. The continuous wave and colour Doppler methods tended to over-estimate the degree of stenosis, whereas MRA showed random over-estimation or under-estimation.

The authors clearly state that the differences in the efficacy of the imaging methods are not due to haemo-dynamic effects in the vessels, and must therefore be the result of differences in the physical methods used in the different imaging procedures, and the different characteristics of the signal associated with each imaging procedure.

A further study by Huston (1993) broadly indicates that conventional angiography outperforms both MRA and Duplex US, but that the areas in which MRA is superior to Duplex and Duplex to MRA are not yet clearly defined.

### 1.3.1. RESOLUTION AND BONE PENETRATION FACTORS DICTATE THE CHOICE OF MRA OR ULTRASOUND

Despite the apparent advantages of Duplex US in blood flow quantification, which are the relative simplicity of the equipment and the cheapness of both the equipment and the performance of the scan, there are two major disadvantages to its adoption as a widespread blood flow imaging technique. The first is that at the frequencies used in extra-cranial ultrasound examinations, i.e. 3-10Mhz, there is insufficient penetration of the skull bones to reflect signals from the intra-cranial arteries. This is reported by de Witt, (1988). She reports that the frequencies used for extra cranial ultrasound examinations are unable to penetrate the bones of the skull, so that it is impossible to image the intracranial circulation. Other anatomical regions, particularly the pelvis, are going to suffer from the same problem, although it is only the skull which presents a continuous bone surface. However it seems that when arteries traverse bony regions, it will not be possible to image them as continuous vessels.

The second problem is that in general, ultrasound images have not achieved the degree of resolution or tissue contrast which is commonly found in magnetic resonance imaging. There are few examples of blood flow imaging in publication, but a recent example (Martin, 1993) shows a lack of clarity in the definition of the vessel compared to that found in an MRA image. It does appear that at the present time, the main value of Duplex US is in its quantitative, rather than its imaging, properties in relation to flow.

#### 1.4 REASONS FOR THE USE OF A ROTATING PHANTOM TO EVALUATE MRA SEQUENCES

The aim of this study is to evaluate the imaging potential of commercially available pulse sequences designed for angiographic purposes. Phantom studies are invaluable in this context because they permit controlled and reproducible images to be obtained for evaluation. Clinical studies designed for the same purpose have the inbuilt problems that no two body vessels have the same geometry, (figure 1.4), even in the same individual, and that blood flow rates can vary greatly between subjects (see chapter 5).

Most flow phantoms are rigid boxes containing linear tubes of varying diameters. (Asai, (1992), Sondergaard (1992), Stahlberg (1986, 1987, 1989, 1990), Shimizu (1986)). Through these the rate of flow of test fluid can be controlled by a pump, with water, water/glycerine or paramagnetically doped water being the usual flow medium. These flow phantoms have all the imaging problems normally encountered with in vivo arterial flow, in that the flow patterns in them are laminar, so that spin dephasing in the flowing medium will lead to image degradation (see Chapter 3). This will complicate the analysis of the response of the imaging sequence to the different rates of flow. It is a factor which cannot be eliminated because all flow media have a finite viscosity, and hence the construction of a tube flow phantom where the flow profile is plug rather than laminar is not possible. Tube flow phantoms will thus produce image quality predictions which are related to specific tube diameters, and which are not easily generalised to anatomical vessels of varying diameter. The results will also be restricted to a limited number of

specific flow rates, because a separate measurement has to be made for each flow rate. This is a lengthy procedure.

A rotating phantom (Nordell (1987, 1988), Tarnawski (1988), Summers (1994)), containing a rigid paramagnetically doped blood equivalent gel has specific advantages over the tube flow model. Motor control of the rate of rotation can produce a continuous range of simulated flow speeds, increasing from the axle to the periphery of the drum. Thus it is possible to look at the mean flow rates encountered in all the major vessels of the body simultaneously and over a wide range, and the problems associated with imaging laminar flow are eliminated. The presence of a second static drum in close proximity to the rotating drum allows a normalisation procedure to be used which eliminates inhomogeneity of the static and RF fields, which might otherwise be mistaken for insensitivity to flow.

### 1.5 THE AIMS OF THIS PROJECT

It is the purpose of this project to consider the basic principles of flow imaging using magnetic resonance angiography, to describe the design and rationale for the various pulse sequences which have been proposed for MRA imaging, and then to compare the efficacy of commercially available MRA sequences in imaging flow at rates normally encountered in the human arterio-venous system. To this end a new rotating drum phantom has been designed.

Its purpose is to utilise a magnetically blood equivalent gel as a scan medium, so that quantitative evaluation of the sensitivity to flow of commercially available pulse sequences can be made. Recommendations regarding appropriate imaging strategies in specific

clinical imaging tasks are made on the basis of the deductions, and inherent limitations in the sequences are clearly defined.

In chapter 2, the basic principles of magnetic resonance imaging are developed, concentrating on the classical description of the precession of proton spins in the applied magnetic field. Chapter 3 develops this theory to show how the behaviour of the spins is affected by the fact that they are in a volume of flowing blood. It describes how this causes problems in imaging which are not encountered in the imaging of static tissue by MR methods, and how in some cases problems can be turned to advantage in terms of image clarity, as in the use of presaturation pulses.

Chapter 4 describes the differences between the MRA sequences commercially available. It shows how gradient echo techniques differ from spin echo techniques, describes the use of refocussing gradients to compensate for the effects of moving spins, and indicates the differences between two fast imaging low flip angle sequences now used for MRA imaging. It also shows how interleaved sequences can be used so that difference images highlighting the vessels containing flowing blood can be reconstructed.

Chapters 5, 6 and 7 are concerned with the design and use of the rotating phantom. Chapter 5 consists of a critical survey of literature on blood flow velocities in different regions of the body. It is vital to know these before scans commence so that the rate of rotation of the phantom can be adjusted to cover the range of body blood velocities as closely as possible. Chapter 6 summarises other flow phantom designs, and describes the structure

and operation of the rotating drum phantom used in this study. Chapter 7 considers the optimum composition of the blood mimicking medium with which the phantom is filled.

Chapter 8 is devoted to the investigation of potential strengths and weaknesses of both FISP and FLASH sequences as derived from the equations for stationary spin behaviour in these gradients. These equations enable the relative saturation of spins at different flip angles to be calculated under the same imaging parameters, and an optimum flip angle for the spins to maximise signal strength can be calculated. This chapter also considers in detail the vital question of whether it is essential to use a phantom gel which has identical magnetic properties to in vivo blood.

Chapter 9 is chiefly devoted to the presentation, graphically and as seen at the console, of the results obtained from scanning the phantom using five different commercially available sequences at 1T, (Siemens Magnetom Impact Scanner) and one sequence at 1.5T (Siemens Magnetom SP Scanner). All these sequences are quoted by the manufacturers as being specifically for angiographic purposes. Considerable space is devoted to discussion of image artefacts present in the phantom scans, to establish whether these are artefacts of the rotating drum, rather than inherent to the pulse sequence used. The default values for sequence parameters quoted by the manufacturers have been used in all cases, so that the results presented here are applicable to these sequences used on any other scanner at these fields.

Chapter 10 presents a detailed evaluation of the scan data displayed slice by slice in graphical form. Each image intensity profile is analysed for discrepancies from the expected ideal signal profile, and changes in image intensity between slices are considered in the same way. Significant new evidence about the velocity dephasing effects produced by moving spins in the encoding gradient fields has been obtained. New aspects of the degeneration of a FISP sequence into a FLASH sequence, under conditions of spin flow, have been discovered. Pertinent criticism has also been levelled at the default values quoted by the manufacturers for use with FLASH sequences for angiographic imaging. The clinical application of each sequence is described.

Chapter 11 considers the application of results derived in the study of longitudinal flow to clinically problematic areas such as the imaging of aneurysms and stenoses. It has been established that no reliable imaging using MRA sequences can be undertaken if longitudinal flow rates are not allowed for. Further imaging problems arise at the sites of abnormalities, and the results of this study throw some light on these.

Chapter 12 defines the new aspects of flow imaging which have been revealed in this study, and highlights new areas of work which remain to be done.

FIG.1.1 Deaths by Cause, Both Sexes, All Ages

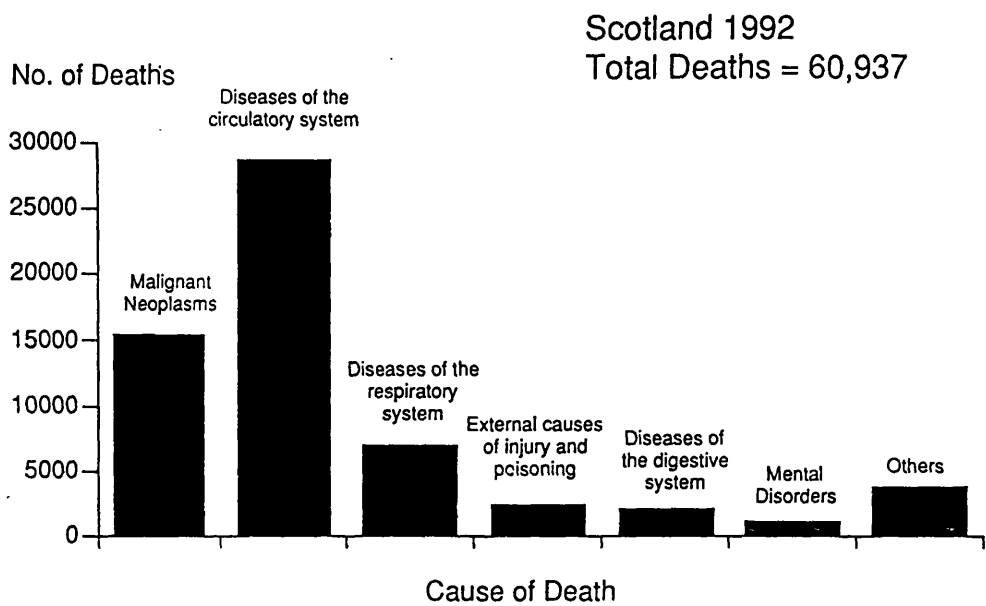
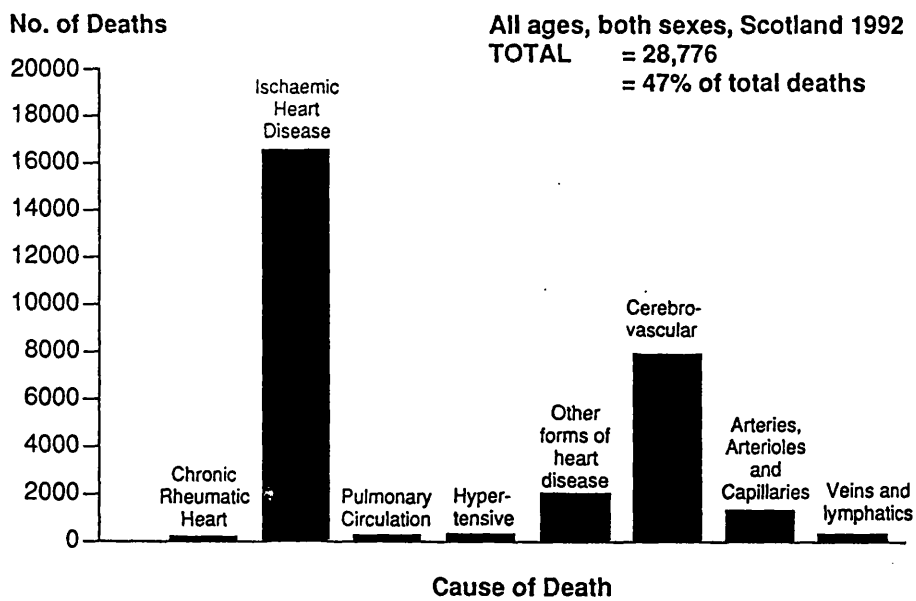
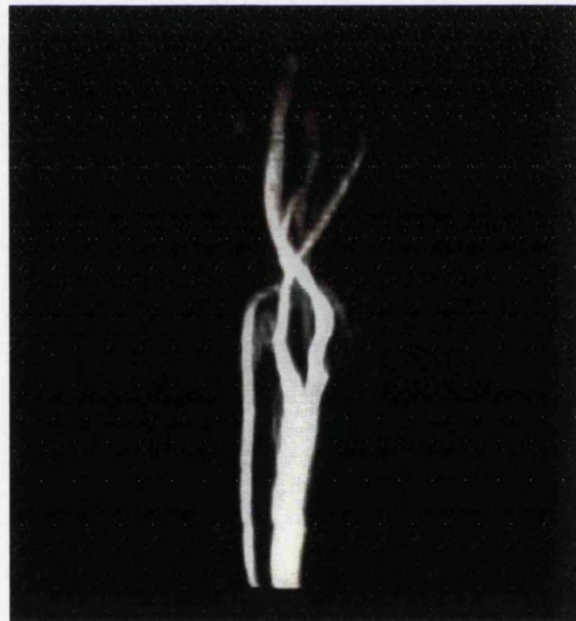


FIG.1.2

### Deaths Due to Diseases of the Circulatory System





**Figure 1.3**  
Conventional angiography (left) and magnetic resonance angiography (right)  
images of the carotid bifurcation.

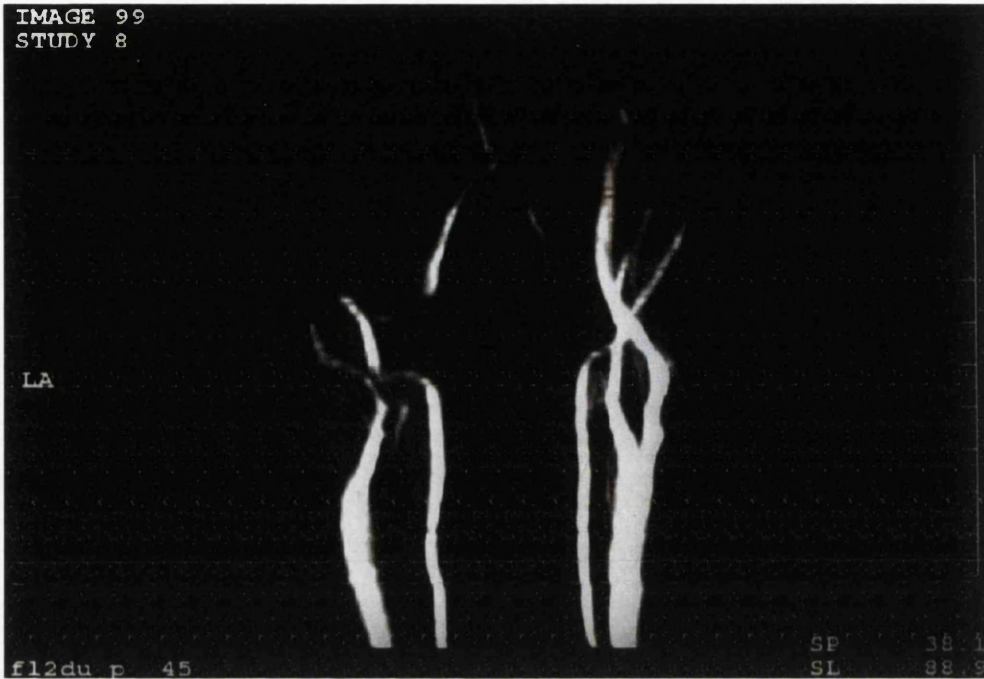


**Figure 1.4**

The necessity for phantom studies is illustrated by this MRA scan of the left and right carotid arteries imaged simultaneously in one subject. Anatomical differences between the two vessels are obvious. Evaluation of sequences using clinical detail cannot provide universal principles for MRA imaging.

## CHAPTER 2 : THE PHYSICAL PRINCIPLES OF MRI

This chapter is an introduction to the components of the MR imaging system. It describes how the RF signal is generated in the specimen of interest, and how the system can differentiate between tissue types and thus how image contrast is generated, using a proton property known as relaxation. The spin echo sequence is described because of its historic importance, it being the first technique used to produce MR images. The difference between this and the gradient echo sequence type is then described, and the features which differentiate the low angle fast imaging sequences which are the main concern of this study from both of these are then given.

The processes of spatially encoding the spins in two dimensional and three dimensional volume acquisitions are described, and the methods used to reconstruct 2D image slices from this data follows. The technique of maximum intensity projection (MIP) is particularly important in angiographic imaging, since it presents a 3D rendition of selective image data to the screen, and permits the generation of continuous images of body vessels with the elimination of static tissue. The chapter concludes with a brief description of the hardware and software of the imaging system.

### 2.1 THE RF SIGNAL

Before proceeding to the specific imaging characteristics of flowing protons in the blood constituents, it is necessary to understand how an MR signal is obtained from a molecule containing a spinning proton. This has its origins in molecular quantum mechanics, which ascribes spin to the nuclear proton. Spin may have values + or - 1/2

only,  $+1/2$  being envisaged as spin up, and  $-1/2$  as spin down. With appropriate stimulus the spin may flip from one state to the other; however it cannot adopt intermediate states. In a sample of protons it is statistically likely that half the protons will have spin up, and the other half spin down. Because it is difficult to comprehend activity on the atomic scale, the proton spins are usually represented vectorially for the whole sample (see Fig.2.1).

If a static field is applied to the specimen, a quantifiable value can be ascribed to the states 'spin up' and 'spin down', which are otherwise useful quantum definitions rather than physical states. Some spins will align themselves with the field, and some spins will align themselves against the field. This is shown in Fig.2.2. Transfer between the two states is achieved by gain or loss of an energy photon.

The effect of the magnetic field on a spinning proton can be likened to the classical case of the effect of a gravitational field on a spinning gyroscope. In both instances the resultant is movement perpendicular to the applied field. Protons are considered to precess about the direction of the magnetic field in the same way as the gyroscope precesses about the direction of the gravitational field. If a variable magnetic pulse is applied at right angles to the static field, the protons begin to precess about their stationary axis (Fig.2.3). They then have two degrees of spin, their quantum spin which causes alignment with or against the static field, and their precessional spin as the magnetic vector, at some angle intermediate between  $0^{\circ}$  and  $90^{\circ}$ , gyrates about the vertical axis. This applied variable magnetic pulse is described as

'radiofrequency' as a means of indicating its frequency and wavelength (Pykett,1982), though in some cases the stimulating frequency is in the audible frequency range (Carr, 1958). The precessional frequency is defined as

$$\omega_{rf} = \gamma B_z$$

where  $\gamma$  = the gyromagnetic ratio,  $\omega_{rf}$  is the precessional frequency of the proton and  $B_z$  is the applied field. The nuclear sample has a total magnetic moment  $M$  as a result of this precession. The frequency of the precession is known as the Larmor frequency and is dependent on the immediate magnetic field strength  $B_0$ , and on a factor  $\gamma$ , the gyromagnetic ratio. This ratio relates the angular momentum of the proton to the magnetic moment which causes it. It is defined as

$$\gamma = e / h m$$

where  $e$  = proton charge,  $m$  = proton mass and  $h$  is Planck's constant.

The absorbed energy is re-radiated when the stimulating RF pulse is removed, the exact profile of the signal which decays exponentially with time depends on the unique physico-chemical environment of the proton, and is known as Free Induction Decay (FID) (figure 2.4).

## 2.2 THE FREE INDUCTION DECAY

It was found that by application of an RF pulse of suitable frequency to a specimen containing precessing protons, some protons could be 'flipped' out of a net  $z$  axis alignment to produce a component of magnetisation in the horizontal or  $xy$  plane. Since this effectively corresponds to a displacement of the magnetisation

vector through  $90^\circ$ , the RF pulse is known as the  $90^\circ$  pulse. Following the application of this pulse, the spins will be in phase (i.e. aligned) at first. The precessing spins will induce an alternating current in the receiver coil, at the precessional frequency. The design of these coils is such that only the transverse component of magnetisation is detected. The amplitude of this signal is found to decrease from its initial maximum value in a monoexponential manner. The mechanism suggested to explain this signal decrease is that as time progresses, the individual spins will precess at different rates. This is because each spin has a magnetic field, and this will slightly modify the field experienced by adjacent spins. Adjacent spins will therefore precess at slightly different frequencies and so gain or lose phase. Because of this dephasing caused by the mutual interaction of the spins, the detected signal will get weaker as time progresses. Consequently after typically a few hundred milliseconds, and depending on various factors including the homogeneity of the field, the detected FID will have fallen to zero because it will be an incoherent summation of the dephased FID's.

The initial magnitude of the FID is proportional to the z component of magnetisation immediately preceding the  $90^\circ$  pulse application. The profile of the FID depends on the proton environment and also on dephasing due to inhomogeneities in the static field.

### 2.3 RELAXATION TIMES

As soon as the RF pulse is switched off, the transverse magnetisation will start to decay to zero, while at the same time the longitudinal magnetisation begins to grow back to its

equilibrium value. The processes determining the return to equilibrium of the longitudinal magnetisation, and the loss of the transverse magnetisation component are called T1 and T2 relaxation processes, respectively.

### **2.3.1 T1 RELAXATION**

T1 relaxation is often called longitudinal relaxation or spin-lattice relaxation. It describes the transfer of energy to or from the spin system as a whole. T1 is the rate constant of the exponential return of the longitudinal magnetisation. As T1 depends on tissue composition, structure and surroundings, hydrogen protons in different tissues have different T1 recovery rates. The exponential nature of the relaxation means that the original longitudinal magnetisation can never be fully regained. T1 is the time taken for 63% of the original longitudinal magnetisation to be regained (Fig.2.5). Some tissues (such as fat) have very rapid recovery rates (the order of 150-250msec), while others have much longer T1 values (e.g. about 3000msec for cerebrospinal fluid). T1 for whole blood is usually quoted as 1200msec at 1.5T, and at 1T as 1000msec. (See chapter 7 for a review of published values).

### **2.3.2 T2 RELAXATION**

T2, transverse, or spin-spin relaxation describes the redistribution of energy between the spins themselves, causing a dephasing of spins with time. Just as different tissues have different T1 relaxation times, they also have different T2 values that are primarily due to different macromolecular environments. One spin affects another by slightly altering the magnetic field experienced by the second spin. The resonant frequency of this second spin will change slightly,

causing an increase or decrease in phase. This is also an exponential process, and T2 is the time for the transverse magnetisation to fall to 37% of its maximum value (Fig.2.6). In fluids the net difference in field due to tumbling molecules tends to even out, producing little phase difference and so a long T2 results (e.g. about 3000msec in CSF). The value of T2 quoted for blood is usually 80-100msec, and is independent of the static field used for imaging (see chapter 7).

### 2.3.3 T2\* RELAXATION

Following a  $90^\circ$  pulse, the signal should decay with a time constant T2, the spin-spin relaxation time. However, the transverse magnetisation decays much faster, with a time constant T2\*, the effective transverse relaxation time. This happens because spins at different locations experience slightly different magnetic fields due to tiny imperfections in the MR system's static magnetic field. This results in slightly different precession frequencies for the different spins. Consequently the spins lose their phase coherence and the transverse magnetisation decays faster than it would on the basis of T2 processes alone. The T2 exponential falls to zero in a time which is typically five times the time it takes for the T2\* exponential to fall to zero, though the exact value will vary from system to system.

## 2.4 THE SPIN ECHO

A tuned receiver coil detects the emf from the precessing proton spin. As has been described, the RF signal due to the transverse magnetisation rapidly falls to zero due to T2\* effects, but the dephasing effects of field imperfections can be eliminated if the

spins are refocussed to give coherent phase at a later time. One method of achieving this is to apply a second RF pulse to the specimen, at a time  $\tau$  after the  $90^0$  pulse, which has the effect of inverting the spins in the xy plane to give a mirror image of their precessional positions before this pulse was applied. Because it has this effect, the pulse is known as a  $180^0$  pulse. The faster precessing spins are now behind the slower spins, and thus in their continued rotation they catch up with these, so that eventually all the spins will be aligned or focussed again, at a time  $\tau$  after the  $180^0$  pulse. The resultant refocussed and rephased transverse magnetisation is known as the spin echo. The time TE, equal to  $2\tau$ , is called the echo time (Fig.2.7).

The amplitude of the first echo is less than that of the FID. The 180deg pulse compensates for  $T2^*$  effects, but 'pure' T2 dephasing effects due to spin-spin interaction will cause a monoexponential amplitude decay. Subsequent rephasing using further 180deg pulses are possible, but for each pulse the amplitude is reduced. After a time greater than  $5 \times T2^*$ , the amplitude of the echo will be within 1% of zero due to T2 dephasing effects, and no further signal can be detected without the application of a second RF pulse.

T1, T2 and  $T2^*$  are time defined characteristics depending on the physico-chemical composition of the tissue being imaged. The parameters which can be controlled by the operator of the MRI system during the imaging procedure are TR, the sequence repetition time, and TE, the time from the application of the RF pulse to the echo. The balance between the values of TR and TE can influence the image contrast, because it changes the extent to which T1 and T2 dominate

in the received signal. The precise effect of TR and TE on image contrast depends on what type of sequence is being used for imaging e.g. spin echo, gradient echo or fast sequence. Generally speaking, for a spin echo sequence, a T1 weighted image has a short TR to increase differential relaxations due to T1, and also a short TE, to minimise signal difference due to T2 relaxation. T2 weighted sequences will have a long TR to minimise differential longitudinal recovery due to T1 relaxation, and long TE to increase differential relaxation due to T2. For other types of sequences this will not necessarily be true.

## 2.5 GRADIENT ECHO REFOCUSSING

As is made clear later, image formation requires the application of magnetic field gradients over milliseconds, during which time dephasing will occur because of these gradients. It was realised by Moran in 1982 that the refocussing of dephased spins could be achieved by applying a gradient in opposition to the one which had caused dephasing. In this way the defocussing effects of the imaging gradient would be eliminated, leaving a signal reduced by the T2\* effect over the time of application of the gradient. The gradient refocussing mechanism is now described.

A phase shift  $\Delta\phi$  is imparted to the spins when a field B is applied. The longer the time of application, and the higher the gradient field at that point, the greater the phase shift. Since  $\omega = \gamma B$ , reversing the direction of B will also reverse the direction of the phase shift, since the spins now precess in the opposite direction. The effect on the spins is that those which were furthest

ahead because they were precessing fastest will now catch up with the slower spins, which had not precessed as far. Thus a refocussed state will be reached. The gradient application times, durations and strengths, are chosen to produce refocussing at a specific echo time TE (figure 2.8).

Use of gradient echo rather than spin echo techniques eliminates the extra time necessary for the  $180^0$  pulse, which is one reason for the relative slowness of spin echo imaging. The time needed for application of the rephasing gradient is typically 6msec, as opposed to 20-40msec for spin echo refocussing. This clearly has considerable advantage in terms of reduction of scan times, diminishing the problems of patient movement during scans, and the ghosting (i.e. phase blurring) of vessels due to physiological motion. The main determinant of acquisition time is however the TR, and an approach used to reduce this is discussed next. The disadvantage of gradient echo sequences is that without a  $180^0$  refocussing pulse, signal losses due to field imperfections are not compensated for, as they are with the spin echo sequence, and therefore the signal will be weaker.

## 2.6 LOW ANGLE FAST IMAGING

Attempts to produce more rapid spin echo sequences resulted either in a limitation of spatial resolution or a decrease in signal to noise ratio. Moreover the  $180^0$  pulses and shorter TR's meant that the statutory patient safety RF level could easily be exceeded for certain multislice sequences (Haase, 1986).

As has been described, gradient echo techniques have proved advantageous over spin echo techniques, giving shorter imaging times. It has proved possible to further reduce repetition times, and hence scan times, by applying an RF pulse which will flip the spins through an angle intermediate between 0 and  $90^{\circ}$ , typically  $40^{\circ}$ . It takes less power to achieve this, so the overall power deposition in the patient is less. It takes less time for the spins to relax back to their unflipped state via the longitudinal relaxation process, and hence imaging times can be shorter. In fact with the use of gradient echo techniques, it is not necessary to wait till the spins have fully relaxed before applying the subsequent RF pulse, and the usual method is to achieve a compromise between optimum scan time and acceptable image contrast. The relative signal intensities from a  $90^{\circ}$  flipped spin and a low angle flipped spin in an identical environment are shown in Fig. 2.9.

It is clear that though the maximum intensity obtained from the  $90^{\circ}$  flipped spin far exceeds that of the  $40^{\circ}$  flipped spin, the different intensity versus time profiles mean that at short repetition times, the low angle flipped spin gives a stronger signal than the  $90^{\circ}$  flipped spin. Thus if the pulse sequence repetition time is reduced from typically 2000msec to around 40msec, it is possible to obtain far faster image acquisitions without a commensurate reduction in signal. Trials have shown (Haase,1986) that comparing these reduced repetition times to spin echo acquisitions, providing the signal to noise ratio is optimised, there is about a 100-fold reduction in the total measurement time, there does not have to be a reduction in resolution, and the total RF power deposition is low. These aspects

have made low angle fast imaging an attractive option, and it now has widespread use in the imaging of both stationary and moving spins.

## **2.7 THE USE OF COMPENSATING GRADIENTS**

Each gradient applied to the tissue specimen to encode a spatial coordinate of the protons along one major axis will have the inevitable effect of dephasing the spins, so that they will have to be refocussed before a further operation, such as the application of a second encoding gradient, can be applied to them. Consequently a compensating gradient has to be applied in conjunction with each read and slice select gradient to overcome dephasing. The location of these gradients in the pulse sequence defines their purpose, and for each type of imaging sequence the position and duration of the compensating gradients will be slightly different.

## **2.8 SPATIAL INFORMATION IN THE 2D SLICE**

Two different types of gradient application are used in spatially encoding the image volume. The slice thickness of a 2D acquisition or the slab thickness of a 3D acquisition are defined by the combined use of an RF pulse and a linearly increasing gradient. For a 2D acquisition, this also spatially encodes the position of the spins along what is usually defined as the z axis.

In the xy plane for 2D imaging, or in the xyz volume for 3D imaging, a second technique, known as spin warp (Edelstein, 1980) is now used. Phase encoding and frequency encoding gradients are employed to impart phase changes to the proton spins which can be decoded on signal detection to assign spatial ordinates to the spins. Spin warp

uses multiple gradients in the phase encoding direction, because without this ambiguity arises in the evaluation of spin location. At present 256 encoding steps are commonly used, though 512 are possible. The number of steps reflects the matrix grid on which the image is reconstructed.

### 2.8.1 SLICE DEFINITION

The slice to be imaged must first be selected in the tissue specimen. This is now achieved on commercial scanners by a technique using two components, the RF pulse and a linearly increasing magnetic gradient. First the gradient is applied orthogonal to the plane of interest. All the protons in its magnetic field precess with a frequency will depend on their spatial location along the gradient, since

$$\omega = \gamma B$$
$$\text{and } B_T = B_0 + z B_z$$

where  $\omega$  is the precessional frequency,  $z$  is the distance moved by the spin in the applied gradient  $B_z$ ,  $B_0$  is the applied static field,  $B_T$  is the total field and  $\gamma$  is the gyromagnetic ratio.

If a narrow band RF pulse is then applied to the tissue, it will promote spins between the two spin states only if its frequencies resonate with the proton frequencies imparted by the gradient and static field combination. Thus an RF pulse containing frequencies of 63.5 to 64.5 MHz will only stimulate a response in the identical region of 63.5-64.5 MHz imparted as precessional frequency by the gradient, even though its complete range may be from 55MHz to 70MHz. The imaged slice which would be achieved in this instance is as shown in Fig.2.10.

To reduce the thickness of the slice, the same RF pulse is applied but the slice selection gradient is made steeper. Thus resonance occurs over the same frequency range but this now corresponds to a smaller spatial dimension. This has implications for the quality of the final image, since the thinner the slice, the higher the resolution. Slice orientation depends on which of the three magnetic field gradients are activated during the RF pulse. These are conventionally along the three major axes, x, y and z, orthogonal to the sagittal, coronal and transverse anatomical planes respectively. Oblique slices are achieved by activating two or more orthogonal gradients simultaneously.

### 2.8.2 FREQUENCY ENCODING

Once the slice has been selected, a second gradient is then applied to the selected plane, along one of its major axes, say x. This is a linearly increasing gradient which goes from negative to positive at the centre of the plane. The total field experienced by the spins can be described by the equation

$$B_T = B_0 + x B_x$$

where  $B_0$  is the static field,  $B_x$  is the applied linear gradient. Again a precessional frequency is imparted to the protons whose value will depend on their location  $x$  in this frequency encoding gradient.

The echo, which is a summation of signals from all the precessing protons, will thus contain a range of frequency information which can be decoded using the Fourier Transform (see section 2.10) for

each proton to give the x spatial co-ordinate of its location in the specimen.

### 2.8.3 PHASE ENCODING

A unique spatial location can only be ascribed to a proton if a second spatial co-ordinate can be allocated to it in the chosen slice. The frequency encoding procedure cannot be repeated along the second axis since the two precessional frequencies which would result could not be separated in the detection process. However a similar encoding gradient applied along the second major axis can be used to modify the phase of the spins. The protons rotate with identical frequency and phase before the application of the gradient. When it is switched on, the precessional frequency increases in proportion to the strength of the local gradient at y:

$$\begin{aligned}\Delta\omega &= \gamma \Delta B \\ &= \gamma (B_0 + y B \gamma)\end{aligned}$$

where the nomenclature is as used before.

When it is switched off, the precessional frequency of all protons returns to the identical initial value. However the fact that some of them have been rotating faster than others during the application of the gradient means that some of the spins will have precessed further than others, and thus each proton has a unique phase depending on its location in the gradient. A single application of the gradient is, however, not enough to separate its effects from that of the frequency encoding gradient, so the strength of the phase encoding gradient has to be incrementally changed over a number of cycles to distinguish its effects from those of the frequency encoding gradient, and to allocate a unique second spatial

coordinate to the spinning proton (see 2.10). This is known as spin-warp (Edelstein, 1980). The sequence is repeated  $N$  times (conventionally 256) to encode phase 256 times along the  $y$  axis. The amplitude of the phase encoding gradient is reduced by  $(n-1)/n$ , (usually 127/128), for each repetition, with reversal of the gradient after 128 repetitions. The frequency encoded signal is resolved into 256 units (simultaneously and without time penalty) to give a  $256 \times 256$  object data matrix for the slice.

## 2.9 3D VOLUME DATA COLLECTION

For a 3D acquisition the volume of interest must first be defined. This is achieved by the application of a slice selection gradient and an RF pulse in a manner similar to that used for the selection of a 2D slice. Typically 2D slice thickness will be 3mm, whereas 3D slab thickness will be 48mm - 80mm. Frequency encoding and phase encoding ( 256 increments) along two of the major axes takes place as for 2D imaging, but the third spatial co-ordinate is obtained by the use of a second phase encoding gradient along the third major axis. This is usually up to 128 increments. The whole of the volume is imaged during each application of the pulse sequence. The frequency encoded signal is sampled typically 256 times. Thus an object data matrix of  $256 \times 256 \times 128$  units is stored in computer memory. Clearly the acquisition of 256 x 128 phase encoding steps is impractical for typical SE TR's of 2000msec (i.e. an acquisition time of 18 hours). Gradient echo sequences with TR's down to 20msec can acquire this data in 10 minutes, and so 3D acquisitions are exclusively performed with the low flip angle gradient sequences.

## 2.10 TWO DIMENSIONAL IMAGE RECONSTRUCTION

- Frequency and phase information collected in the time domain from the FID is converted to spatial information as x, y and z locations in the reconstructed image. The reconstruction process is done using Fourier Transforms (FT's), and since the data is collected as discrete units and not in continuous form, the discrete form of the transform (DFT) is used, involving series summation rather than integration. This can be performed on either a 2D or a 3D object data set. At each location the reconstruction is stored as a wave with what are, in mathematical terms, real and imaginary parts, these being orthogonal:

$$\psi_{rf} = \underset{\text{real (R)}}{A \cos \omega t} + \underset{\text{imaginary (I)}}{B \sin \omega t}$$

(Wood, 1992)

In practical terms two FID signals are obtained by the detector coil, referred to as the cosine phase of  $\psi_{rf}$  and the sine phase of  $\psi_{rf}$  respectively. These are combined for ease of description into a complex signal description,

$$S(t) = S(t_1) + i S(t_2)$$

A coarse reconstruction, which would reduce total image acquisition time, is possible, e.g. 160 x 256 matrix can be reconstructed using the same object data. However resolution will be lost, and in the case of a velocity image, dephasing effects in the voxel will be greater (see below). It is impossible to reconstruct to a finer grid than that of the original data, without introducing artefacts due to aliasing.

Pixel intensity can be real (R), imaginary (I), modulus (M) or phase ( $\phi$ ). For a modulus image, the information extracted from the reconstructed wave is

$$M = \sqrt{R^2 + I^2}$$

for each location, and this is mapped to the screen as pixel intensity. A phase image can also be reconstructed, but this is not as common. Here the pixel intensity is proportional to the phase of the detected signal, i.e.

$$\phi = I / R$$

is the quantity represented by the pixel intensity.

### 2.10.1 THREE DIMENSIONAL IMAGE RECONSTRUCTION- MIP and MPR

The maximum intensity projection (MIP) method of displaying blood flow is the most common type of image reconstruction obtained from the scanned data set. The inflow techniques used when imaging flowing blood ensure that the blood pixels are the brightest in the image (provided that saturation and spin dephasing effects do not reduce blood spin signal intensities to levels comparable with those of stationary tissue).

A ray tracing technique is used, in which the observer is considered to be at a point outside the object data set. At his vantage point, linear rays will reach him which have travelled from a point source on the far side of the data set. As they intersect the data, they automatically highlight the pixel of greatest intensity along their path, and it is this intensity which is presented to the observer (Lacy, 1993, Ruggieri, 1989). For angiography this means that the blood pixels are highlighted, and so the observer is presented with an image of selected blood vessels and no background tissue.

Multiple- projection reconstruction (MPR) is a program to allow the reconstruction of MIPs from a variety of ray emission points. The clinical value of this is that vessels tend to overlay each other, and the observer has access to different anatomical detail in each view.

## 2.11 MRI HARDWARE

### 2.11.1. THE MAGNET

Below 0.3T, resistive magnets are used, typically requiring currents of several hundred amps through the coil windings. A typical arrangement of four resistive coils which can be used to produce such a field is shown in Fig.2.11. Air or water cooling dissipates heat generated. For stronger fields, produced by larger currents, conventional cooling is no longer practical and the phenomenon of superconductivity must be utilised. This allows large currents at zero resistance to flow (no resistance = no heat). Typical bore diameter for imaging systems is 1m. The flux density may vary from 0.05 - 2Tm<sup>-1</sup> and field homogeneity is typically 20ppm or better over the central 50cm.

The superconductive windings are constructed using niobium-titanium alloy strands contained within copper wires. To maintain the superconducting state, it is necessary to immerse the magnet windings in liquid He at 4.3K. Other insulating shields are included.

The static field is only maintained at stated value in the patient scan area, and falls rapidly in strength with distance (Fig.2.12).

### 2.11.2. MAGNETIC FIELD GRADIENTS

Three sets of gradient coils generate magnetic fields, which vary linearly in magnitude in the x, y and z directions. Most imaging applications require only static gradients that can be switched on and off as required, with only the overall amplitude being changed. Some fast imaging methods such as echo planar require the gradients to be switched very rapidly in a non linear fashion. Gradient power supplies must be capable of driving very high currents and providing rapid switching.

### 2.11.3 DURATION AND MAGNITUDE OF GRADIENT PULSES

The figures presented below indicate the order of magnitude of the encoding gradients used in MRI, as compared with the strength of the static field. The figures are quoted by authors in conjunction with their own research, since manufacturers do not give this information directly. The figures also show how improvements in associated electronic circuitry have reduced gradient switching times, with an associated reduction in patient scan times.

**Author- Stahlberg, (1988)**  
Scanner Type - Not quoted  
STATIC FIELD = 0.5T  
Slice thickness = 6 - 10mm.  
Slice selective gradient amplitudes = 0.0225 - 0.0135 Tm<sup>-1</sup>  
All gradients rise and fall time = 1.5msec.

**Author- Cronqvist, (1994)**

Scanner Type - Siemens Impact 1.0T

STATIC FIELD = 1T

Maximum gradient =  $0.015 \text{ Tm}^{-1}$

Gradient rise time = 1.0msec

Slice thickness = 3mm minimum

**Author - Brockstedt, (1992)**

Scanner Type- Siemens Magnetom Vision

STATIC FIELD = 1.5T

Maximum gradient =  $0.025 \text{ Tm}^{-1}$

Diffusion encoding lobes, amplitude =  $0.22 \text{ Tm}^{-1}$

Gradient rise time = 1.2msec.

#### **2.11.4. RADIO FREQUENCY SYSTEMS**

For a fixed frequency system, the RF source can be obtained from quartz crystal operators, but if a variable frequency system is used for multi- imaging applications, a frequency synthesiser would be required. Pulse construction is carried out before power amplification of the signal, this being to 17kW in some systems now in use.

#### **2.11.5. TRANSMIT AND RECEIVE COIL**

The transmitter coil has to provide as uniform a field as possible, and conventionally a pair of saddle coils or a birdcage coil is used. The receiver coil has to provide as high a signal to noise ratio as possible. Some probes will provide both the transmit and receive functions, whilst others have more specific construction to perform only one function. Usually the two coils are orthogonal, which prevent large currents being induced in the receiver coil. They are also orthogonal to the B field, and hence their axes are generally in the xy plane. In imaging, most of the surface coils act as receivers only, although the body and head coils may act as transmitters and receivers. In order to optimise the received

signal, the receiver coils should be as physically close to the part of the body being imaged as possible.

#### **2.11.6. RECEIVER AND DETECTION SYSTEM**

The receiver and detector system are designed to accept only the signal associated with the transverse component of magnetisation of the proton spins. The high degree of amplification required is followed by a frequency filter. A phase sensitive detector measures the phase variations of the signal with respect to a reference signal.

#### **2.11.7. COMPUTER HARDWARE**

Scanner control is through the central processing unit of a mini or microcomputer. It allows operator communication and control of the system and also storage, archive and display facilities. Some functions, such as gradient control, control of the RF system and some of the processing equipment, are often given to a dedicated microprocessor. Transformed images are stored on disk memory. A patient study typically takes up 6 Mbytes. Optical disks are used for archiving. The flexibility of image storage means that image data can be accessed from more than one console at the same time.

#### **2.11.8 COMPUTER SOFTWARE**

Scanner control and image generation are achieved by a standard software package. All pulse sequence gradients are software controlled, and are activated by operator selection of sequence also logged using standard software at the console. Software updates are introduced from time to time, their purpose being to upgrade

existing scanner facilities, introduce new sequences to the scanner, and allow additional coils to be used with the scanner.

## **2.12 CONCLUSION**

A brief introduction to the complete MR imaging system has been outlined in this chapter. All the processes involved in the generation of clinical MR images have been mentioned, and on the basis of this, the aspects of MR imaging unique to the scanning of flowing spins are now described in Chapter 3.

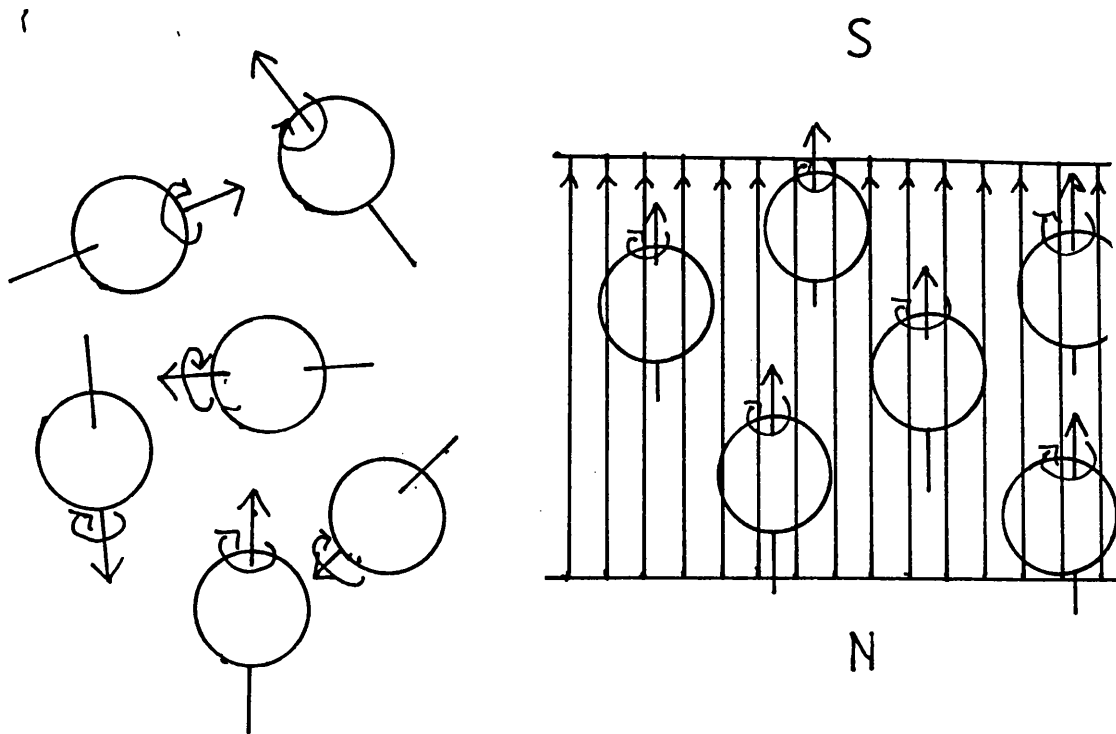


Fig. 2.1 Random orientation of dipoles in the absence of an external magnetic field.

Fig. 2.2 NMR sensitive nuclei align themselves with the static field  $B_0$  creating a net magnetic moment in the sample.

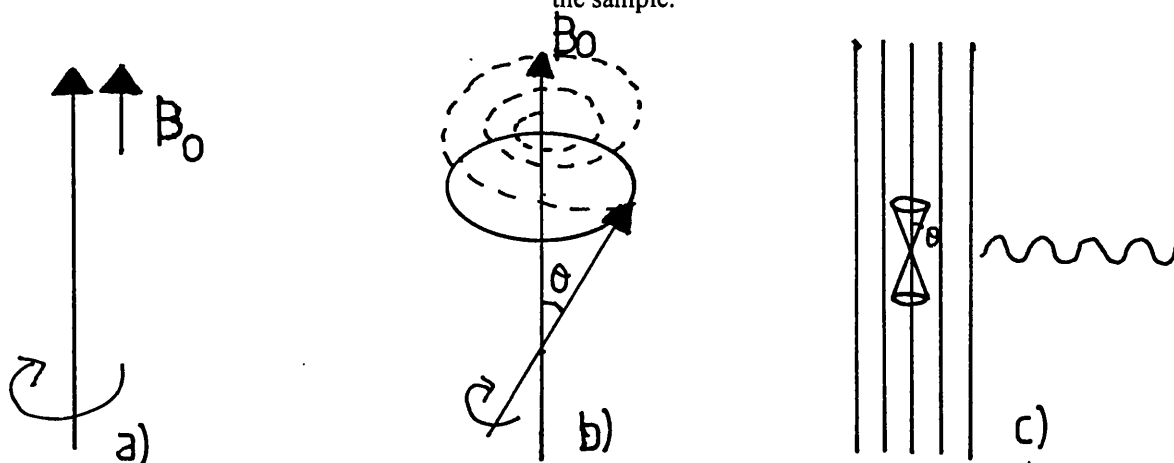


FIG. 2.3 THE SIGNAL GENERATION PROCESS. The spinning proton aligns along the static field, (a). When the RF pulse is applied, (b), perpendicular to the static field, the proton spin properties make it precess about the static field direction. The angle between the magnetisation vector and the static field increases as long as the RF pulse is turned on (c). Precessional motion continues at angle  $\theta$  after the RF pulse is turned off, and the magnetisation vector describes the walls of a cone. The circulating proton gradually loses energy in the form of RF radiation (Pykett, 1983).

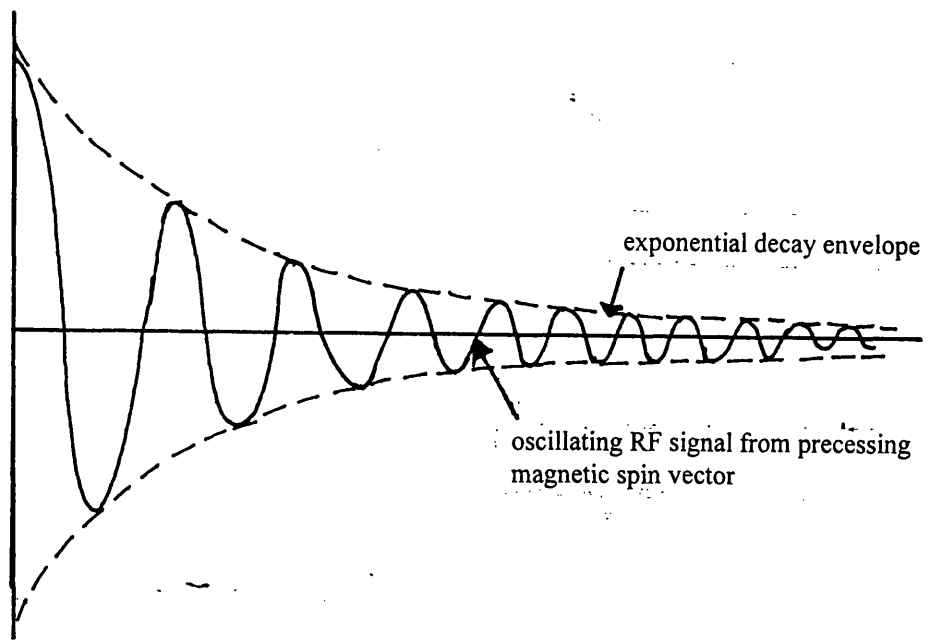


FIG.2.4 Characteristics of the free induction decay.

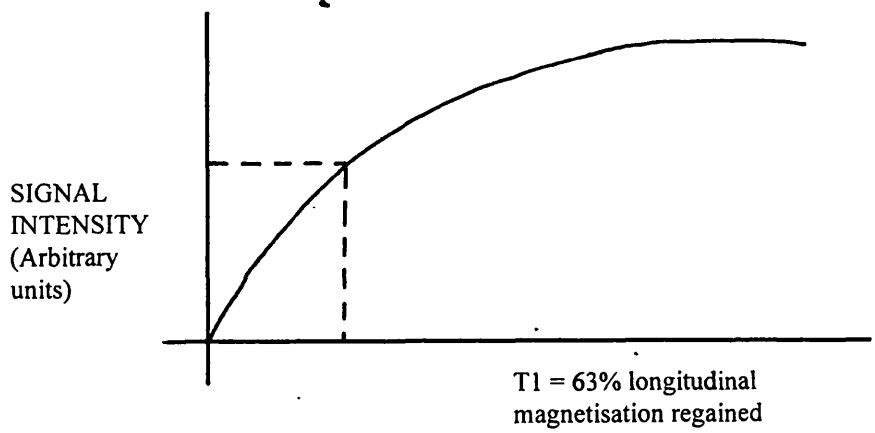


FIG.2.5 T1 relaxation

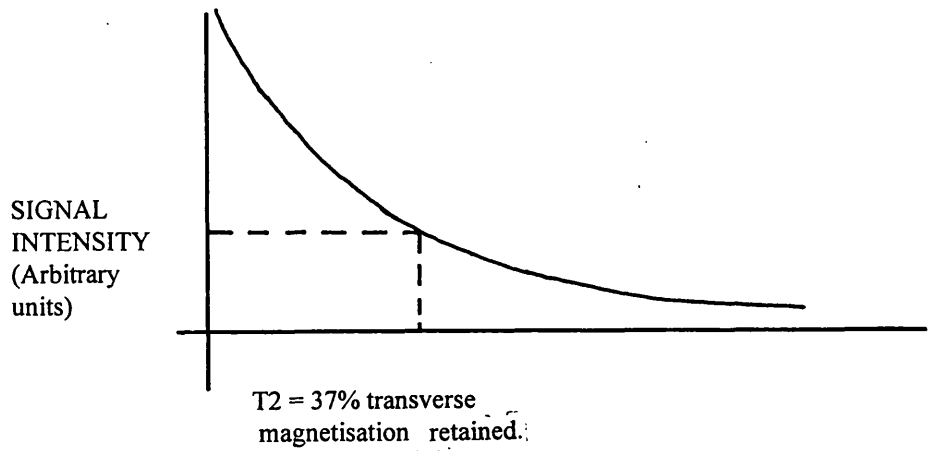
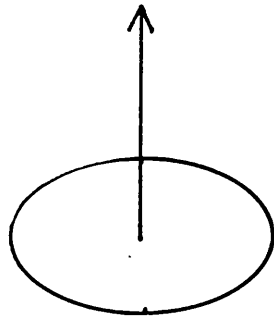
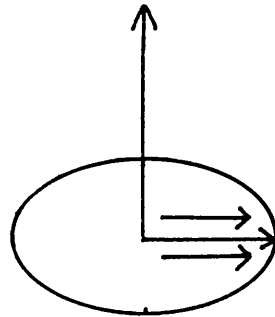


FIG.2.6 T2 relaxation

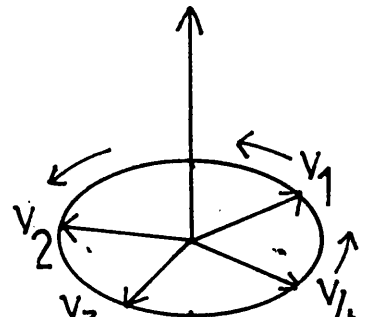
FIG.2.7 Behaviour of spins during the spin-echo sequence.



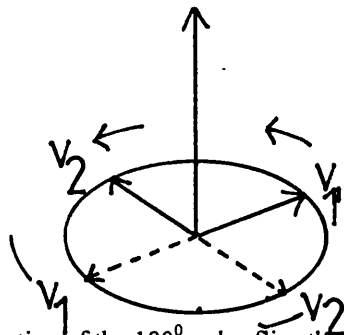
a) Initially all the spins align along the direction of the static field).



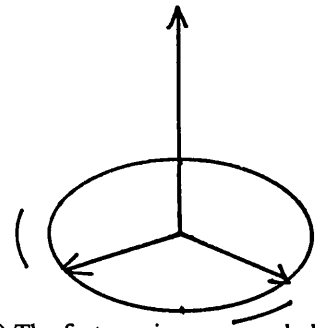
b) The  $90^\circ$  pulse flips all spins into the transverse plane. All the spins are in phase.



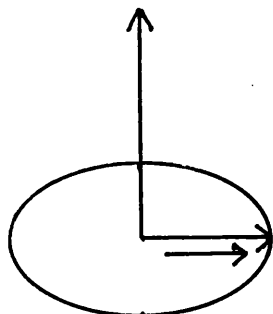
c) Different local fields (spin-spin interaction) means that some spins precess faster than other. Transverse dephasing results.



d) Application of the  $180^\circ$  pulse flips the spins through  $180^\circ$  in the transverse plane, so that their new positions are the mirror image of their old positions.

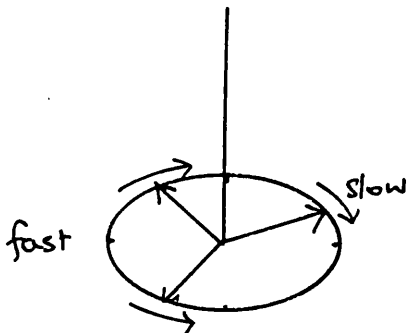
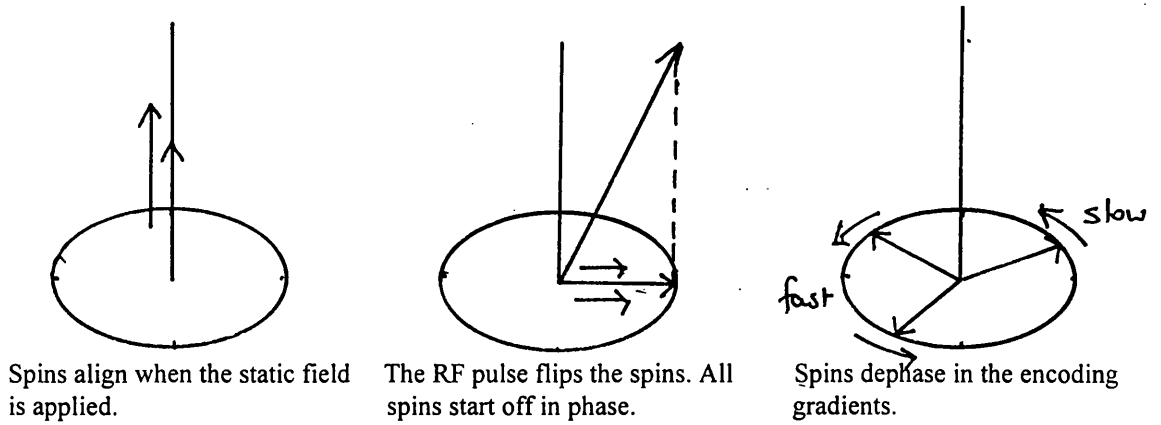


e) The faster spins are now behind the slower spins and catch up with them as they precess.

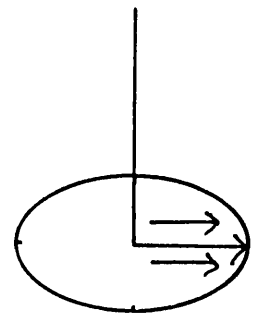


f) Eventually there will be an instant in time when all the spins are re-aligned in the transverse plane. The maximum RF signal (the echo) is detected, and the time which has elapsed between the application of the RF pulse and the detection of the echo is called the echo time TE.

FIG.2.8 Gradient echo sequence- effect of gradients on proton spins.



To achieve maximum signal at the echo, a reverse polarity gradient is used prior to echo detection. Since  $\omega = \gamma B$ , the angular velocity of the spins now reverses, and so does their direction of precession. The fast spins are now spatially behind the slow spins, and catch up with them in time.



The magnitude and timing of this gradient are such that all the spins are refocussed at the centre of the echo.

The phase of the spins is not changed by application of GE refocussing, although this is the case when the  $180^\circ$  pulse is used to refocus spins in SE. Thus the degree of refocussing and the time taken to refocuss will be different for the two types of sequence.

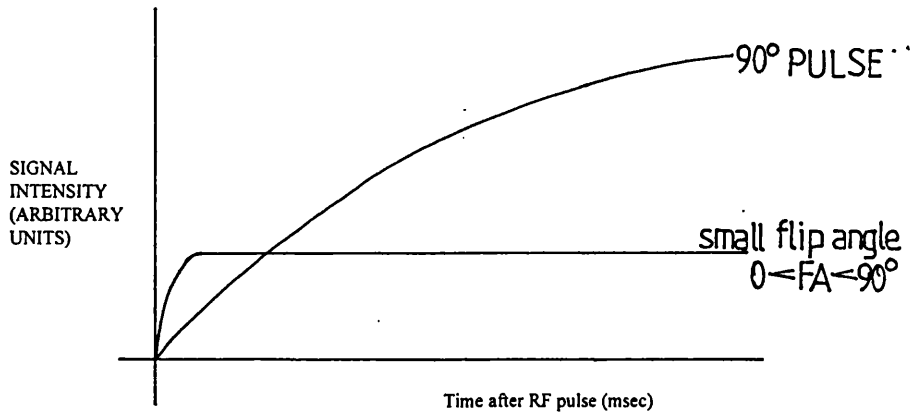
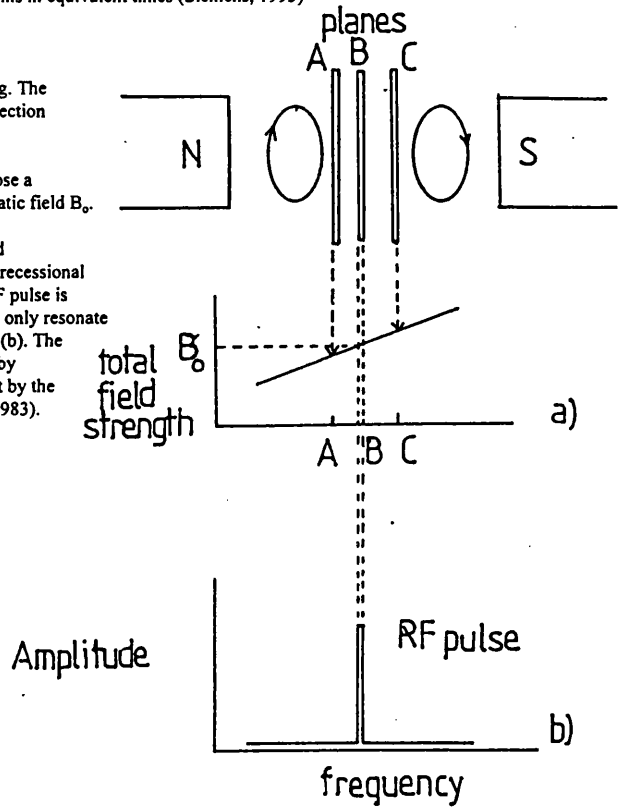


FIG.2.9 Comparative signal obtained using a flip angle of 90° and a low flip angle between 0° and 90°, from the free induction decay of the spins in equivalent times (Siemens, 1993)

FIG.2.10 Plane selection in NMR imaging. The same technique is used for 2D slice selection and 3D slab selection.

The pair of circular gradient coils impose a linear magnetic field gradient on the static field  $B_0$ . Planes at A, B, and C will experience successively higher total magnetic field strengths (a). Since  $\omega = \gamma B$ , the proton precessional rate will increase in proportion. The RF pulse is of a specific frequency such that it will only resonate with those nuclei within a single plane (b). The definition of the plane is thus selected by correspondence of frequencies, and not by the spatial range of the RF pulse (Pykett, 1983).



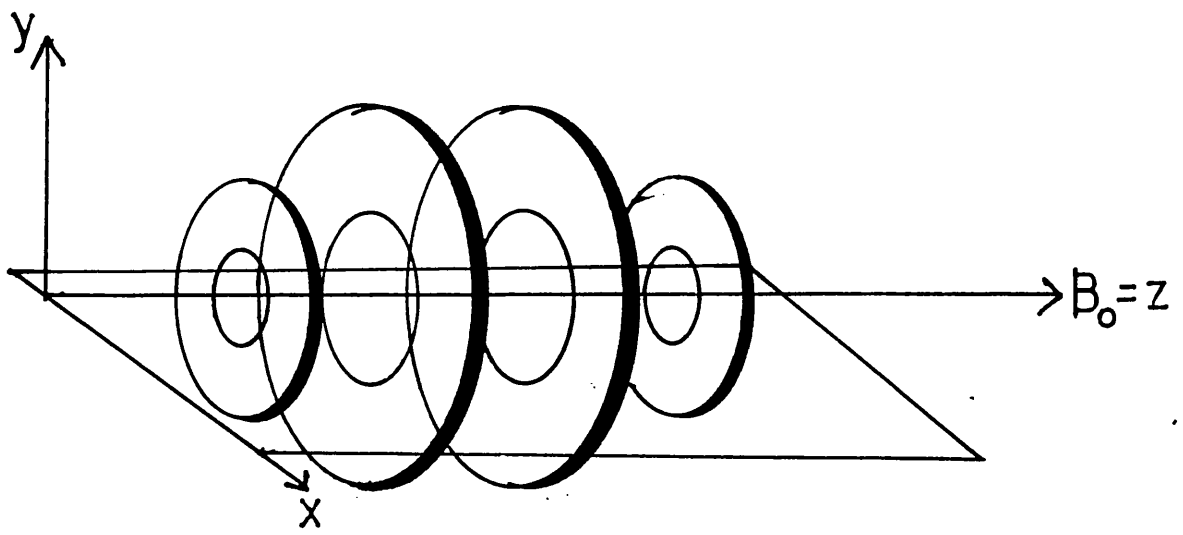


FIG.2.11 Resistive coils of the MR imager static field. 4 coils are often used in clinical MR imaging applications (Pykett, 1983).

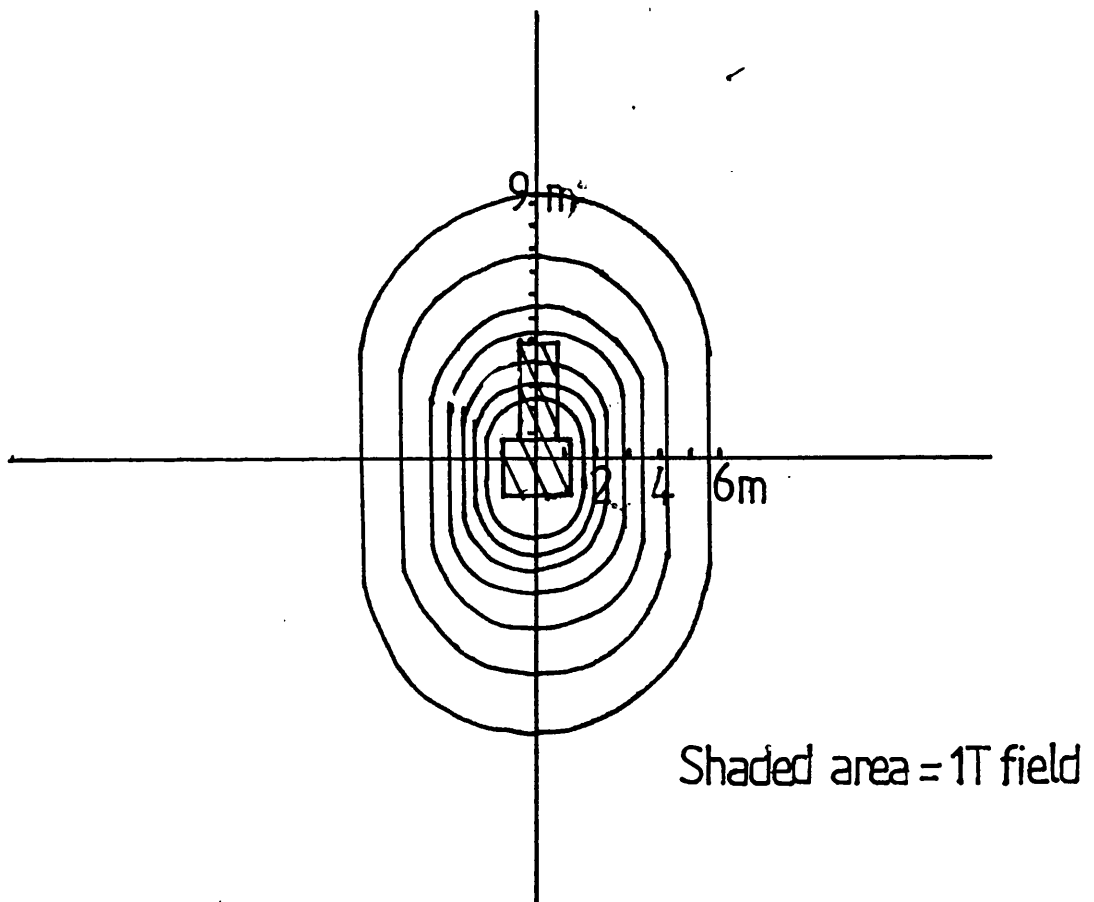


FIG.2.12 Static field of Magnetom Impact 1T scanner (Siemens 1993). Field strength is only appreciable within the patient scanning area. At distances greater than 1m the field falls very rapidly and is soon comparable to the earth's static field.

## **CHAPTER 3: PRINCIPLES OF MRA - TIME OF FLIGHT IMAGING**

The basic elements of MR imaging have been described in chapter 2. This chapter describes how the very movement of blood spins, a source of image deterioration in tissue MR images due to movement artefact, can be exploited to give enhanced contrast to blood vessels under appropriate scan conditions.

The chapter further describes how the range of flow rates, which are encountered even in a single vessel under longitudinal flow conditions, can cause loss of clarity in the image of the vessel. Two effects can be distinguished. Firstly there is signal loss at slow flow rates due to a phenomenon known as saturation. This effect depends on the longitudinal relaxation properties of the spins. Secondly there is signal loss which is found only to occur at higher flow rates, and which is known as spin dephasing due to motion, or simply as spin dephasing, or alternatively but equivalently as velocity dephasing. This effect depends on the transverse relaxation properties of the spins. The chapter concludes by describing a technique for overcoming the spin dephasing effect, by introducing further gradient lobes to counter the changes in phase resulting from the encoding gradients.

### **3.1 SPIN SATURATION**

#### **3.1.1. EFFECT OF REPEATED RF PULSES ON STATIC TISSUE SPINS**

As has been described in Chapter 2, T1 is the time for a proton to regain 63% of its longitudinal magnetisation, and T2 is the time for it to fall to 37% of its maximum transverse magnetisation. If the

signal detection time TE is set at 10msec for example, then there will be a significant difference in the signal detected from blood protons for which T1 is 1100msec and T2 is 85-100msec, and from bone marrow protons, where T1 is 103msec and T2 is 28msec.

The stationary spins which are contained in the defined image, whether slice or slab, are subjected to a large number of consecutive RF pulses during the imaging procedure. In a 2D slice, the following are applicable:

1. The RF pulse and the slice select gradient define the slice thickness.
2. The frequency encoding gradient is applied along one orthogonal axis of the slice.
3. For completely unambiguous spatial encoding along the second orthogonal axis, a stepped gradient is applied 256 times, necessitating 256 applications of the pulse sequence.

The stationary tissue spins in the defined slab will be subject to all of these gradients. The effect of repeated pulse application on the proton spins must therefore be considered. At the first RF pulse, the spin is flipped through an angle intermediate between  $0^\circ$  and  $90^\circ$ . Subsequently T1 relaxation occurs. If TR is short compared with T1, little of the original longitudinal magnetisation will have been regained before the next RF pulse is applied. Considerable transverse magnetisation will however still be present. The subsequent RF pulse will impart further flip to the spin, which will again undergo limited relaxation before the third RF pulse. Eventually an equilibrium state is reached where the limited

relaxation of the spin during TR is equal to the decrease in longitudinal magnetisation imparted by the subsequent RF pulse. This is shown schematically and graphically in Fig.3.1.

Saturation occurs when the measurable longitudinal component of magnetisation is minimised. When fast imaging sequences are used, where by definition the flip angle is intermediate between  $0^{\circ}$  and  $90^{\circ}$ , the spins will still retain some longitudinal magnetisation even where the saturation effect is at a maximum (Siebert, 1992) (Fig.3.2). The number of applications of the pulse sequence needed to bring about maximum saturation for the sequence is thus flip angle dependent (Siemens, 1993). For static tissue, the degree of saturation depends on the relative magnitudes of TR for the imaging sequence, and the various T1's for the bound proton spins. It is this factor which produces tissue contrast.

In the case of a 3D volume acquisition, the same criteria apply. Encoding gradients are applied to the whole of the image volume at each pulse sequence repetition, the total number of applications being

(No. encoding steps on phase encoding axis) x (No. encoding steps on phase encoded slab select axis)

Thus since the whole of the image volume is encoded at each pulse sequence application, these protons will receive a greater number of consecutive RF pulses than will be the case with a 2D slice

acquisition. Stationary proton spins will reach maximum saturation and tissue contrast will ensue by the mechanism described above.

### **3.1.2 SATURATION EFFECTS IN FLOWING SPINS**

The movement of blood spins into and out of the imaged volume, at a rate dependent on their velocity, is clearly going to affect the extent to which they are affected by saturation during the imaging process.

Body blood flow rates range from  $0-180\text{cmsec}^{-1}$  in a healthy subject (see Chapter 5). Thus although stationary tissue spins remain in the image volume for the whole of the scan time, longitudinally flowing spins will spend little time in the imaged volume, typically of maximum thickness 8cm, compared with the total scan times. At the higher velocities they will not be contained in the image volume for much longer than a single sequence repetition, and it is even possible that if the flow rates are abnormally high, spins which receive an RF pulse on entering the volume will have left it altogether before the echo can be detected. The saturation behaviour of flowing blood spins will thus be different from that of stationary tissue spins because of their movement during scan time, and this aspect of flow imaging is now considered in detail.

### **3.1.3 BLOOD FLOW MODEL**

A 'plug' model has been devised to describe the flow of blood in veins and arteries. The direction of flow is assumed to be everywhere parallel to the axis of the vessel, and the rate of flow is assumed to be the same at all points across the vessel lumen. This is the simplest model which can be adopted for vascular flow,

and it does not take into account viscous effects at the vessel walls. The accuracy with which this model mimics in vivo flow is not considered here (See section 3.4.2). To follow the flow of blood through the vessel, a volume of constant thickness containing blood is assumed to move along the vessel. 'Bolus tracking' is the name given to the process which labels a volume of blood and then follows its process along a vessel.

#### **3.1.4 TIME OF FLIGHT IMAGING**

To image an artery or vein, slice or slab selection is applied to the specimen. An RF pulse is applied which excites all proton spins in the imaged volume, including those of the blood contained in the volume at the time of application. What happens then is that these blood spins flow out of the volume before the spin or gradient echo can be obtained, and they are replaced by fresh spins flowing from outside the defined volume (Fig.3.3). How many spins are replaced will depend on the velocity of the blood. The spins of the inflowing blood have not been stimulated by the RF pulse, and are said to be unsaturated. However the stationary spins in the surrounding tissue are said to be saturated, as they receive repeated pulses from the RF and gradient stimuli applied to the slab. Image contrast is generated because of the difference in signal intensity from unsaturated blood spins and saturated tissue spins. This process is known as 'inflow-outflow' imaging, because of the movement of the blood, or less correctly but more commonly 'Time-Of-Flight (TOF)' imaging.

### 3.1.5 SATURATION EFFECTS IN 3D TOF IMAGING

As the blood flows into the selected slab, its state will gradually change from unsaturated to saturated. This is because once it has travelled into the slab, it is subject to the RF pulse applied during further sequence repetitions. The behaviour of the blood relative to the application of 2D sequential imaging slices and a 3D constant imaging slab is not the same, and the two cases are treated separately.

For 3D slab imaging, where encoding gradients are applied to the whole volume throughout the imaging procedure, the blood volume in the imaged slab consists of both saturated spins which were in the volume at the time of irradiation, and fresh or unsaturated spins which have flowed into the volume during TR. How much blood is replaced depends on the blood velocity (Fig. 3.4). The outflow spins start to relax once they leave the slab. Within the slab, there are now spins which have already been stimulated by the RF pulse during TR1, and fresh spins which have just flowed into the volume. Unless TR is comparable to T1 for the blood spins, spin saturation builds up as described in 3.1.1. and the longitudinal component of magnetisation for the proton spins is consequently reduced. By contrast, transverse magnetisation is increasing with spin saturation, and it is the transverse component of magnetisation only which is detected at echo. The normal imaged state of stationary tissue is that the spins are at maximum saturation, and the preferred imaged state of blood spins is that they are totally unsaturated. Conventional image reconstruction which portrays static tissue as dark and blood vessels as bright is thus giving darker grey scale shades to spins with high transverse magnetisation, and

bright or white grey scale shades to spins with lower transverse magnetisation. The difference in saturation levels of saturated stationary tissue spins and unsaturated blood spins flowing into the image volume is the result of the movement of the blood spins, rather than the result of their different relaxation properties. The resultant bright appearance of blood spins in the reconstructed image is known as paradoxical enhancement.

During TR3, the slab will contain blood spins in four states, spins which have received three, two and one RF pulse, and fresh spins (Fig.3.5). The signal from the blood in the volume detected at echo will not be constant, but will increase in the transverse plane as the distance into the slab increases and the degree of the saturation of the blood increases. The degree of contrast between the blood and the stationary tissue will thus decrease with depth into the slab.

This effect has important consequences in clinical imaging since the signal intensity from a long vessel in the image volume will get lower the further the distance from the start edge of the scan volume. The initial brightness or whiteness of the vessel will deteriorate through shades of grey to black, the extent to which this occurs depending on the blood speed and the pulse sequence repetition time. A dark grey or black blood vessel will be difficult to distinguish from the surrounding stationary tissue. Thus a signal void or blind spot arises simply because the pulse sequence chosen for imaging has inappropriate sequence parameters in relation to the blood spin flow rate. A clinician then has the problem that the

appearance of the imaged vessel is identical to that of a stenosed vessel, and a diagnostic error may then arise.

### **3.2 SATURATION EFFECTS IN 2D TOF IMAGING**

When the vessel is imaged as a stacked sequence of 2D slices, the chances of saturation of spins are not so great. The RF pulse being used in conjunction with the slice select gradient is only applied to the defined slice, and not to the whole of the required image volume, at each acquisition.

The spins in the slice during TR1 receive their first RF pulse. When TR2 is applied to the adjacent slice, the spins will only receive a second RF pulse if they are contained exactly within that slice. If their velocity has carried them further into the volume to be imaged, they will be unaffected by TR2, and they will have started to relax (Fig.3.6). Thus with 2D imaging, there is more likelihood that each of the spins will be stimulated once only during the imaging procedure, and thus less chance that they will become saturated. Signal deterioration in the volume is less likely to occur particularly if the slices are acquired in 'ascending', i.e. sequential, rather than 'interleaved' order, as is ideally done in angiographic acquisitions, since it is only at very slow flow rates that spins will be present in two adjacent slices during consecutive acquisitions.

### **3.3 QUANTITATIVE EVALUATION OF BLOOD FLOW RATE EFFECT ON SATURATION**

It appears that the imaging problems caused by saturation of blood spins arise from slow blood flow rates. The appellation 'slow' is relative to the pulse sequence repetition time, as is shown below.

For a slab thickness of 80mm as typically encountered in 3D imaging,

TR = 500msec for a typical spin-echo sequence, so blood spins receive only one RF pulse on passage through the volume if they travel at a velocity of

$$\begin{aligned}v &= \frac{80 \text{ (mm)}}{500 \text{ (msec)}} \\ &= 16 \text{ cmsec}^{-1}\end{aligned}$$

Blood saturates after approximately 10RF pulses, depending on the flip angle used (see above). If spin echo sequences are used, blood will saturate after  $10 \times 500 = 5000\text{msec} = 5\text{sec}$ .

For the spin to have remained in the imaging slab for this length of time, it will have a velocity of less than

$$\begin{aligned}v &= \frac{80 \text{ (mm)}}{5 \text{ (sec)}} \\ &= 1.6\text{mmsec}^{-1} \\ &= 0.16 \text{ cmsec}^{-1}\end{aligned}$$

If however a fast imaging sequence (FISP or FLASH, see chapter 4), is used, where the TR is typically 40msec, the blood will saturate after  $10 \times 40 = 400\text{msec} = 0.4\text{sec}$ , and for it to have remained in the imaging slab for that length of time its maximum velocity will be

$$\begin{aligned}v &= \frac{80 \text{ (mm)}}{0.4\text{sec}} \\ &= 200\text{msec}^{-1} \\ &= 20\text{cmsec}^{-1}\end{aligned}$$

Thus it is more likely that there will be signal losses due to saturation if these fast imaging sequences are used. These have to be weighed against the considerable advantage of reduced imaging time (~10% of that for a spin echo sequence used for the same investigation) which reduces potential motion artefacts, such as patient movement over extended periods of time, or by respiration. It is one of the purposes of this thesis to show that with suitable choice of fast imaging sequence, saturation effects can be minimised, and at the same time total scan times can be kept to a minimum. (see Chapters 9 and 10).

#### **3.4.1 PRESATURATION TECHNIQUE : THE ELIMINATION OF UNWANTED VESSELS**

Once the saturation of blood spins was fully understood, it became clear that the phenomenon could be turned to diagnostic advantage. The clarity of an angiogram normally depends on the availability of unsaturated inflowing blood spins in the vessels of interest. However it is sometimes the case that an artery of interest may be obscured by a vein overlying it, or vice versa. It is also the case that the direction of flow in adjacent arteries and veins is usually in opposite directions. Consequently if a slab can be defined adjacent to the vein whose image is required, and on the side of the inflowing venous blood, and a series of RF pulses applied to this, venous blood spins flowing from this region into the 'true' slab will be saturated compared to arterial blood spins flowing into the slab from the opposite direction. The venous spins will image dark, and the arterial spins will image bright, under normal TOF imaging procedures, and hence the vein can effectively be eliminated from the image (Figs.3.7, 3.8).

### 3.4.2 SPATIAL MISREGISTRATION DUE TO FLOW

The discussion above describes the way in which paradoxical enhancement of blood spins is a result of their velocity. A further effect is noticed in angiographic images which is also due to spin movement. For a vessel which is inclined at an angle  $\phi$  relative to the defined orthogonal imaging axes, readout occurs after the spins have moved a distance  $A/\cos\phi$  during time TE (Fig. 3.9).

There is no such movement for the spins in static tissue. Thus at the time of detection, the blood proton spins will have moved relative to the static tissue spins which surrounded them when the RF pulse was applied, and the reconstructed image will record the position of the vessel as displaced from its true anatomical position. This artefact will be reduced in sequences which have lower values of TE.

### 3.5 MAGNETISATION TRANSFER CONTRAST EFFECTS

This is a technique which has been developed to overcome saturation effects encountered at low flow rates. Spins saturate when they reach an equilibrium angular displacement on repeated application of the RF pulse. This is the normal imaging condition for stationary spins, but the aim of MRA is to image flowing spins in an unsaturated condition to achieve a bright signal and good contrast. Saturation of flowing spins at slow velocities can be delayed if the pulse angle applied to them increases with depth in the image volume. Stationary spins will saturate at different flip angles according to their depth in the image volume, and will appear dark. Blood spins will experience a greater flip angle as they progress

through the volume, will not saturate, and will maintain a bright signal relative to the stationary tissue.

Because the RF pulse has a finite bandwidth in all pulse sequences, all imaged blood benefits from the magnetisation transfer contrast effect, and the effects of saturation in slowly flowing blood are mitigated somewhat because of this. In magnetisation transfer contrast (MTC) sequences, however, the effect is deliberately enhanced.

### **3.6 SIGNAL LOSS AT HIGH SPIN VELOCITIES - SPIN DEPHASING**

In 3.1.5 it has been adequately demonstrated that signal losses arises at low spin velocities due to spin saturation. Inspection of images representing pulse sequence response to moving spins at a range of velocities, notably those obtained by scanning the rotating phantom under controlled conditions in this study (see chapters 9 and 10), show a further region of signal loss at higher velocities. This cannot be caused by saturation because the spins leave the image volume too quickly for this to occur. Another mechanism known as spin dephasing is at work here, and this is now discussed.

#### **3.6.1 MOTION - DEPENDENT TRANSVERSE PLANE SPIN PHASE FACTOR**

A proton spin is made to precess by the application of an RF pulse. A selected group of protons spins can be made to precess if a gradient is applied at the same time as the RF pulse, these two usually being orthogonal. Under these conditions, the spins precess in phase. If however a linear gradient is now applied along one of the orthogonal axes, the precessional rates of adjacent spins will depend on the strength of the applied gradient at their exact

location, and at the time of detection this will appear as a transverse phase differential in the collected signal. This has already been described in 2.8.2 and 2.8.3 as the spatial encoding technique applied in MRI. In particular, 256 encoding steps are used in the phase encoding direction to uniquely ascribe a spatial ordinate to the spins.

If the spins are stationary, the gradient they are subjected to always has the same magnitude. However, moving spins will have travelled in the encoding gradient field during and between gradient applications, and so will be responding to a different field strength. In particular, a stationary spin in a phase encoding gradient will have a positive going phase change imparted to it on the first half of the 256 step cycle, and a negative phase change of exactly the same size on the negative going half of the cycle. Thus the resultant change of phase for the spin is zero (Fig.3.10). If the spin is moving in the encoding gradients, however, the phase change it receives on the positive going half of the cycle is not the same as that on the negative going half of the cycle, since it has moved to a new location in the gradient, and experiences a magnetic field of different magnitude (Fig.3.10 again). There is thus a resultant change in transverse phase imparted by the spin motion. Its value will depend on the exact value of its velocity and how far it has moved in the gradient, and will thus be unique to the spin. Its effect in imaging terms will be that dephasing of spin vectors has arisen because of motion in the encoding gradients, and that this can result in reduced signal intensity, since the resultant voxel signal intensity will be reduced on spin vector summation.

### 3.6.2 MATHEMATICAL ANALYSIS OF SPIN DEPHASING

This situation has been analysed thoroughly in mathematical terms, notably by Carr and Purcell (1954) and Hahn (1960). Carr and Purcell were considering moving spins in spin echo sequence gradients, and found that they had to treat the effect on phase before the  $180^\circ$  pulse separately from that after the pulse. For a linear magnetic gradient  $G = G(t)$ , and a proton at position  $x = x(t)$ , the phase change  $\Delta\phi$  is

$$\Delta\phi = \int_0^{TE/2} \gamma G \cdot x dt + \int_{TE/2}^{TE} \gamma G \cdot x dt$$

$TE/2$  is the time for the  $180^\circ$  pulse. This equation can be integrated under constant velocity conditions where  $dx/dt = v$  and  $G$  are constants, to become

$$\Delta\phi = 1/4 \gamma G \cdot v \cdot TE^2$$

Thus with spin echo gradients, the transverse phase shift due to motion is proportional both to the velocity of the spin and to the square of the echo time.

Hahn (1960) arrived at an identical equation for spin dephasing to that of Carr and Purcell. His concern was not to study the effect of pulse sequence gradients on moving spins. He was looking for a method of detecting small changes in sea water level caused by local disturbances, and, knowing that the Larmor precession of proton spins could be affected by motion in an encoding gradient, he sought to use the magnitude of transverse dephasing induced in sea water protons to measure the change in sea water level.

The result of his analysis was that the phase shift  $\Delta\phi$  for spins of velocity  $v$  detected after motion for a time  $t$  in a gradient  $G$  was

$$\Delta\phi = \frac{\gamma G v t^2}{2}$$

Thus from his different starting point he also arrived at the conclusion that the magnitude of the shift in transverse magnetisation, induced by longitudinal motion in the encoding gradient, was proportional to the velocity of the spin in the direction of the gradient, and to the time that the spin spent in the gradient. The difference in the factor of 2 between the two equations is because of the different starting points of the two analyses. Carr and Purcell's analysis is based specifically on the effect of spin-echo sequence pulses and gradients on flowing spins. Hahn on the other hand begins by considering sea water spins themselves; he then applies a general encoding gradient  $G(t)$ . Both authors show  $v$  and  $t^2$  dependence on phase, and subsequent authors (Stahlberg (1987), Gatenby (1988)) have validated this.

### **3.6.3 THE EFFECT OF SPIN DEPHASING DUE TO VELOCITY ON IMAGE INTENSITY.**

It is immediately clear is that a phase differential due to spin velocity is inevitably incorporated into the image of the vessel lumen. The effect of this on image intensity is shown graphically in Figs.3.11 and 3.12. The laminar flow profile across the vessel is illustrated. Hahn's equation makes it clear that the phases of adjacent spins will depend on their velocity, so a phase profile of the vessel can immediately be obtained. For image reconstruction, phases per pixel are the important factor. The phase differences between adjacent spins will not depend on the absolute magnitude of their velocities, but on the difference between their velocities. The pixel by pixel velocity differentials are shown. Next is

illustrated the transverse vector map for these dephased spins within each voxel. The phase differential which cause these are solely due to spin motion, they would not be present for stationary spins.

It is immediately clear that the signal intensity across the vessel lumen will not be constant. At the walls, the phase differentials are great and vector addition of spin signal intensity only gives a low value. At the centre of the vessel, the differentials are not so great, for even though the spin velocities are greatest here, the velocity profile is more uniform. Hence this part of the vessel will image quite brightly. How much the velocity dephasing effect will affect the quality of the image of the vessel will depend on the laminar flow profile. In a very narrow vessel, with very high flow rates, the laminar flow profile will be so steep that it is possible that dephasing effects will destroy the image of the vessel lumen altogether. Conversely, in a wide vessel with slow flow, the profile will be fairly uniform for the whole of the width of the vessel, and dephasing will not significantly mar the image. The relative effects in a few body vessels are shown in Fig. 3.13.

### **3.7 GRADIENT MOMENT NULLING TECHNIQUES**

Signal loss due to spin dephasing can be prevented if the spin moments  $M_0(t)$  introduced by the spatial encoding gradients can be nulled or negated. This is done by introducing subsidiary gradients specifically designed to act in opposition to the space encoding effects, as far as the effect on transverse phase is concerned. They are timed in the sequence in such a way that their effects compensate for loss of signal intensity, but do not negate the

accuracy of spatial encoding. Picker systems use the Motion Artefact Suppression Technique (MAST), ( Duerk, 1989), Siemens use Gradient Motion Refocussing (Laub and Kaiser, 1989) and GE use FLOW COMPensation (FLOW COMP) (Duerk, 1989). In practice, since any motion of spins in any gradient will lead to spin dephasing effects, the best that can be achieved is that the signal will be a maximum (i.e. dephasing effects will be zero) at time TE which is equivalent to the centre of the echo detection. The gradients are incapable of maintaining complete refocussing of spins for the duration of the echo.

### 3.7.1 DERIVATION OF THE PROFILE OF REFOCUSSING GRADIENT LOBES

Work in this field derives from the work of Moran (1982). He built on the work of Lauterbur (1973). Lauterbur used a spatial imaging gradient to modulate the FID signal so that the phase of the detected spin signal was dependent on the position of the spin in the gradient.

$$\text{i.e.} \quad M = \gamma \int G(t)r(t) dt$$

This spatial encoding process, which is fundamental to MR imaging, has already been referred to. If the spins are moving, an additional factor is introduced into the transverse plane of the spins, as described in detail in 3.4. Thus when the phase of the spin is decoded by a detector, it contains an artefact or error,  $\Delta\phi_v$ . This has two effects. Firstly the spatial location ascribed to the spin will not be accurate, the spin will appear to be shifted from its true position by an amount proportional to  $\Delta\phi_v$ . This is responsible for ghosting in images as described in 3.5 . Secondly,

the signal intensity within the reconstructed image pixels will be reduced because of incoherence or partial incoherence of adjacent spin signals.

Moran proposed a method of overcoming the change of phase incorporated into the detected signal because of the movement of the spin, by using a velocity phase modulation which was explicitly independent of spatial location. He suggested a special NMR phase modulation sequence, in the form of new encoding gradients, which was directly analogous to the gradients that Lauterbur used to sensitise the MR imaging process to spatial location. The overall effect of these gradients is to compensate for spin dephasing and hence they are frequently referred to as refocussing gradients. It can be appreciated that to devise such gradients is relatively simple and effective when the vessel being imaged is linear and lies parallel to one of the orthogonal axes dictated by commercial scanner geometry. However when the vessel is oblique or tortuous, and when flow has components relative to two or three orthogonal axes, whose encoding gradients will all have spin dephasing potential, the situation is far more complex. The achievement of total refocussing at the time of echo will be far more difficult to achieve, and the effects of flow on the image will be more complicated and more difficult to predict as a result.

Laub and Kaiser (1988) started with Carr and Purcell's equation (3.6.1) and use it to explain what form the proposed NMR phase modulation should take. They change the form of the integral so that they consider the whole of the imaging interval  $t$  as one unit,

without considering the separate events which occur during the imaging interval. Thus

$$\phi(t) = \gamma_0 \int_0^t G(t) r(t) dt$$

They then expand the integral using the standard Taylor series

$$x(t) = x_0 + \frac{dx}{dt} t + \frac{1}{2} \frac{d^2x}{dt^2} t^2 + \frac{1}{3} \frac{d^3x}{dt^3} t^3 + \dots$$

Substituting this into the change of phase equation, they show that  $\Delta\phi$  can also be expressed as a summed series of increasing powers of  $t$ :

$$\begin{aligned} \Delta\phi &= \gamma_0 \int_0^t G(t) \cdot \left( x_0 + \frac{dx}{dt} t + \frac{1}{2} \frac{d^2x}{dt^2} t^2 + \frac{1}{3} \frac{d^3x}{dt^3} t^3 + \dots \right) \\ &= \phi_{\text{stat}} + \phi_{\text{vel}} + \phi_{\text{acc}} + \text{higher order terms.} \end{aligned}$$

Thus with this mathematical treatment, the total phase change may be described as a summation of effects due to the static behaviour of the spins in the gradients and also any motion and acceleration which they may have in these gradients. Laub and Kaiser conclude that if the spins are to be rephased at time of echo, so that the maximum signal may be detected, the summation of transverse phase terms must equal zero at the echo. Gradient lobes needed to achieve this can be devised by arranging for each of  $\phi_{\text{vel}}$ ,  $\phi_{\text{acc}}$  and higher order terms to be zero.

It has been found impossible in practice to compensate adequately for dephasing effects due to spin acceleration. However for a normal spin echo sequence applied to angiography, the relative magnitude of these effects has been calculated to be

Static spin dephasing	0.06v (cause of spatial misregistration)
Velocity dephasing	1.07v
Acceleration dephasing	0.013v

(Haacke, 1987) i.e. the acceleration dephasing effect is negligible under normal imaging conditions.

### 3.7.2 EFFECTIVENESS OF GRADIENT MOTION REFOCUSING

Gradient motion rephasing (GMR) lobes are designed to ensure that the spins are in focus at the centre of the echo, and sequences can be designed to ensure that this is true for all blood velocities at that point in time (Fig.3.14). The exact shape of the refocussing gradient must reflect the gradient in which the spins were moving when the velocity dephasing occurred, and it must also reflect the range of velocities encountered in laminar flow in the vessel of interest. Thus the design of refocussing gradients must depend on the slice/slab selection and spatial encoding gradients already present in the pulse sequence in which they are to be applied. The velocity of blood flow in the vessel of interest, which will dominate the degree of spin dephasing encountered during image data collection, must also have some bearing on compensating or refocussing gradient design. Thus not all pulse sequences will be equally effective in imaging all blood flow rates. Some degree of inability to refocus spins and hence image blood vessels clearly is necessarily built into angiographic sequences because of the precise and limited nature of gradient strengths, pulse duration times and pulse switching times. Haacke (1987) notes that the calibration and timing of the gradients to obtain zero phase at the echo is crucial in the implementation of any GMR sequence, and that even small calibration errors can lead to significant phase effects when the velocities are large. Finite gradient rise times and eddy currents

can also cause complications, as can inhomogeneities in the static field. The incorporation of refocussing gradients into a pulse sequence will inevitably increase the repetition time TR, and hence the total scan time will increase.

### 3.8 CONCLUSION

This chapter has made it clear that there are unique features to the imaging of flowing blood in the context of magnetic resonance imaging. Paradoxical enhancement which ensures that blood spins will, in perfect imaging conditions, be the brightest element of an angiographic image, has been shown to be the result of the inflow and outflow of spins into the image volume.

The different nature of the two processes by which blood spins lose imaging signal intensity has been delineated, and it has been made clear that signal voids can arise in clinical images if care is not taken to select a pulse sequence which is matched to the blood flow range in the vessel of interest. Saturation, which reduces signal intensity at low spin velocities, has been described as a feature of longitudinal spin relaxation. Spin dephasing at high velocities is on the other hand a transverse magnetisation effect.

It has been shown that saturation effects can be reduced by appropriate choice of pulse sequence parameters, and that there are

significant differences in the effect of this signal loss mechanism in 2D and 3D image data acquisitions.

It has also been shown that serious attempts have been made to reduce the effects of spin dephasing on image quality by introducing additional gradient lobes. This technique is known as Gradient Motion Refocussing when used with the Siemens scanners. The effect described qualitatively by considering the different magnitudes of the gradient lobes applied to the spins, and quantitatively by employing a mathematical analysis. This latter shows that there are two quantities which affect the magnitude of transverse dephasing, one being the velocity of the individual spins, and the second being the square of the time that they spend in the encoding gradient. The methods which have been adopted to date to calculate the profile of the gradient lobes which should be used to offset these effects has been described. Details have also being given of how the spin dephasing effect will modify signal intensity across the vessel lumen in laminar flow.

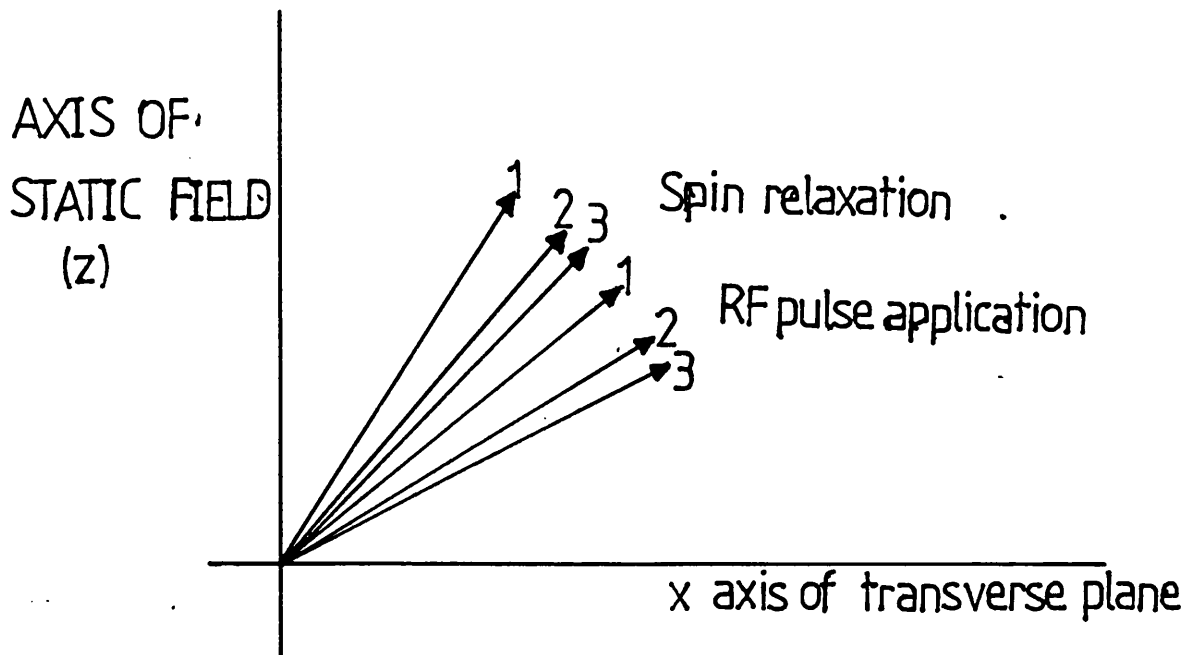


FIG.3.1 Relative inclination of the spin vector after subsequent applications of the RF pulse. TR is less than T1 for the spins, so longitudinal relaxation is incomplete during TR. The second RF pulse will increase the inclination of the spin vector, and relaxation during TR2 will result in a smaller component of longitudinal magnetisation than at the end of TR1. After several RF pulses the increase in inclination when the RF pulse is applied is equal to the loss in inclination when the RF pulse is removed.

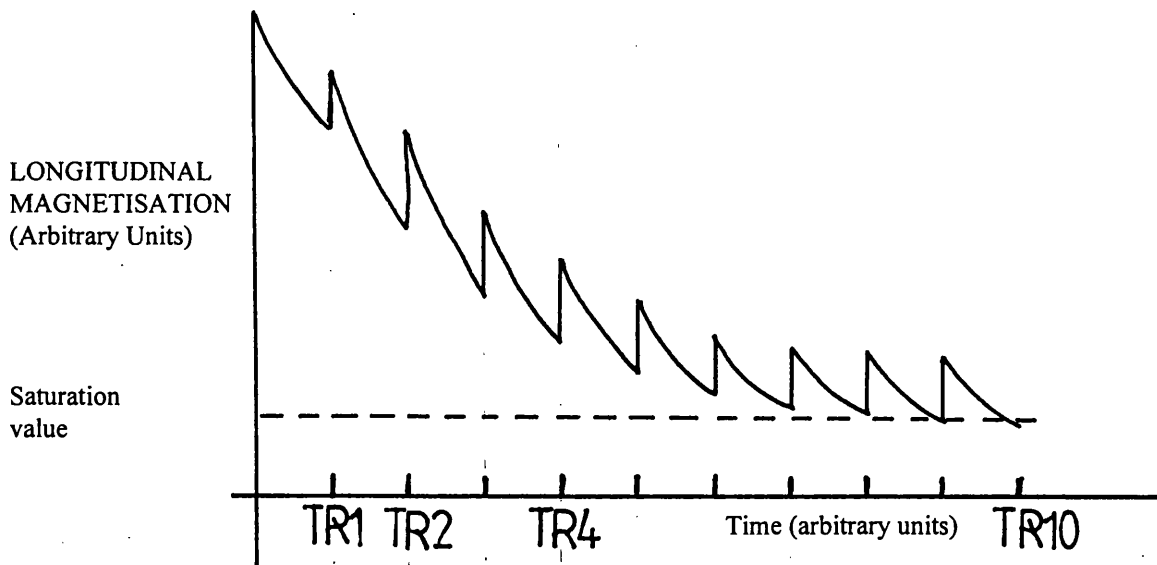


FIG.3.2 : Loss in longitudinal magnetisation on repeated applications of the RF pulse.

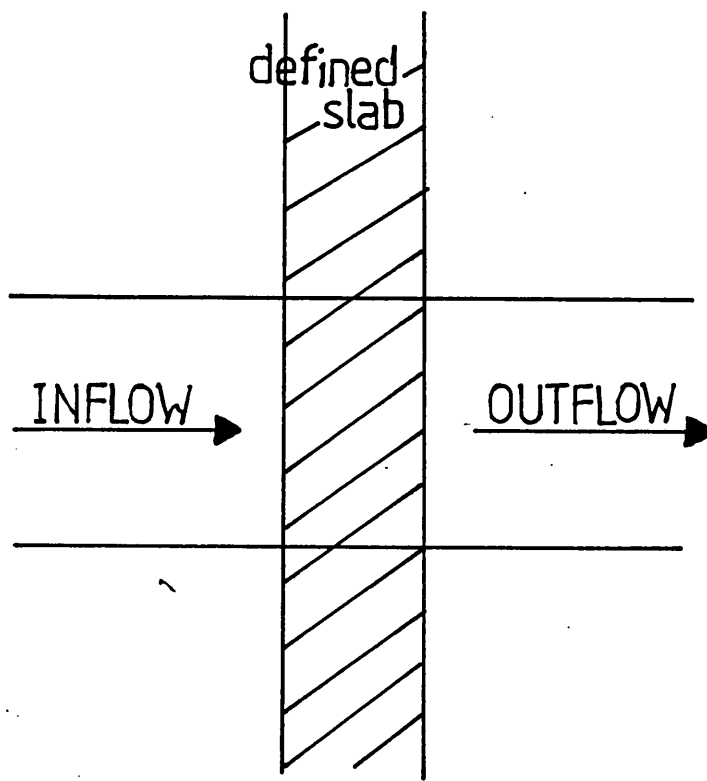


FIG.3.3 Inflow and outflow into imaged slab for 3D acquisitions.

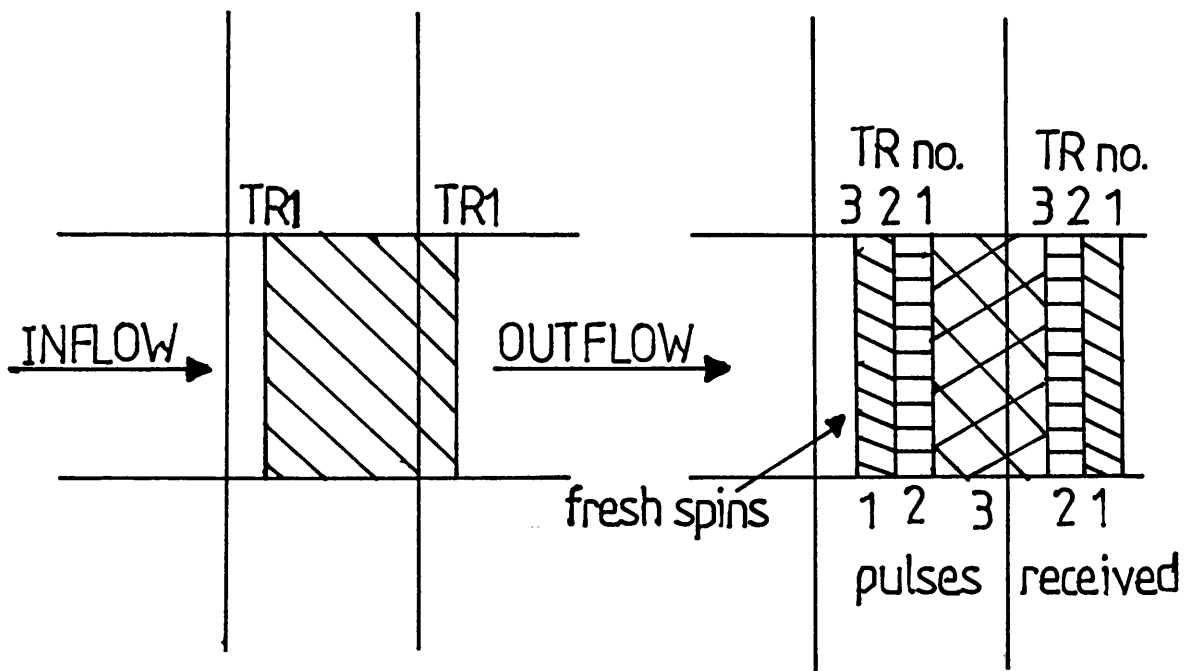


FIG.3.4 Saturation effects in 3D acquisitions.

Only spins in the imaged slice receive the RF pulse; For static tissue the same spins always get the RF pulse. Because blood spins are moving they get different RF pulses depending on their speed. During TR1 all the blood spins in the image volume get one RF pulse. Some then flow out of the volume and are replaced by the inflow of fresh spins.

FIG.3.5 Spin velocity effect on saturation.

The degree of saturation of blood spins depends on how far they move during TR. Slow flowing spins will receive many repeated RF pulses and will saturate. Fast flowing spins may leave the image volume before TR2.

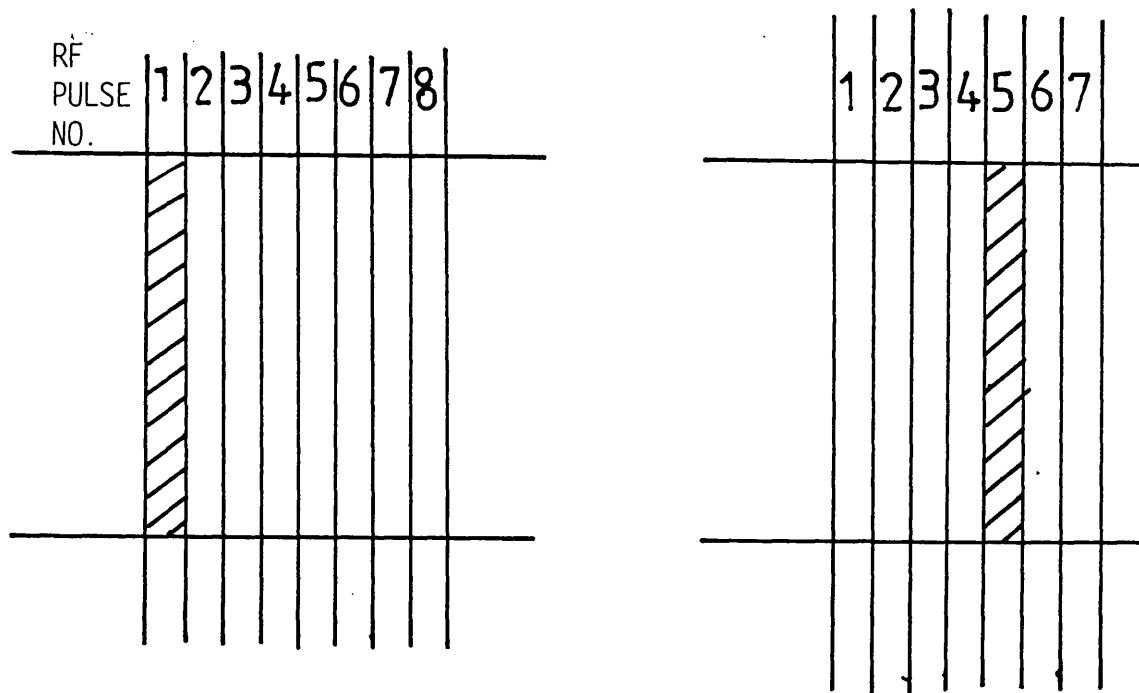


FIG.3.6 Saturation effects in 2D imaging. These are different from those for 3D imaging because the RF pulse is effective over a much smaller spatial range. Blood spins flipped during TR1 may have flowed far down the vessel before TR2 is applied. TR2 will then be applied to fresh spins and there is no saturation. Saturation only occurs if

$$\text{spin velocity} = \text{slice thickness} / \text{TR}$$

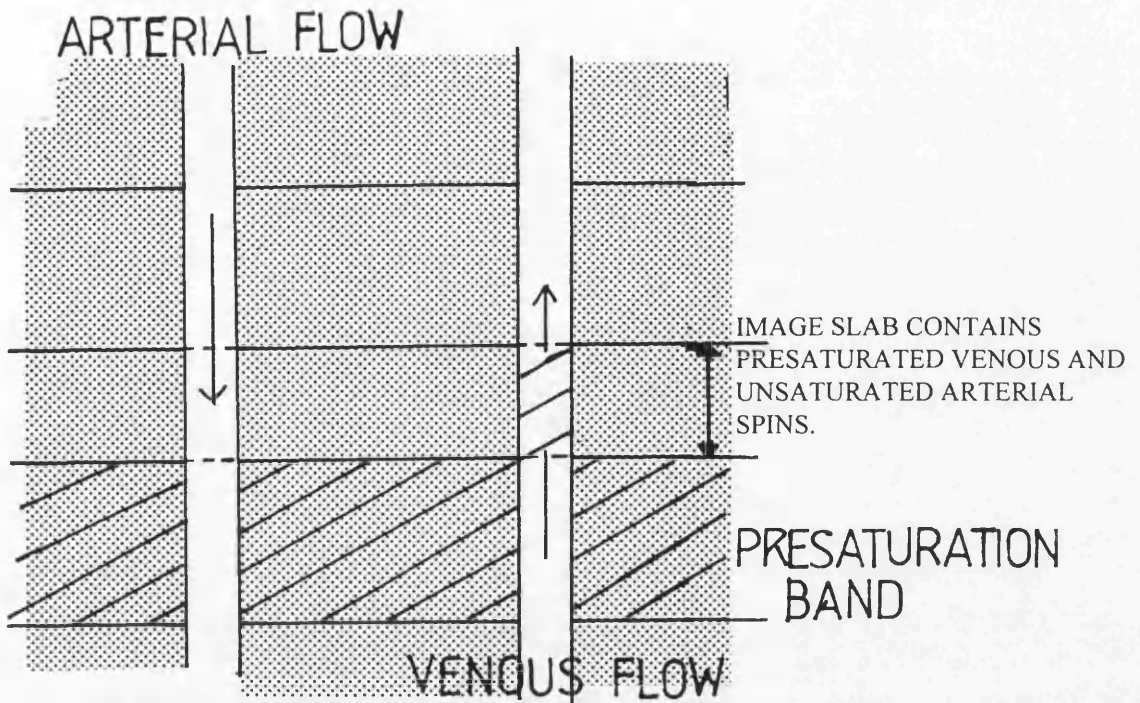


FIG.3.7 : Presaturation in vessel elimination.

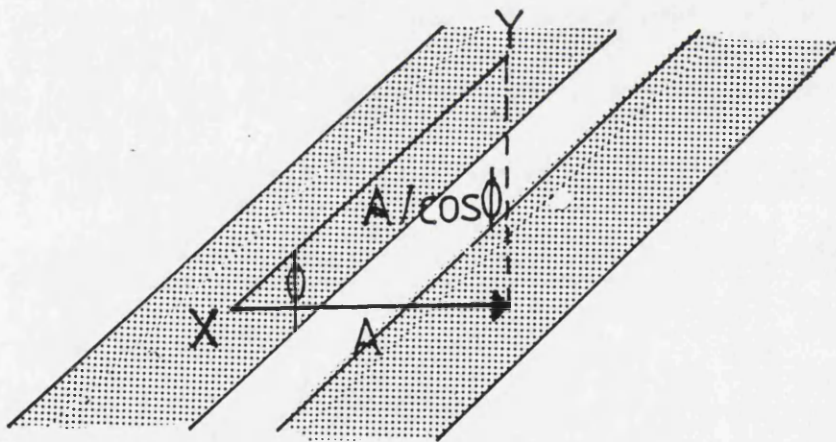
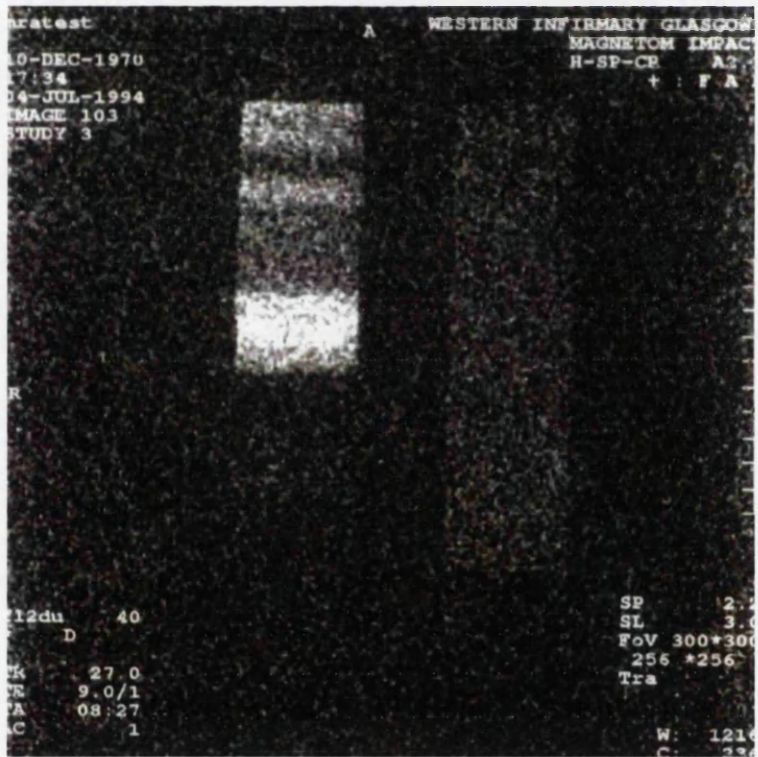
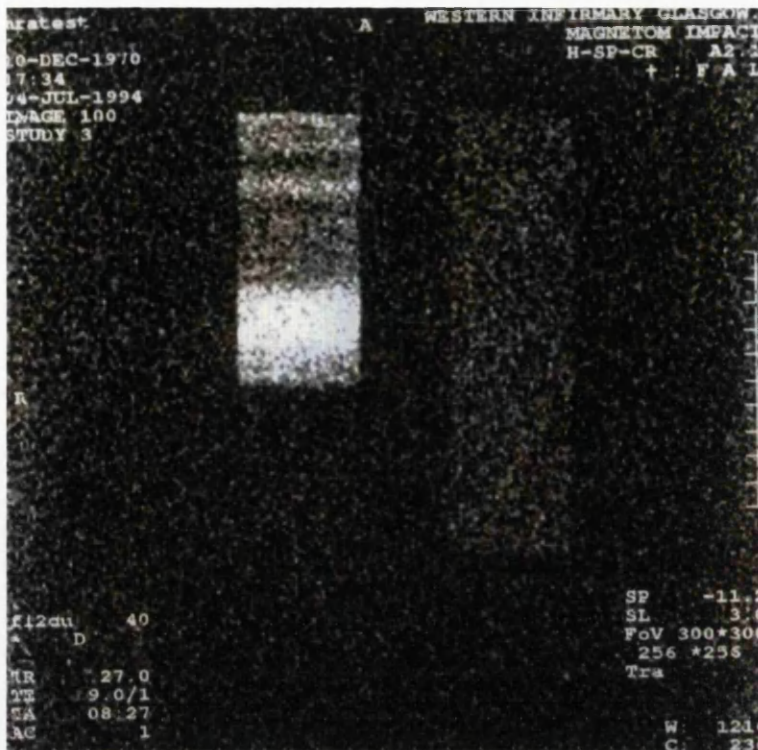


FIG.3.9 A spin moving with velocity  $A/\cos\phi$  in a vessel inclined at angle  $\phi$  will appear displaced by a horizontal distance A. This is because the spins move from X to Y between the application of the RF pulse and detection of the echo. Blood vessels superimpose on static tissue, and image clarity is lost.



**Figure 3.8**

The action of the presaturation pulse is revealed in this scan. The lower half of the rotating drum has been eliminated from the image by using a presaturation pulse which eliminates flow into the image volume. Flow out of the image volume is unaffected, and the top half of the drum appears clearly. The poor quality of this image is due to the fact that a low value of TR has been used in this acquisition. The banded appearance of the rotating half of the drum is explained in Chapter 9.

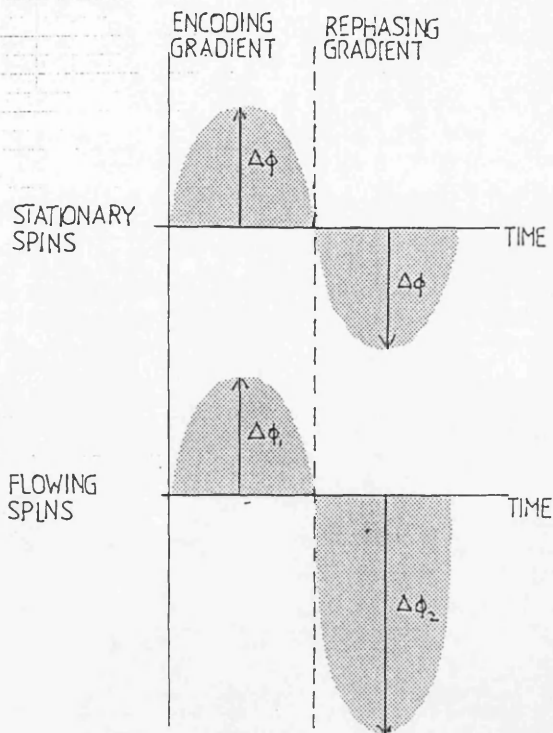
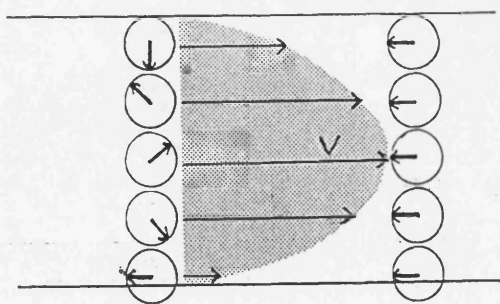


FIG.3.10 Phase change due to spin motion in encoding gradients. All gradient applications result in a change in the transverse phase of the spins. Dephasing gradients of the reverse polarity are applied to offset these. For a stationary spin, the magnitude of the gradient at the location of the spin is constant, so the resultant phase is zero. For a moving spin, the magnitude of the gradient at rephasing has changed, because the spin has moved in the field. The resultant phase is not zero, and spin dephasing due to velocity has occurred.



RELATIVE PHASES ACROSS LAMINAR FLOW PROFILE

FIG.3.11 Phase differentials across the vessel lumen due to laminar flow. AB represents the position of the spins at the start of TR. Faster moving spins in the centre of the vessel travel furthest in the gradient and receive the biggest change in phase.

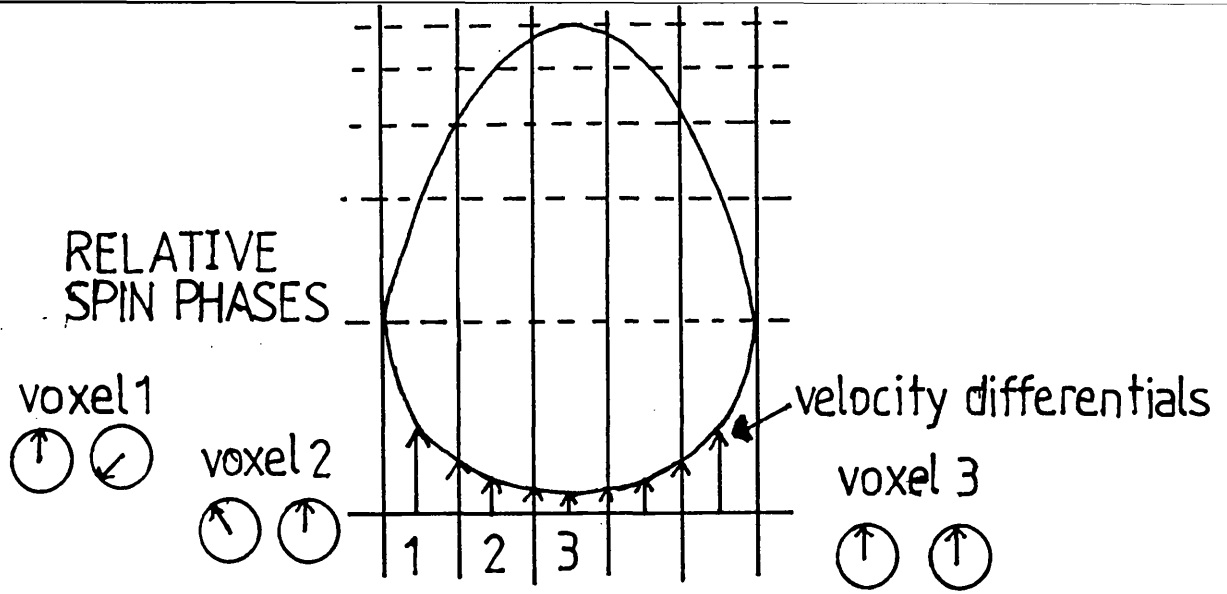


FIG.3.12 Effect on image intensity due to spin dephasing.

Spin phases are nearly the same at the centre of the vessel. At the walls where the velocity increases from zero rapidly along the laminar flow profile, the phase differentials between adjacent spins are much larger. Partial volume effects resulting from the summation of dephased spins will be much greater in the edge pixels, and signal loss at the vessel walls is likely.

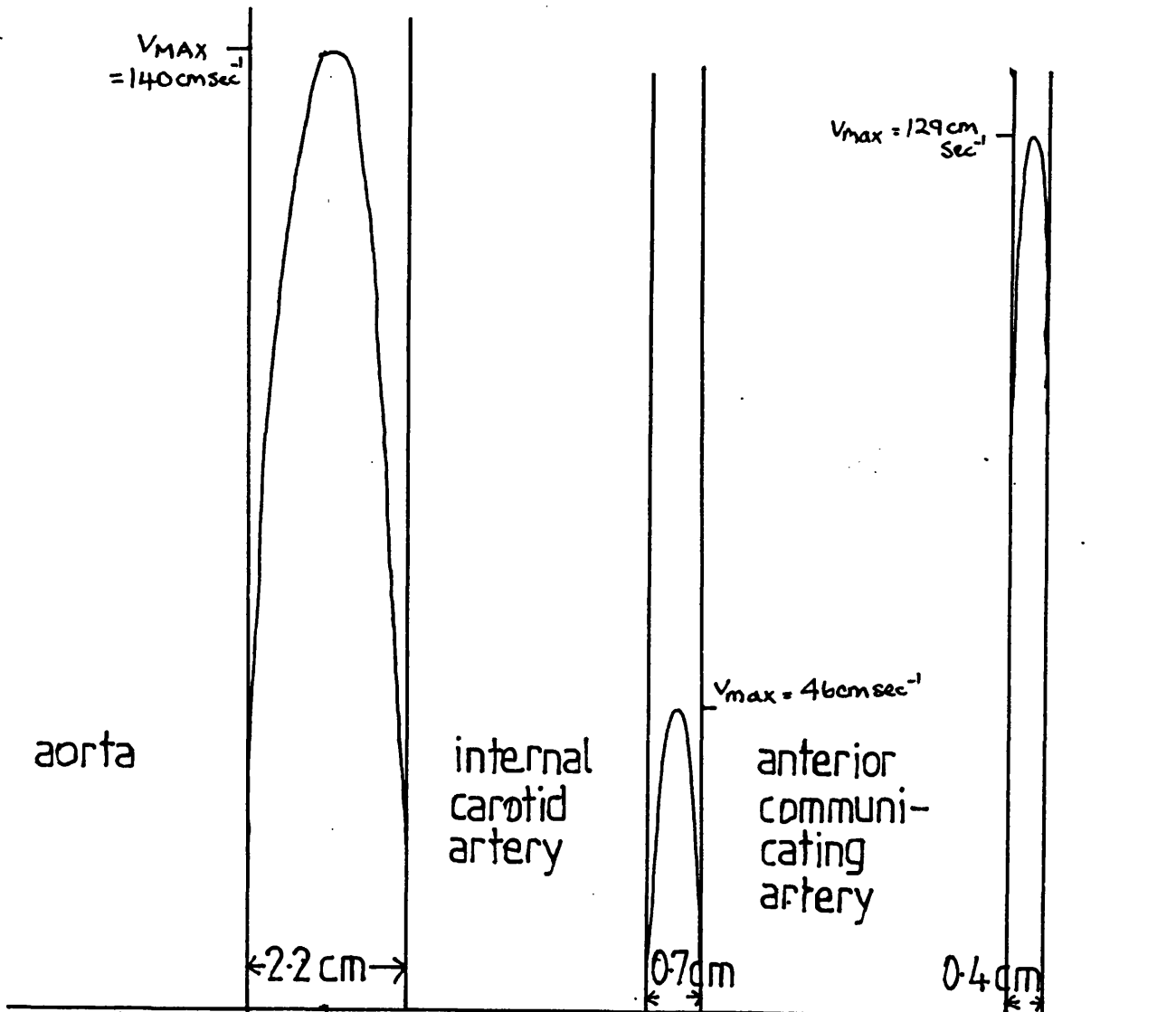
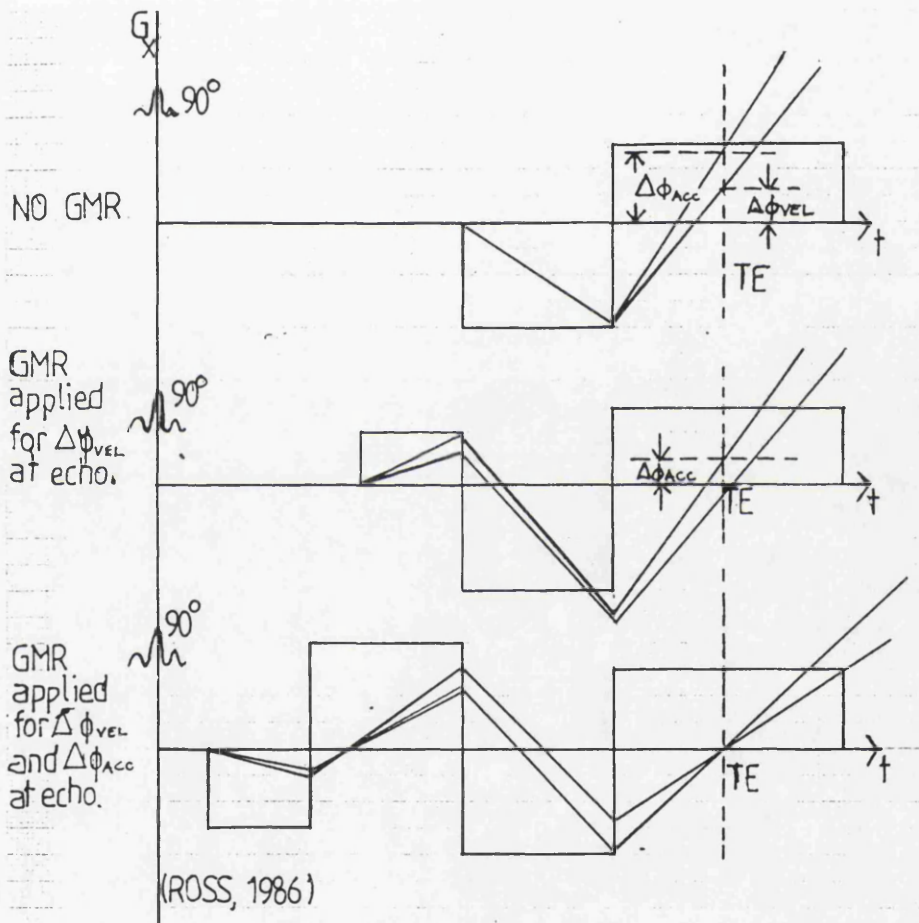


FIG.3.13 Laminar flow profile in major body vessels.

The vessel diameters are normal size, and the spin velocity vectors are scaled to 1/10th length.

FIG.3.14 Effects of gradient motion refocussing. Dephasing at echo due to velocity and acceleration of spins is shown separately. GMR is then applied to ensure that dephasing due to velocity is overcome, thus enhancing the signal obtained at echo. It is more difficult to overcome dephasing due to spin acceleration, but this can be done by using more gradient lobes, or enhancing those already applied to overcome velocity dephasing.



## CHAPTER 4 : PULSE SEQUENCES USED IN MRA

### 4.1 INTRODUCTION

Early MR imaging used the spin echo, saturation recovery and inversion recovery sequences, for all anatomical views. It was possible to image arterial flow with these sequences, the chief problem being that the TR's, particularly for the more common spin echo sequences, were long, so that total acquisition times for the volumes needed in the cases of arterial and venous flow were long, and so the images could easily be affected by patient movement (Manning, 1993). This chapter considers the advantages of applying fast imaging sequences which have reduced TR's because they use flip angles of less than  $90^0$ , and typically of the order of  $40^0$ , to image blood flow. The chief advantage can be illustrated as follows: normal spin echo ( $90^0$  RF flip angle) recovery to 95% of signal maximum occurs at TR's of about 600, 1500 and 6000msec for fat, muscle and CSF, at 1.5T respectively. With a  $20^0$  excitation pulse, however, 95% recovery occurs at TR's of 150, 400 and 1500msec also at 1.5T, respectively, yielding an approximate four fold reduction in imaging time.

### 4.2 TIME-OF-FLIGHT FAST IMAGING SEQUENCES

#### 4.2.1 THE FAST LOW ANGLE SINGLE SHOT (FLASH) SEQUENCE

The principle of fast low angle magnetic resonance imaging has already been described in Chapter 2. The potential imaging advantages of these sequences have already been listed, and they are so great that considerable effort has been expended to make fast imaging a commercial proposition, in that it has been developed to the point of being clinically viable. For the Siemens Magnetom

Impact Scanners used throughout this project, two types of fast imaging sequences are available. The first of these is the Fast Low Angle Single sHot (FLASH) sequence (Haase, 1986).

The RF pulse - slice select gradient combination was chosen to give a reduced flip angle whose exact value depended on the clinical application, but which was typically  $40^{\circ}$ . The unique feature of this sequence was the use of a spoiler pulse, which completely destroyed (i.e. defocussed) the relatively large residual transverse magnetisation after the echo was detected. This would otherwise remain before the application of the next RF pulse because of the greatly reduced TR. Wood (1987) has established that the spoiler gradients are most effective when applied along the slice select direction. This dephasing procedure had no precedent in the spin echo and gradient echo sequences which had been used prior to this. This FLASH gradient sequence is shown in Fig.4.1, and representation of the behaviour of stationary spins during each pulse/gradient application is in Fig. 4.2. The modified behaviour of moving spins in the same gradients is illustrated in Fig. 4.3.

The use of FLASH sequences for in vivo flow measurement was first reported by Matthaei, (1987). These authors used a ECG triggered pulse, and obtained 'reproducible delineation of time variant flow in the arterial system', which they thought to be the result of the inflow of unsaturated spins into the imaging plane. They also found it possible to quantify flow rate in the great vessels, using the same sequence.

#### 4.2.2 BLOOD FLOW IMAGING USING THE FLASH SEQUENCE

It is clear from the discussion of the recovery of longitudinal magnetisation for the FLASH sequence given above, that the strength of the signal resulting from this sequence will be different to that obtained from a spin echo sequence. The signal from tissue stimulated by the spin echo sequence is

$$S_{SE} = M_0 (e^{-TE/T2}) (1 - 2e^{-(TR - TE/2)/T1} + e^{-TR/T1})$$

where  $M_0$  is the initial longitudinal magnetisation, and all other constants have already been defined (Hendrick,1992).

For tissue imaged using FLASH the signal is

$$S_{FL} = \frac{M_0 (1 - e^{-TR/T1}) \sin\alpha}{(1 - \cos\alpha e^{-TE/T2*})} e^{-TE/T2*}$$

(Hendrick, 1992).  $\alpha$  is the flip angle. This is a specific form of the equation for the signal achieved when gradient echo imaging is undertaken, FLASH being a fast low flip angle gradient echo sequence. The behaviour of these two signals over a period of time is shown in Fig 2.9. Though the spin echo signal rises to a considerably higher value eventually, over short time intervals the FLASH signal is stronger, and hence there are image contrast advantages to using this sequence when small TR values are involved. The strength of the signal from the FLASH sequence is again flip angle dependent, though the overall profile is dictated by the combination of pulses and gradients used during its application.

This sequence appears to be particularly valuable in the imaging of flowing spins because

i) imaging times are much reduced, thus time dependent artefacts such as signal voids because of saturation are much fewer than in the case of spin echo flow imaging.

ii) problems of spin dephasing can be eliminated between repetitions by the use of the spoiler pulse. This would appear to be particularly useful when imaging moving spins, because apart from the  $T2^*$  effects, there are dephasing effects due to motion.

iii) image contrast is better at short TR.

Velocity dephasing effects which would mar the echo can be compensated for by the use of Gradient Motion Refocussing. Additional gradients can be applied in both the phase encoding and frequency encoding directions before signal detection, to maximise transverse magnetisation. FLASH sequences are usually used in the 2D mode when imaging blood, the 3D application being the imaging of static tissue.

#### 4.2.3 STEADY STATE FREE PRECESSION IN MAGNETIC RESONANCE

Carr (1959) devised a method of obtaining a FID which maximised the intensity of the transverse magnetisation. His sequence used sufficient refocussing gradients to ensure that the transverse magnetisation remained constant for the duration of the pulse sequence. He did not derive this sequence for the purposes of medical imaging; rather he was concerned about the possible benefits of imaging with flip angles intermediate between  $0^\circ$  and  $90^\circ$ , and this led him to take a fresh look at transverse magnetisation. In conventional spin echo imaging, with a flip angle of  $90^\circ$ , the spin flips directly into the transverse plane with the application of the RF pulse. With an intermediate flip angle, it appeared that new

transverse plane effects might be possible. The sequence is referred to as steady state free precession (SSFP) because in periods of time equal to or shorter than the spin relaxation times, the detected signal does not undergo significant changes in amplitude.

The implementation of this sequence involves the following steps. Its essential and unique feature is that the oscillating RF field be phase coherent from pulse to pulse. Thus when the RF pulse is applied, the phase of the resulting flipped spins in the transverse plane will always be identical. Following this, T2 dephasing effects in the transverse plane will follow a predictable and repeatable pattern for each pulse sequence application, and hence it is possible to plan the application of refocussing gradients which will ensure that, to all intents and purposes, the transverse magnetisation is constant. A great advantage of this sequence, as described by Carr, is that effects of field inhomogeneity can be eliminated to a large extent. This is why T2 rather than T2\* effects are important in transverse dephasing.

Carr showed that the detected signal was flip angle dependent. The null point at the centre of response for subsequent RF pulses of the same sign is indicated in Fig. 4.4. Practically it was found advantageous to eliminate this by reversing the phase of the RF pulse on alternate applications, thus shifting the entire response by  $180^\circ$ . These graphs also indicate the spatial periodicity of the SSFP response. The spatial wavelength is defined as the distance that must be moved in the applied gradient, such that the difference

in the precession angle during the time TR (between RF pulses) is  $2\pi$ .

#### 4.2.4 FREE PRECESSION IN THE STEADY STATE (FISP) SEQUENCES

FISP sequences are a practical and commercially available application of the SSFP sequences designed by Carr. Their implementation did not follow until 1986 (Oppelt), by which time considerable research and development had been devoted to the application of spin echo sequences to both stationary tissue and flow imaging. The practical problem of patient movement during scan times had become of paramount importance, and it had become imperative to devise methods of reducing scan times. Carr's paper of 1959 highlighted the fact that it was not necessary to use a flip angle of  $90^\circ$ . Oppelt et al. then realised that the pulse sequence repetition time could be reduced if the flip angle was reduced, since less time had then to be left for spin relaxation before the next RF pulse could be applied. If gradient echo refocussing techniques were incorporated into the sequence rather than spin echo refocussing techniques, repetition times could be further reduced. This was the case because the longitudinal relaxation of the spins did not have to be complete before the echo could be obtained.

The gradients involved in the imaging of static tissue spins by SSFP, as used in the free precession in the steady state (FISP) sequence devised by Oppelt, are shown in Fig. 4.5. The behaviour of stationary spins during the application of the pulse sequence gradients is illustrated in Fig. 4.6.

In the application of FISP to stationary spins, the RF pulse flips the spins through an angle intermediate between 0 and  $90^0$  (Fig.4.6a). The inclined spin then has both a longitudinal and a transverse component of magnetisation. All the spins are in phase in the transverse plane at this time, and the requirement that the phase of the RF pulse be the same every time it is applied ensures that the transverse phase of the spins is always the same at this stage of the sequence. T2 (rather than T2\*) effects dominate in this plane, and the spins dephase due to the application of the encoding gradients (Fig.4.6b). Meanwhile there is some longitudinal relaxation (Fig.4.6c).

When the slice or slab select gradient is applied, transverse dephasing results. A compensating gradient is applied immediately to refocuss the spins (Fig.4.6d). The read gradient is applied next, and this is also followed by a compensating gradient pulse. Phase encoding is timed to coincide with frequency encoding, and the echo is subsequently detected. The compensating gradients which have been applied ensure that there is maximum compensation for the slice select and read gradients at the centre of the echo. (Fig.4.6e).

However there is remnant dephasing due to the application of the phase encoding gradient (Fig. 4.6f). This would seriously weaken the FISP signal detected at the next application of the RF pulse, since it would prevent a steady state of transverse magnetisation being maintained.

To overcome this, the spins are focussed again before the RF pulse is reapplied. The sequence of 256 steps of gradient applied to

spatially encode the spins is re-applied in the reverse order, without subsequent echo detection. Thus the spatial encoding potential of these gradients is not used, and they are employed simply to rephase the spins. This is the mechanism used in the FISP sequence to maintain transverse magnetisation at a constant value.

#### **4.2.5 BLOOD IMAGING USING THE FISP SEQUENCE**

FISP has all the fast sequence advantages which FLASH has when it is applied to the imaging of blood flow. However the gradients it contains which affect spin behaviour in the transverse plane are significantly different to those of FLASH, and these will produce different imaging signal response. Additional gradients(GMR) to compensate for motion effects can be used with this sequence, and they are usually applied in both the slice /slab and read directions simultaneously. They are only rarely applied in the phase encoding direction because of the problems which would be encountered in compensating for the 256 steps used in phase encoding. Blood flow imaging is conventionally done by using 3D sequences, probably because of the efficacy of the phase-encoding gradient refocussing mechanism, and to obtain optimum image resolution by maximising the number of partitions in reconstruction. The detailed behaviour of flowing spins in FISP gradients is now described.

#### **4.2.6. BEHAVIOUR OF FLOWING SPINS IN THE FISP GRADIENTS**

Since any movement of spins in any field will cause spin dephasing, a detailed examination of the effect of FISP gradients on moving spins is necessary, if the potential strengths and pitfalls of the sequence in flow imaging are to be discussed. Their response is shown in figure 4.7.

Because of the spatial periodicity of the magnetisation in SSFP and because there is a finite time over which the steady state is established, there is an inherent flow sensitivity of interest in this technique. Moving spins will establish a different steady state response as they move in the encoding gradients, and they will be particularly affected by the periodic spatial variation in magnetisation, mentioned in 4.2.3. This effect of this on moving spins has been simulated through a computer program, and comparative results are presented in Fig.4.8 for static and moving spins, for total signal collected over 100 cycles of an SSFP pulse sequence (Patz, 1988). Fig.4.8 indicates clearly that little or no signal can be expected from spins imaged with any type of SSFP sequence, since the resultant intensity is zero for virtually the whole of the spatial wavelength.

A qualitative explanation of the problems that will arise in imaging flowing spins with an SSFP sequence is illustrated in Fig. 4.8. This type of sequence is unique in that it contains an additional set of phase encoding gradients, which are used to maintain the steady state of transverse magnetisation for stationary spins. The phase encoding gradient is the most complex encoding gradient since it involves the use of a sequence of 256 stepped gradient pulses. For a static spin, the position of the spin relative to the phase encoding gradient is the same, both when the gradient is used to spatially encode the spins, and when it is used simply to compensate for dephasing effects. In the case of a moving spin in flowing blood however, the spin is constantly moving through the encoding gradient. The magnitude of the 256 steps which are responsible for spatially encoding it are not the same as the magnitude of the 256

steps which are refocussing it. Indeed, it is likely that the effect of this second application will be to further dephase the spins. This will affect the detected signal in a unique way, and is discussed fully in chapters 9 and 10.

### 4.3 MAGNITUDE CONTRAST SEQUENCES

This scan technique can be used in blood flow imaging to give a subtraction image from which stationary tissue surrounding the vessels can be eliminated. The intensity of the blood signal is enhanced to maximum brightness at the same time. The chosen pulse sequence which may conventionally be spin echo, FISP, or FLASH is applied twice in an interleaved sequence. On the first application, velocity compensating gradients are used which compensate for velocity dephasing effects to the maximum extent. The signal from the blood spins is thereby maximised, whereas the signal from the stationary spins is unaffected. On the second application, velocity uncompensating gradients are used, which dephase the moving blood spins prior to echo, and again have no effect on the stationary spins. The signal from the blood spins is therefore minimised, whereas the signal from the stationary tissue is unaffected. On subtraction of the two images, maximum difference between the two blood signals give maximum vessel intensity in the reconstructed image. The stationary tissue on the other hand is eliminated from the image, since its intensity is the same in the two acquisitions.

Magnitude contrast is achieved in one of two ways in commercially available sequences. The first adjusts the phase of the RF pulse so that on the first application it is alternating, and on the second it is non-alternating. This means that the flipped spins first move

in a positive direction, and then on the second application move in the negative direction. This technique is applied in Constructive Interference in the Steady State sequences (CISS) (Casselmann et al, 1993).

In its second application the velocity compensation is achieved by the means of gradient motion rephasing. Velocity compensation (rephase) gradients are applied in the first sequence, and velocity uncompensation (dephase) gradients in the second application (Fig.4.9). They are known as rephase-dephase sequences as a result.

#### **4.4 CONCLUSION**

This chapter has described in detail the different gradient lobe structures of the FLASH and FISP low flip angle fast imaging pulse sequences. The advantages of these sequences over spin echo have been discussed. Both sequences were designed in the first place to image stationary spins, and their effect on these spins during a single pulse sequence application has been illustrated. However both sequences are also commonly used in practice to image flowing spins, and it is this application which is the concern of this thesis. The behaviour of flowing spins in the two sequences has been described, and indications have been given that their imaging capabilities for flowing spins will be markedly different. This is expanded upon in chapters 9 and 10.

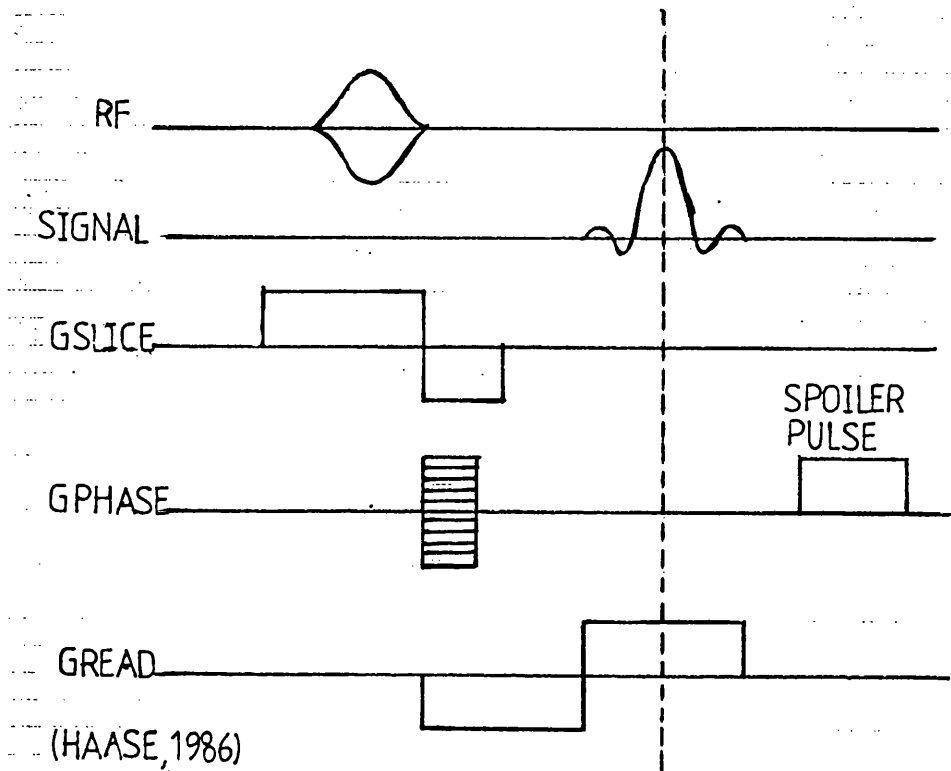
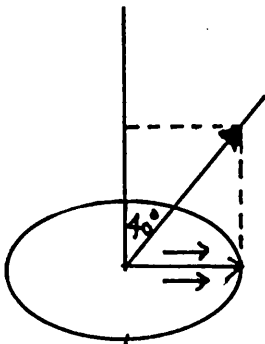


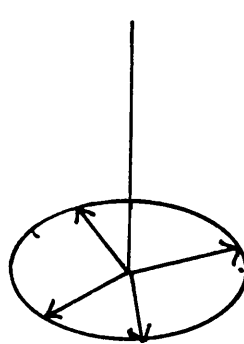
FIG.4.1 Gradients applied during the FLASH pulse sequence. The sequence can be used in this form for both stationary and flowing spins. However when used specifically for flow imaging, GMR is usually applied along the slice/slab and read axes.

This is basically a fast gradient echo sequence with the unique feature that a spoiler pulse is applied after the acquisition of the echo. This completely destroys any remnant transverse magnetisation by totally dephasing the spins, and its effect can be achieved either by the use of additional gradients, or by the use of a second RF pulse.

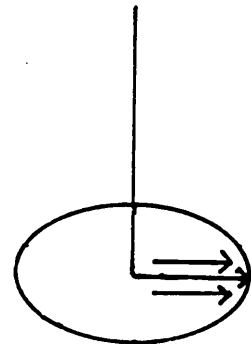
FIG.4.2 : Spin behaviour during application of FLASH pulse sequence gradients.



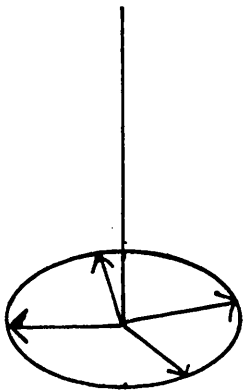
a) A low flip angle RF pulse is applied which introduces a transverse component of magnetisation. All spins are in phase.



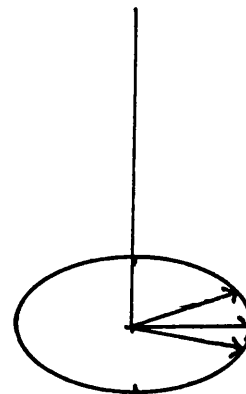
b)  $T_2^*$  effects dephase the spins in the transverse plane. G slice also produces dephasing effects.



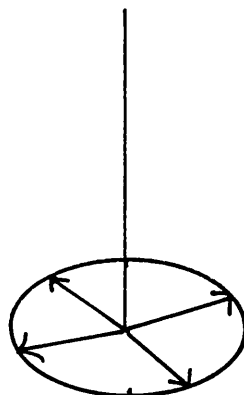
c) These effects are compensated for by a second gradient lobe, applied in the reverse direction.  $T_2^*$  effects are still apparent.



d) Application of  $G_{\text{phase}}$  and  $G_{\text{read}}$  gradients dephase the spins in the transverse plane.

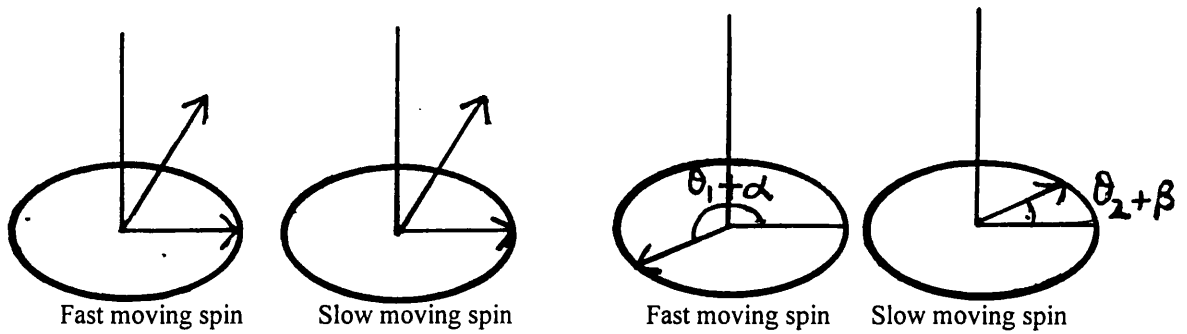


e) The gradient echo lobe refocusses the spins for maximum signal detection, overcoming  $G_{\text{phase}}$  and  $G_{\text{read}}$  dephasing effects.  $T_2^*$  effects are not accounted for. However they are not significant as in the spin echo sequence as  $TE$  is shorter.



f) A spoiler pulse is then applied which destroys remanent transverse magnetisation, before the next RF pulse is applied.

FIG.4.3 : FLASH sequence imaging of flowing spins.



Both spins are in phase immediately following the RF pulse

GPHASE, GREAD are applied simultaneously.  $\theta$  is spatial phase differential for adjacent spins,  $\alpha$  is phase shift for fast spin,  $\beta$  is phase shift for slow spin.

The echo is obtained with this phase differential between the spins. There is very little or no signal in the transverse plane because of spin dephasing due to motion. The spoiler pulse which follows is only effective in the case of slowly moving spins, where there may be some remnant of transverse magnetisation following the echo.

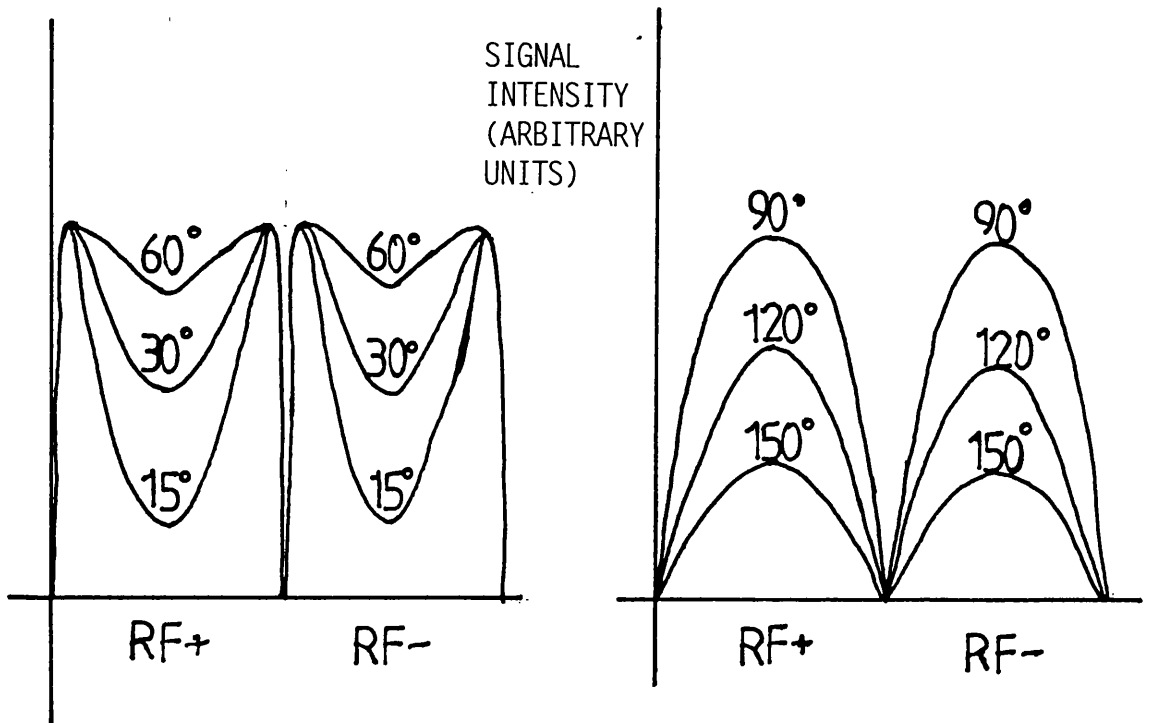
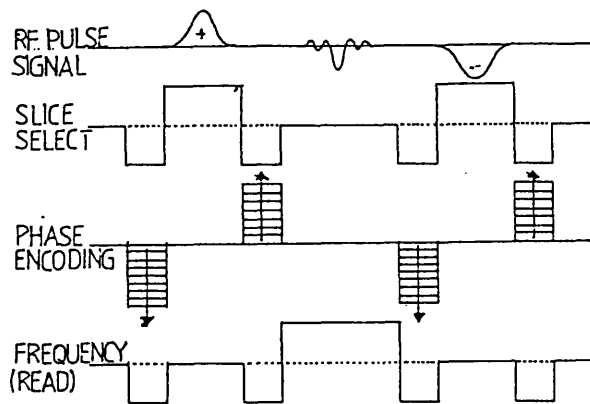


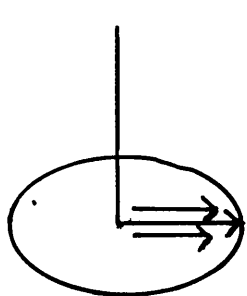
FIG.4.4 SSFP imaging- The dependence of the detected signal strength on the flip angle applied in the sequence is shown.



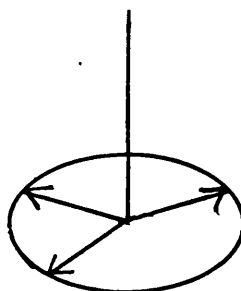
FISP GRADIENTS (OPPELT, 1986)

FIG.4.5 Gradients applied during FISP pulse sequence both when the sequence is used to image stationary spins and when it is used to image flowing spins. Gradient motion rephasing is applied in the frequency (read) and slice select directions, in addition to the compensating gradients applied for dephasing effects of these gradients on stationary spins, and is not shown in this diagram. The unique features of this sequence are the constant phase of the RF pulse on application, and the rewinder pulse which ensures steady state free precession in the transverse plane.

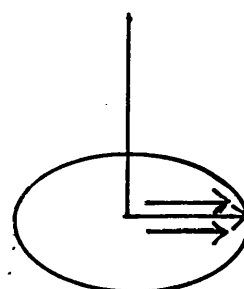
FIG.4.6 Behaviour of stationary spins in FISP gradients.



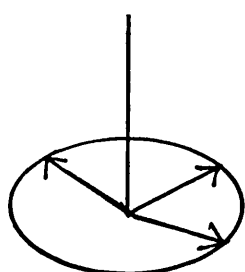
a) RF pulse and slice select gradient flip spins.



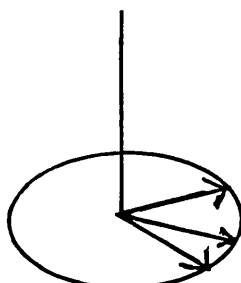
b) Spin dephasing is induced by slice select gradient.



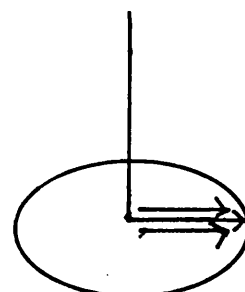
c) and is compensated for by additional gradient lobe.



d) GREAD and GPHASE inevitably dephase spins



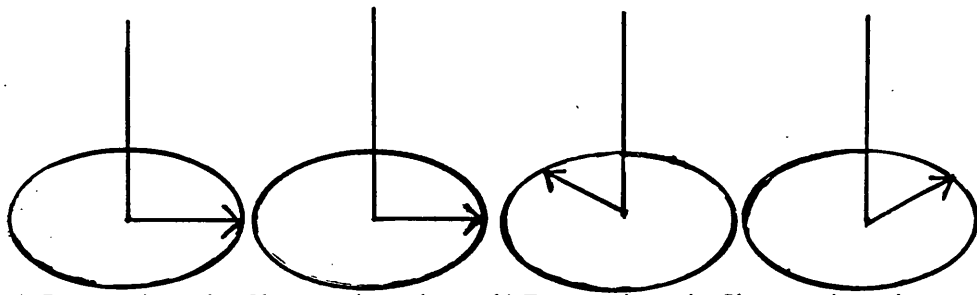
e) Compensating lobes refocus for GREAD



f) Following the echo rewriter gradients refocus for GPHASE

This last feature is unique to FISP sequences. no other sequence uses a set of gradients which exactly match the phase encoding gradients to compensate for the phase differentials which these set up. The timing of these after the echo ensures that there is maximum phase coherence in the transverse plane before the next RF pulse is applied. Maintenance of the phase of the RF pulse between applications ensures that it does not itself have a dephasing effect in the transverse plane.

FIG.4.7 Behaviour of flowing spins in FISP gradients.

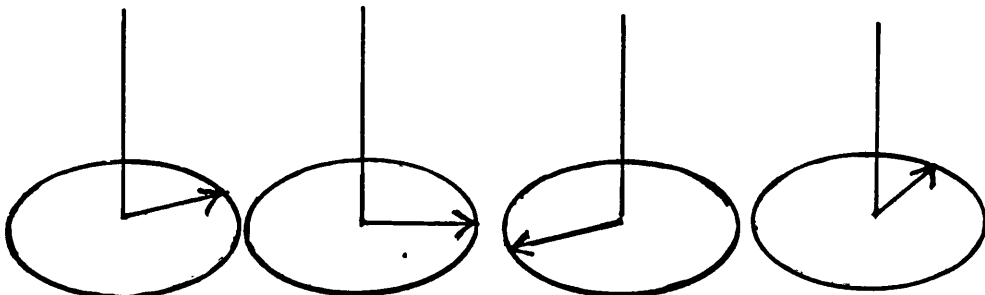


a) Fast moving spin Slow moving spin

b) Fast moving spin Slow moving spin

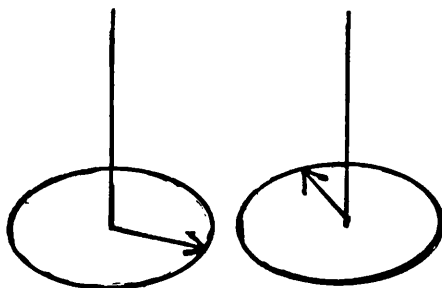
Spins are in phase immediately after RF pulse and slice select.

Fast spins dephase more than slow spins due to slice select.



c) Compensating gradient counteracts the slice select dephasing. Both spins have moved in the gradients by an amount depending on their speed, so refocussing is not complete.

d) GPHASE and GREAD dephase spins. Effect is greatest for fast spins.



e) Application of the rewinder gradient increases the differential between slow and fast spin phases because of relative motion in the gradients. Neither spin reverts to its non-dephased state because both have moved in the gradients.

Application of the rewinder gradients results in further relative dephasing of the spins.

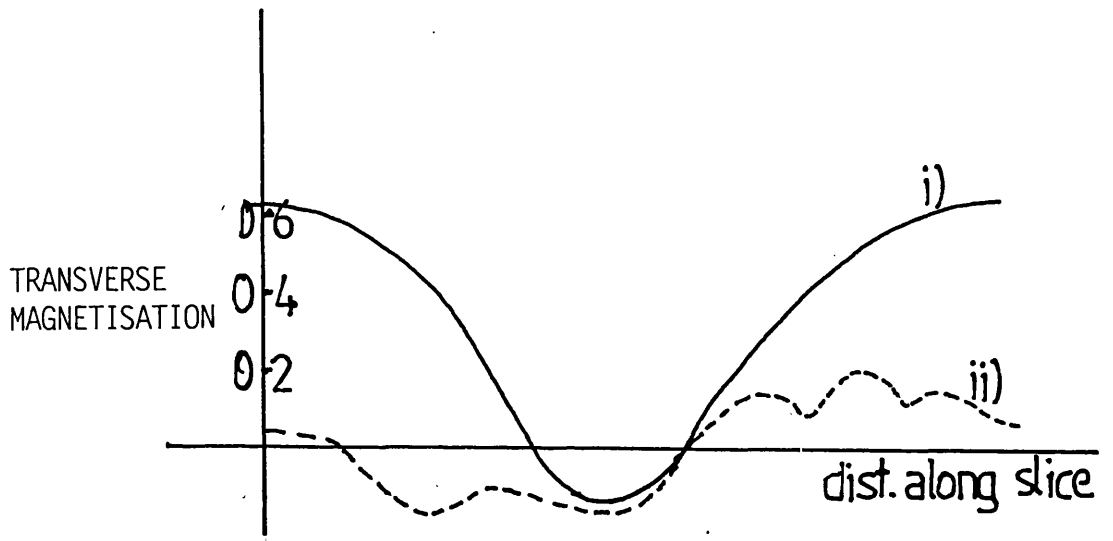
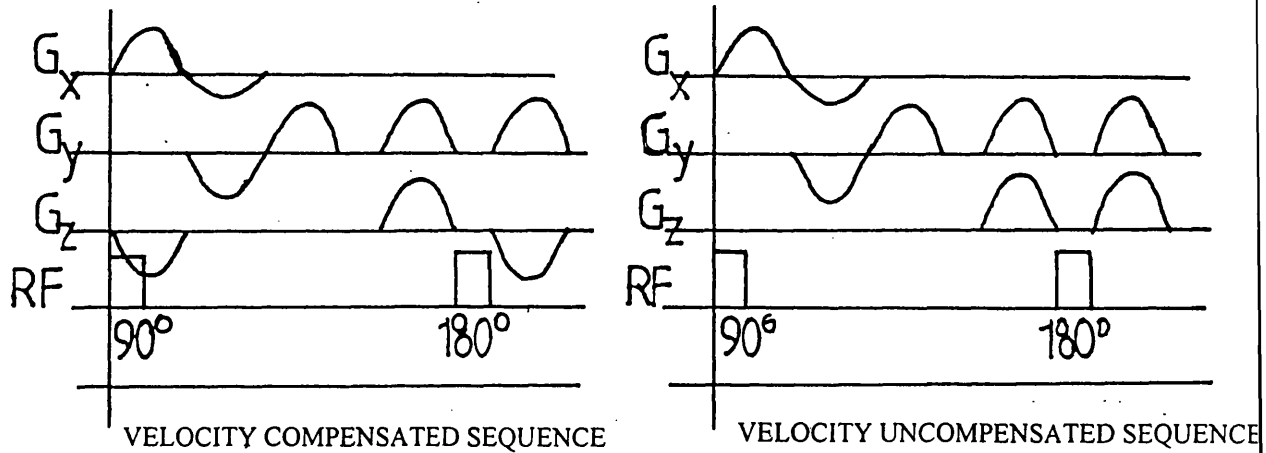


FIG.4.8 Computer simulation of the transverse magnetisation from i) stationary and ii) flowing spins using the FISP pulse sequence. 100 sequences were simulated (Patz 1988).

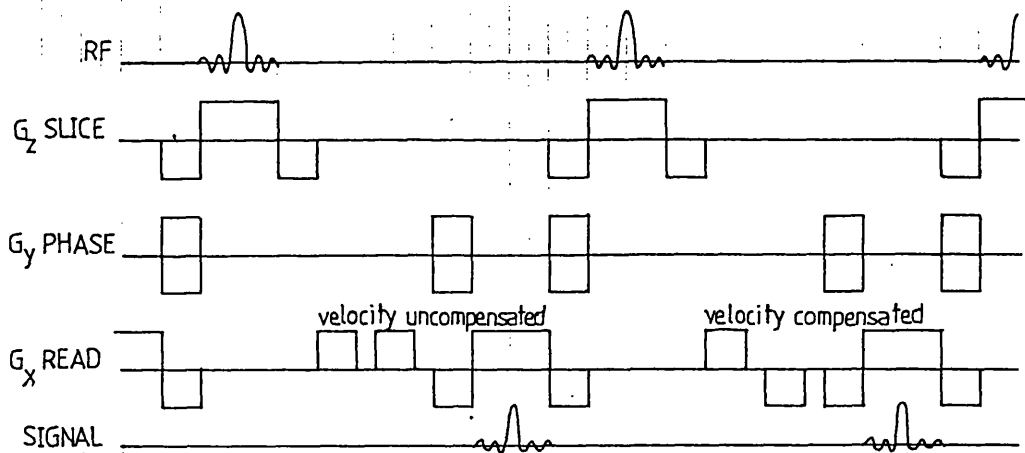
**FIG.4.9: THE MAGNITUDE CONTRAST SEQUENCE**

Any sequence type can be used as the basis for this interleaved method of imaging. One repetition of the sequence has maximum compensation for velocity dephasing effects, ensuring a strong signal from flowing spins. The next repetition has no velocity compensation. By subtraction of the two signals obtained in the image reconstruction process, a maximum difference signal is obtained. By contrast the stationary tissue images with the same intensity in both applications, since it is unaffected by the compensating gradients. It disappears on subtraction of the two images.

Here a) shows a spin echo sequence used in magnitude contrast, and b) shows the application of FISP.



a) Spin echo sequence the base unit for magnitude contrast imaging.



b) FISP the base unit for magnitude contrast imaging.

## **CHAPTER 5 : BLOOD FLOW RATES IN THE HUMAN BODY- a critical review of the literature, and of the recommended MRA pulse sequences for producing vascular visibility.**

The preceding chapters have dealt in detail with the dephasing effect produced between proton spins in a sample of flowing blood. The model used has been that of longitudinal laminar flow, and the changes in signal intensity which will arise because of the range of velocities across the diameter of the tube due to such flow, have been discussed in detail. Signal intensity across the vessel lumen varies because of the intra-voxel vector addition of proton spins at a variety of angles due to velocity induced dephasing.

In this chapter a critical review of the literature of blood flow estimates is made. A theoretical model to calculate blood flow is applied and compared with the literature results. From this values are assumed and will be used later to evaluate clinical applicability of MRA sequences. A critical appraisal is made of MRA sequences recommended by the manufacturer for certain anatomical regions, and inconsistencies are highlighted.

### **5.1.1 BLOOD FLOW RATES IN THE MAJOR ARTERIES**

The anatomical situation is more complicated than this simple model of longitudinal flow suggests. An anatomical atlas (Gray's Anatomy, 3rd Edn., 1989) indicates that very few vessels are longitudinal and non-branching for any great length. A vessel may bifurcate and it may contain tortuosities which take it through angles of anything from 0 - 180° relative to any of the three major axes. Before dealing with these variations, which will give rise to flow and

hence to imaging abnormalities, there are two more fundamental problems to consider; i) the velocity of arterial blood is not the same in all vessels, and ii) that in all arteries the flow is not steady but is pulsatile, this effect being most marked in vessels closest to the heart. Thus we have to consider not laminar flow, but pulsatile laminar flow over a considerable range of mean velocities. Will the relative dephasing effects induced by the expected flow rates be too great to be compensated for- i.e. will the spins not be refocussed by the gradients in the chosen sequence, so that the final signal intensity is too low to make the image clinically acceptable?

A search of readily available literature on blood flow indicates that most work has been done to date on volume flow through specific organs and regions of the body. This total volume flow, usually quoted in millilitres per second, cannot be broken down into linear flow rate through specific vessels since data on the number and diameter of specific vessels is not given. Such figures have been obtained as a result of, and for use in, physiological investigations such as transfer of waste products into the urinary system from the blood in the kidneys (Samson Wright, 1989). It is clear, however, that these volume flow rates are not appropriate when blood flow rates for imaging purposes are considered. The MR operator does not need to know what volume of blood in millilitres per second passes into and out of the cerebral cortex in one second. He rather requires to know the linear flow rate in centimetres per second through the separate vessels which feed the blood stream into, round and out of the cerebral cortex, for example through the

posterior communicating artery, or through the polygonal vasculature of the Circle of Willis.

The same new imaging techniques which require that the operator has a fairly accurate idea of the vessel linear blood flow rate being scanned are also providing the means to obtain accurate flow rate values. Doppler Ultrasound provides an illustration. In one application (DUPLEX), an image of the vessel will be generated. A modified application of Doppler US will give auditory signals instead of vessel delineation, (see chapter 1) and from this linear flow rates can be calculated. Several authors have now published papers which summarise extended experimental evaluations of flow rates obtained using Doppler (Hatsukami, (1992), Martin (1993)). Other papers yield isolated values for specific vessels as a result of specialised study. For example, Sondergaard (1992) in an evaluation of ECG gating, obtained  $45\text{cmsec}^{-1}$  for peak flow rate in the popliteal artery.

Similarly MRI pulse sequences may be specifically designed and applied to obtain quantitative blood flow rates, without actually giving an image of the vessel of interest. An MR pulse sequence designed to measure quantitatively blood flow rate may first be used to establish the flow rate in the patient vessel, and a second sequence designed to provide a VDU image may then be chosen appropriate to the known flow rate, to image the vessel of interest with maximum diagnostic advantage.

### 5.1.2 AN EQUATION FOR LINEAR FLOW RATE

The work which has been done on linear flow rate through major vessels shows some discrepancy of opinion as to reliable values. A rule of thumb quoted in Samson Wright (1989) shows that it is possible to calculate the blood velocity in any body vessel provided that a suitable value is first chosen for the velocity in the aorta, this being the primary artery. As the arteries subdivide, the radius of the individual branches decreases, but the total cross-sectional area increases. It can be shown that

$$\text{Rate of flow} = \frac{\text{rate of flow in parent vessel}}{\text{ratio of vessel area in branches to area of parent vessel}}$$

(Samson Wright). Thus the end point of the aorta is a total of about 8000 small arteries each with an internal radius of 0.5mm, and total cross-sectional area 16 times that of the aorta. On the above model the rate of flow will be aortic flow/16 .

### 5.1.3 SURVEY OF BLOOD FLOW RATES IN THE MAJOR ARTERIES

The computational model described above may be used to calculate flow rates in defined vessels provided that a reliable value is obtained for the flow rate in the aorta. This is in itself a complex consideration, because the variation in aortic flow rate is considerable during the cardiac cycle as a result of pulsatile flow. Figure 5.1 indicates typical blood velocity variation in the abdominal aorta during one cardiac cycle, and shows that the peak velocity varies over a dynamic range of  $130\text{cmsec}^{-1}$  during the cycle (Sondergaard, 1992). Although pulsatility is most marked in the aorta, it is present to some extent in all arteries, the velocity range decreasing as distance from the heart increases. There will

clearly be an appreciable difference between the numerical values of maximum flow rate at diastole, maximum flow rate at systole, minimum flow rate and mean flow rate taken as the average throughout the cardiac cycle. In addition, flow across the vessel lumen is laminar, and its velocity varies between zero at the vessel walls, rising to a maximum along a parabolic velocity distribution at the centre of the vessel lumen. For each value of flow rate quoted in the literature, it must be established which of these possible values is referred to before comparison can be made of values obtained by different authors.

Magnetic resonance angiography sequences can be used to establish flow rate values by utilising the change of phase induced in the spins by motion in the encoding gradients. The technique is known as velocity mapping (Killner (1993), Maier (1994)). Most commonly the phase shift imparted to spins by their motion in the encoding gradients, i.e. the velocity dephasing effect, is used to obtain a value for spin velocity using a form of the equation quoted in 3.6.1:

$$\phi = \gamma v \int_{t_0}^{t_e} G_s(t) (t - t_0) dt$$

where  $\gamma$  = the gyromagnetic ratio,  $t_0$  is the instant of the RF pulse,  $t_e$  = instant of echo,  $G_s$  = amplitude of section select gradient.

To obtain a mean value over the cardiac cycle, cine techniques have to be used to acquire multiple images (Meier, 1988), and an average flow rate can then be established.

Values for the peak aortic flow rate established by different authors are:

**Table 5.1 : PEAK ARTERIAL FLOW RATE (cmsec<sup>-1</sup>)**

70.0 (Meier,1988)
107.2 (Mogelvang,1989)
105.0 (Stahlberg, 1988)
100.0 (Stahlberg,1989)
140.0(Sondergaard, 1992)

The average of these quoted peak flow rates is 104cmsec<sup>-1</sup>. This has been used in the Samson Wright equation as a start value for aortic flow in both thoracic and abdominal directions, and the values of flow rates for other major vessels have been calculated using the Samson Wright equation. They are included in SAMSON WRIGHT A) in Table 5.2. A second set of values of arterial flow rates has also been obtained using the highest aortic flow rate value quoted here, 140cmsec<sup>-1</sup> (Sondergaard). These predicted values are shown in SAMSON WRIGHT B) in Table 5.2. Both sets of values can then be compared with experimentally determined values measured in a range of body vessels by several authors.

There is some correlation between the experimentally measured values and the calculated values when the maximum aortic flow rate of 140cmsec<sup>-1</sup> is used as a starting point. Discrepancies between other arterial flow rates derive from this and experimentally measured values for these vessels may be the result of poor guesswork about the ratios of vessel diameters. The lower aortic rate obtained as the mean of the peak flow rates obtained using MRA techniques

correlated poorly with the experimentally determined values. The experimental values are obtained using Duplex US techniques, and authors have pointed to the fact that blood flow rates have been found to vary depending on the measurement technique employed (Sondergaard, 1992). The relative reliability of the different techniques has not yet been established.

With Duplex US flow rate measurements, the reflected US signal is displayed as a trace on the cathode ray oscilloscope screen, and direct calibrated measurement can be used to obtain peak flow rates at diastole or systole, minimum flow rates, or mean flow rates over the cardiac cycle. The value achieved across the vessel lumen depends on the US frequency used to establish the flow rate. Hatsukami (1992) uses maximum reflected frequency to quote centre stream velocity data for peak systolic velocities. Martin (1993) presents mean, peak and end systolic velocities grouped according to age range. In table 5.2 the peak systolic velocity for the age range 40-59 is quoted. Dewitt (1988) establishes peak velocity for diastolic flow.

It is debatable whether the peak flow rate or the mean flow rate is the best indicator for the clinician engaged in imaging flowing blood. Pulsatile flow is characteristic of all arterial flow, though the variation in flow rate because of it is most pronounced in the aorta. To ensure good image quality in magnetic resonance angiography, a pulse sequence must be used which can encode laminar flow at the highest pulsatile flow rate as well as at the lowest velocity.

Table 5.2

FLOW RATES FOR MAJOR VESSELS, AVERAGED FOR PULSATILE FLOW ( $\text{cm sec}^{-1}$ )

VESSEL	GANONG	MARTIN	HATSUKAMI	SAMSON	WRIGHT	STARK,	DEWITT
(A)	(B)	BRADLEY					
AORTA	140 ± 40			104	140	140 ± 40	
EXTERNAL	119 ± 21		98 ± 20	52	70	119 ± 21	
ILIAC							
COMMON	114 ± 24		80 ± 20			114 ± 24	
FEMORAL							
SUPERFICIAL	90±13		65 ± 20			90 ± 13	
FEMORAL							
POPLITEAL	69 ± 13	±	30 ± 45			69 ± 13	
COMMON	100 ± 20			50	70	100 ± 20	
CAROTID							
INTERNAL	100 ± 20			30	40	100 ± 20	
CAROTID							
VERTEBRAL	36 ± 9		58 ± 5			36 ± 9	36 ± 9
BASILAR	42 ± 10		61 ± 5	10	10	42 ± 10	42 ± 10
ANTERIOR			88 ± 6				52 ± 12
CEREBRAL							
MIDDLE			105 ± 6				62 ± 12
CEREBRAL							
POSTERIOR			72 ± 5				42 ± 10
CEREBRAL							
TIBIAL			45 ± 20	15	22		
PERONEAL			45 ± 20				
OPHTHALMIC							24 ± 8
CAROTID SIPHON							54 ± 3

All values listed by Stark and Bradley are taken from DeWitt and Wechsler (1988) apart from the values for tibial and peroneal arteries, which come from Jager, Ricketts and Strandness Jnr : Duplex scanning for the evaluation of lower limb arterial disease, in Bernstein (ed) : Non-invasive diagnostic technique in vascular disease; St. Louis. Ganong uses the same sources. Martin and Hatsukami provide original data.

#### 5.1.4 BLOOD FLOW RATES ADOPTED IN THIS STUDY

The following values have been adopted in this study, as appearing to be consensus values based on the figures quoted in Table 5.2:

Table 5.3

#### ARTERIAL FLOW RATES

averaged for pulsatile flow( $\text{cmsec}^{-1}$ )

These represent the maximum flow rate of the laminar flow profile.

ARTERY	v $\text{cmsec}^{-1}$
Aorta	140
External iliac	110
Common femoral	95
Superficial femoral	80
Popliteal	60
Common carotid	90
Internal carotid	90
Vertebral	40
Basilar	40
Anterior cerebral	60
Middle cerebral	70
Posterior cerebral	50
Tibial	60
Peroneal	60

#### 5.1.5 ANOMALIES IN FLOW RATE VALUES

The flow rates in the table above can only be taken as a fair guide to individual values. Blood flow rates can show marked variation with the age of the patient. BoecherSchnarz (1994) tested patients with subarachnoid haemorrhage, and included in the clinical study measurement of basal artery blood velocity. The 800 subjects were divided into two age groups, less than 55 years and more than 55

years. Blood flow measurements were taken in the basal cerebral arteries for at least three weeks following the onset of haemorrhage. Velocities were banded  $<90\text{cmsec}^{-1}$ ,  $90 - 120 \text{ cmsec}^{-1}$ ,  $120-160\text{cmsec}^{-1}$ , and  $>160 \text{ cmsec}^{-1}$ . The age dependence of velocity in subjects in the same state of health is revealed by the fact that whilst 32% of the population younger than 55 years had a basal artery velocity of greater than  $160\text{cmsec}^{-1}$ , none of the older age group had this blood velocity. Similarly, whilst 63% of the older group had slow flow less than  $90\text{cmsec}^{-1}$ , only 14% of the younger group had this velocity. These figures thus indicate that to use a single figure as a blueprint for velocity in a vessel of interest may be very misleading, unless reference is made to the age and state of health of the patient, since they are significantly different from the figures quoted by reference to recent literature in Table 5.3.

Evidence also exists to show that the flow rates through aneurysms (Nadel, 1990) and stenoses (Sitzer, 1993) are markedly different from those in the same vessel without clinical abnormality. For example, imaging problems in the region of a stenosis are to be expected if the intracranial parent vessel shows normal flow in the range  $30-45\text{cmsec}^{-1}$ , and an 85% stenosis in the vessel then increases the flow rate locally to  $100\text{cmsec}^{-1}$  (Sitzer, 1993). Sitzer's work also shows that for 20% stenosis of the carotid artery as estimated by conventional angiography, the peak flow rate is  $50\text{cmsec}^{-1}$ . In the same vessel for an estimated stenosis of 80%, the peak velocity is

250cmsec<sup>-1</sup>. This problem has not been sufficiently recognised elsewhere, even though it does have serious clinical implications. The practice at present in MRA clinical imaging is to estimate the degree of stenosis from the length of the signal void which follows it. If the pulse sequence used in imaging cannot detect the fast velocities encountered at the stenosis, then a false signal void may appear in the image because of this factor, and not because of the clinical condition of the vessel. Inaccurate diagnosis at this point might then lead to the patient undergoing a subsequent and unnecessary conventional angiogram, with its high associated procedural risks.

There is also evidence to show that there is wide variation in anatomical detail between individuals. That this will lead to variation in blood flow rate in non-average vessels can be seen from the use of the Samson Wright formula quoted above, where the ratio of the area of the parent to the child vessels is dominant in the calculation of relative flow rates. Detailed work has been done on anatomical variation in the vessels of the Circle of Willis (Gloger, (1994), Patruş (1994), der Zwan (1993)). The Circle of Willis is probably one of the most complicated sections of vascular geometry in the human body. It is also one of the regions where anatomical detail may vary greatly from individual to individual. 60% of Circles of Willis display anomalies. Commonly occurring variations from the normal or mean vasculature are:

1. The cerebral artery may be absent altogether, it may be hypoplastic, or it may be double or triple.

2. In 10% of subjects, one of the contributory vessels is narrowed, so that its role as a collateral route is impaired.
3. Segments of anterior and posterior cerebral arteries may be missing.
4. Increased vessel diameter may alter blood flow routes round the Circle of Willis.

In such cases, the clinician is faced with a multiplicity of imaging problems. Blood flow rates may differ greatly from established and expected values, due to changes in vessel diameter. Some segments of vessels may be absent from images because they are not anatomically present, and not because of poor imaging technique. The direction of flow in a specific vessel may even be different from that expected, and so if presaturation bands are applied, the vessel may erroneously not appear in the image. The clinician should at least be certain that the sequence he has chosen to obtain an MRA image of the Circle of Willis is the appropriate one for the potential range of longitudinal blood flow rates encountered in the component vessels, and the value of the phantom work done in this study is that it can help determine if this is true.

## **5.2 PULSATILE FLOW**

Arterial flow is pulsatile, unlike venous flow which is unrestricted except for the passage through valves. Pulsatile flow (der Graaf, 1992) is most marked in the aorta, where the pressure variations due to diastole and systole of the heart ventricles is carried over into the nearest voiding vessels. It cannot be regarded as having disappeared even in the most distant arteriole branches where, however, the much reduced flow rates mean that the velocity range

will be much less. The technique of cardiac gating is usually applied when imaging the aorta because of the large velocity range. The electrical signal which triggers the beat of the heart, and which can be detected by electrodes placed on the chest wall, is used to trigger the repeat in time of the MRA pulse sequence used in imaging- i.e. TR can be affected by the heart rate of the individual. Thus signal detection is always at a fixed point in the cardiac cycle, ensuring that the blood flow rate at the time of imaging is constant. even though the velocity may change by up to  $100\text{cmsec}^{-1}$  in the cardiac cycle. Without cardiac gating, the same sequence would have to image a random selection of velocities with equally random dephasing. On systole blood flow reaches a maximum in a positive direction, on diastole blood flow reaches a maximum in a negative direction, and for each velocity at and between these extremes the blood spins will assume a unique degree of dephasing. When the signals are summed in computer memory, there will be incoherent summation of the spin vectors, with resultant low intensity in the reconstructed image.

der Graaf (1992) monitored the pulsatility of flow in a range of major body vessels, and also recorded the change in signal intensity from a defined vessel volume during the cardiac cycle. He studied the abdominal aorta, the femoral arteries, the popliteal arteries, the aortic arch, and the internal carotid arteries. Blood flow was quoted in millilitres per second. For all but the internal carotid arteries, blood flow reaches a forward going maximum on diastole,

and achieves a reversal of direction to give a negative maximum on systole. In the internal carotid arteries, and, it may be assumed, in other cranial vessels more distant than these from the heart, reversal of flow direction does not occur. Values he obtained were

VESSEL	FLOW RANGE DURING CARDIAC CYCLE (ml/sec)
Internal carotids	+5 to +25
Abdominal aorta	-10 to +180
Femoral arteries	-2 to +25
Popliteal arteries	-4 to +10

Though these values suffer from the fact of being measured in ml/sec, as far as this study is concerned, they do provide a means of comparing the pulsatile effect in different body vessels. The changes in image intensity noted by der Graaf were found when he used a 2D TOF sequence with flip angles of  $30^{\circ}$  and  $60^{\circ}$ , the exact sequence not being specified. He found fairly uniform signal intensity at  $30^{\circ}$ , regardless of flow profile, whilst the scans obtained at  $60^{\circ}$  were considerably more sensitive to flow profile over the cardiac cycle.

For effective imaging, a sequence has to be available which will respond equally well to the whole range of velocities encountered in longitudinal flow in the vessels of interest. If this is not achieved signals similar to stationary tissue, if not signal voids, will be encountered. Cardiac gating would be deemed unnecessary if it were proved that the MRA sequence used could produce a uniform image intensity at all the velocities encountered in the vessel of

interest. There is the further problem of laminar flow across the vessel of interest, for which the sequence is required to respond equally well to zero velocity at the vessel wall and the maximum flow rate encountered at the centre of the strength of the drum phantom evaluation of sequences used in this is that signal intensities for each pulse sequence can be exactly monitored at controlled and known velocities, over a wide and continuous range simultaneously. The efficacy of the sequence in the clinical situation depends on this.

### 5.3 APPLICATION OF STANDARD MRA SEQUENCES TO MAJOR VESSELS.

That the effects of velocity dephasing introduced by different flow rates, not to mention the associated laminar flow, are not yet fully understood or confidently handled, is indicated by the range of sequences which is commercially available to scan different anatomical regions.

Standard angiographic sequences for the Siemens Magnetom Impact 1T scanner are included in Table 5.4 . They are listed according to the flow rate they are supposed to be able to image. It is clear that there is no pattern or regularity to the way the sequences are appended to particular vessels. The operator is given no clear reason for choosing one sequence in preference to another.

Aortic flow in the thorax apparently presents no major problems. There is only one sequence (FISP 3D) which is recommended for scans of this vessel, and the operator has only to choose whether to scan with a flip angle of  $40^{\circ}$  or  $20^{\circ}$ . Although the same range of

velocities is quoted for aortic flow in the abdomen, it is stated that a FLASH 2D sequence will give optimum image quality for this region. The FISP3D sequence used for the thoracic aorta is also recommended for the carotids in the skull. However although the velocity is of the same order of magnitude, the operator is not recommended to use a flip angle of  $40^{\circ}$ , but is given the option to do double slab imaging as well as single slab imaging. For carotids in the neck, where the flow rate is slightly higher, though still lower than aortic flow rate, there is only one recommendation, a FLASH 2D sequence. The other options presented contain presaturation pulses which will eliminate venous flow from the images. It is left to the operator to decide at what point carotid neck flow becomes carotid head flow, so that they can apply a FISP 3D sequence rather than a FLASH 2D sequence. Why it is necessary to change from one sequence to the other is not described.

The intra-cranial circulation presents the greatest problems to the operator since the region contains both vessels where the flow is regarded as slow ( $30-45\text{cmsec}^{-1}$ ) and also vessels where the flow is regarded as fairly fast ( $45-60\text{cmsec}^{-1}$ ). Should the operator opt to concentrate on imaging the lower velocities in this region, by choosing a FLASH 2D sequence, or a REPHASE-DEPHASE sequence which uses interleaved FISP 3D sequences to produce a subtraction image? On the other hand, it may be thought that the higher velocities in the ICV circulation will dominate the image, in which case the operator may select a FISP 3D sequence with sequence parameters different to those of the REPHASE-DEPHASE option.

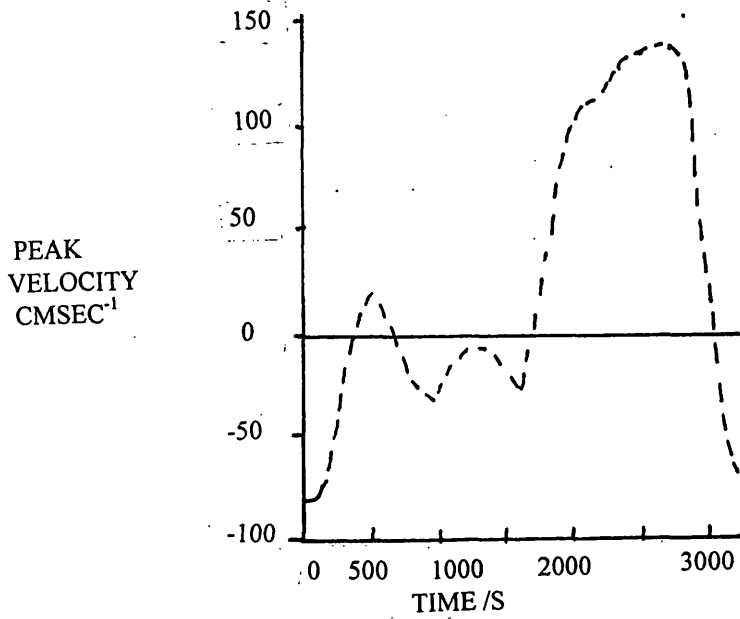
The descriptive notes to accompany the prescribed sequences indicate the potential strengths of each option. However it is only by trial and error, and by the accumulation of clinical imaging experience, that the real strengths and weaknesses of these different sequences will become apparent. Pre-clinical trials based on scans of the rotating phantom can, on the other hand, give a good indication of which sequence will best cope with the longitudinal velocities encountered anatomically, and give the operator confidence that he is likely to obtain the best clinical information. It is also likely that a sequence chosen on the basis of such quantitative evaluation will give the best results for any clinical abnormalities encountered in the region, since at least it is guaranteed to give optimum image quality in the velocity range encountered.

#### 5.4 CONCLUSION

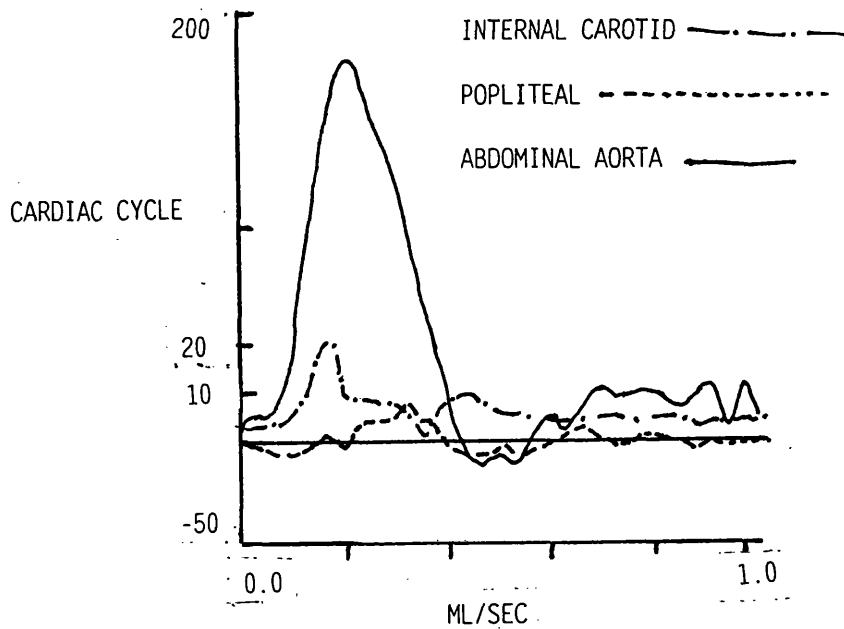
This chapter has highlighted the many problems which may be encountered in trying to establish the rate of blood flow in the vessel of interest. It has been shown conclusively that blood flow rates in a vessel of interest will depend greatly on the age and state of health of the individual. Flow rates quoted in the literature have to be examined to see exactly which parameter of pulsatile laminar flow they represent, and it has been shown that such values can be at best only an order of magnitude guide to the actual flow rate in the patient to be scanned. A case has been made for the inclusion of flow rate measurement in the individual vessel

between blood velocity and appropriate pulse sequence. It is the premise of this study that diagnostic inaccuracies occur because the pulse sequence will not detect spins at all longitudinal flow rates encountered, and it appears that the only sure way to overcome this problem is to establish individual patient vessel flow rate before the scan to image the vessel is done. The increase in discomfort to the patient because total scan time is increased if a velocity measurement is done before imaging is undertaken, is counterbalanced by the guaranteed increased accuracy of the image then obtained.

FIG. 5.1 Variation in blood flow rate during the cardiac cycle.



a) Phantom simulation of aortic flow in the abdominal aorta. Peak longitudinal flow rate across the tube lumen is quoted in  $\text{cmsec}^{-1}$  (Sondergaard, 1992).



b) Comparative pulsatile flow in the abdominal aorta, the popliteal artery and the internal carotid artery. Volumetric flow in  $\text{mlsec}^{-1}$  is illustrated (de Graaf, 1992).

## CHAPTER 6 : THE DESIGN OF THE ROTATING DRUM PHANTOM

The purpose of the phantom used in this study, as has been described in the first chapter, is to permit quantifiable and controllable studies of flow. In an evaluation of the applicability of various angiographic sequences to clinical imaging of blood flow in the body arterial system, it is essential first of all to know how each sequence will cope with the longitudinal flow rates commonly encountered in these vessels. If a sequence produces poor quality images of longitudinal flow because of velocity dephasing effects, it can then be assumed that it will not perform satisfactorily in more complex flow situations, such as those encountered in tortuosities, aneurysms and stenoses. In this chapter flow phantoms are reviewed and compared. The design of the rotating phantom is described, and a novel approach is taken to overcome local abnormalities in image intensity which has not been identified as a source of error by previous investigators.

### 6.1 TUBE PHANTOMS

The first and most common approach to this problem has been to mimic vessels of the arterial system using plastic tubing, which is usually mounted for convenience in a perspex box containing a supporting gel (Fig.6.1). The different vessel diameters are represented by tubing of various diameters, and blood flow rates are simulated by using a variable pressure head for the liquid flow.

Phantoms of this kind have been constructed to look at effects of longitudinal flow rates, (Stahlberg 1986, 1987, 1989) effect of flow at different rates round bends of different angles (Asai, 1992), and

to look at the effects of constrictions on flow, such as would be encountered with a stenosis (Sondergaard 1992, Stahlberg 1990, 1992). Different percentages of the tube diameter can be restricted by the use of plastic barriers in the tube.

The problem with these phantoms is that they study too many problems at once. The flow down the plastic tubing is probably laminar, and so the flow profile will depend on the viscosity of the liquid used. However authors do not attempt to simulate the viscosity of in vivo blood. Shimizu (1986) and Asai (1992) used water flowing through vinyl tubes. Other authors do acknowledge that since MRA relies on the signal generated by magnetic spins, it may be important to simulate the magnetic properties of flowing blood in the flow medium used, and in these cases they introduce ions into the water. Duerk and Pattany (1988) use copper sulphate, and Sondergaard (1992) uses manganese chloride. Kilner (1991) uses a rotating drum phantom filled with water doped with copper sulphate. He does not indicate how he deals with the problem of the movement of the water in the drum during its rotation. Valk (1986) uses in vitro bovine blood. This may appear to be a better choice, but the relaxation properties of blood alter once it has left the carcass. The change in the relaxation properties of human blood once it leaves the body are commented on in chapter 7.

There is a practical problem to taking the tube phantom approach in that it proves to be a lengthy process to arrange flow conditions which simulate the accepted range of flow velocities in the human body, and most authors limit themselves to studying a limited number of discrete velocities.

## 6.2 ROTATING DRUM PHANTOMS

The second approach to the problem of studying the imaging of blood flow has been to use a drum phantom which rotates at a constant and measured rate (Nordell 1988, Tarnawski, 1988, Wirestam 1994, Summers 1994). The drum is filled with a rigid gel, with each point in the gel moving with a rotational velocity which depends on its radial position within the drum. In other words, a range of velocities is generated simultaneously.

Two of these phantoms use a single drum (Summers, Tarnawski). In Tarnawski's model, the drum is driven by a stepper motor necessitating a very long driving belt to the rotating drum. Summers' abstract does not give design details. The phantom developed by Nordell (1988), on the other hand, consists of three drums, the centre one which rotates, and two narrower stationary disks which lie on either side of the rotating drum, all containing the same gel. Nordell reconstructs phase images from his scan data (see chapter 2), and the function of the stationary gels seems to be to test that indeed there is constant signal intensity across them, by reconstructing the phase image for each of the static drums. The signal for these has zero gradient, in comparison to the linearly increasing signal obtained across the rotating gel. The static drums thus monitor imaging performance in that discrepancies from the constant horizontal signal for the static drums would indicate that there were local inhomogeneities in imaging conditions.. The phantom used by Wirestam does not employ a static reference drum, nor does that of Tarnawski.

When the rotating phantom used in the study described in this thesis was designed, it was also appreciated that the images of the rotating gel could be marred by local irregularities in the signal generation and detection process such as those due to inhomogeneities in coil geometry (Condon 1987a). These would themselves impart signal intensity variations to the image. Any disturbance in the detected signal would be a gradual and not a catastrophic change, but it would falsify results which would otherwise be assumed to be dependent only on the velocity of the rotating gel spins. This system inhomogeneity factor can be eliminated from the evaluation process by including a static drum of dimensions equivalent to those of the rotating drum, and as close to it as possible, in the rotating phantom design. If the signal from the rotating gel is divided by the signal from the static gel - i.e. the signal is normalised, the resulting intensity is indicative of sequence response to velocity only, to within the experimental limitations of the equipment. The normalisation procedure provides a quantitative method of eliminating inhomogeneities from the signal evaluation procedure, and is an improvement on the qualitative comparison undertaken by Nordell. It is later proved (see chapter 8) that normalisation of image intensity has a second function which was not foreseen when the phantom was designed. It is proved in this chapter that deductions about image intensity made on the basis of phantom scans can be applied to in vivo scans only if there is good correlation between the relaxation properties of the phantom gel and of in vivo blood. Calculations presented in this chapter reveal that the normalised image intensities are independent of relaxation times, and hence information for use in the clinical situation can be extrapolated directly from the phantom scan data. This latter

aspect of the normalisation procedure is, as far as the author knows, unique to this study.

### 6.3 BLOOD FLOW VELOCITY SIMULATION BY THE ROTATING DRUM PHANTOM

It is convenient to think of the rigid gel in the drum as a series of concentric annuli. Concentric rings of the rigid gel in the drum move with different rotational velocities which depend on their radius of rotation in the drum (Fig. 6.2). The laws of circular motion apply to the drum, so that at a distance  $r$  from its centre, and for a drum rotating at an angular velocity  $\omega$  radians per second, the tangential velocity of the drum is

$$v = r \omega \quad \text{cmsec}^{-1}$$

### 6.4 DESIGN DETAILS FOR THE ROTATING DRUM PHANTOM

The rotating drum phantom is shown in entirety in Fig.6.3 with the details of the drums shown in Fig. 6.4. The drums are constructed of perspex and are each 19.1cm in diameter and 5.0cm thick. They are mounted on a perspex axle of diameter 2.6cm, the separation of the drums being 1.7cm. The internal diameter of the phantom is 18.6cm. Because a conventional electric motor cannot be used in the magnetic field of the imager, the rotating drum is driven by an air motor controlled by the pressure of compressed air, from a 4bar supply. The motor is valve controlled, and connected to the rotating drum by a driving belt housed in a perspex casing, rotation rates of 60-120rpm being possible. This means that longitudinal flow rates from 7 - 110cmsec<sup>-1</sup> can be studied, depending on the rate of rotation. The rate of rotation can be monitored frequently during the scan by counting the number of appearances of a horizontal black bar stuck

to the thickness of the drum, for a constant time interval. The gel is introduced into and removed from the drum by use of holes in the circular face which are sealed by means of rubber disks and plastic washers.

The overall length of the base of the phantom is 1.5m, and the weight of the base, coupled with the inertia of the drums, is sufficient to ensure that there is no lateral or vertical movement of the drums, or any associated vibration, during their rotation.

It is a limitation of the phantom that it cannot at present achieve higher rates of rotation. Normal body blood flow rates have been shown, in chapter 5, to encompass the range  $0-180\text{cmsec}^{-1}$ , and in cases of vessel abnormality or patient illness they may rise to twice these flow rates. To enable this range to be simulated by the phantom,

- a) a higher pressure air supply could have been used.
- b) A gear wheel with a smaller number of cogs could have been added to the rotating drum.

A second limitation is that the plane of rotation of the phantom is fixed at present to align with that defined by the slice/slab (z) axis and the phase encoding (y) axis of the MR scanner. Thus only the effects of these two encoding gradients on the spins can be

tested, and no experimentation is possible along the frequency encoding axis. To achieve this, the plane of the rotating and static drums would have to be rotated through  $90^{\circ}$ . The rotation of the drum under these circumstances would necessitate the introduction of a worm gear system.

## **6.5 CONCLUSION**

This chapter has indicated that it is necessary to take into account the relaxation properties of in vivo blood when constructing the imaged medium used in the rotating phantom. The work which has been undertaken in this study to devise a gel which mimics the magnetic properties of in vivo blood as closely as possible is described in the next chapter.

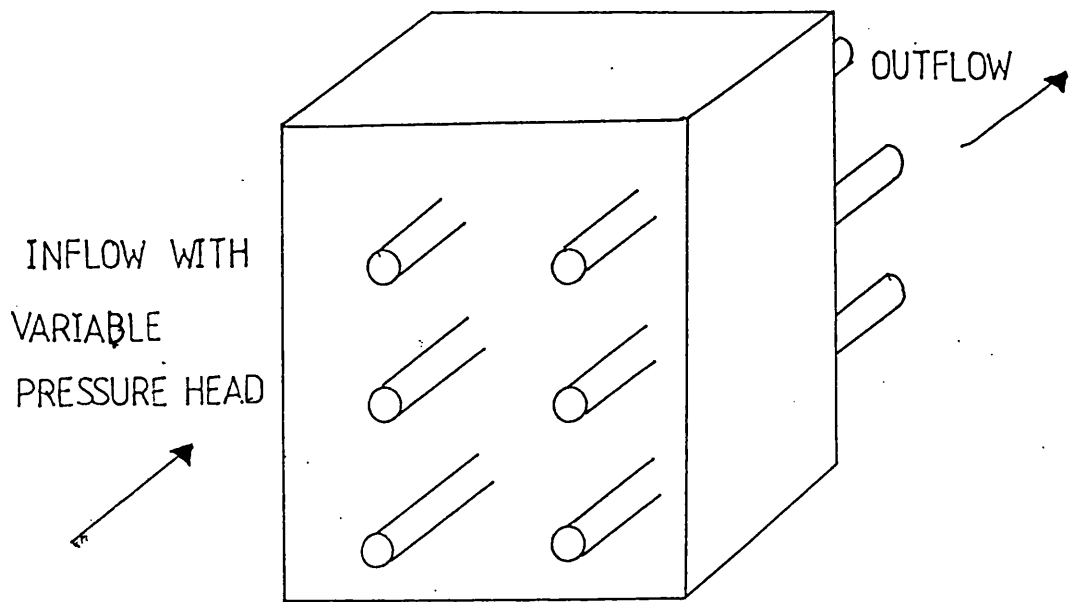
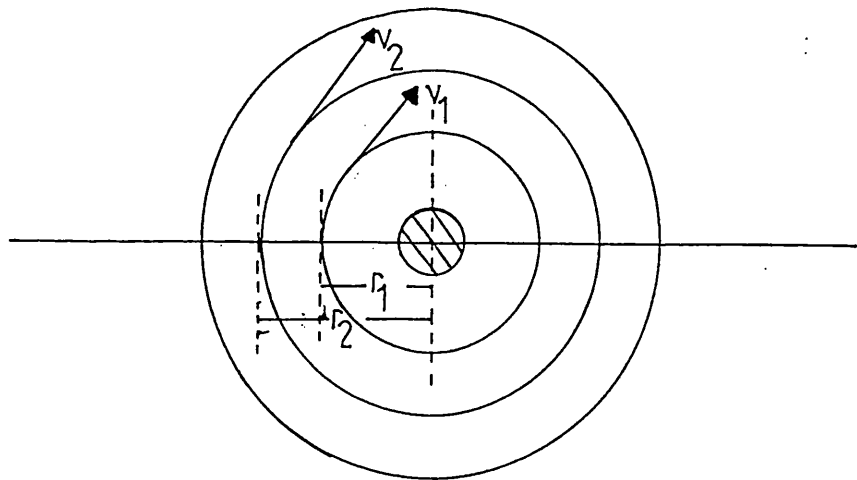
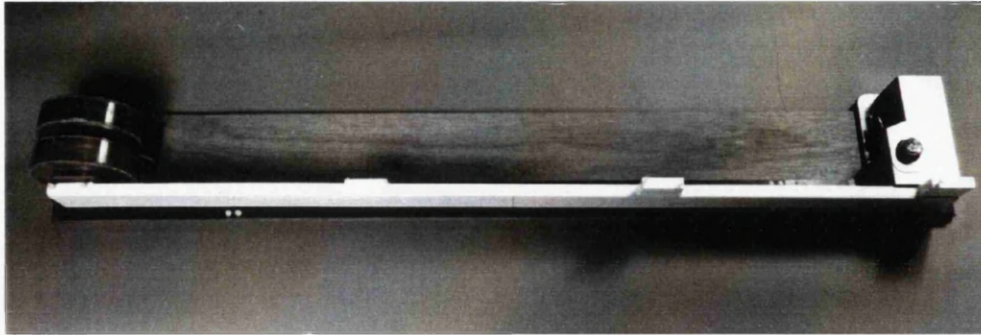


FIG.6.1 Schematic drawing of a tube flow phantom.



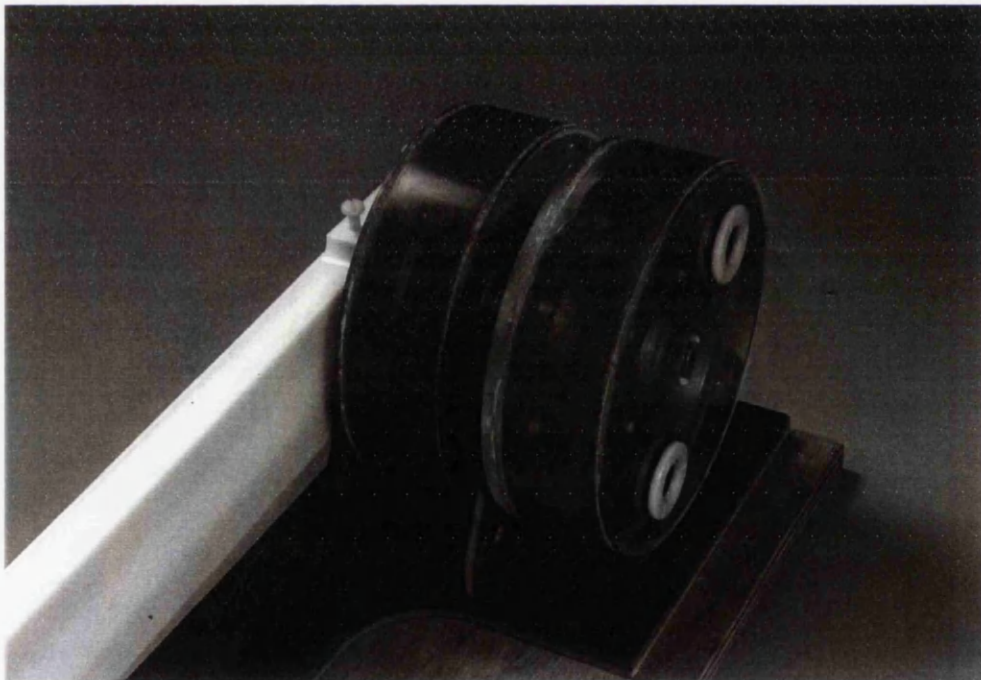
$$v = r \omega$$

FIG.6.2 Simulation of different flow rates by the rotating drum phantom. Gel annuli of different radii have tangential velocities in accordance with the formula.



**Figure 6.3**

Aerial view of the complete rotating phantom. The housing of the air motor and the control valve are on the right, and the two drums are on the left. The perspex casing for the driving belt which runs between the motor and the drums can be clearly seen.



**Figure 6.4**

The rotating drum is adjacent to the perspex casing surrounding the driving belt. The static drum is as close as is practically possible. The drums are shown gel filled. The perspex washers holding the rubber diaphragms covering the holes used to fill the drum with gel are clearly visible.

## CHAPTER 7: PREPARATION OF A BLOOD EQUIVALENT GEL FOR MRA PURPOSES

### 7.1 CRITICAL APPRAISAL OF PREVIOUSLY PUBLISHED RELAXATION TIMES FOR BLOOD

Chapter 6 has given a description of the construction of the drum phantom. For this phantom to be effective in evaluation of magnetic resonance angiography sequences, it must contain a medium which mimics in vivo blood. If this can be achieved, conclusions about sequence performance derived from images obtained by scanning the rotating phantom, can then be applied to the clinical imaging of in vivo arterial and venous blood flow. The property of blood spins which is relevant to MRA is their relaxation times, since this is the factor on which image contrast depends. In this chapter, a critical appraisal of published values of blood relaxation behaviour yields highly variable results. Target values are chosen to be mimicked by the gel as a result of a survey of published values, and experiments are performed using paramagnetic doping of the gel to reach target values. However it is found that some modification of these target values is necessary because both the magnetic and the mechanical properties of the gel medium have to be considered when the gel is prepared for experimental use.

### 7.2 CRITIQUE OF EXISTING LITERATURE ON BLOOD RELAXATION TIME VALUES

Since blood is a body tissue, various attempts have been made to obtain the values of  $T_1$  and  $T_2$  for it. Beall (1984) lists the following blood parameters as being relevant to its relaxation properties:

1. The frequency of the static field in which it is scanned.
2. Blood temperature.
3. Blood pH.
4. Differences in haematocrit-i.e. ratio of cell volume to total blood volume.
5. Blood composition depending on state of health of patient. the relevant blood elements are
  - i) water present,
  - ii) cationic content- potassium, sodium, cobalt, iron, copper and manganese all contributing.

Each of these elements has a unique value of T1 and T2 and the resultant value for blood will depend on the assimilated contributions from each of these components. The viscosity of blood is a physical property which will contribute to the definition of the laminar flow profile, but will not affect its magnetic relaxation properties.

A survey of recent literature shows that there is no consensus as to the values of the relaxation times for in vivo blood. Authors frequently quote a numerical value which is then used extensively in their work, but substantiation for the value is not given. Siemens Angiographic Data (1993) quotes T1 as 1000msec at 1T and 1200msec at 1.5T. A value for T2 does not appear in their literature. Edelman (1992) states that "the T1 and T2 relaxation times for blood, which is a complex mixture of red blood cells, cellular elements and plasma, depend on several factors, including hematocrit, viscosity and oxygen saturation. The T1 relaxation time is long, of the order of 1sec =1000msec. The T2 relaxation time is also long, of the

order of 200-250msec for arterial blood, or 50-75 msec shorter - i.e. 125-175msec for venous blood at 1.5T".

Blood consists of a fluid portion (plasma) containing erythrocytes (red blood cells) and leucocytes (white blood cells). Plasma itself consists of approximately 91% water, 7% proteins and 2% other electrolytes and biochemicals. From an MRA point of view, most of the signal obtained from flowing blood is produced by the haemoglobin and water protons. The blood pH can also affect relaxation times. The values graphed in Figs.7.1(a) and 7.1(b) (Beall, 1984) show how dependent T1 and T2 are on the constitution of the blood studied. In addition, they can be expected to vary in certain types of disease. The effect of the haemoglobin concentration is marked. If only the erythrocytes are considered, T2 can vary from 30msec to 600msec depending on whether the blood is deoxygenated from a patient with sickle cell anaemia, or oxygenated from a healthy individual.

Beall (1984) quotes a wide range of values for relaxation times for in vivo blood from different authors, though these tend to be measured at lower static fields, typically 0.44T-1.03T, as indicated by the use of frequencies of 19-44MHz. However by using the frequency and hence field dependent data quoted by Beall, values at higher fields can be obtained from the data of figs 7.1(a) and 7.1(b):

At 1T :	T1 =	925 msec,	T2 =	150msec.
At 1.5T :	T1 =	945 msec,	T2 =	150msec.

Authors agree that T1 and T2 are field and hence frequency dependent. Smith (1981, 1982, 1983) quotes T1 for in vivo human

blood at 1.7MHz as 355, whilst Koivula (1982) states 900msec at 19.8MHz and 33<sup>0</sup>C, and von Grodd and Schmitt (1983) gives T1 = 893msec and T2 = 362msec at 20MHz and 40<sup>0</sup>C. These values highlight the fact that relaxation times are also temperature dependent. Work on other body tissues (Bottomley, 1984) has shown that these values also depend on whether the measurements are made in vivo or in vitro, since deoxygenation begins as soon as the blood is extracted from the body. In vivo measurements are also affected by the age of the subject (Bottomley, 1984).

One detailed study of the dependence of relaxation times for venous blood on field strength has been carried out by Stadelmann (1991). Blood was taken from the vena cava of the same individual and it was shown that while T1 continues to rise as the field strength increases, a point is reached where T2 starts to decrease. Similarly T1 is shown to rise continuously as the temperature of the blood increases, whereas at higher temperatures T2 was found to decrease as the temperature continued to rise. In vivo and in vitro blood samples were compared for T1 and T2 values, and were found to differ depending on the different concentrations of anticoagulants. The authors conclude that different values must occur for arterial and venous blood because of the different state of the haemoglobin in the two cases. It can be concluded that though it may be expected that the general principles of variation of relaxation time for venous blood will also apply to arterial blood, imaging conditions for the two types of flow will have to be different because of their different relaxation times.

Condon (1987b) gives a detailed account of sources of error which can affect the experimental evaluation of T1 and T2. The temperature of samples, pulse and gradient imperfections, the use of non-ideal pulse time parameters in the data acquisition, and diffusion effects in the sample under study, were all found to be of some importance. None of the authors from whose work T1 and T2 values quoted in this study have commented on the possible effects of experimental conditions, and the error in their stated values is not apparent.

### **7.3 WATER AS A BLOOD-MIMICKING MEDIUM FOR MRA PURPOSES**

When constructing a blood-mimicking medium for use in phantom work, authors have adopted a variety of approaches. It is common to use water only in flow phantoms consisting of tubes of various diameters. The assumption is that its viscosity is similar to that of blood, and that this will have bearing on the imaged results, and also that its relaxation times are similar (Asai, 1992). The assumptions are not substantiated by quoted values, the T1 and T2 of water being nearer 3000msec (Condon 1987b). Some authors use a water and glycerine mixture, but it not clear whether they do this to improve the comparison of the viscosities, or to improve the comparison of the relaxation times. Summers (1994) carried out an investigation of the role of imaging parameters in phase mapping flow measurements, for which they doped the water with methyl cellulose and sodium chloride. However they do not quote the values of T1 and T2 that they were trying to achieve.

Stahlberg (1986) obtained the following values for water imaged at 0.5T:

$$\begin{aligned} T1 &= 1700 - 3200 \text{ msec} \\ T2 &= 1550 - 1900 \text{ msec} \end{aligned}$$

For comparison at the same static field he then quotes the appropriate value of T1 for in vivo blood as being 500msec. These figures show that there is little similarity in relaxation times between blood and water. The inference is that the authors who use this medium in their sequence evaluation work consider that it is flow per se which is the factor of interest, and not the flow of proton spins.

Stahlberg and the Scandinavian Flow Group have done fairly extensive phantom studies on slow flow at 0-5cmsec<sup>-1</sup> (i.e. velocities encountered in the peripheral vessels) using spin echo sequences. This work has involved both tube flow phantoms and a rotating drum containing a static gel and these have both been discussed in detail in chapter 6. For the tube flow phantoms (Stahlberg, 1986) the T1 and T2 values of blood are emulated by doping the water with manganese ions to give T1 = 500msec and T2 = 100msec at 0.25T. At 1.5T ( Sondergaard, 1992) an ion concentration is used which produces a T1 of 800msec. Siemens publish a value in their documentation for the clinical application of MRA sequences of 1100msec at 1.5T for in vivo blood (Siemens, 1993).

Nordell (1988), describes a rotating drum phantom filled with a static gelatine gel doped with an unspecified paramagnetic substance. This rotating phantom was used to reconstruct phase images in a trial to test whether the phase shift, measured by the

image intensity, was directly proportional to the spin velocity. Nordell regards the relaxation times of the spins as being irrelevant to the image intensity with phase image reconstruction, and states that the exact composition of the gel, and hence its magnetic properties, are not important. This may be true for phase image evaluation, but it is not true for modulus image evaluation.

Tarnawski's published rotating phantom work reported in 1988 mentions the use of a manganese chloride doped gel, which results in a T1 of 428msec and a T2 of 125msec at 1T.

#### **7.4 A PARAMAGNETICALLY DOPED RIGID GEL**

The most detailed work on the subject of the preparation of blood mimicking gels for MRA purposes has been done by Walker et al (1988). They were concerned to devise static gels with tissue mimicking properties for use in NMR relaxation time measurements, their object being to provide a set of standard calibration gels which could be used to test different NMR imaging systems, and also different software devised for calculating T1 and T2. They chose agarose as a base material because in its hydrated state it bears some similarity to tissue, since at the microscopic level it appears as a network of fibres formed from double helices. It is also electrically neutral. For the former reason, they chose it in preference to agar which is an impure multi-charged polysaccharide, although this has similar setting properties. It is not in fact clear that the fibrous nature of the agarose gel would be a necessary or indeed advantageous feature in phantom design, since it cannot be more than a gross representation of human tissue, and

cannot mimic the great diversity of tissue forms found in the human body. The physical properties of the gel such as electrical conductivity, T1 and T2 values obtained, mechanical stability and robustness over time, are more relevant to phantom work for MRA. Walker et al use gadolinium chloride to vary the paramagnetic ion concentration of their gel. One advantage of this salt is that its temperature dependence is smaller than that of most of the other paramagnetic ions. It is interesting to note that the T1 of the gel is primarily determined by the paramagnetic concentration, and the T2 by the agarose concentration.

#### **7.5 PREPARATION OF PHANTOM GEL USED IN THIS STUDY**

Although the gels of Walker et al. were designed to be used in static phantoms, they can in principle be used in a rotating phantom which simulates blood flow by circular rotatory motion of a gel filled and motor driven drum. The gel used in this study is based on the work done by Walker et al, although there are significant differences between the constitution of their gel and the one used in this study. Firstly, because of cost and availability, agar rather than agarose was tested as a setting gel. Manganese chloride rather than gadolinium chloride was used as the paramagnetic doping material because this was considered to stand a better chance of mimicking the T1/T2 ratio of blood (approx. 11 : 1). In water solution gadolinium chloride starts out with a T1/T2 ratio of approximately 1 : 1. Manganese chloride has a ratio of approximately 2.4 : 1 (Condon 1986, Walker 1988). The concentrations quoted by Walker et al. were taken as appropriate order of magnitude figures, but to optimise results nine test gels were prepared and scanned to evaluate their relaxation times. Three concentrations of agar gel

were used, and from each, three samples at different manganese chloride concentrations were prepared. A laboratory electronic balance reading to  $10^{-3}$ g was used to prepare the agar and manganese chloride samples for solution. The water volumes in which these were dissolved were measured using a millilitre graduated measuring cylinder, which gave comparable accuracy. The solutions were prepared in litre beakers, heated on an electrical hot plate, and stirred continuously with a magnetic stirrer. The agar concentration varied from 1% to 1.5%, and for each agar concentration, the manganese chloride concentration was varied from 0.005 to 0.2%

T1 and T2 were then obtained for each of the gel samples using standard spin echo sequences. The following sequence parameters were used in the four scans obtained:

1. TR = 2500msec, TE = 30msec.
2. TR = 2500msec, TE = 100msec.
3. TR = 2500msec, TE = 15msec.
4. TR = 500msec, TE = 15msec.

The first pair of readings at constant TR enabled T2 to be evaluated for each gel sample. The second pair of readings at constant TE enabled T1 to be evaluated for each gel sample. This can be achieved as follows (Breger, 1989):

For a spin echo sequence, the strength of the signal is given by

$$S_{SE} = k (e^{-TE/T2}) (1 - 2 e^{-(TR-TE/2)/T1} + e^{-TR/T1})$$

where k is a constant. If TR is much greater than TE, as has been achieved in the first pair of values quoted above, the equation can be simplified:

$$S_{SE} \sim k e^{-TE/T2} (1 - e^{-TR/T1})$$

Now if two sequences are obtained with the same value of TR but different values of TE, the ratio of the signals obtained will be equal to

$$\frac{S_{SE1}}{S_{SE2}} = \frac{e^{-TE/T1}}{e^{-TE/T2}}$$

$$\text{and } \ln \left( \frac{S_{SE1}}{S_{SE2}} \right) = \frac{-1 (TE1 - TE2)}{T2}$$

$$\text{and thus } T2 = \frac{- (TE1 - TE2)}{\ln \frac{S_{SE1}}{S_{SE2}}}$$

The spin echo signal equation is used in a different way to obtain an equation which will yield a value of T1, where TR is now different but the component ( $e^{-TE/T2}$ ) is the same for both sequences and so cancels:

$$\frac{S_{SE1}}{S_{SE2}} = \frac{(1 - e^{-TR1/T1})}{(1 - e^{-TR2/T2})}$$

$$\text{and } \ln \frac{S_{SE1}}{S_{SE2}} = \frac{-1 (TR1 - TR2)}{T1}$$

This equation is solved for T1 by applying a range of T1 values, using a pre-generated look-up table, to find which value of T1 best fits the signal ratio obtained.

By this means T1 and T2 for each of the nine sample gels were obtained. These values are listed in the table below. They are compared with the values which have been adopted for this study by consideration of the available data presented in the opening paragraphs of this chapter on experimentally determined relaxation times for in vivo human blood:

at 1.5 T      T1 = 1100 msec, T2 =100msec  
 at 1T        T1 = 1000msec, T2 =100msec.

T2 is independent of static field, and hence the value adopted is representative of quoted values obtained under different experimental conditions.

**Table 7.1      RELAXATION TIMES OF EXPERIMENTAL GELS**

SAMPLE NO.	T1(msec)	T2(msec)	Conc.agar(%)	Conc.MnCl <sub>2</sub> (%)
1	1363.8±24.9	105.7±1.7	1.0	0.005
2	678.3 ± 9.1	77.1± 0.9	1.0	0.01
3	392.8 ± 5.5	55.2± 0.9	1.0	0.02
4	1412.7 ±31.9	110.4±31.9	1.25	0.005
5	681.4 ± 13.1	74.5± 1.5	1.25	0.01
6	401.7 ± 6.8	54.9 ± 0.8	1.25	0.02
7	1270.2 ±25.9	85.8 ± 1.7	1.5	0.005
8	650.3 ± 12.0	67.3± 1.2	1.5	0.01
9	371.4 ± 5.9	48.9 ±0.9	1.5	0.02

With this selection of values, it was clear that for the nine samples of gel, scanned at 1.5T, the sample numbered 7 as listed, with T1 = 1270msec and T2 = 86msec, has relaxation times closest to those of arterial blood. These are the values for a 1.5% agar, 0.005% manganese chloride solution gel. At this stage the problem that the gel itself might not be rigid enough to prevent deformation and random movement under rotation was considered, as was the problem that the gel might deteriorate during the time taken to complete the scans. Tests were done on the feasibility of adding coloured dye to the gel, by injecting dye solution into sample tubes of gel to check for diffusion effects. If the dye were subsequently injected into the gel of the rotating drum, any movement of the dye

would act as a marker for deformation of the gel during rotation. In practice however it was found that small air bubbles inevitably collected in the gel as it cooled to the solid state, and the position of the air bubbles could thus be used to detect gel movement.

## 7.6 GELATINE AS A SUBSTITUTE FOR AGAR AS THE SETTING AGENT

It became apparent that certain properties of the agar gel could render it a less than optimum medium for this application, and that gelatine might be a better alternative. Gelatine does not have the problems in preparation and handling that agar has. Agar is slow to dissolve, and its contraction on cooling increases with time, apparently due to the evaporation of the water content. Such air spaces in the drum meant that it could not be guaranteed that the gel would remain stationary in the drum. Gelatine shows less contraction on initial cooling, and maintains its initial condition for up to a month before degenerating into a semi-liquid state. It can be dissolved in water below its boiling point, and its lower melting point means that it could be replaced in the drum without damaging it. Agar on the other hand requires autoclave temperatures above 100°C before it will dissolve in aqueous solution. A solidified agar has to be heated above 80°C before it will reliquify to be poured out of the drum. These temperatures place considerable strain on the adhesive used to secure the perspex parts of the drum disk.

The concentration of agar and manganese chloride already established as providing a gel with relaxation properties as near to those of in

vivo blood as achievable under the available experimental conditions were used as a guide to the constituents of the gelatine gel. The ionic content was not changed. The setting agent concentration was increased from 1.5% to 6%. The was readily soluble, and the set gel could be removed from the drum with the aid of a water bath at approximately 60°C. The T1 value of the gel depends on its manganese chloride content, and its T2 value depends on the setting agent concentration, so it was expected that there would be good correspondence between the T1 of the agar and gelatine gels, but some variation in the respective T2 values.

The gel showed little contraction on cooling, and any air spaces which did arise were filled while the gel was still in liquid form, without apparent formation of an interface. Air bubble formation in the drum on the cooling of the gel was minimal, and the few microbubbles which did arise were used to check that the gel did not slip inside the drum on its rotation. The gel remained rigid at rotation rates of 114rpm. It deteriorated to a semi-liquid form after about a month, and then complete replacement of the gel, using identical concentrations of gelatine and manganese chloride, was undertaken. The laboratory conditions under which the gel was puerperal were the same at each replenishment.

The procedure used to find the relaxation times for this gelatine gel was the same as that used for the agar samples. A spin echo sequence with the following scan parameters was used on subsequent acquisitions:

For calculation of T2:

TR = 500msec, TE = 15msec

TR = 2500mssec, TE = 15msec

For calculation of T1:

TR = 2500msec, TE = 30msec

TR = 2500msec, TE = 100msec.

Using these values and the standard software of the Siemens Magnetom SP scanner, values of T1 = 1100msec and T2 = 400msec were obtained for the gelatine based gel. These compare with the figures of T1 = 1100msec and T2 = 100msec assumed for in vivo blood relaxation times under these scan conditions.

The value of T2 for the gelatine gel is not very satisfactory, and had more time been available, it would have been advantageous to repeat the detailed procedure used for the agar gel, to establish a concentration of gelatine which would give a T2 value for the gel nearer to that for in vivo blood. In this study, the practical problems of obtaining a gel with good rigidity under extensive rotation, good lasting properties over a period of time, and ease of handling, have taken precedence over the need to produce a gel whose relaxation properties match those of in vivo blood exactly.

The T1 and T2 values for this gel were measured by the same procedure as that used for the agar samples, using a spin echo sequence and the following scan parameters on subsequent acquisitions:

For calculation of T2:

TR = 500msec, TE = 15msec

TR = 2500mssec, TE = 15msec

For calculation of T1:

TR = 2500msec, TE = 30msec

TR = 2500msec, TE = 100msec.

Using these values and the standard software of the Siemens Magnetom SP scanner, values of T1 = 1100msec and T2 = 400msec were obtained for the gelatine based gel. these compare with the figures of T1 = 1100msec and T2 = 100msec adopted for in vivo blood relaxation times under these scan conditions.

#### **7.7 POSSIBLE ERRORS IN PHANTOM EVALUATION OF SEQUENCES DUE TO INACCURATE GEL RELAXATION TIMES.**

The T1 and T2 values of the completed gelatine gel, prepared as 6% gelatine and 0.005% manganese chloride, were obtained at 1.5T as T1= 1100msec, and T2 = 400msec. The T1 is still consistent with the findings of Walker et al. because the concentration of the paramagnetic salt is the same. However the T2 value has been sacrificed to some extent to the advantages of the mechanical properties of a gelatine over an agar gel. FISP and FLASH sequences produce signals which depend to different extents on the T1 and T2 parameters of the medium scanned. Thus if the gel in the rotating phantom does not have relaxation properties identical to those of in vivo blood, the image intensities obtained by scanning the phantom gel at different velocities are not going to be representative of those which would be obtained from in vivo blood at the same velocities. The "error" in phantom image intensities relative to

those which could be obtained if in vivo blood were scanned depends on the imaging sequence used. This problem is discussed in more detail in chapter 8, and a method of eliminating this potential source of error when making predictions for optimum clinical scan conditions on the basis of phantom scan result is discussed.

FIG.7.1a) FREQUENCY AND CELL TYPE DEPENDENCE OF T1 FOR VARIOUS STATES OF WHOLE BLOOD

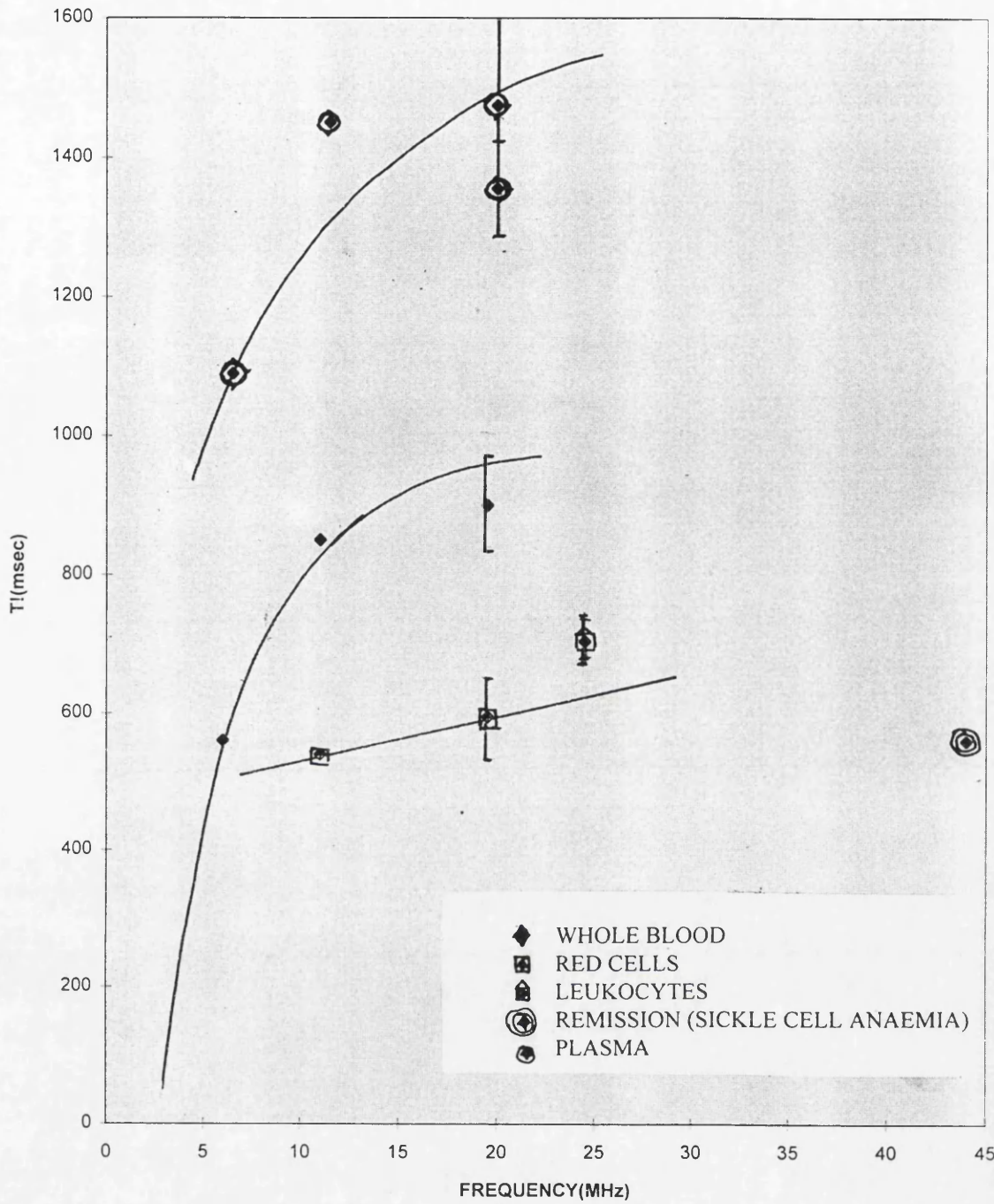
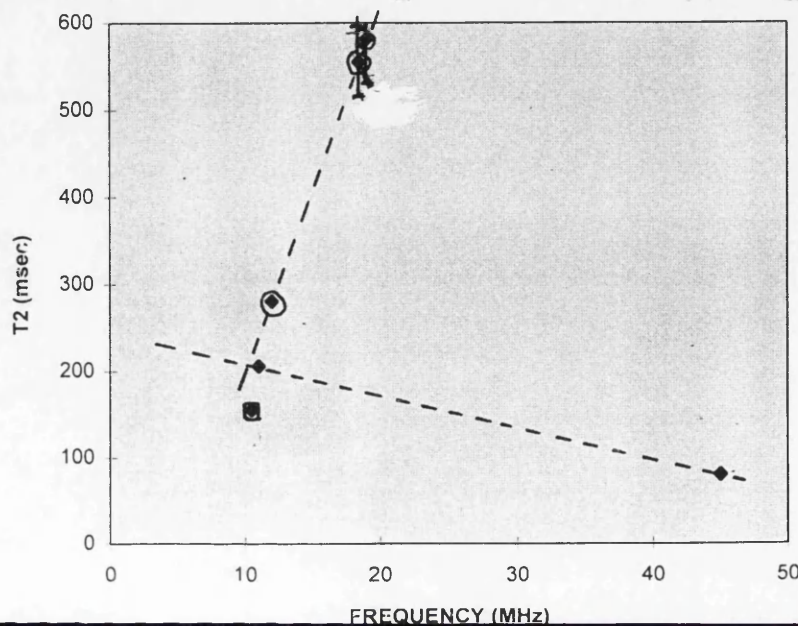


FIG. 7.1b) CELL TYPE DEPENDENCE OF T2 FOR VARIOUS STATES OF WHOLE BLOOD



## CHAPTER 8 : EVALUATION OF OPTIMUM PULSE SEQUENCE PARAMETERS AND COMPARISON WITH STANDARD CLINICAL VALUES

This chapter uses MR theory to examine the effect that the use of different sequence parameters- flip angle, repetition time and echo time, will have on the signal strength obtained when the FISP and FLASH sequences are used. These are calculated for stationary spins, since equations do not exist for signal strength under conditions of flow, when inflow saturation and spin dephasing effects act in addition to the usual spin-spin and spin-lattice interactions. They will however have bearing on the signal that can be expected under conditions of flow; for example, relative saturation effects for stationary spins at flip angles of  $20^{\circ}$  and  $40^{\circ}$  will be matched in the behaviour of flowing spins. Once optimum parameters have been established, they are compared with clinical parameters provided as 'standard' by Siemens. This analysis reveals as yet unrecognised limitations in these sequences.

Inspection of the ideal signal equation for stationary proton spins when FISP and FLASH sequences are applied shows that  $T2^*$  must be known for quantitative evaluation of signal strength.  $T2^*$  is thus first obtained for the gel used in the rotating phantom, based on measurements obtained with field echo sequences.

The chapter concludes by evaluating in detail the errors which may be introduced into phantom work if a paramagnetically doped medium whose relaxation times do not exactly match those of flowing blood is used. It is assumed that conclusions reached from the analysis of phantom images can then be applied in the clinical situation, and

the extent to which this is true if relaxation times for in vivo blood are not matched in the phantom is calculated. This has important consequences both for the validation of the conclusions reached in this study, and also for the validation of conclusions reached by other authors working in the same field.

### 8.1 MATHEMATICAL DEFINITION OF FISP AND FLASH SIGNALS

The FLASH pulse sequence signal obtained as the ideal signal from stationary spins has the equation

$$S_{FL} = \frac{M_0 (1 - e^{-\frac{TR}{T1}}) \sin\alpha e^{-\frac{TE}{T2^*}}}{(1 - \cos\alpha e^{-\frac{TR}{T1}})}$$

(Hendrick, 1992)

The equation for the FISP pulse sequence signal, again the ideal signal which can be obtained from stationary spins, is

$$S_{FI} = \frac{M_0 \sin\alpha e^{-\frac{TE}{T2^*}}}{T1/T2 + 1 - \cos\alpha (T1/T2 - 1)}$$

(Hendrick, 1992)

There are some aspects of the FISP and FLASH sequences which can be appreciated from the form of these equations.

1. The exponential decay due to T2\* effects in the transverse plane is the same in both sequences. This result is true both for the application of one pulse sequence, and for repeated applications, regardless of the fact that for FISP transverse magnetisation is maintained in a steady state, whilst for FLASH, it is destroyed between pulse sequence applications.

2. The FLASH sequence equation does not contain a T2 component as such. This is because the spoiler pulse is applied at the end of each repetition so that the transverse magnetisation does not contribute to the echo.

3. The FISP equation on the other hand contains components of both longitudinal and transverse magnetisation, represented by the inclusion of T1 and T2. The signal is independent of the pulse sequence repetition time TR, this being due to the fact that the contribution of the transverse magnetisation to the signal is maintained constant. The change in longitudinal magnetisation due to spin relaxation is negligible at the short TR's used in fast imaging.

By substitution of typical values for the constants T1, T2, T2\*, TR, TE and  $\alpha$  used in the imaging of flowing blood spins using FISP and FLASH sequences, into these mathematical expressions, the following values can be calculated :

1. Optimum flip angle for FISP and FLASH sequences.
2. Flip angle dependence of saturation effects.
3. Dependence of FISP sequence signal intensity on sequence parameters FA, TR and TE, and hence optimum values of these for flow imaging.
4. Dependence of FLASH sequence signal intensity on sequence parameters FA, TR and TE, and hence optimum values of these for flow imaging.
5. The effect on signal intensity for both FISP and FLASH sequences if the relaxation times of the imaged protons change. The real value of this calculation in the context of this thesis is that

differences in detected signal between the gel used in the rotating drum phantom and those which would be obtained from in vivo blood under the same conditions can be established. This calculation is crucial in validating the phantom study results as a true indicator of the clinical imaging potential of the pulse sequences tested.

### 8.1.2 ESTIMATION OF T2\* FOR A STANDARD SAMPLE

As has been indicated in the introduction to this chapter, the value of T2\* is required before FISP and FLASH ideal signal strengths can be calculated. By its physical nature, T2\* is a machine dependent parameter, and hence it must be obtained locally on the scanner used in the phantom studies. Here a viable ratio of T2\* : T2 is obtained using a standard sample scanned with a gradient echo sequence. Two scans of the sample were performed to obtain the following signal strengths:

SEQUENCE USED	T2* SCAN RESULTS	SIGNAL STRENGTH (arbitrary units)
FLASH with TE = 30msec		1914
FLASH with TE = 60msec		1260
SPIN ECHO with TE = 30msec		1100
SPIN ECHO with TE = 60msec		1032

### 8.2.1. CALCULATION OF T2\*

These signal intensities are then used to calculate T2\* in the following manner:

The FLASH sequence signal equation is

$$S_{FL} = \frac{M_0 (1 - e^{-\frac{TR}{T1}}) \sin \alpha e^{-\frac{TE}{T2^*}}}{(1 - e^{-\frac{TR}{T1}} \cos \alpha)}$$

(Hendrick, 1992).

In this application the flip angle is cancelled from the ensuing calculation, because T1 and TR are the same for both FLASH sequences.

At TE = 30msec,

$$1914 = S_1 = \text{const. } e^{-30/T2^*}$$

At TE = 60msec,

$$1260 = S_2 = \text{const. } e^{-60/T2^*}$$

So eliminating the constant by division,

$$\frac{1914}{1260} = \frac{e^{-30/T2^*}}{e^{-60/T2^*}}$$

$$\ln \frac{(1914)}{1260} = - \frac{1}{T2^*} (30 - 60)$$

$$\text{and } T2^* = 61$$

### 8.2.2. CALCULATION OF T2 FOR THE SAME SAMPLE

Using the equation for the spin echo sequence, as shown in chapter 7,

$$\begin{aligned} T2 &= \frac{-(TE1 - TE2)}{\ln (S_{SE1} / S_{SE2})} \\ &= \frac{-(TE1 - TE2)}{\ln (1100/1032)} \\ &= 398 \end{aligned}$$

Thus in this application the required ratio is

$$T2^* / T2 = 61 / 398 = 0.15 = 1/6\text{th}$$

to a reasonable approximation.

This established ratio between the two values can now be used to obtain T2\* for in vivo blood, since T2 = 85msec. Thus

$$T2^* = T2/6 = 85/6 = 15 \text{ approx.} \quad (\text{IN VIVO BLOOD})$$

T2\* for the gel used in this study can also be calculated, since its T2 is known to be 400msec:

$$T2^* = T2/6 = 400/6 = 65 \text{ approx.} \quad (\text{ROTATING PHANTOM GEL})$$

These two T2\* values are now utilised in the calculation of optimum imaging conditions, and relative image intensities, for the FLASH and FISP pulse sequences.

### 8.3 OPTIMUM FLIP ANGLE FOR IMAGING OF IN VIVO BLOOD USING FISP SEQUENCES.

The FISP signal quoted in 8.1 is seen to be a maximum if

$$\alpha = \frac{\cos^{-1} \frac{-(T1/T2 - 1)}{(T1/T2 + 1)}}{}$$

Substituting values of T1 = 1000msec and T2 = 100msec for blood at 1T, the optimal value in terms of maximum detected signal strength for stationary blood spins is

$$\alpha = \frac{\cos^{-1} \frac{-(1000/100 - 1)}{(1000/100 + 1)}}{}$$

$$\alpha = \frac{\cos^{-1} (10 - 1)}{(10 + 1)} = \cos^{-1} 0.82$$

$$\text{so } \alpha = 35^{\circ}.$$

This calculated value compares with flip angles of 20° for slower flow rates and 40° for faster flow rates recommended by Siemens for angiographic use of FISP3D sequences (Siemens, 1993). It can also be compared with the value of 15° recommended when the FISP 3D sequence is used in the REPHASE-DEPHASE subtraction procedure. Future rotating phantom studies could compare the image intensities

achieved by using these different flip angles to image spins at a defined range of flow rates, as a verification of the predicted optimum value of  $35^{\circ}$ .

#### 8.4 OPTIMUM FLIP ANGLE FOR IMAGING IN VIVO BLOOD USING THE FLASH SEQUENCE

The signal detected when a FLASH sequence is used is a maximum when the flip angle is

$$\alpha = \cos^{-1} e^{-TR/T1}$$

This is evident from the FLASH signal equation, where by minimising the denominator, the dividend is maximised (8.1).  $\alpha$  is known as the Ernst angle, and it is pulse sequence repetition time dependent. For the FLASH sequences used in this study, the TR's were 39 and 40msec. Using  $T1 = 1000\text{sec}$  at  $1T$ ,

$$\begin{aligned} \text{Ernst angle} &= \cos^{-1}( e^{-40/1000} ) \\ &= 16.3^{\circ} \end{aligned}$$

This calculation does not appear to have been performed for in vivo blood by Siemens, who recommend that FLASH should be used with flip angles of  $35^{\circ}$  or  $40^{\circ}$  in angiographic application. Further tests with the rotating phantom could be done to compare the image intensity obtained at these different flip angles for a defined range of flow rates. This would reveal the efficacy of this predicted optimum flip angle as compared to those recommended for use at the present time.

Maier (1994) states that with a gradient echo sequence, and for blood whose  $T1$  is taken to be 850msec, when it is imaged at  $1.5T$ , the optimum flip angle is  $14^{\circ}$ . He does not say whether this is an

experimental or a calculated finding. Ruggieri(1989) has undertaken extensive tests of the FISP 3D sequence under clinical conditions. He alters the pulse sequence parameters of flip angle, repetition time and echo time systematically and concludes that a flip angle of  $15^{\circ}$  gives best contrast throughout the image volume. With larger flip angles, enhanced contrast between blood spins and stationary tissue on entering the image volume could be lost as the spins penetrated the volume. Calculations presented here confirm that this effect is due to saturation build up with pulse sequence repetition times normally used in angiographic scans.

The author has already commented on the shortcomings inherent in any clinical evaluation of imaging sequences (chapter one). Maier's value of flip angle quoted here is additionally suspect because he does not give any definite details of the type of sequence he is using. To the author's knowledge the calculation of optimum flip angles for use with FLASH and FISP sequences has not been published previously, and it provides a useful standard by which to gauge the relative effects of saturation and spin dephasing on the detected signal.

### **8.5 FLIP ANGLE EFFECTS ON SATURATION.**

When FISP and FLASH pulse sequences are used to image flowing rather than stationary spins, the detected signal is a combination of effects. At low velocities, the ideal signal is moderated by saturation effects, and this effect will reduce the optimum signal

which would be obtained from stationary spins under the same conditions. Thus when devising optimum pulse sequence parameters for use with flowing spins, the contrast and saturation effects have to be weighed against each other.

Saturation results because the pulse sequence repetition time is not long enough for the spins to regain their pre- RF - pulsed state. It would appear to be the case that for a constant TR, such as 40msec which is typically used for fast imaging, relaxation to the pre-flipped state would be more complete, the lower the flip angle. The equation for the longitudinal relaxation of a spin flipped through an angle  $\alpha$  is

$$M_z(\tau) = M_0 ( 1 - e^{-\tau/T1} ) + M_{z0} \cos\alpha e^{-\tau/T1}$$

(Waugh, 1970). Here T1 is the longitudinal relaxation,  $\tau$  is the time interval for transverse magnetisation to decay to zero,  $M_0$  = thermal equilibrium magnetisation, and  $M_{z0}$  = the magnitude of the spin magnetisation vector along the direction of the static field  $B_0$ .

This equation describes how the inclination of the spin to its undisturbed alignment with the static field varies during the pulse sequence. The recovery of longitudinal magnetisation is unique to the pulse sequence used, depending on the flip angle and repetition time chosen, as well as on the relaxation properties of the proton spin.

The first factor, containing  $M_0$ , is assumed to be constant during imaging, and is not relevant when considering the response of the spin to the pulse sequence gradients. The following calculations are undertaken to quantify the recovery of longitudinal magnetisation of the spin after each pulse sequence application.

For blood,  $T1 = 1000\text{msec}$  at  $1T$ ,  $TR = 40\text{msec}$  approx. for fast imaging applications. Using these values, the factor  $e^{-TR/T1}$  is evaluated as  $0.96$ . The longitudinal magnetisation at the end of one pulse sequence for different flip angles can now be calculated as a fraction of  $M_{z0}$ , the initial longitudinal magnetisation of the unflipped spin:

$$\begin{aligned} \text{At FA} = 15^\circ, \quad M_z(t = 40) &= M_0 (1 - 0.96) + M_{z0} \cos 15^\circ (0.96) \\ &= 0.965M_0 + 0.93 (M_{z0}) \end{aligned}$$

Thus there is 7% reduction in longitudinal magnetisation  $M_{z0}$  after the application of one RF pulse, and consequently when the next pulse sequence is applied, saturation effects will only accrue slowly because the undisturbed longitudinal magnetisation is nearly recovered during the sequence repetition time. However when the flip angle is increased to  $20^\circ$ , it is evident that saturation will build up much more quickly:

$$\text{At FA} = 20^\circ, \quad M_z(t = 40) = 0.965M_0 + 0.90 (M_{z0})$$

i.e. a 10% approx. reduction in longitudinal magnetisation of this spin for the same pulse sequence repetition time means that

saturation effects build up more quickly with this larger flip angle, for the same repetition time.

$$\text{At FA} = 40^\circ, M_z(t = 40) = 0.965M_0 + 0.74 (M_{z0})$$

i.e. there is a 26% reduction in longitudinal magnetisation after one pulse sequence application. There is thus a complex relationship between increase in flip angle and decrease in signal due to saturation, the increase being more than linear.

### 8.6 EFFECT ON FISP SIGNAL STRENGTH OF CHANGING SEQUENCE PARAMETERS.

The equation for the ideal FISP sequence signal for stationary spins is given at the start of this chapter. By substituting the appropriate values of TR, TE and FA used for these sequences as applied in this study, relative signal strengths can be evaluated. Deterioration in signal strength due to movement of spins under different scan conditions will then become apparent. In no case does TR affect the detected signal because steady state free precession is maintained.

**Table 8.2 RELATIVE SIGNAL STRENGTHS OBTAINED IN FISP 3D SCANS USING A RANGE OF PULSE SEQUENCE PARAMETERS**

FA(deg.)	TE(msec.)	RELATIVE SIGNAL STRENGTH
15	6	0.076
15	14	0.04
20	14	0.05
15	10	0.06
20	10	0.07
40	10	0.076

The relevance of these results to the imaging of flowing spins can be seen if they are studied alongside the saturation effects detailed in section 8.5. The results presented here show that optimal contrast between dark stationary tissue and flowing blood is obtained with increasing flip angle. However, during the pulse sequence repetition times used for blood imaging, longitudinal spin relaxation is nearly complete for small flip angles, whereas it is incomplete for larger angles, so that saturation effects are noticeable. The experimental image data obtained with the phantom scans is a direct measure of the relative importance of these two effects at the velocities represented by the rotating drum phantom.

The rephase-dephase sequence ( $TE = 14\text{msec}$ ,  $FA = 15^\circ$ ) used in the study has a relatively long echo time, necessitated by the use of the velocity compensating-decompensating gradients in addition to those normally applied during the FISP sequence. The flip angle is also low. The above calculations show that a larger flip angle is needed at the higher echo time, to maintain a strong signal. Thus since it is inevitable that a longer than usual echo time is used for FISP in the rephase-dephase application, the conclusion we reach on the basis of the above values is that best results will be obtained when a larger flip angle is also used. This calculation does not appear to have been done elsewhere, and this conclusion does not yet appear in other published literature. The offset of possible increase in saturation effects for moving spins would have to be considered alongside this.

## 8.7 EFFECT ON THE FLASH SEQUENCE OF CHANGING SEQUENCE PARAMETERS

Siemens (1993) recommend that the following sequence parameters are used:

Fast flow rates : TR = 40msec, TE = 10msec, FA = 40°

Slow flow rates : TR = 39msec, TE = 10msec, FA = 35°

The difference in TR in the two sequences changes the exponential factor of the FLASH equation quoted at the beginning of this chapter from  $e^{-39/1000}$  to  $e^{-40/1000}$  which will not have a significant effect on signal strength. It must thus be the flip angle which dominates, and the effect of this has been calculated for the FLASH sequence, as has the result of using the same values of TR and TE, but scanning at the calculated optimum flip angle of 16.3°.

For in vivo blood at 1T, T1 = 1000 and T2 = 85 msec. T2\* = T2/6 = 15approx.

For the ideal signal detected when using the FLASH sequence,

$$(1 - e^{-TR/T1} \cos \alpha)$$

$e^{-TE/T2^*}$  will be constant for all applications, as will M<sub>0</sub>. The differences in the term  $e^{-TR/T1}$  are negligible. Thus  $e^{-TE/T2^*}$  will be constant for all applications, as will M<sub>0</sub>. The differences in the term  $e^{-TR/T1}$  are negligible. Thus

$$\frac{S_{35}}{S_{40}} = \frac{\sin 35 / (1 - 0.97 \cos 35)}{\sin 40 / (1 - 0.97 \cos 40)}$$

$$= 1.1$$

$$\frac{S_{16.3}}{S_{40}} = \frac{\sin 16.3 / (1 - 0.97 \cos 16.3)}{\sin 40 / (1 - 0.97 \cos 40)}$$

$$= 1.45$$

So the effect of imaging at a large flip angle with the FLASH sequence is actually that the signal strength is reduced, and an optimum signal strength is obtained at a numerically lower angle. Since saturation effects are also less likely to occur at all blood speeds if the flip angle is lower, it would appear that the best results would indeed be obtained using  $FA = 16^\circ$ . In practice, in details given by manufacturers for clinical imaging, it appears to have been assumed that the FLASH sequence will mirror FISP sequence behaviour, and will give a stronger signal and thus better image contrast at higher flip angles. The disproof of this is itself is a very valuable contribution to the physics of clinical imaging.

#### 8.8 HOW CLOSELY SHOULD THE RELAXATION TIMES OF THE SCANNED GEL MIMIC THOSE OF IN VIVO BLOOD ?

It has been one of the aims of this study to produce a gel for use in the rotating drum phantom which will mimic the magnetic properties of in vivo blood as closely as possible. As has been discussed in chapter 7, there has been some necessary shortfall in this aim. The obtained values at 1.5T are

In vivo blood             $T1 = 1100\text{msec}$ ,  $T2 = 100\text{msec}$

Drum gel                 $T1 = 1100\text{msec}$ ,  $T2 = 400\text{msec}$

As has already been stated, the accuracy of the  $T2$  value was sacrificed to maintain the robustness of the gel under rapid rotation of the drum.

Below, the relative signal strengths for blood and the phantom gel are calculated using the equations for the static spin signals obtained from the use of FISP and FLASH pulse sequences. These are quoted in 8.1, and represent the maximum or ideal signal which can

be expected, when saturation or spin dephasing effects are not present.

For FISP sequence scans (both at TR = 36msec) :

FA =  $40^{\circ}$ , TE = 10msec  $S_{\text{blood}} = 0.1M_0$ ,  $S_{\text{gel}} = 0.16 M_0$ .

**Signal reduction = 60%**

FA =  $20^{\circ}$ , TE = 10msec  $S_{\text{blood}} = 0.08M_0$ ,  $S_{\text{gel}} = 0.14 M_0$ .

**Signal reduction = 75%**

i.e. If the FISP 3D sequences which have been used with the the rotating phantom gel were applied to the imaging of in vivo blood, the signal detected from the blood would be 60% lower at a flip angle of  $20^{\circ}$ , and 70% lower at a flip angle of  $40^{\circ}$ . Thus the single slice images obtained by scanning the rotating phantom are not in themselves a good indicator of their capacity to image in vivo blood. They indicate the trends in signal intensity which can be expected when imaging longitudinal blood flow, but not the absolute values of intensity.

For FLASH sequence scans :

FA =  $40^{\circ}$ , TE = 10msec, TR = 40msec

$S_{\text{blood}} = 0.51M_0$ ,  $S_{\text{gel}} = 0.73 M_0$ . **Signal increase = 50%.**

FA =  $20^{\circ}$ , TE = 10msec, TR = 40msec.

$S_{\text{blood}} = 0.22M_0$ ,  $S_{\text{gel}} = 0.32M_0$ . **Signal increase = 50%.**

i.e. by contrast to the case of the FISP sequence, when the FLASH 2D sequences are used with in vivo blood rather than with rotating phantom gel, a signal increase is to be expected, of the order of 50% at flip angles of  $20^{\circ}$  (approximately the Ernst angle), and  $40^{\circ}$ .

Again the changes in signal intensity with velocity obtained by scanning the rotating phantom only indicate the trends in change in intensity which will be apparent when imaging in vivo blood at different flow rates.

The signal increase in the case of the FLASH sequence and the signal reduction in the case of the FISP sequence are the results of the different modes of echo generation in these two sequences. FLASH eliminates the transverse component of magnetisation between acquisitions, whereas FISP applies additional rephasing gradients to maintain steady state free precession.

These calculations make it clear that the difference in the T2 values of in vivo blood and drum gel is creating large differences in signal strength when calculated for stationary spins in these two media. It is against these ideal stationary values that the sequences are analysed to evaluate moving spin effects at different velocities. It is crucial to use a gel with relaxation times identical to those of in vivo blood if only a single rotating gel is being scanned, otherwise the resulting signal values cannot be taken as a reliable indication of how the sequence will perform when it is used clinically with in vivo blood flow. Other authors who have published work on modulus imaging with flow phantoms have not taken this into consideration, and it is a potential source of deficiency in their phantom study conclusions.

The further merit of this study is that the absolute signal intensities from the rotating gel images have not been used in quantitative pulse sequence evaluation. The absolute image intensity

values have been normalised against the signal from the identical static gel drum placed as close as possible to the rotating drum in the scanner fields. The normalised image intensity is a index which is independent of the relaxation properties of the gel, and depends only on the response of the sequence to the gel spins at the controlled range of velocities used. Thus the phantom scan image data provides a reliable guide to the applicability of the pulse sequences for in vivo blood imaging at body blood velocities.

## 8.9 CONCLUSION

This chapter has provided valuable insights into the behaviour of FISP and FLASH sequences which it would be difficult and time consuming to test experimentally. The work on the effect of flip angle on spin saturation provides a useful guide when contrast enhancement effects have to be balanced against saturation effects. Further phantom scans at a flip angle of  $16.3^{\circ}$  using the FLASH 2D sequence with TR = 40msec and TE=10msec should now be undertaken to verify that this is indeed the optimum flip angle for use with the sequence under these flow imaging conditions.

The discussion of the effect on image intensity of the relaxation parameters of the imaged medium, and the further discussion of the normalisation procedure adopted in this study, has proved conclusively that any conclusions derived in later chapters about the relative merits of the six pulse sequences tested in this study on gel spins at different velocities can be applied directly to the imaging of in vivo blood spins. This is a unique feature of the results obtained in this rotating phantom study, since no other author has evaluated this aspect of the applicability of phantom

scan results. Because this guarantee exists, it can be assumed that any indications that signal voids or blind spots will arise when the tested pulse sequences are used to image longitudinal flow with the rotating drum phantom will also apply when imaging in vivo blood. The need to be able to differentiate between these signal voids inherent to the pulse sequence and those signal voids which are the result of vascular abnormality and unique to the anatomy and physiology of the patient under clinical scrutiny is the fundamental reason for this study. Thus the relevance of these phantom study results to diagnostic imaging is proved.

If sequences are chosen for use in clinical imaging which are known to be capable of imaging flow over the velocity range encountered in the vessel of interest, without producing spurious blind spots or signal voids, the clinician can then feel certain that any abnormality detected will be found at surgery.

## CHAPTER 9 : QUALITATIVE EVALUATION OF ROTATING DRUM PHANTOM SCANS OBTAINED USING SIX MRA PULSE SEQUENCES.

### 9.1 INTRODUCTION : CLINICAL EVALUATION OF PULSE SEQUENCES

Both the FISP and the FLASH pulse sequences were developed in the context of the imaging of stationary tissue. They overcame the main disadvantage encountered using spin echo sequences in the clinical context, which was that during the long scan times the patient could move, which would lead to blurring in the reconstructed images. The procedures used at the time of discovery to validate these sequences and to develop optimal pulse sequence parameters are not available in the literature.

The advantage of the short imaging time also led to the use of these sequences for angiographic scanning. When Gradient Motion Refocussing techniques were developed subsequent to the design of the FISP and FLASH sequences themselves, these were incorporated into the existing sequences to overcome the dephasing problems unique to flowing spins.

Pulse sequence evaluation has taken place since FISP and FLASH sequences designated for angiographic purposes have been made available on commercial scanners. Clinical trials on patients have been undertaken to test the effects of different pulse sequence

repetition times, echo times and flip angles on image quality. Image evaluation has been through observer based methods such as receiver operated characteristic (ROC) curves, and sensitivity and specificity calculations. The statistical validity of the patient sample size is not frequently commented on.

Ruggieri (1989) undertook one such evaluation using 35 healthy volunteers aged between 18 and 24 years. A FISP sequence available on a Siemens Magnetom 1.5T scanner was tested for its ability to image the intracranial circulation. The echo time was constant for all the tests. For each value of TR chosen, a range of flip angle sizes was used. The pulse sequence evaluation then consisted of a comparison of the image quality of all these parametric combinations tested on the 35 volunteers. Images were scored on the following criteria:

- a) Signal voids present.
- b) Continuity of vessels.
- c) Vessel definition.
- d) Brightness or relative difference in signal intensity from background. Some subjectivity in the evaluation is acknowledged.

Another study by Masaryk (1989) used two patient populations. The first was a group of 18 patients with low probability of cerebrovascular disease, and the second a group of 40 patients with

suspected cerebrovascular disease or abnormality. The mean age of the subjects was 34 years, the age range being 1 week to 87 years. A Siemens 1.5T Magnetom scanner was used to test GE FISP sequences. The area of interest was the Circle of Willis, and the MRA image quality was evaluated against DSA images available for 27 out of the 40 patients. The evaluation was made by two neuro-radiologists.

The problems inherent in any clinical evaluation of pulse sequences have already been outlined in chapter one, and further substantiated in chapter 5. the ideal experimental test situation is one in which the experimental conditions are precisely known, and are repeatable from test to test. Patient anatomy is variable between subjects, as a patient blood flow rates, and these very conditions throw into doubt the validity of extrapolating from one patient population to another. Phantoms studies enable pulse sequences to be tested at precisely known flow rates, under precisely controlled and reproducible flow conditions. The superiority of a rotating phantom over tube phantoms for this purpose has been described in chapters one and six.

In this chapter the details of the rotating phantom evaluation of the pulse sequences is described. The types and imaging parameters of the chosen sequences are given, and the reason for this choice of sequences for evaluation is explained. The phantom scan procedure is described, and the normalising procedure applied to the image signal is described.

The velocity vector of the gel in the rotating phantom is tangential to the circle of motion. The gel recirculates through the image volume many times during the scan, and in the course of one rotation it will undergo a number of pulse sequence applications depending on its rate of rotation, and the repetition time of the pulse sequence. These factors are not present when longitudinal arterial blood flow is imaged, the image medium (in vivo blood) moving straight through the scan volume once only. Thus it is possible that there will be some features of the image slices of the rotating phantom which would not appear in longitudinal blood flow imaging. The six sets of phantom scan images are scrutinised to find where such artefacts exist, so that true motion related phenomena can be separated and differentiated from recirculation artefacts. Although other groups have used rotating drum phantoms, the potential for such recirculation artefacts has not been recognised.

Photographic representations of typical console images from the six phantom scans are then presented, and their essential features described, to establish a qualitative appreciation of the different imaging capabilities of the sequences. A semi-quantitative evaluation is then created by the presentation of the image signal intensity across the complete image volume in 3D surface form.

#### **9.1.1 FISP AND FLASH SEQUENCES USED IN THIS STUDY**

The available list of fifteen MR angiographic sequences was scrutinised for sequence type and applicability to flow rates of different values. The sequences fall into the two broad categories so far described in this thesis, i.e. FISP and FLASH. Although both these sequence types are available on the scanner in 2D and 3D

TABLE 9.1

PULSE SEQUENCES AVAILABLE FOR MRA AND EVALUATED IN THIS STUDY

SEQUENCE NAME	SIEMENS MAGNETOM IMPACT 1T SCANNER			APPROPRIATE VELOCITY	OTHER USES OF SEQUENCE
	FA	TR	TE		
FISP3D_10rb108.ufa	40	35	10	100-180cmsec <sup>-1</sup>	FA = 20, TR = 36, TE = 10 can be applied for the same velocity range.
FISP3D_10rb108.ufa	20	36	10	35 -180cmsec <sup>-1</sup>	The same parameters are recommended for I) 35-70cmsec <sup>-1</sup> II) carotids (head), v< 115cmsec <sup>-1</sup> III) carotids (neck), v< 180cmsec <sup>-1</sup>
FLASH2D_s_10rb78.ufa	35	40	10	35-44cmsec <sup>-1</sup>	
FLASH2D_s_10rb78.ufa	40	39	10	60 - 180cmsec <sup>-1</sup>	FA =40, TR = 44, TE = 10 can be used for 60-140cmsec <sup>-1</sup>
FISP3D_14rdb108.ufa	15	50	14/14	30 - 45cmsec <sup>-1</sup>	Recommended for slow ICV and peripherals.
FLASH2D_su_10rb78.ufa					The efficacy of the pre-saturation pulse was evaluated qualitatively only.
		SIEMENS MAGNETOM SP 1.5T SCANNER			
FISP3D_64_6rb195.ufa	15	36	6	30 -70cmsec <sup>-1</sup>	

THE APPROPRIATE VELOCITY VALUES WERE OBTAINED BY MATCHING THE NAMED BLOOD VESSELS QUOTED BY THE MANUFACTURER AS APPROPRIATE FOR THE SEQUENCE, WITH THE BLOOD FLOW RATE FOR THAT VESSEL STATED IN CHAPTER 5.

applications, the practice is that when imaging blood flow, FISP is applied in the 3D mode and FLASH in the 2D mode. What then differentiates one FISP scan from another, or one FLASH scan from another, is the choice of parameters applied to the sequence when it is run i.e. the TR, TE and FA values. The nomenclature applied to the sequences within each of the two broad groups indicates the limiting values which can be applied to these parameters for that choice of sequence name, machine constraints being set on these values in a particular sequence.

From the list of sequences available for the Siemens 1T Magnetom Impact Scanner, the following appeared to be most useful in clinical terms, and hence were selected for evaluation. The use of the terms 'slow' and 'fast' in the pulse sequence descriptions and evaluations which follow is somewhat arbitrary. Since only one sequence purports in any way to be able to image the very slow body flow rates found in the extremities, of the order of  $1\text{cmsec}^{-1}$ , the term 'slow flow' has been used when velocities of  $30\text{-}70\text{cmsec}^{-1}$  are referred to. These are the slow flow velocities of the intracranial circulation. 'Fast flow' refers to flow rates of  $70\text{cmsec}^{-1}$  and above, such velocities being more typical of the arteries of the neck, thorax and abdomen.

#### **FISP 3D PULSE SEQUENCES:**

Scanned at 1T:

1. A FISP 3D sequence designed to give good definition over the velocity range  $v = 100 - 180\text{cmsec}^{-1}$ .

2. A FISP 3D sequence designed to image equally well at  $v = 35-70$   $\text{cmsec}^{-1}$  (fast ICV) or at  $v = 115-180\text{cmsec}^{-1}$  (neck and head carotids). This sequence thus appears to be appropriate for all velocities between  $35-180\text{cmsec}^{-1}$ .

3. A REPHASE-DEPHASE sequence based on FISP 3D interleaved sequences also specified for slow flow,  $30-45\text{cmsec}^{-1}$ .

Scanned at 1.5T:

4. A FISP pulse sequence designed to image slow intra-cranial flow between 30 and 45  $\text{cmsec}^{-1}$ . This sequence is also specified for peripheral vasculature where the flow rates can be those of the capillary network and as low as  $1\text{cmsec}^{-1}$ .

#### **FLASH 2D PULSE SEQUENCES :**

Scanned at 1T:

5. A FLASH 2D pulse sequence designed to image slow flow at  $30-45\text{cmsec}^{-1}$ .

6. A FLASH 2D pulse sequence designed to image all velocities from  $60-180\text{cmsec}^{-1}$ .

#### **9.1.2 FACTORS WHICH DIFFERENTIATE THE CHOSEN SEQUENCES**

Scrutiny of the sequence parameters recommended for imaging in each of these velocity ranges reveals the following:

3. A FLASH 2D sequence designed to image slow flow at  $v = 30-45\text{cmsec}^{-1}$ .

4. A FLASH 2D sequence designed to image all velocities from 60-180cmsec<sup>-1</sup>.

Scrutiny of the sequence parameters recommended for imaging in each of these velocity ranges reveals the following:

1. The FISP3D sequence with FA = 20<sup>0</sup>, TR = 36msec, TE = 10msec seems to be applicable to blood flow at a wide range of velocities. The same sequence parameters are applied for this sequence whether it is being used to image very fast flow in the aorta and carotids of the head and neck (v = 100-180cmsec<sup>-1</sup>) or to intra-cranial 'fast' flow (35-70cmsec<sup>-1</sup>) i.e. this sequence is supposed to image velocities of 35-180cmsec<sup>-1</sup> equally well. The option to image with FA = 40<sup>0</sup>, TR = 36msec, TE = 10msec (i.e. the flip angle is doubled and the TR and TE are the same) is recommended for the thoracic aorta, where the velocity is no greater than that in the vessels mentioned above. The apparent difference in the imaging capability of this sequence is that it is not required to image slow flow at all.

2. The REPHASE-DEPHASE image is reconstructed from two interleaved FISP 3D sequences, each of which uses FA = 15<sup>0</sup>, and TE = 14msec. Because of this, a longer TR of 50msec is used to incorporate the two echoes. This sequence is designated to image flow between 30-45cmsec<sup>-1</sup>. When the FISP3D sequence described above is used to measure velocity in this range, the flip angle is 20<sup>0</sup> and the TE is 10msec. Any differences in image quality at this low velocity range have to be evaluated in terms of these changes in sequence parameters.

3. The FLASH 2D sequence appears to be very sensitive to change in flip angle. For the sequence specified for slow flow, (v = 30-

45cmsec<sup>-1</sup>) and that specified for fast flow ( $v= 60-180\text{cmsec}^{-1}$ ), the TR values (40, 39msec respectively) are nearly identical. For imaging slow flow, the recommended flip angle is 35<sup>0</sup>, and for fast flow it is 40<sup>0</sup>. No information is available about the difference in pulse sequence gradients used in these two sequences. Because the other parameters are so close in value, any differences in performance of these two sequences appear to be due to the different flip angles used.

### 9.1.3 PULSE SEQUENCE PARAMETERS USED IN THE SCANS

The scans were performed by mimicking a 65kg patient, surrounding the rotating phantom with the standard staticbody loading phantom, a hollow perspex oval sectional cylinder, the walls of which are filled with saline.

#### SCAN PARAMETERS USED WITH ALL FLASH 2D SEQUENCES

Number of slices = 16  
Minimum slice thickness = 3mm  
Distance factor 0.5 = 1.5mm  
FOV = 300mm  
Matrix = 256 x 256

#### SCAN PARAMETERS USED WITH ALL FISP 3D SEQUENCES

Number of slices = 32  
Slab thickness = 48mm  
FOV = 300mm  
Matrix = 256 x 256

The rotation rate of the phantom was controlled by the valve linking a 4bar air cylinder to the phantom motor. The rate of rotation was checked before and after each scan to ensure that a change in rotation rate had not occurred during the time of the measurements. To simulate the higher blood velocities, the phantom was rotated at 114rpm with velocities of 11 to 110cmsec<sup>-1</sup> between the axle and the

periphery of the drum. When the scan sequence was designed to image slower velocities the rotation rate was reduced to 67rpm, so that the imaged range was 7-67cmsec<sup>-1</sup>.

It was not possible to test longitudinal flowrates up to 180cmsec<sup>-1</sup>, the limit encountered in normal arterial flow, in this study. The pressure of the available air supply was such that the rate of revolution of the drum could not be increased beyond 114rpm. Further work at higher velocities would require modification of the phantom design by the inclusion of a gearing system. This further work has not been possible in this study, and it is essential that the sequences specified for higher velocity ranges are tested at these increased velocities before guaranteed recommendations can be made about their efficacy for clinical imaging at higher flow rates. It is shown in chapter ten that some new aspects of velocity dephasing appear as the result of this study which are not previously related in existing literature on the subject. It is possible that further novel aspects of spin behaviour would be observed at higher spin velocities, and it cannot be assumed that extrapolation from results presented here will accurately predict the behaviour of spins at higher velocities, or provide a guide to the imaging capability of the sequence at these velocities.

## **9.2.EVALUATION OF SEQUENCE PERFORMANCE : NORMALISATION OF THE ROTATING DRUM IMAGE SIGNAL**

The standard software for the scanner includes the function to present a graphed profile of pixel intensities across an operator

selected chord on the image. The software will only consider a chord one pixel wide, and it does not eliminate random intensity fluctuations by smoothing over neighbouring pixels, for instance by sampling a 3 pixel wide band. Statistical fluctuations dominate the profile, and it does not give a true picture of the trends of intensity evident in the image. Hence a novel method of producing this information has been devised.

For all the imaged slices, for all sequences, a 1cm grid was applied to the console screen using standard software, so that the length of each phantom image could be accurately referenced, and positional comparisons made from image to image. The mean and standard deviation of the pixel intensity in each centimetre length of both the rotating and the static phantom drum slice alongside it was obtained, again using standard software. This process ensured that the intensities of the image of interest, that of the rotating drum, could be normalised by dividing measured intensities by the corresponding values for the static drum (Fig.9.1). This is an essential part of the image evaluation process, and the reasons for this have been fully discussed in chapter 8. The normalisation procedure has the additional advantage that any signal fluctuations arising from localised system inhomogeneities are also eliminated. Typical reconstructed normalised image intensity profiles are shown in Fig.9.2.

The analytical procedure described was followed in all cases, except in that of the FLASH 2D sequence designed to image velocities of 60- 180cmsec<sup>-1</sup>. For this sequence, dark bars appeared at changing intervals on all the scanned slices (figure 9.3). Their position and

intensity is such that a false impression of the trend in image intensity with increasing distance and velocity from the axis of rotation is obtained if pixels are sampled in a 1cm. box, because of the smoothing effect between very bright and dark bar intensities. For these images, mean pixel intensities were obtained at positions indicated as areas of brightness surrounding the prominent dark bars. These positions differed from slice to slice, and consequently intensities could not be constructed graphically by computer, and manual graphing has been necessary. Signal normalisation was performed in the same way.

Artefacts of a different nature were seen on one of the FISP 3D scans (see figure 9.4). These also have the appearance of bars crossing the short diameter of the imaged slices. However in contrast to those described above, the bars are much narrower and more numerous, and the difference in intensity between the bright regions and the dark regions is less marked. The bars are also curved at the edges, this being a definite and regular feature which appears on more than one slice image. Because the changes in signal intensity due to these bands are much smaller and less easily separable from surrounding higher signal than in the case of the FLASH 2D scan described above, the mean signal intensity was measured at 1cm intervals across the imaged slices averaging across the intensity fluctuations.

### **9.2.1 DISCUSSION OF IMAGE ARTEFACTS DUE TO THE ROTATION OF THE GEL IN THE DRUM.**

The rotating phantom simulates the continuous range of flow rates which may be encountered in body arteries. At the first rotation

rate used, 67rpm, the rotating drum generated a velocity range of 7-67cmsec<sup>-1</sup>, whereas at the higher rotation rate of 114rpm, the simulated range was 11-110cmsec<sup>-1</sup>. However, whereas longitudinally flowing in vivo blood will pass through the image volume once only, the phantom gel rotates repeatedly through the image volume during the acquisitions. Thus there may be some features of the drum phantom images which are purely the result of this rotational motion, and which will not be present in images of longitudinal in vivo flow. These aspects of the images must be established before prognoses can be made about the efficacy of the sequences for in vivo imaging, based on the observed results of the phantom scans.

#### **9.2.1.1 ARTEFACTS IN THE FLASH 2D DRUM PHANTOM IMAGES : BARS OF REDUCED SIGNAL INTENSITY**

Prominent dark bands are seen on the phantom scan slices obtained for gel speeds of 10 -110cmsec<sup>-1</sup> using a FLASH sequence for which TR = 40msec, TE = 10 msec and FA = 40<sup>0</sup> (figure 9.3). These effects are not apparent when the gel is simulating velocities of 7-67cmsec<sup>-1</sup>, and the FLASH scan parameters are TR = 39msec, TE = 10msec and FA = 35<sup>0</sup>.

Two factors appear to be responsible for these bands. The first is the use of a flip angle of 40<sup>0</sup>. Calculations presented in chapter 8 show that for a flip angle of this magnitude, and a sequence repetition time of 36-40 msec, the flipped spin does not relax completely during the sequence and only achieves 80% of its original longitudinal magnetisation during this time. In contrast, spins with flip angles of 15 or 20<sup>0</sup> will achieve 97% of this initial longitudinal magnetisation during this same time. It thus appears

that significant saturation effects will occur if a flip angle of  $40^\circ$  is used, but that these are unlikely if a flip angle of  $15^\circ$  or  $20^\circ$  is used.

The second factor involved in the generation of these dark bands is the rate of rotation of the drum relative to the repetition time for the pulse sequence. The possibility of spin saturation arises as the gel circulates because it will receive more than one RF pulse during one revolution. Fig. 9.5 shows how the intensity minima are spatially located relative to the dimensions of the rotating drum. They appear to fall on radial lines which lie symmetrically about the vertical axis. The velocity profile (i.e. magnitude of the vertical component of velocity) is constant for each slice, so any effects which are due to the movement of the spins in the applied gradients (i.e. velocity dephasing effects) would be expected to be the same along each slice. Clearly this is not the case, and so an explanation which is related to the rotation of the gel must apply.

It is possible to predict how saturation effects at  $40^\circ$  can give rise to these minima (Fig.9.6). Consider the central axis slab of imaged gel as being a convenient reference slice. At a rotation rate of 114rpm the gel revolves through  $360^\circ$  in 530msec. The T1 value for the gel is 1100msec, (which is the time for 63% longitudinal relaxation when the flip angle used is  $90^\circ$  rather than  $40^\circ$ ) and so it is likely that the spins will not have fully relaxed during the revolution. On the next of the 256 pulses which are used to encode the slice, saturation will begin to build up. By the time imaging of this slice is complete, the gel will have achieved a significant degree of saturation.

When imaging of the next slice begins, this first slice of gel will fall into the new imaged volume at definite times during the imaging procedure. The first slice of gel will be inclined to the second slice of gel at times of signal acquisition, and the angle of inclination will depend precisely on the sequence repetition time, and the rate of rotation of the drum. If the motor speed had been set so that the rotation rate was 60rpm, 120rpm, etc. no angular overlap would have occurred, since the first imaged slice would be parallel to the second imaged slice at time of acquisition. The inclinations at which overlap of slices will occur have been calculated for 114rpm and TR = 39msec. These predicted minima are illustrated in Fig.9.7, and within the limits of accuracy of the analytical technique employed, correspond to the observed locations of the intensity minima. More accurate simulation could be achieved by iterative computer programming.

The useful conclusion to this analysis is that the dark bands which are a feature of the imaged slices of the rotating drum using the sequences FLASH 2D, FA = 40°, TR = 39msec, TE = 10msec, would not occur if these same sequences were used to image blood flowing only once through an imaged volume. The results which are reliable are the trend in brightness taken for the FLASH 2D slice, when the dark minima are ignored altogether. Image measurement shows that the minima for the FLASH scan achieve a mean value of 75% of expected brightness.

Similar effects are not observed for the FLASH 2D scan for which the FA = 35°, TR = 40msec, TE = 10msec because the drum was rotated at the slower rate of 67r.p.m during this scan. This means that the

time of one revolution is 885msec, which is comparable with the T1 for the gel. Thus despite the fact that the flip angle is large enough to achieve significant saturation for consecutive pulse applications, the gel spins have adequate time to relax before by rotation they arrive back at their original orientation.

#### 9.2.1.2 ARTEFACTS IN FISP 3D DRUM PHANTOM IMAGES : ZEBRA STRIPES

There are several revealing differences in the appearance of the darker intensity bands on the FISP scan at FA = 40° (figure 9.4). Firstly, the bands are much more numerous, and their separation is of the order of 2-3mm. Secondly, the decreases in intensity of the bands is far less. Thirdly, the bands are curved at the edges. It is possible that there may be some saturation effects resulting from the rotation of a slab of gel of thickness 48mm between RF pulses, and this is tested by the same predictive method as was used for the FLASH 2D scan above (figure 9.8). For this sequence, all the spins in the image volume are flipped for each application of the RF pulse. Some saturation is thus to be expected, since a total of 256 x 256 x 32 repetitions of the pulse sequence are applied during the scan. However figure 9.8 makes it clear that because of the size of the image volume, there will not be precise locations where signal loss will accumulate, and the signal reduction will appear as a general effect throughout the image volume. It will depress the signal intensities by a fairly constant multiplicative factor, but it will not produce precisely defined regions of signal loss which will then be observed as dark bars. These bars must result from some unique property of the FISP sequence which is not present in the FLASH sequence.

FISP pulse sequences are designed to maintain free precession in the steady state, and the gradients which are used to ensure this produce a unique feature in the encoded spins. The first application of the phase encoding gradients ensures that each spin has a unique set of 256 phase increments, depending on their exact location in the gradient. The rewinder gradients ensure that dephasing effects are eliminated and transverse magnetisation is retained in the steady state. On repetition of the pulse sequence, the transverse phase will be stepped up, and phases of  $0-2\pi$ ,  $2\pi-4\pi$ ,  $4\pi-6\pi$  etc. result where the spins are in stronger gradients. It is the maintenance of constant transverse magnetisation which is responsible for this periodicity of phase, and it does not appear in the FLASH sequence which uses a spoiler pulse on the transverse magnetisation. When the echo is detected, the system will not differentiate between phase angles of  $\theta$  and  $2\pi + \theta$ , and if a phase image is reconstructed rather than a modulus image, the image will appear as a range of bright and dark regular bands, known as zebra stripes. These are bright for phases of  $0, 2\pi, 4\pi, 6\pi$  etc, and dark for phases of  $\pi, 3\pi, 5\pi$  etc.. A schematic representation of this effect is shown in Fig. 9.9(a) .

If the spins are moving, the spin phases are modulated by the motion induced transverse phase change. Spins of the same phase, particularly  $90^0$  (bright) and  $180^0$  (dark) will no longer occur at the same spatial ordinate along the vessel, but at some location defined by their relative velocities. The observed pattern of bright and dark bands in the phase image is shown in Fig. 9.9(b), for moving spins.

These zebra stripes which are clearly present in the phase image will also affect the modulus image, but in a less definite way. Spin phase appears in the modulus image when the total pixel intensity due to summation of the phases of the spins in the image voxel is calculated. When spin dephasing due to velocity arises, the modulus intensity contains a phase dependent component:

$$M_z = \sqrt{(R \cos \phi)^2 + I^2}$$

where R and I are the real and imaginary components of the phase vector, and  $\phi$  is the phase angle. The  $\cos \phi$  factor ensures that the intensity of the modulus image will be periodic with velocity, until velocities are reached when the spin dephasing effect dominates to such an extent that the pixel intensity drops altogether below the ideal value.

This effect is not observed in the FISP scan where the flip angle is  $20^\circ$ , nor do they occur in the REPHASE DEPHASE scan which uses a FISP pulse sequence with a flip angle of  $15^\circ$ . The change in transverse phase induced by motion in the applied gradients is dependent on the flip angle in a complex way (Patz, 1988). The indication of the image intensities in these three cases is that spin dephasing effects are greater in the case of a low flip angle, and that for flip angles of  $15^\circ$  and  $20^\circ$  they are random enough to ensure that the periodic zebra stripe pattern is completely destroyed. The relative spin dephasing produced at a flip angle of  $40^\circ$ , at the same range of velocities, is less, and hence the images retain some of the zebra stripe pattern.

The periodicity of the FISP scan slice intensity is not an artefact due to the rotation of the phantom drum. It is rather an inherent effect of the FISP sequence itself, when it is used to image flowing spins, and it can be used to explain artefacts in clinical in vivo blood flow images (figure 9.10). Its presence can lead to misdiagnosis, and its effects and its implications for the efficacy of tested pulse sequences for clinical use are discussed fully in chapter 10.

### 9.3 QUALITATIVE OBSERVATIONS ON THE IMAGED SLICES.

For each of the FISP sequences, a set of 32 image slices was obtained, and for each of the FLASH scans, a set of 16 image slices was obtained. Visual inspection of these slices reveals differentiating features due to the different scan parameters and pulse sequence lobes, and photographs of a representative selection of slices is appended to show these. A descriptive summary and discussion of the appearance of slices follows.

#### 9.3.1 FISP 3D PULSE SEQUENCES TESTED AT 1T

##### 9.3.1.1 FISP 3D, $FA = 40^\circ$ , $TR = 36\text{msec}$ , $TE = 10\text{msec}$ . (Figure 9.4)

This sequence is designed to image velocities up to  $180\text{cmsec}^{-1}$ . The drum, rotating at a velocity of 114rpm, has a velocity of  $110\text{cmsec}^{-1}$  at the periphery-i.e. it is mimicking velocities of 10-110 $\text{cmsec}^{-1}$ .

All the image slices for this sequence are marred by striations, which are not a function of the rotation of the drum, but are zebra stripe artefacts arising from the gradients used in the sequence, as indicated above in the discussion of drum artefacts (9.2.1.2).

Inspection shows that apart from these variations in intensity, the image intensity is not constant across the slices, particularly at the edges of the imaged slab. Here spin flow into the slab images more brightly than flow out of the slab, for virtually the whole range of velocities scanned.

On slices which lie in the middle of the imaged volume, the image intensity is more constant despite the direction of rotation. Signal loss is apparent at the edge of the slices, where the velocity of the spins is greatest.

#### **9.3.1.2 FISP3D, FA = 20°, TR = 36msec, TE = 10msec. (Figure 9.11)**

This sequence is supposedly usable for all velocities 30-180cmsec<sup>-1</sup>, but is specifically recommended for the ranges 35-75cmsec<sup>-1</sup> and 100-180cmsec<sup>-1</sup>.

Signal intensities appear to be greater at all velocities when this sequence is used as compared with the sequence described in 9.3.1. It gives weaker intensities for velocities of less than 50cmsec<sup>-1</sup>, and signal losses at high velocities at the ends of the slices are noted, where velocities of 76-110cmsec<sup>-1</sup> are produced by the drum.

#### **9.3.1.3 REPHASE-DEPHASE FISP 3D, FA = 15°, TR = 50msec, TE = 14/14msec (Figure 9.12).**

This sequence is designed to image flow in the range 30-45cmsec<sup>-1</sup>.

The TR of this sequence is longer than normal because it is run twice on each acquisition.

Two echoes are obtained, the TE for each detection being 14msec. Velocity dephasing compensatory gradients are applied during the first of the two interleaved sequences, but not on the second. The stationary background spins give the same intensity on each acquisition, and these are eliminated on subtraction.

The console image of figure 9.12 indicates that the final image quality is indeed uniform across all the slices. However this is not the effect that the rephase-dephase sequence should produce under these scan conditions. At the greater radii of the drum, the number of fresh spins entering unit scan volume in unit time is greater. If the rephase-dephase gradients maintain constancy of spin signal, the image should actually get brighter with increasing radius, because of this volume effect. That this is not the case proves that the rephase-dephase gradients are not effective.

It is also clear that this sequence produces an image of poorer quality than that of other FISP scans. The pixel intensities from the stationary and rotating drum slices are hardly distinguishable from the random intensities due to background noise. The differences between this and other FISP 3D acquisitions described is that the flip angle is very low. Calculations in chapter 8 show that a better response would be obtained if a flip angle of  $20^{\circ}$  and a TR of 10msec are used.

### 9.3.2 FISP 3D SEQUENCES USED AT 1.5T

#### 9.3.2.1 FISP 3D, FA = 15°, TR = 36msec, TE = 6msec (Figures 9.13, 9.14, 9.15).

This sequence is recommended by the manufacturer to image flow rates between 30 and 70cmsec<sup>-1</sup>. The slices presented in figures 9.13, 9.14, and 9.15 show firstly that the signal intensity is quite strong at the centre of the drum, and that here the rotating drum signal is significantly stronger than that from the stationary drum. The signal detected from the moving spins increases to a maximum for velocities of about 35cmsec<sup>-1</sup>, at which point there is a dramatic decrease with further rise of spin velocity, and the signal quickly falls until it is no more than background noise level. Above velocities of 55cmsec<sup>-1</sup> there is no detectable signal from the moving spins. The response of this pulse sequence is very clearly heavily dependent on the velocity of the imaged spins, and the quality of the signal deteriorates as the spin velocity increases much more markedly than with any of the other pulse sequences tested. Either the pulse sequence parameters are inappropriate for the range of spin velocities for which the sequence is recommended, or the reconstruction matrix of 160 x 256 is too coarse, or gradient lobes are incorporated which are not usually found in MRA sequences and which are affecting the image quality.

The strengths of phantom evaluation of pulse sequences is clearly revealed in this example, since the exact velocities at which signal loss occurs can be obtained, and further tests which would be necessary to isolate which of the possible causes is actually responsible for poor image loss can be precisely specified.

### 9.3.3 FLASH 2D SEQUENCES USED AT 1T.

#### 9.3.3.1 FLASH 2D, FA = 35°, TR = 40msec, TE = 10msec. (Figures 9.16)

This sequence is recommended for very slow flow, 30-45cmsec<sup>-1</sup>.

At a rotation rate of 67rpm, the drum is mimicking velocities of 7-64cmsec<sup>-1</sup>. The selected slices show strong signal intensity at all velocities, although the signal to noise ratio appears to be worse at the edges of the imaged volume. The slices were imaged in the ascending mode with a distance factor of 0.5. The central slices of the volume show fairly constant signal intensity for all velocities, for both directions of flow.

#### 9.3.3.2 FLASH 2D, FA = 40°, TR = 39msec, TE = 10msec. (Figure 9.17, 9.18)

This sequence is designed to measure blood flow in the range 60-180cmsec<sup>-1</sup>. The slices were imaged in the ascending mode with a distance factor of 0.5.

The position and relative intensity of the dark bars described in 9.2.1.1 can be clearly seen on the photographs. However, since it is apparent that these result from the rotation of the phantom, the feature of interest is the bright intensity on which they are

superimposed. The signal intensity appears to be maintained for all velocities from  $50\text{cmsec}^{-1}$  upwards, the dark region at the centre of the slices being fairly constant in width and resulting from multiple overlap of consecutive and partially saturated gel slices during imaging. There appears to be little difference between the two sequences as a result of increasing the flip angle from  $35^\circ$  to  $40^\circ$ .

#### **9.4 3D SURFACE COMPUTER RECONSTRUCTIONS OF NORMALISED IMAGE SLICE INTENSITY DATA.**

A more quantitative appraisal of the scan data can be obtained by reconstructing the normalised image intensity data, obtained statistically, in a 3D graphical form. This presents the consecutive 2D slice image intensity profiles as a continuum formed from the surface they encompass when they are stacked together as a 3D volume. The surfaces will give instant appraisal of changes in image intensity across the whole of the scanned volume (figures 9.19(a) -9.24). If there is a change in the performance of the sequence in imaging spins at a specific velocity, it will appear as a change in magnitude and orientation of the 3D surface. The relative performance of each sequence can then be evaluated on the following criteria:

1. The regions of the scan volume where the normalised signal intensity for the rotating drum images are greater than unity can be established. This means that the sequence is imaging moving spins better than stationary spins, and therefore allowing differentiation between the two.

2. The range of velocities for which the signal falls below the ideal can also be established. It may be that signal loss is random, or there may be specific ranges of velocities for which the signal is reduced for each scan application. These regions of signal reduction may be the same for each pulse sequence, or it may be established that different sequences have good signal response to different spin velocity ranges. All of these must be examined to see whether they can be explained in terms of saturation and spin dephasing.

3. The maximum normalised signal intensities can be compared from slice to slice throughout the reconstructed stack. It is possible that the same pattern of intensities occurs from slice to slice, although the different depths of the slices in the image volume may have an effect on observed intensities.

4. As a conclusion, the best sequence for imaging a specific anatomical region can be defined, from its performance over the range of longitudinal flow rates encountered in the region.

The information which can be obtained about behaviour of flowing spins in the velocity ranges  $7-67\text{cmsec}^{-1}$  or  $10-110\text{cmsec}^{-1}$ , (depending on the selected rotation rate for the drum) is now discussed for each of the six sequences tested in this study.

#### **SEQUENCES USED AT 1T:**

##### **9.4.1 FISP 3D SEQUENCE DESIGNED FOR VELOCITIES UP TO $180\text{cmsec}^{-1}$ .**

Figs. 9.17(a) and (b) show that this sequence responds very poorly to velocities below  $40\text{cmsec}^{-1}$  where the normalised signal intensity is less than unity, and that the response is fairly consistent

throughout the thickness of the imaged slab. The signal intensity rises with velocity up to  $100\text{cmsec}^{-1}$  and then remains almost constant over the remainder of the imaged range of  $100\text{-}110\text{cmsec}^{-1}$ . This is equivalent to a loss of signal from high velocity spins, and it detracts from the manufacturer's claim that the sequence will image velocities up to  $180\text{cmsec}^{-1}$ . The signal shows anomalous reduction in two regions of the scan volume: in the region of slices 1-5, which image spins flowing out of the volume (top), and in the region of slices 21-26, which image spins flowing out of the volume (bottom), the real imaging thickness of both these volumes being  $0.75\text{cm}$ .

#### **9.4.2 FISP 3D SEQUENCE DESIGNED FOR VELOCITIES BETWEEN 35 and $180\text{cmsec}^{-1}$**

Figs. 9.20(a) and (b) show a fairly uniform increase in signal intensity with distance from the centre of the drum. This is to be expected if the pulse sequence will detect flowing spins at all velocities equally well. There is a noticeable shortfall in intensity where the spins leave the image volume for flow out of the image volume in both directions, and this appears first at high velocities, and gradually extends to the whole velocity range scanned. The normalised signal intensity is on average 1.25. There appears to be limited signal loss at low velocities.

#### **9.4.3 FLASH SEQUENCE DESIGNED FOR VELOCITIES BETWEEN 30 AND $45\text{CMSEC}^{-1}$ .**

This sequence gives a strong signal at all velocities, with a normalised intensity always greater than 2. The signal strength appears to rise in proportion to the radius and hence the velocity

of the drum (figure 9.21). This increase is curtailed at about  $60\text{cmsec}^{-1}$  and the sequence does not respond so well to velocities in the range  $60\text{-}67\text{cmsec}^{-1}$ . However the sequence fulfils its claim to be able to image velocities in the range  $30\text{-}45\text{cmsec}^{-1}$ .

#### **9.4.4 FLASH SEQUENCE DESIGNED TO IMAGE VELOCITIES BETWEEN 60 and $180\text{cmsec}^{-1}$ .**

This data cannot be reconstructed in 3D form because of the irregularity with which the bright imaging intensities were sampled. Instead it is presented as a series of consecutive slice profiles, from which the constancy of the image intensity from slice to slice can be read (Fig. 9.22). There is some signal loss at the periphery of the slices, where velocities greater than  $90\text{cmsec}^{-1}$  are mimicked by the drum.

#### **9.4.5 REPHASE-DEPHASE FISP SEQUENCE DESIGNED FOR FLOW RATES BETWEEN 30 and $45\text{cmsec}^{-1}$ .**

This is another sequence available for imaging the flow range  $30\text{-}45\text{cmsec}^{-1}$ . The graphical form of the data for the rephase-dephase sequence (Fig.9.23) indicates that the sequence images the whole range of velocities for which it is prescribed at constant intensity when they are simulated in the rotating drum phantom. However this constancy indicates that the detected signal from faster flowing spins is actually less than that from slowly moving spins, since the increased volume of imaged spins at higher radii implies that the signal should increase with radius if there are no factors detrimental to image intensity to be considered. The signal strength at all velocities is poor, the normalised value ranging from 0.79 to 1.2.

## FISP 3D SEQUENCE USED AT 1.5T:

### 9.4.6 FISP 3D SEQUENCE DESIGNED TO IMAGE SLOW FLOW AT 1.5T.

The normalised signal intensity is greater than 1, and rises with the increased linear velocity of the rotating drum, up to about  $35\text{cmsec}^{-1}$  (Fig.9.24). This is the lowest range of velocities encountered in normal human subjects, and would be apparent only in the slowest intra-cranial flow, and in the peripheral circulation. Above this there is a dramatic decrease in the signal intensity with the linear velocity of the drum, and above  $55\text{cmsec}^{-1}$ , the normalised signal is only comparable to background noise intensities in the phantom image.

## 9.5 SUMMARY

This chapter has introduced in some detail the major differences in imaging response of the tested pulse sequences to a range of flow velocities typical of those encountered in the major arteries of the body. Some valuable information about the applicability of each sequence in clinical imaging is already evident. The FISP 3D scans at  $\text{FA} = 20^\circ$  and  $\text{FA} = 40^\circ$  have numerous dark bands crossing them, which do not appear on the other FISP or FLASH scan images. These have been shown to be inherent in the performance of the FISP sequence when it is imaging flowing spins under these conditions, and hence they will also reduce the quality of clinical images. Apart from this, their response to the different velocities of the flowing spins is fairly good across the tested flow range. On the other hand, the FISP 3D sequence which uses  $\text{FA} = 15^\circ$ ,  $\text{TR} = 36\text{msec}$  and  $\text{TE} = 6\text{msec}$  at 1.5T has a marked poor response to spin velocities

above  $55\text{cmsec}^{-1}$ , and would give signal voids if used above this velocity purely because of this.

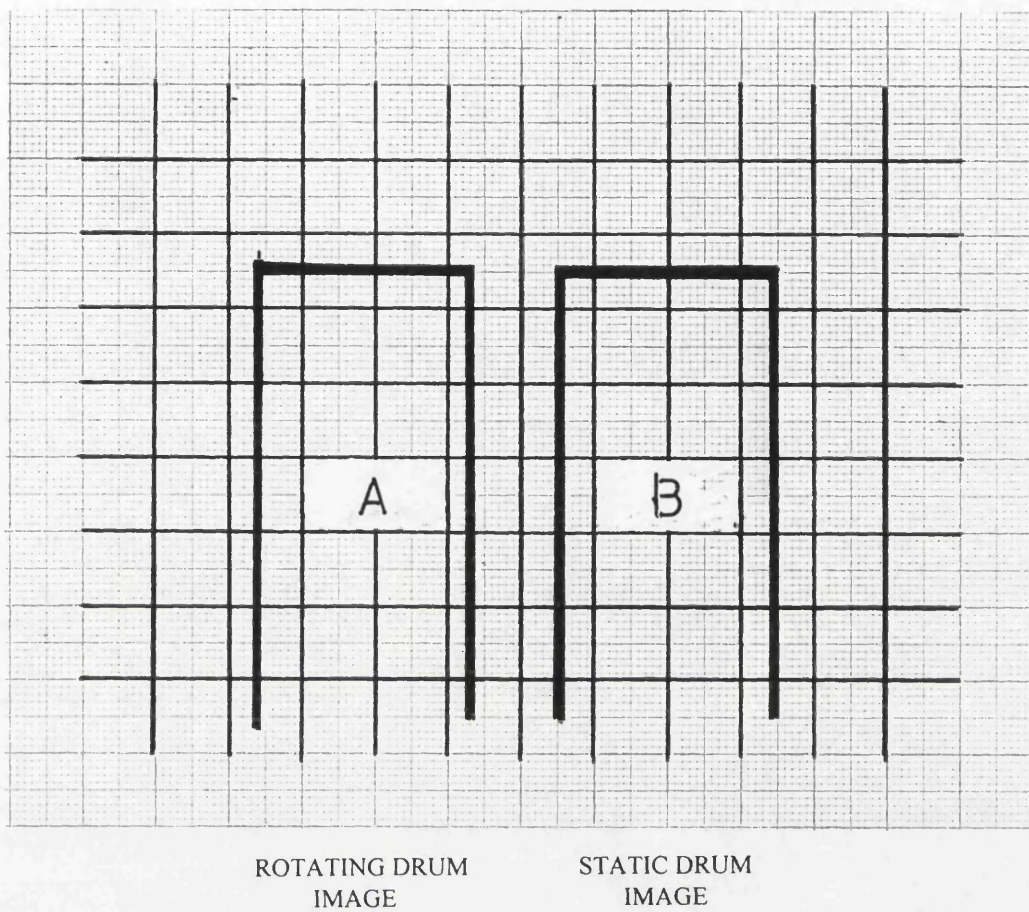
The rephase-dephase sequence using FISP 3D and tested at  $7\text{-}67\text{cmsec}^{-1}$  gives a signal from the rotating drum which is very little different to that from the static drum, and both are only marginally different from background noise, being lower than this in some areas. This is the poorest sequence of all in its response to flowing spins, and it appears that the gradients which are specially incorporated in the sequence to compensate and un-compensate for flowing spins, so that a difference image can be obtained, are inappropriately chosen. Other factors may be that the sequence uses a low echo time, and that the reconstruction matrix is coarser than that used with the other sequences.

Both FLASH sequences show a good response to spin velocity at the ranges tested, and the normalised image intensity presented in 2D profile and 3D surface form show that it is greater on average in both cases than for any of the 3D FISP scans. The dark bars which appear as artefacts on the FLASH 2D,  $\text{FA} = 40^\circ$  scan images have been proven to be artefacts of the rotating drum. They will not affect clinical images in which the blood only flows through the image volume once, since the analysis presented shows that they do not arise during the scanning of a single imaged slice, but build up as adjacent slices are subsequently scanned, the gel continually circulating through these slices.

It thus appears that these two sequences have greater potential for the imaging of flowing spins than do any of the FISP sequences. In

the following chapter, a much more quantitative evaluation of each of these six sequences is presented, and the mechanisms by which image intensity loss occurs are fully discussed.

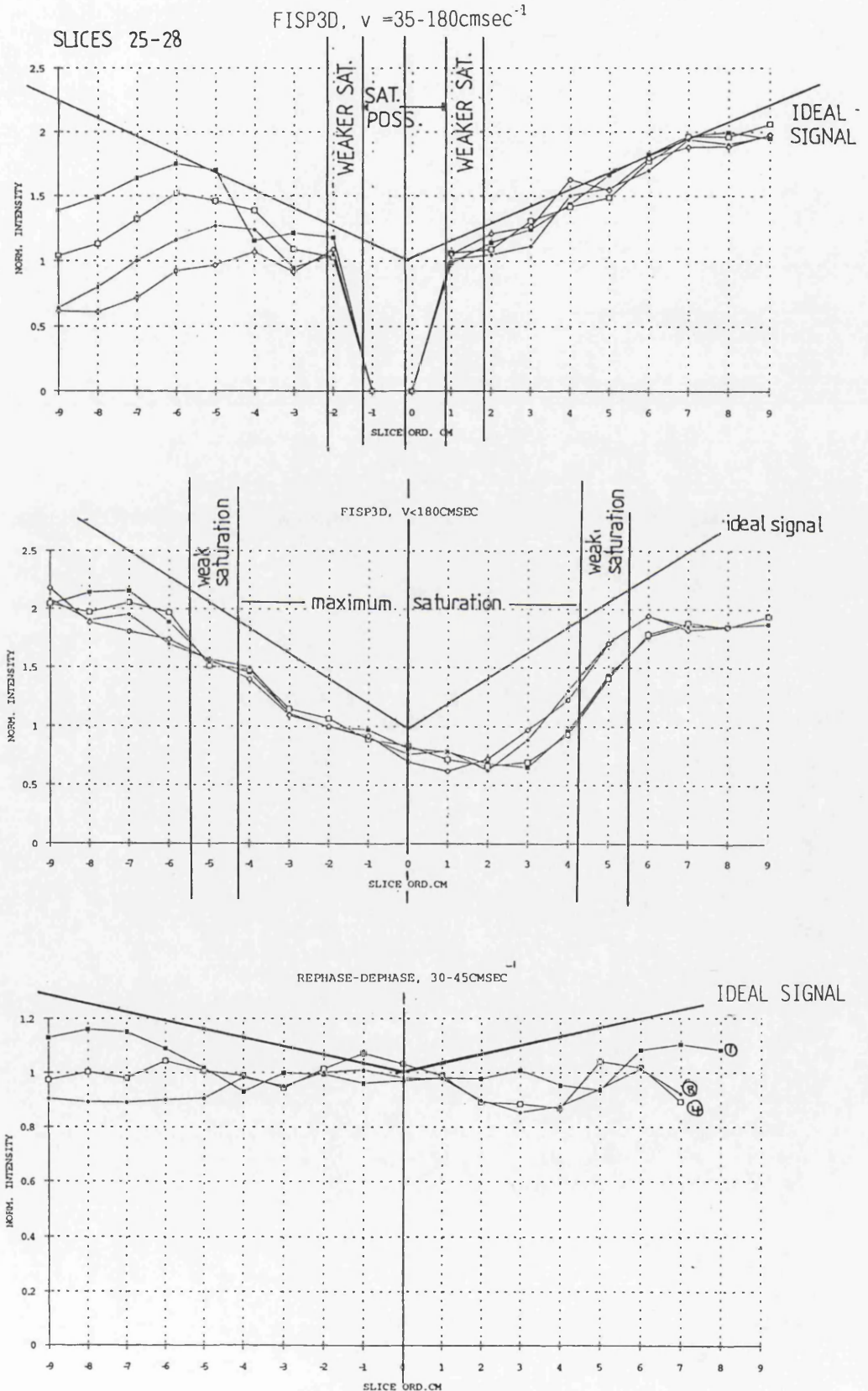
FIG 9.1 Statistical technique used to obtain the normalised signal intensity from all scan slices.



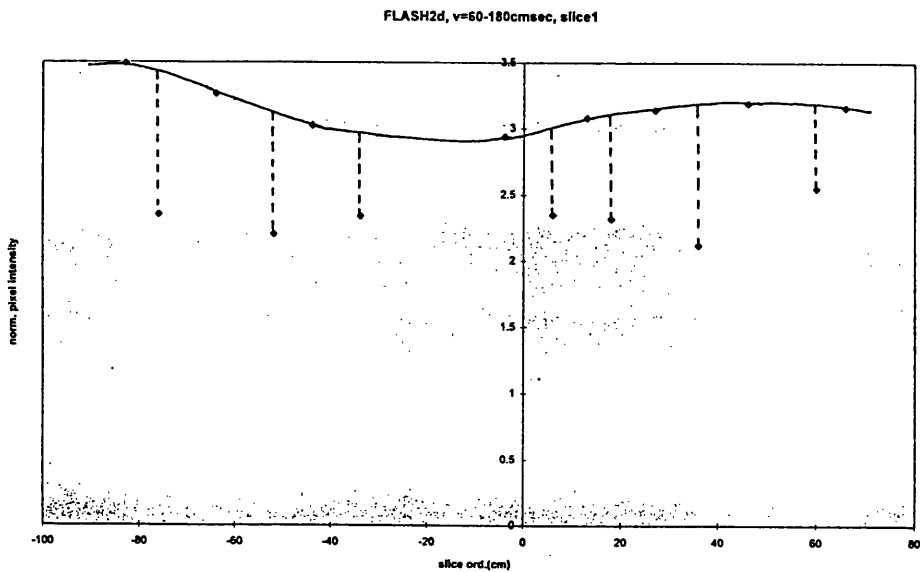
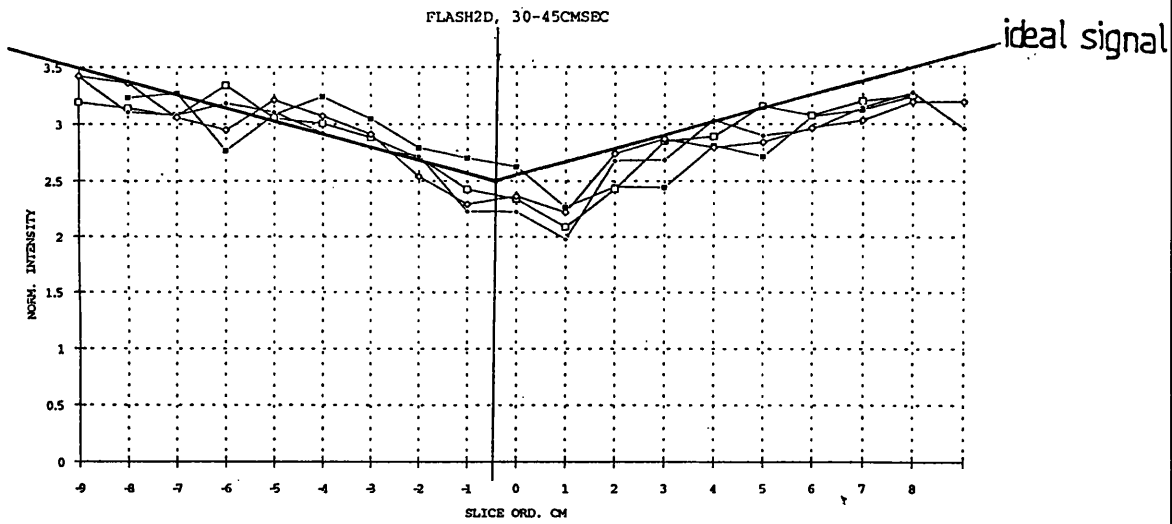
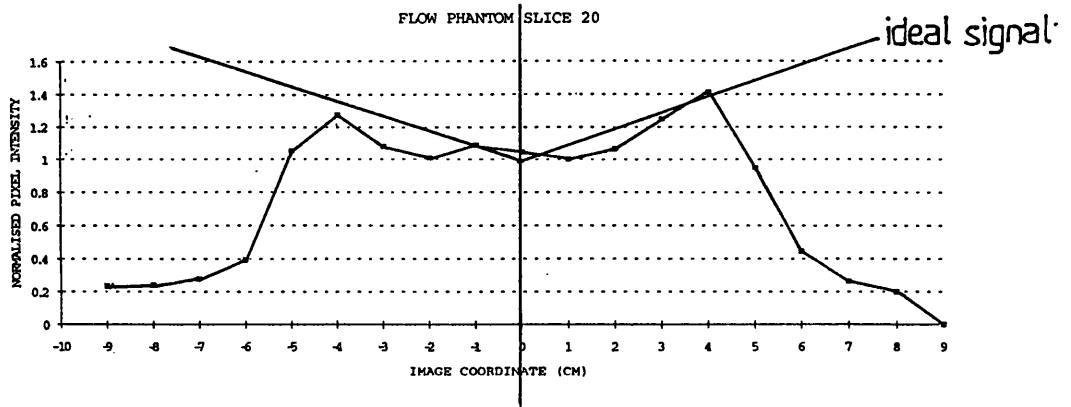
Standard scanner software applies a 1 cm grid to the image so that identical areas can be sampled for the rotating drum and the static drum images.

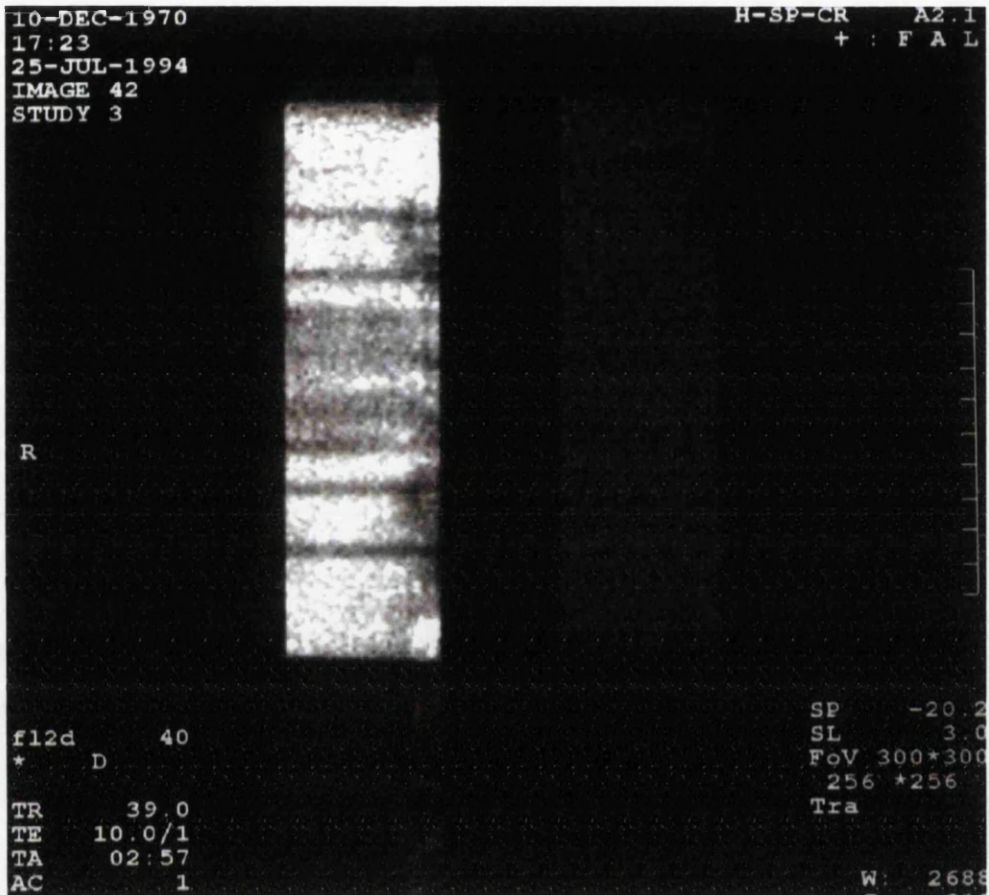
$$\text{Normalised signal intensity} = \frac{\text{mean pixel count A}}{\text{mean pixel count B}}$$

FIG.9.2 Sample reconstructed normalised image intensity profiles for the six pulse sequences evaluated in this study. The ideal signal line has been added after scrutiny of all the slices obtained for each scan, to establish the maximum signal intensity which could have been achieved. Discrepancies from the ideal, for each reconstructed slice, indicate where saturation and spin dephasing are causing signal reduction. Comparison can be made of the strength of the normalised detected signal for the six pulse sequences.



FISP3D,  $v=30-70\text{cmsec}^{-1}$  STATIC FIELD=1.5T





**Figure 9.3**

Artefacts produced by the scan of the rotating phantom using FLASH 2D, FA =  $40^\circ$ , TR = 39msec, TE = 10msec are shown. Prominent dark bands cross the drum slice. The central region of the slice, close to the axle, has an extensive area of reduced, but not uniform intensity. The bar artefacts are not replicated in the stationary drum.

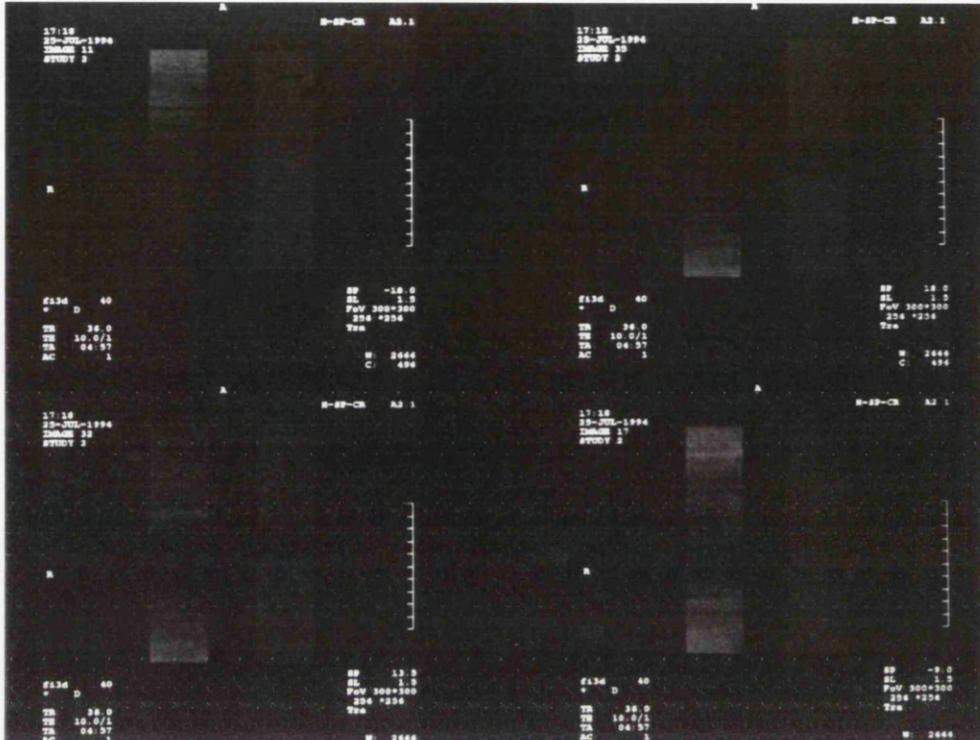


**Figure 9.4**

FISP 3D scan at  $FA = 40^\circ$ . Numerous dark bands or zebra stripes mar these images. The effects of the direction of flow on brightness can also be seen.

FIG.9.5 Observed minima in FLASH 2D, FA =  $40^\circ$ , TR = 39msec, TE = 10msec scan of the rotating drum phantom. The locations of the minima are shown as dark dots. Some experimental error is incurred in determining these positions, because the method of sampling the image slice pixel intensities is not exact. Within these experimental limits, it can be seen that the minima lie symmetrically about the vertical axis of the image volume. They also lie on well defined radial lines whose inclinations have been measured. Comparison can then be made between these experimentally determined locations, and those which have been predicted for this scan.

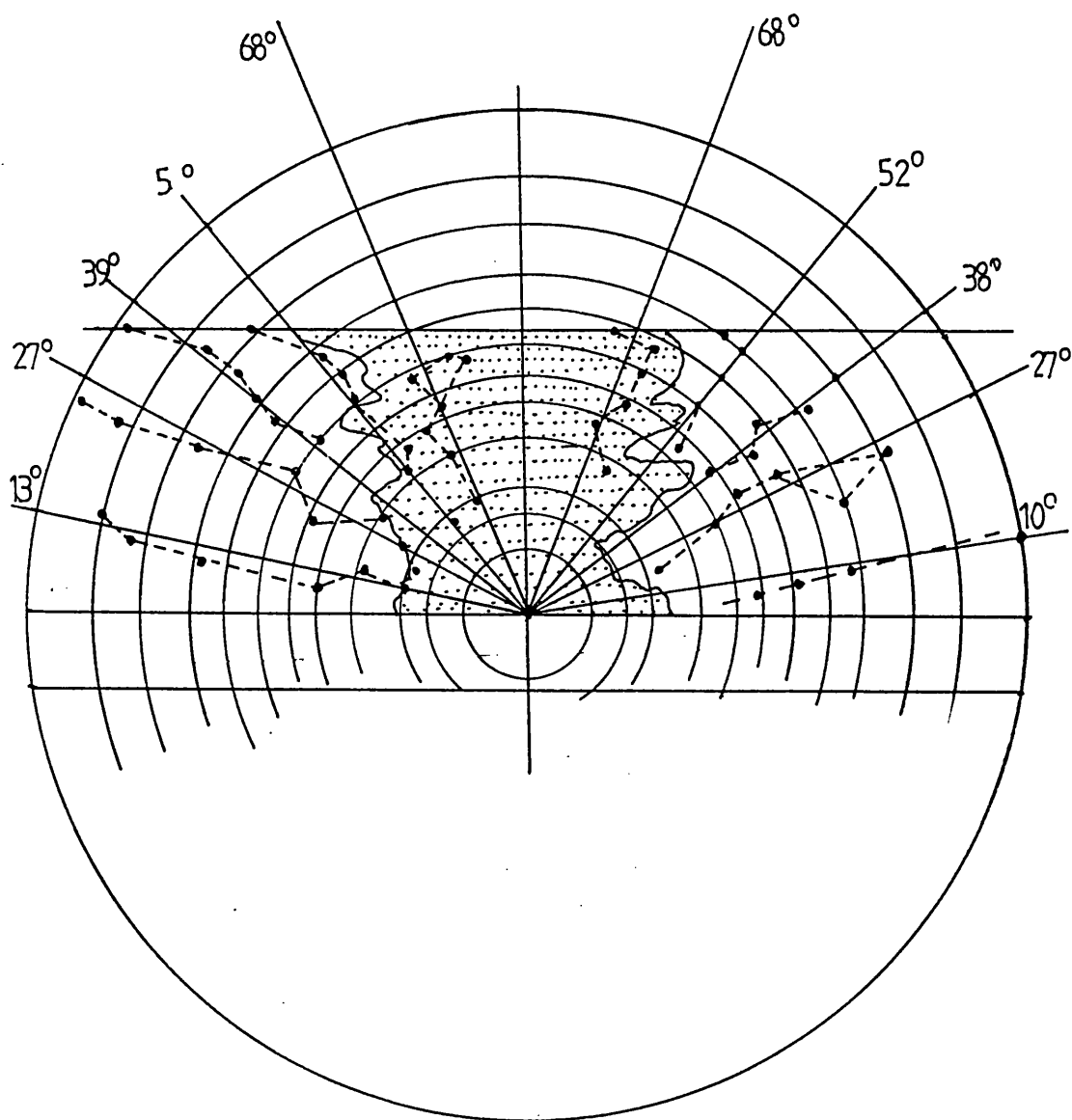


FIG.9.6  
BUILD UP OF SATURATION EFFECTS IN THE ROTATING DRUM  
GEL WHEN A FLASH 2D SEQUENCE IS USED.

Central (RF1,2,3 4) and more peripheral (RF1\*, 2\*, 3\*,4\*) slices are illustrated.

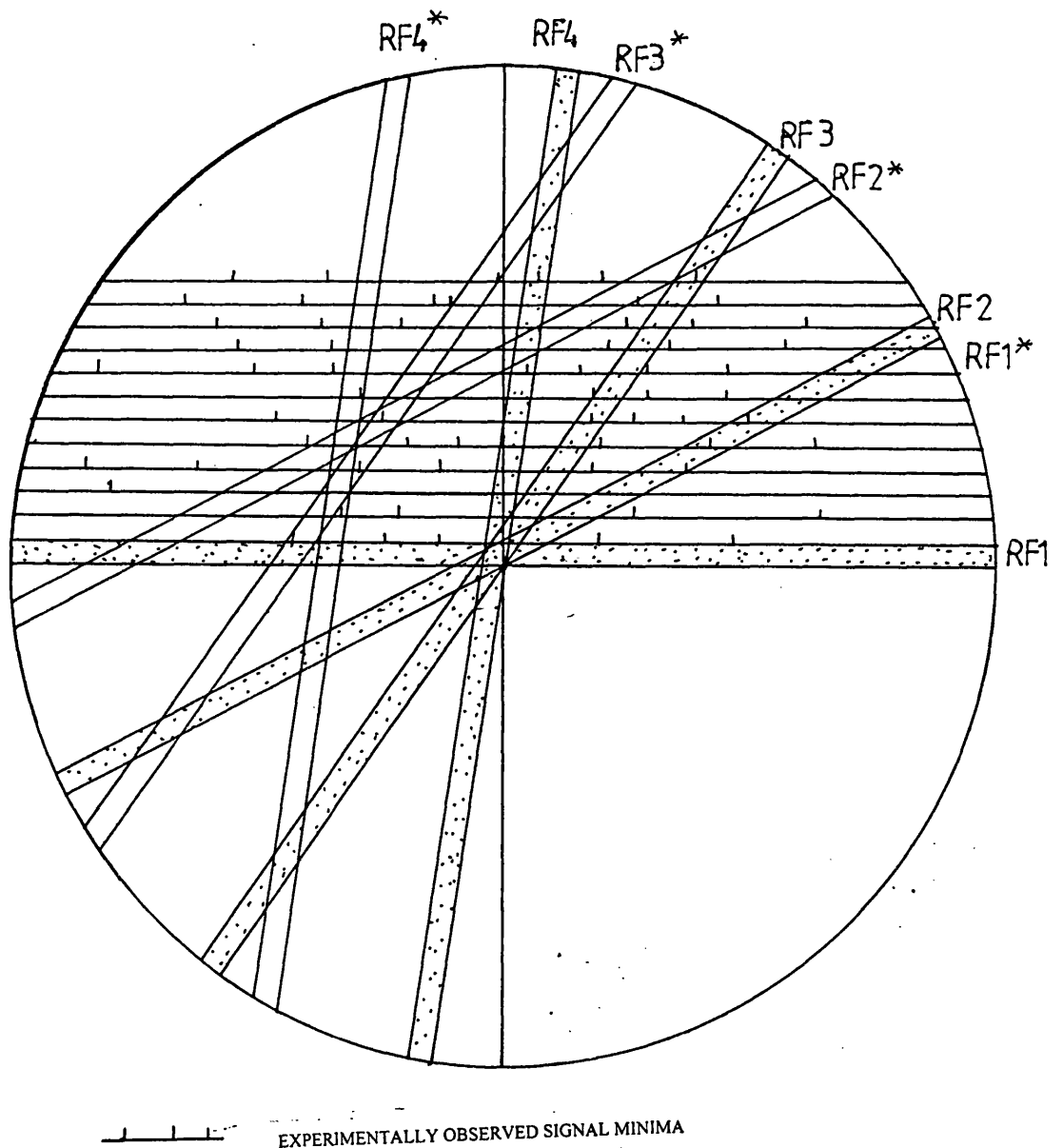


FIG.9.7

CALCULATION OF POSSIBLE LOCATIONS OF REGIONS OF MINIMUM INTENSITY RESULTING FROM THE USE OF THE SEQUENCE FLASH 2D, FA = 40°, TR = 39MSEC, TE = 10MSEC.

Drum phantom rotating at 114rpm = 1.9 revs per second.

TR = 39msec.

No. of pulse sequence repetitions per imaged slice = 256

No. of revolutions completed during the scanning of 1 slice = 18.3

The table shows the relative inclinations of imaged slices at the end of the scanning of each slice. The inclination of one slice to the next is calculated assuming that the previous slice is horizontal. Each slice is compared to the previous slice only, since more detailed work would necessitate the use of computer programming with iterative subroutines. The estimated locations of minimum signal can hence be taken as a fair guide only, though it is likely that saturation effects will be greatest between adjacent slices, since gel spins relax once slice imaging is completed.

SLICE NO.	Revs. completed during scan of slice	Inclination of slice to previous slice at which saturation effects are possible.
1	18.3	$108^{\circ} = (90 + 18)^{\circ}$
2	36.6	$216^{\circ} = (180 + 36)^{\circ}$
3	54.9	$324^{\circ} = (360 - 36)^{\circ}$
4	73.2	$72^{\circ} = (90 - 18)^{\circ}$
5	91.5	$180^{\circ}$
6	109.8	$288^{\circ} = (270 + 18)^{\circ}$
7	128.1	$36^{\circ}$
8	146.4	$144^{\circ} = (180 - 36)^{\circ}$
9	164.7	$252^{\circ} = (270 - 18)^{\circ}$
10	183	$0^{\circ}$

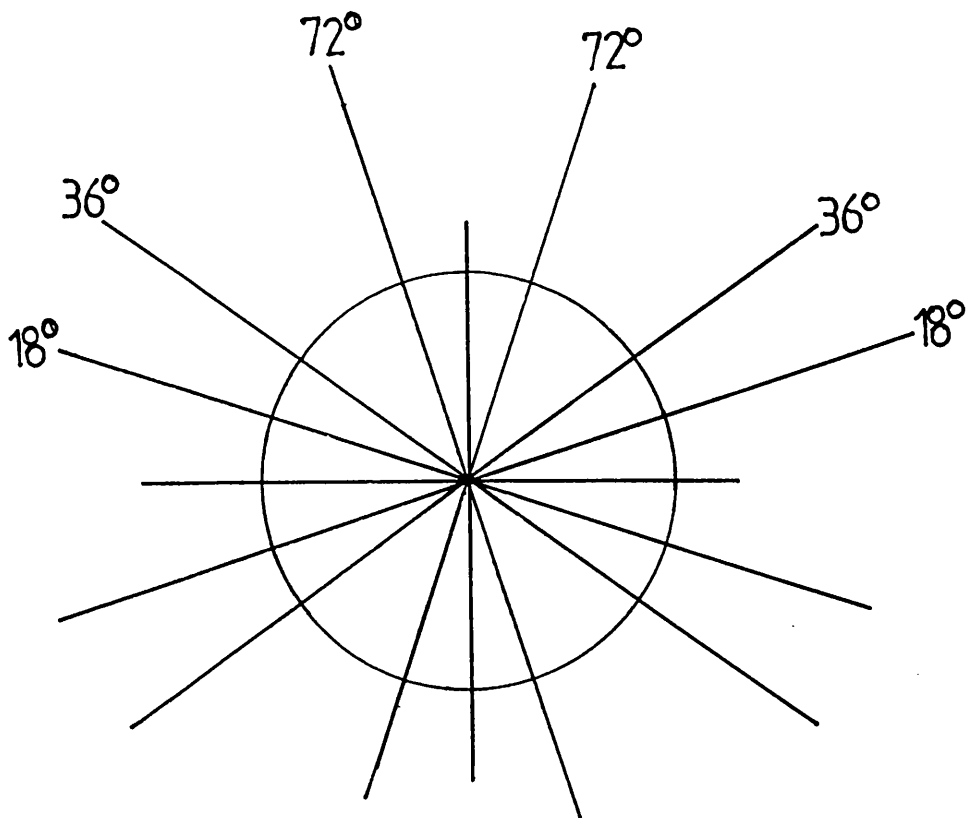


FIG.9.8 Saturation effects in 3D imaging. The location of the start scan volume (RF1) is shown. Before the application of the second RF pulse this image volume has rotated to RF2. Further pulse sequence application occurs after further rotation of the irradiated gel (RF3). Thus there may be some overall signal reduction throughout the scan volume because of gel saturation, but there will not be well defined locations where there is an abnormally high signal loss resulting in the appearance of dark bars on the image slices of the drum. It does not appear that saturation effects can be responsible for the formation of zebra stripes in FISP 3D images.

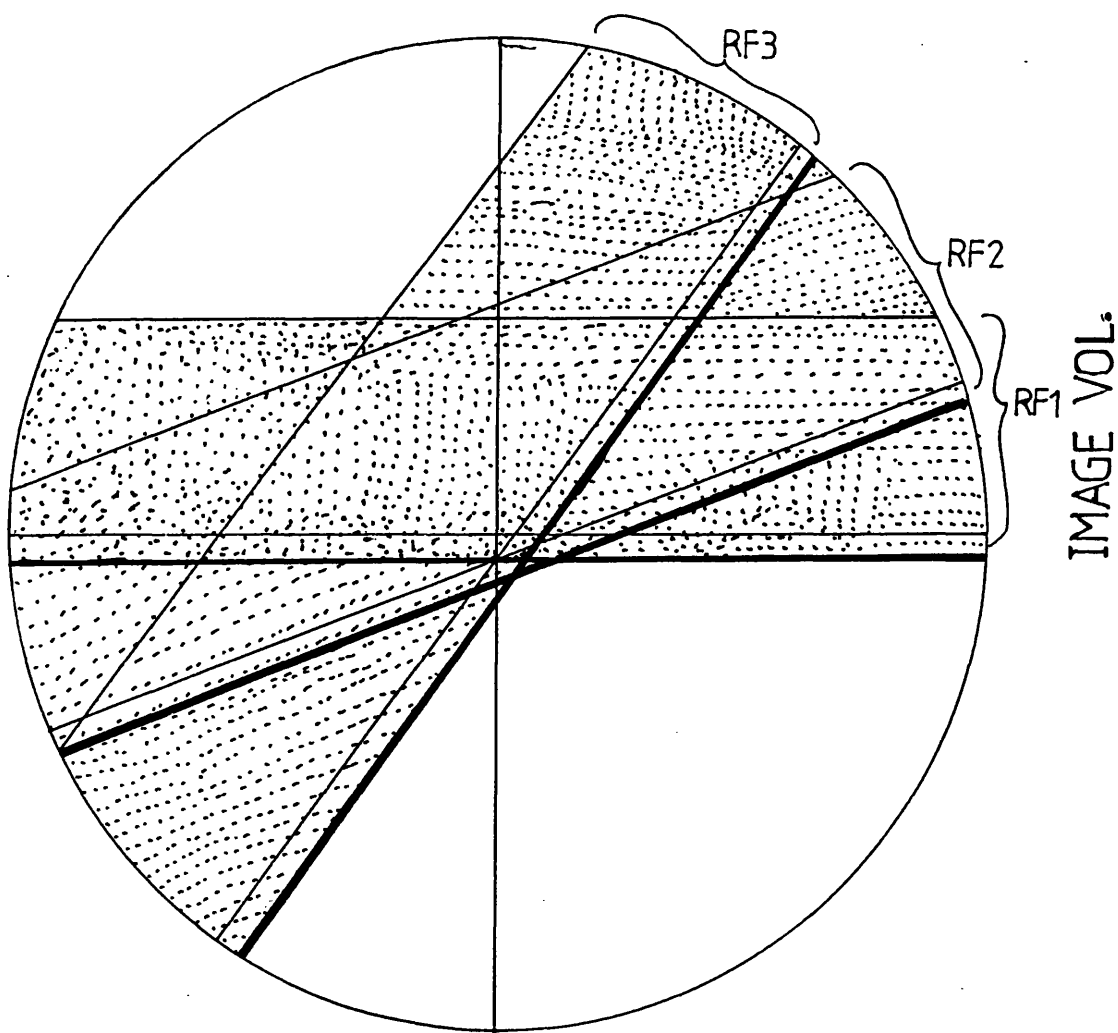
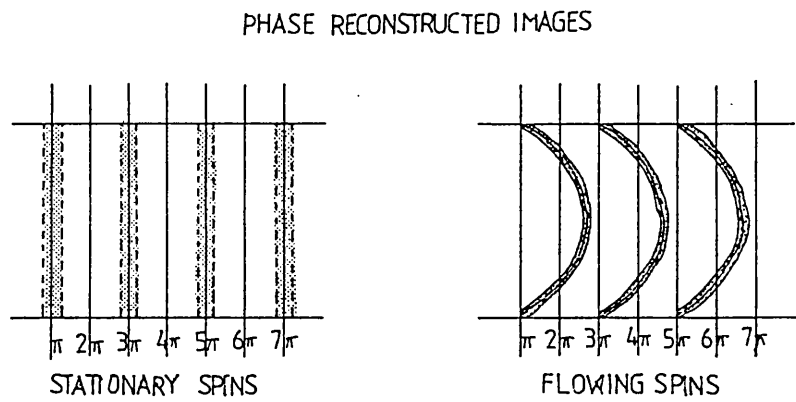


FIG.9.9 Formation of zebra stripes in FISP 3D phase images.



- a) Stationary spins imaged by FISP sequences. Phase image reconstruction signal intensity shown schematically.
- b) Flowing spins imaged by FISP sequences. Phase image reconstruction signal intensity shown schematically.



**Figure 9.10**

Zebra stripe artefacts appear clearly in the anterior cerebral and anterior communicating arteries of these FISP 3D scans.

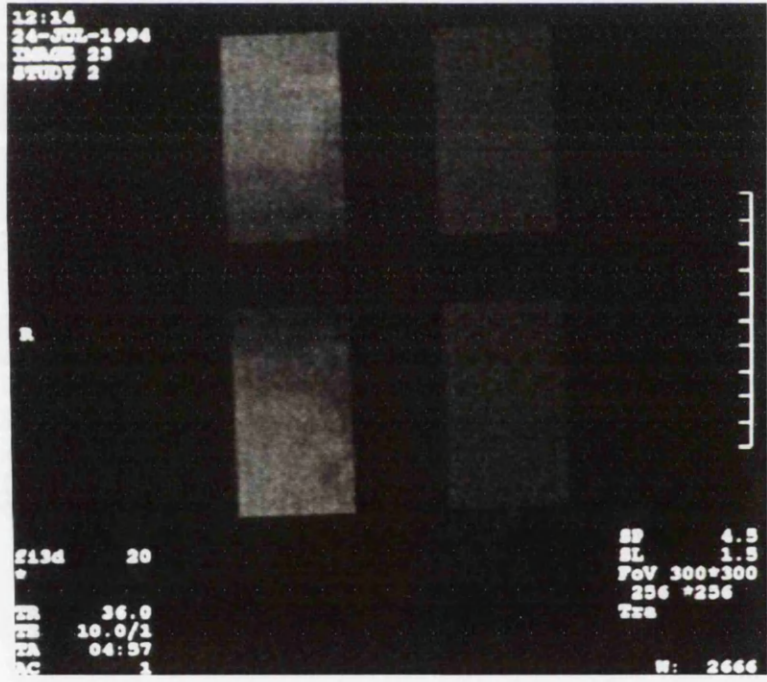
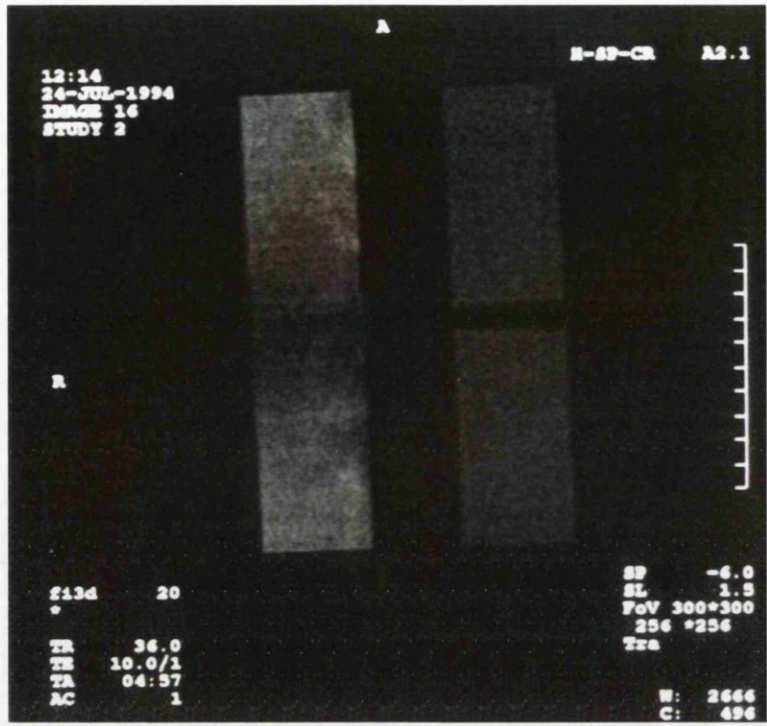


**Figure 9.11**  
 Typical image slices obtained by scanning the rotating drum phantom using the sequence FISP 3D, FA = 20°, TR = 36msec, TE = 10msec. The intensity of the rotating drum image shows differences depending on direction of gel movement. Zebra stripe artefacts are less prominent than in Figure 9.4. Image intensity increases as the distance from the centre of the drum increases.

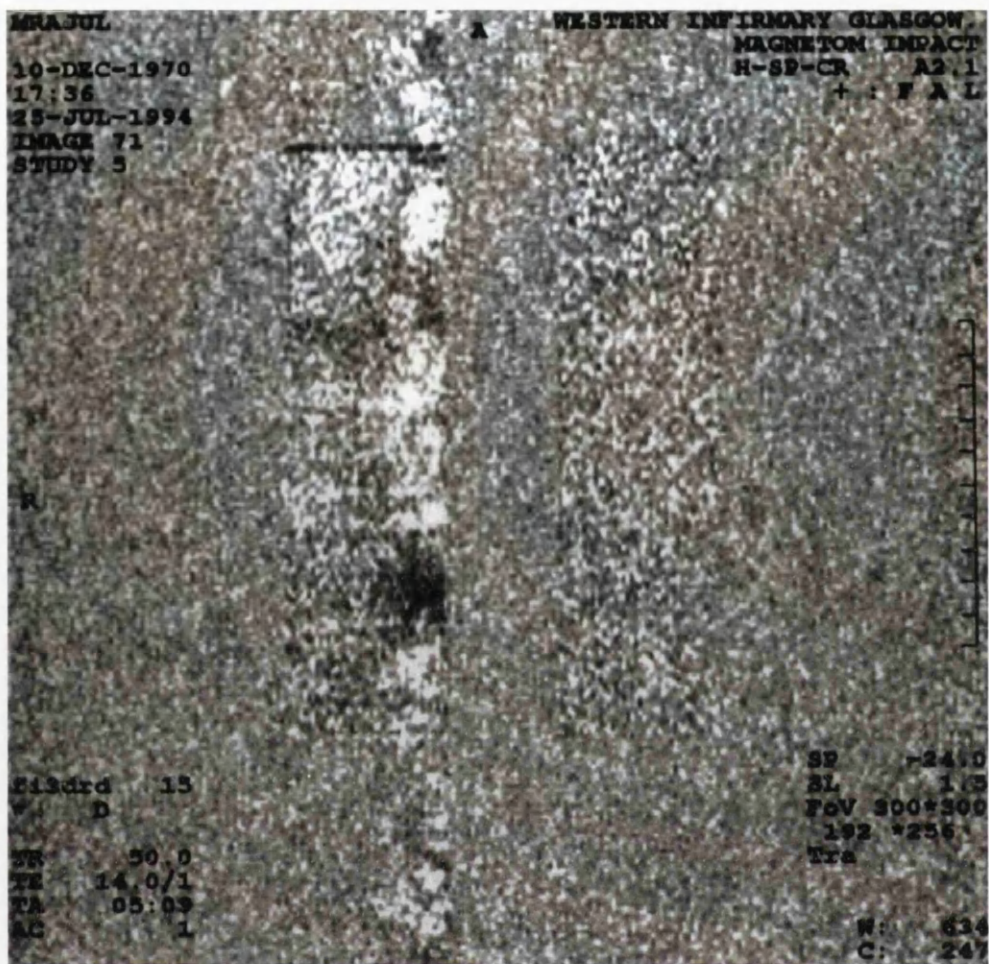


**Figure 9.12**

REPHASE DEPHASE sequence based on FISP 3D, FA = 15°, TR = 50 msec, TE = 14 msec. Zebra stripes are not visible in these scans. The poor quality of these images is apparent since the difference between slice signal and background noise pixels is not great. The slice images appear to be constant in intensity across their whole width. In some cases the static drum has imaged more brightly than the rotating drum.

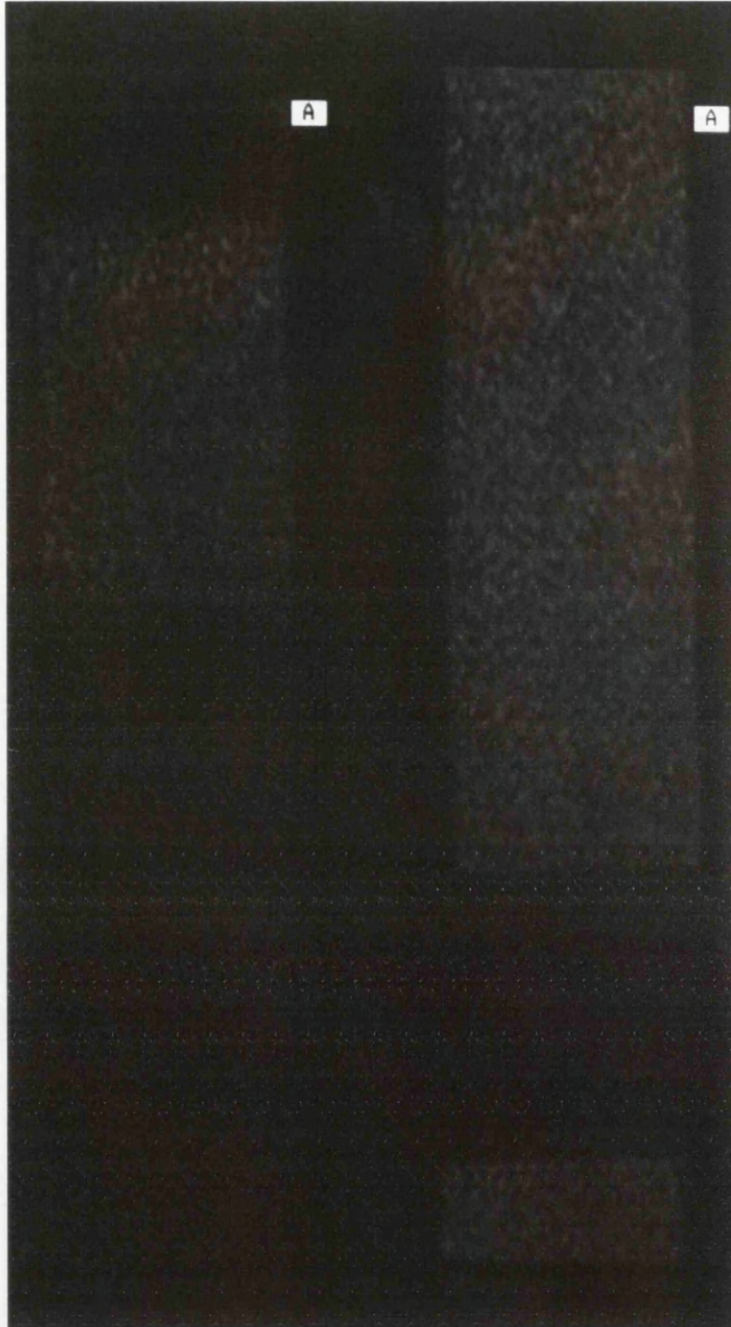


**Figure 9.13**

This scan and Figures 9.14 and 9.15 were obtained at  $FA = 15^\circ$ ,  $TR = 36$  msec,  $TE = 6$  msec using FISP 3D. Failure of the sequence to encode faster moving spins is clearly shown. Changes in brightness with distance in the image volume are apparent.

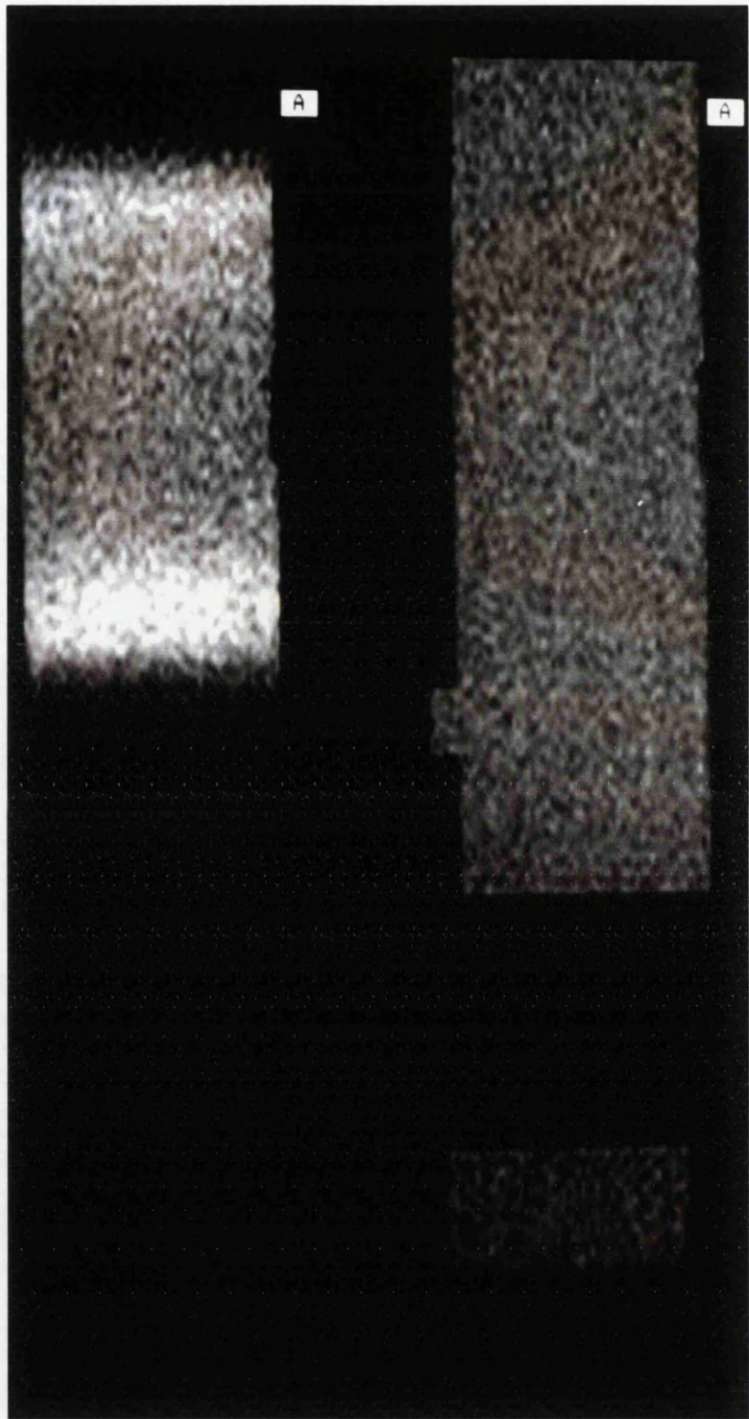


**Figure 9.14**

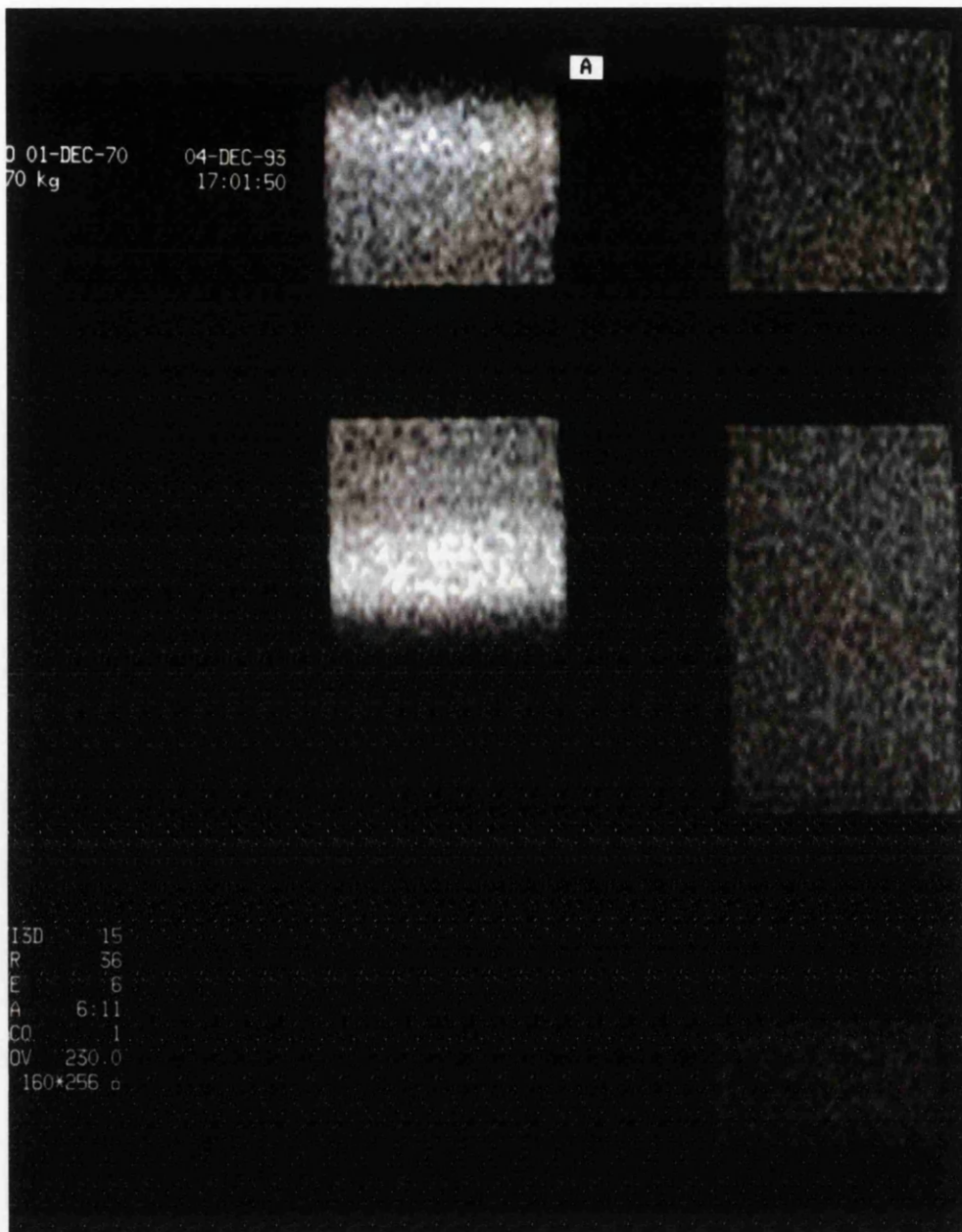
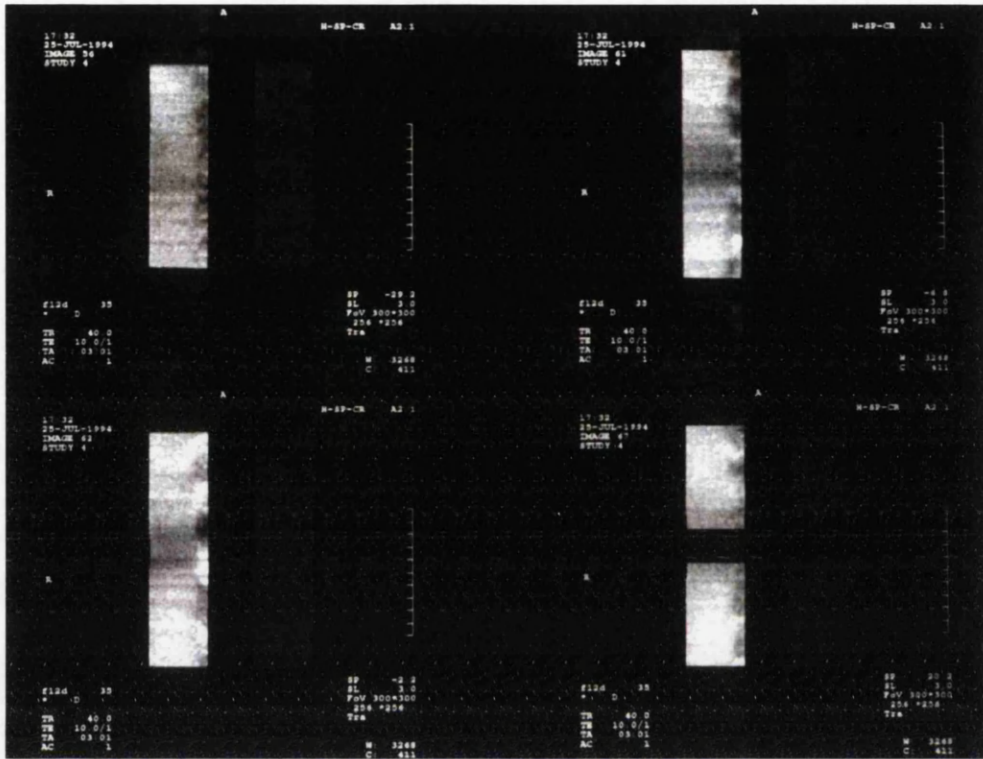


Figure 9.15



**Figure 9.16**

The phantom scanned using  $FA=35^\circ$ ,  $TR=40\text{msec}$ ,  $TE=10\text{msec}$ . The velocity range illustrated in this scan is  $7\text{-}67\text{cmsec}^{-1}$ . The dark bar artefacts are less prominent at this lower flip angle and lower velocity range.



**Figure 9.17**

The phantom scanned using the sequence FLASH 2D, FA = 40°, TR = 39msec, TE = 10msec. Comparison of these images with that of Figure 9.3 show that the position of the dark bars depends on the distance of the slice from the centre of the image volume.

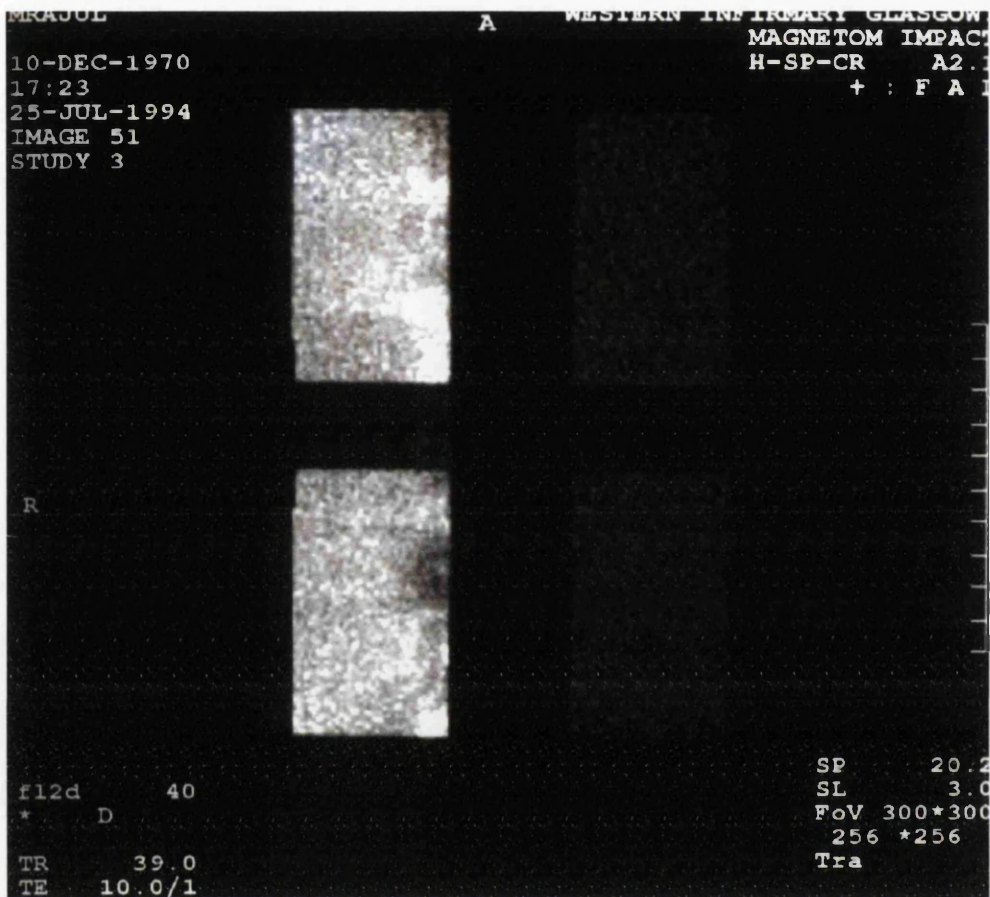


**Figure 9.18**

The central axis slice for the scan FLASH 2D, FA = 40°, TR = 39 msec, TE = 10 msec. Saturation effects in the rotating drum give reduced intensity at all velocities.

FIG.9.19a) FISP3D,  $V < 180 \text{CMSEC}$

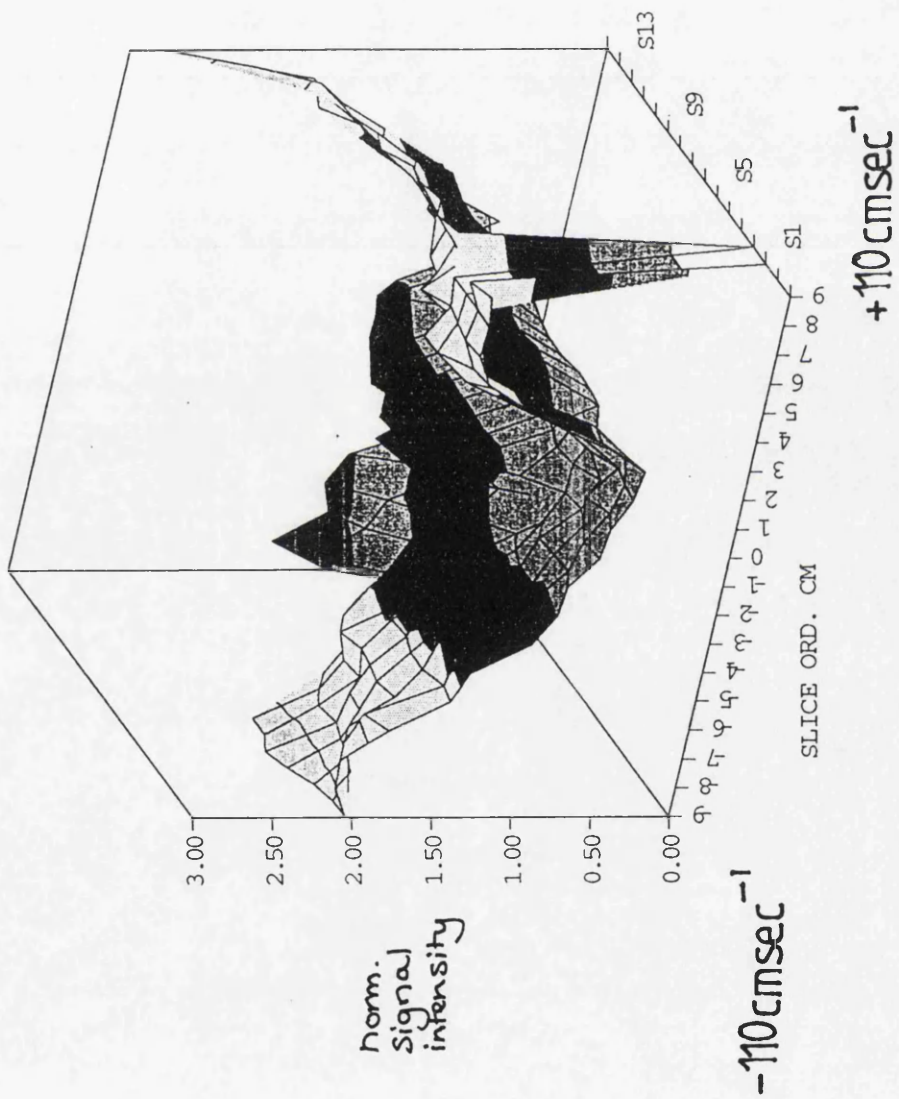


FIG.9.19b) FISP 3D,  $V < 180 \text{CMSEC}$

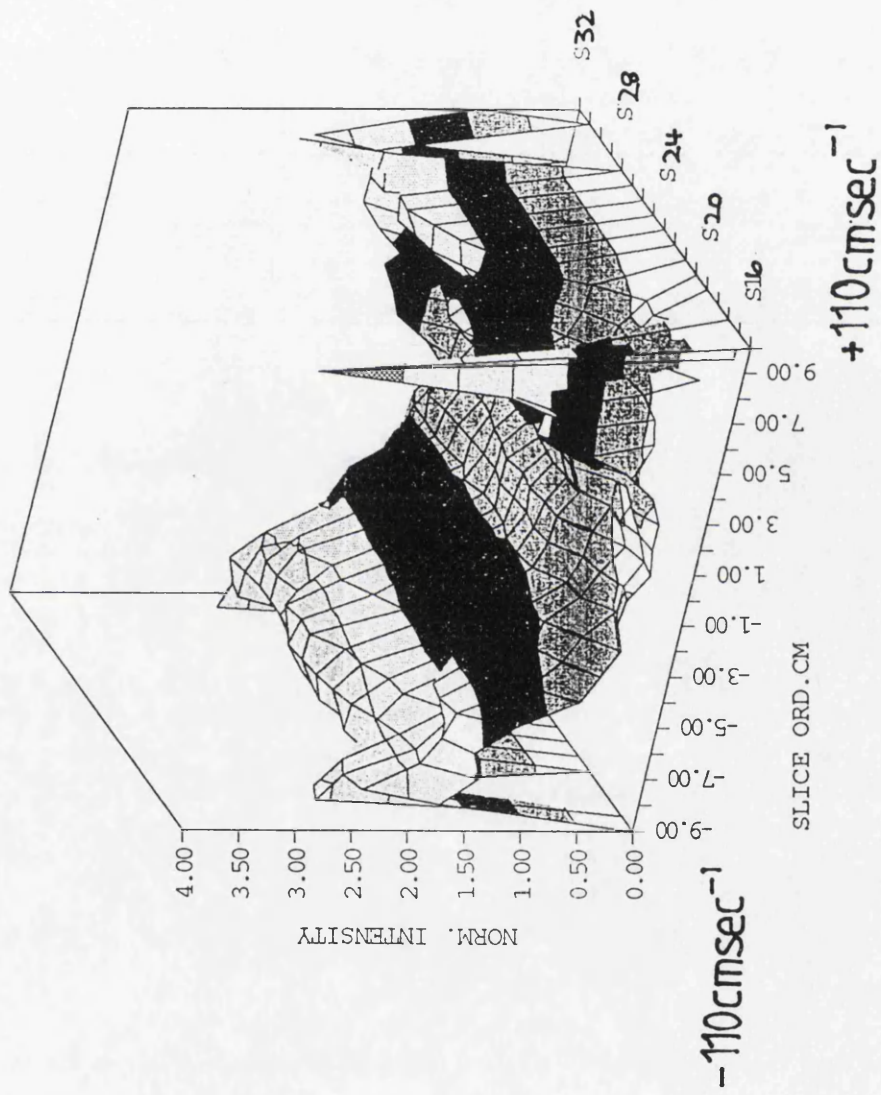


FIG.9.20a) FISP 3D,  $v = 35-180\text{cmsec}$

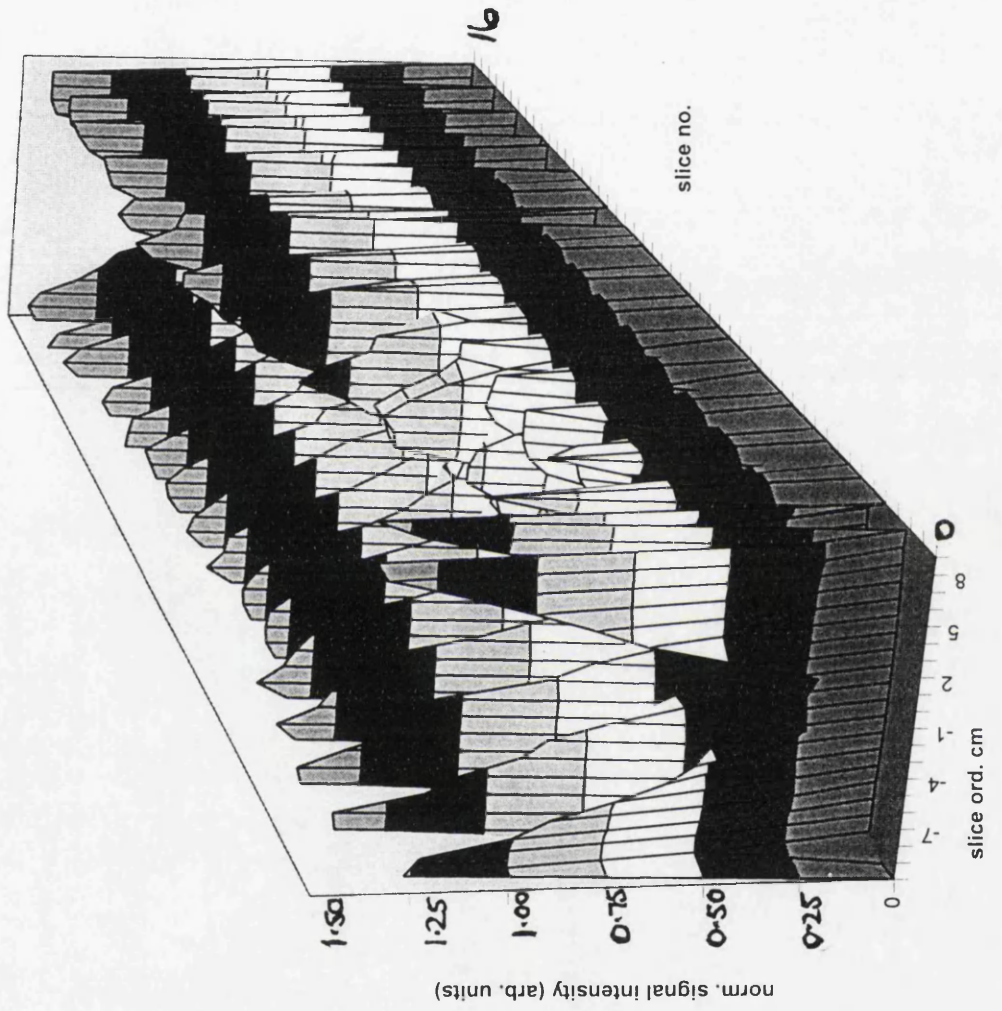


FIG. 9.20b) FISP3D,  $v=35-180\text{cmsec}$

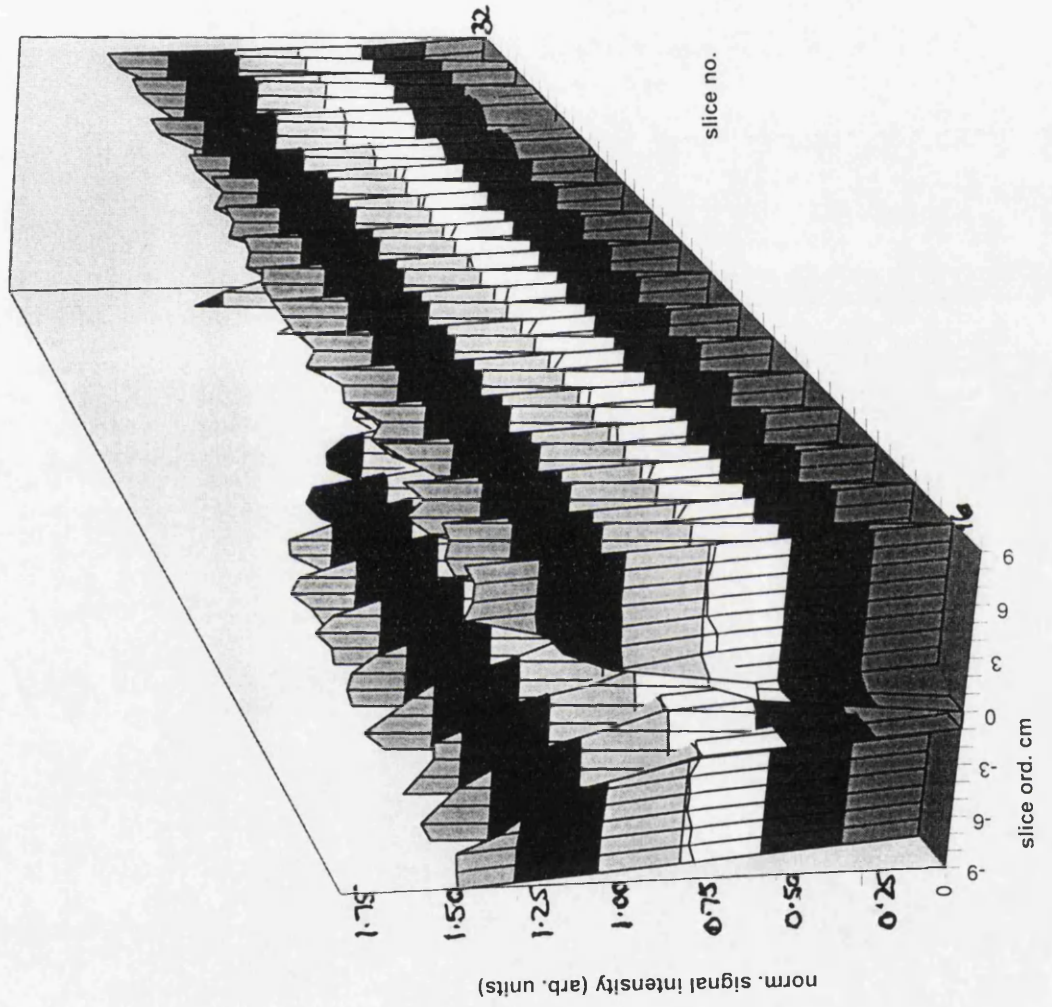
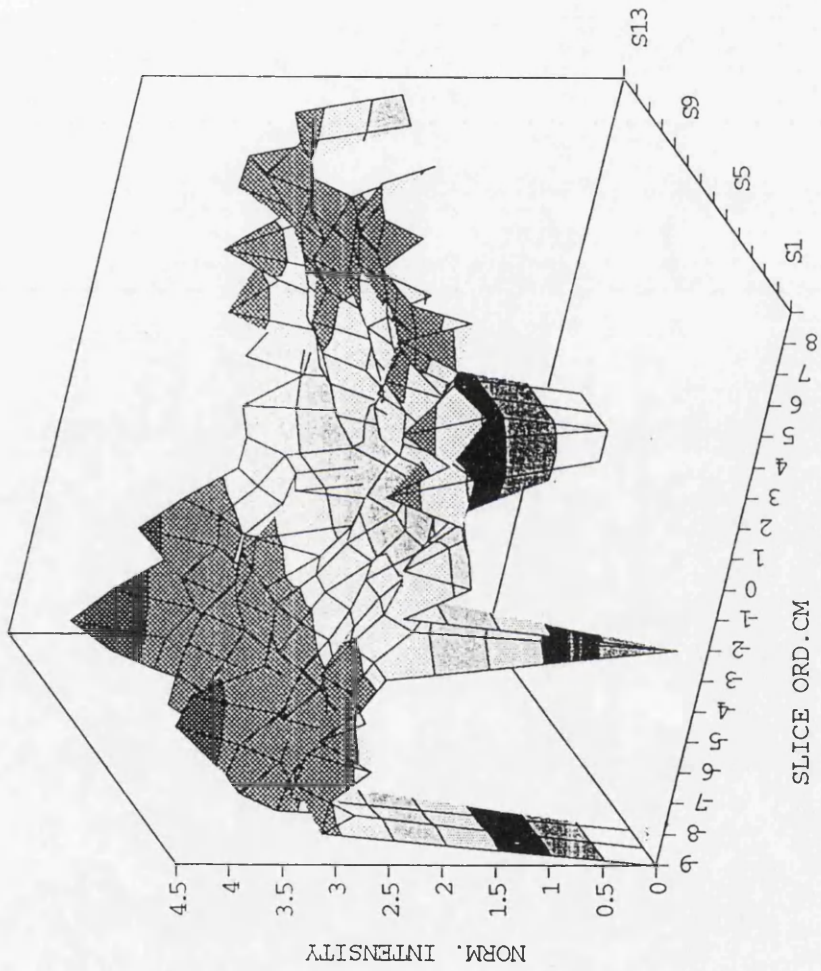


FIG.9.21 FLASH2D,  $30 < V < 45 \text{CMSEC}$



NORMALISED SIGNAL INTENSITY FLASH 60-180cm

FIG. 9.22  
SLICE  
NO.

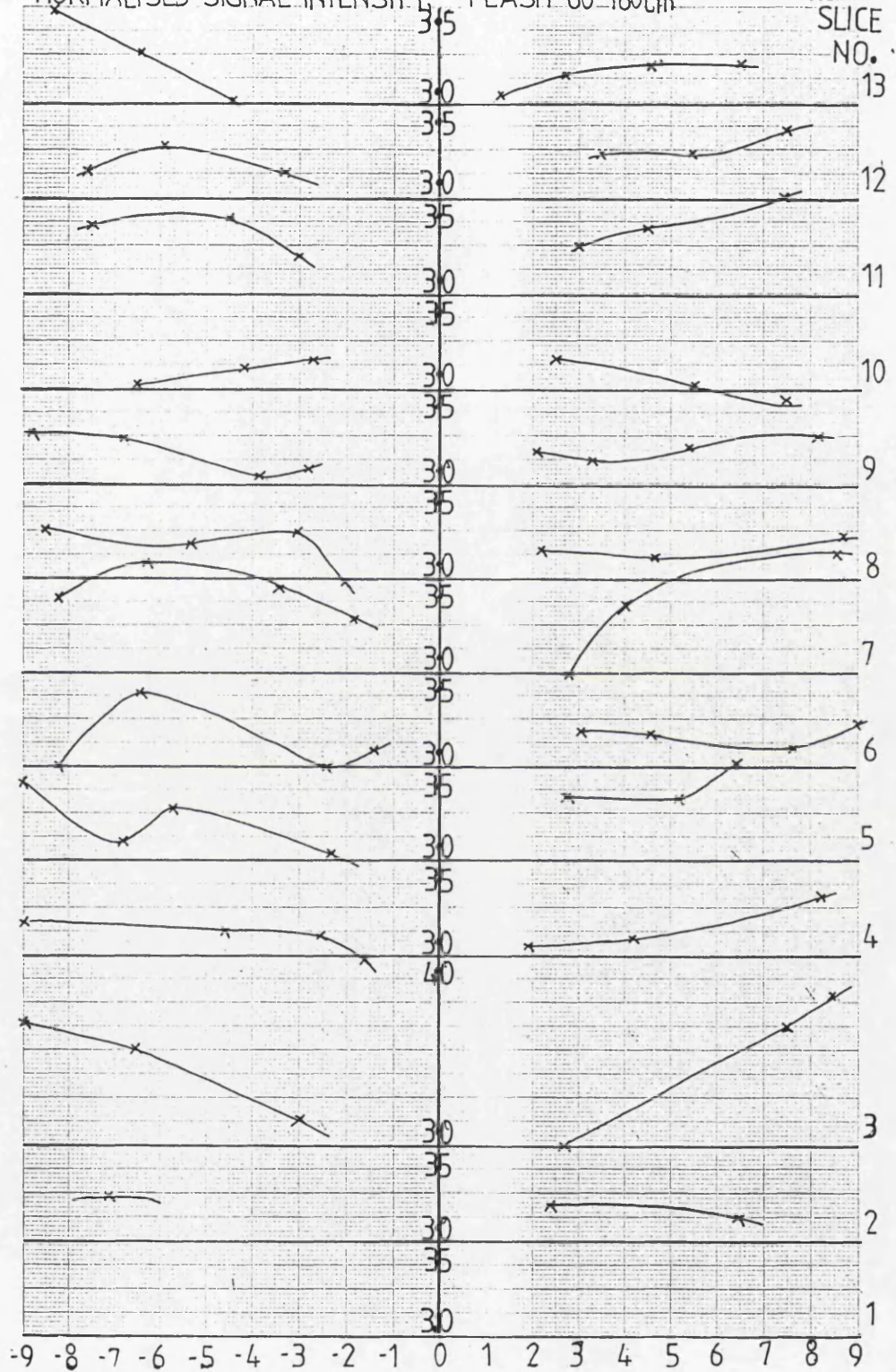


FIG.9.23 · REPHASE-DEPHASE,  $30 < V < 45 \text{ CMSEC}$

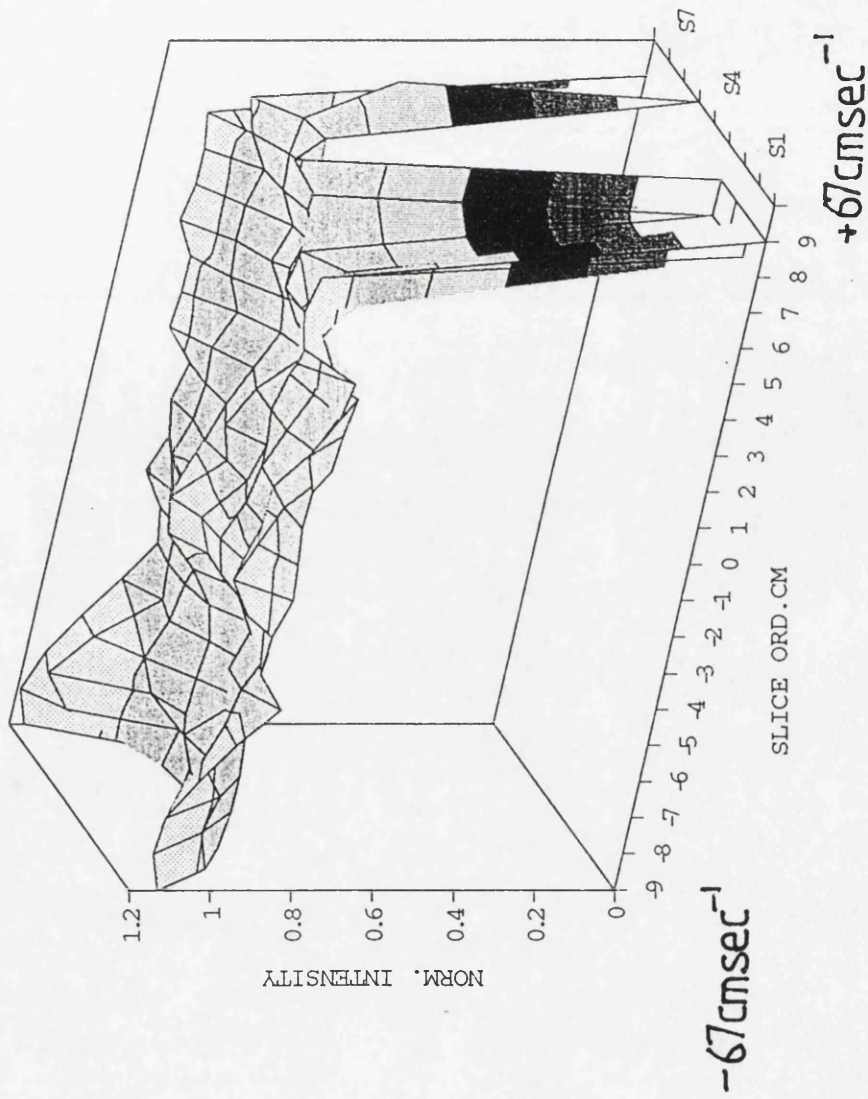
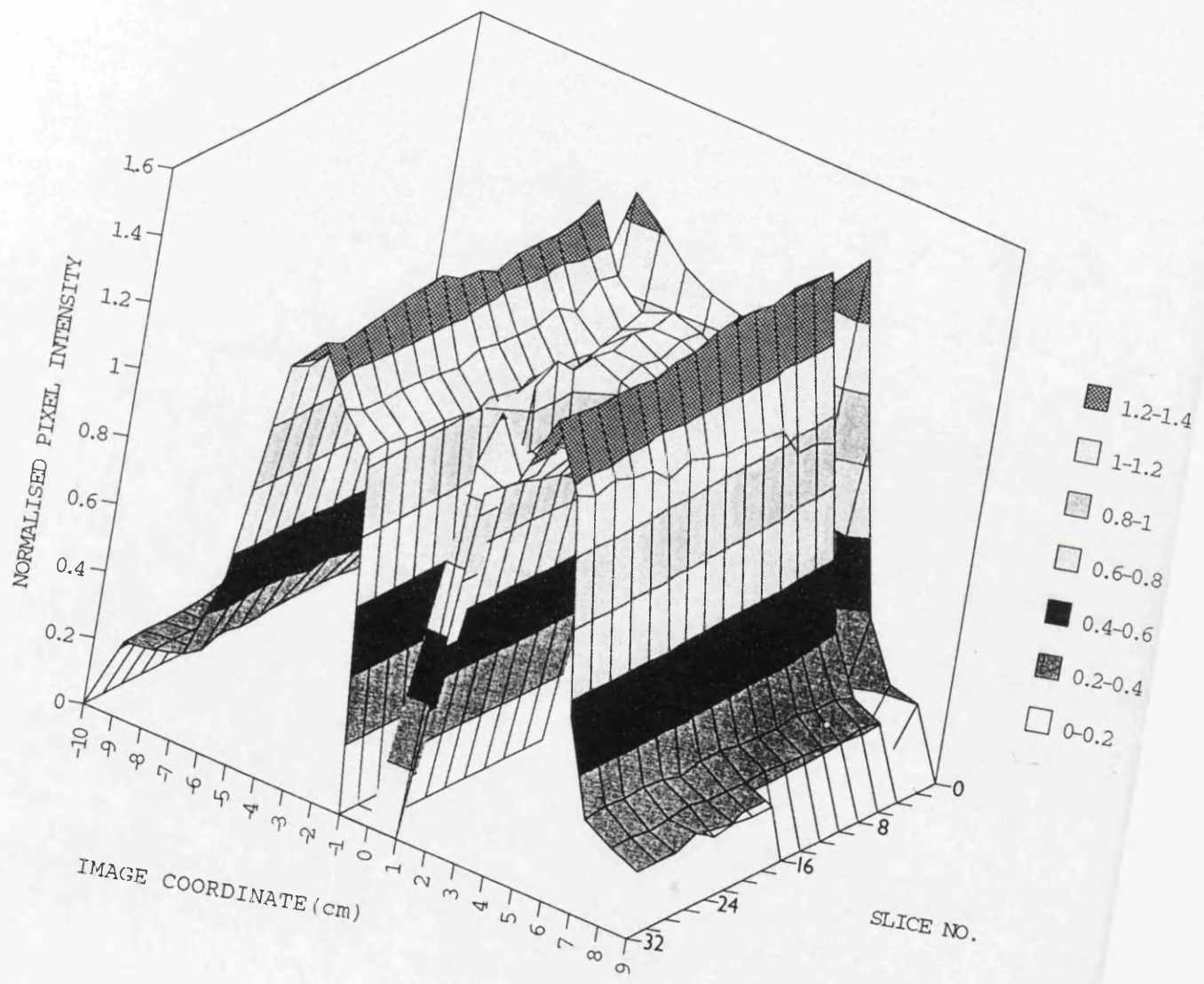


FIG.9.24 FISP3D SLOW FLOW



# CHAPTER 10 : QUANTITATIVE COMPARISON OF IDEAL AND EXPERIMENTAL RESPONSE OF PULSE SEQUENCES IN THE IMAGING OF FLOWING SPINS.

## 10.1 INTRODUCTION

Problems are encountered when imaging moving spins which do not occur in the case of stationary spins. These have already been described in some detail. In chapter 3, the saturation effect was described, as it applies to stationary spins, and the phenomenon of paradoxical enhancement made possible by the difference in degree of saturation of blood spins and stationary tissue spins due to the inflow of fresh spins into the imaging volume, was described. In the same chapter, the unique characteristic of flowing spins which is that additional dephasing arises due to the movement of the spins in the encoding gradients, was also described. In the light of the results described in the previous chapter, this chapter attempts to establish and differentiate between the effect that these two phenomena have on the ability of the different sequences used in this study to image flowing spins. In order to optimise the clinical utility of MRA, certain questions need to be answered: i) Is scanning in the 2D mode likely to give a more accurate data set by building up a stacked set of slices to construct the image volume, than repeated scanning of the total volume which is done when a 3D data acquisition is performed? ii) Are there significant differences in the ability of the sequences to image flowing spins, given that the difference between the FISP sequences used is in the choice of the three sequence parameters FA (flip angle), TR (repetition time), and TE (echo time). iii) If there were no artefacts due to the movement of the spins in the encoding gradients, what signal would be expected from the rotating drum?

For a slice or slab of defined thickness, the volume of gel containing fresh spins flowing through it increases as the radius of the drum increases. Thus a linear increase in signal intensity with radius, and hence with drum linear velocity, would be expected. This linear increase can then be compared with the signal obtained from each scanned phantom slice, presented in graphical form. Any discrepancies between expected and actual signal intensities has then to be explained in terms either of saturation effects, or of velocity dephasing effects.

In order to answer the questions posed above, this chapter is devoted firstly to establishing the nature of the ideal theoretical signal intensity. The motion of the spins in the encoding gradients is then analysed, so that potential sources of velocity dephasing because of relative motion between a spin and an encoding gradient can be established. Subsequently each pulse sequence scan is presented graphically in the form of slice intensity profiles, and the way in which they depart from the theoretical ideal is studied. For the six sequences tested in this study, the effects of saturation and velocity dephasing, at the range of velocities imaged by the slice, are described. The effect on spins as they move through the image volume between slices is also considered. The signal intensity profiles are compared from slice to slice. If they are not the same, there is an indication that the behaviour of the spins is affected by the time they spend in the image volume, as well as on their velocity. Saturation and velocity dephasing have been presented in chapter 3 as being causes of signal loss. The presentation of quantitative scan image intensities in this

chapter makes possible exact evaluation of the effect of these two potential sources of signal deterioration.

A second value of the quantitative presentation is that the range of velocities for which moving spins are imaged at clinically viable intensities can be established for each of the test sequences, by applying a normalised signal intensity threshold. It has been shown in earlier chapters that this will be a reliable guide to the applicability of each sequence in imaging in vivo blood flow.

All the tested sequences are related to specific anatomical areas which the manufacturer perceives to be particularly appropriate for their use. Thus some sequences are designated for the arteries of the head and neck but not the thorax, and others are designed to be used for the extremities only. The different applications arise because the flow rates in the different body arteries depends on their anatomical location. In chapter 5 a literature search was undertaken to establish what these flow rates are. This work can now be applied in the evaluation of sequences. For example, the sequence may be recommended by the manufacturer to image the carotid arteries in the neck. The accepted longitudinal flow rate in the carotid arteries is  $80\text{-}120\text{cmsec}^{-1}$ . The sequence is used to image the flow phantom rotating at a controlled rate so that the contours of the drum encompass velocities from  $7\text{cmsec}^{-1}$  at the margin of the axis to  $110\text{cmsec}^{-1}$  at the periphery. If the imaged slices of the drum do not show their ideal signal brightness across their whole length, then velocities exist in this range which the gradients of the pulse sequence cannot properly encode. Signal reduction and even signal voids may arise if this sequence is used to image the common carotid

arteries, and any diagnostic conclusions drawn from the images may be fallible.

This imaging problem has not previously been defined, and its solution is fundamental to the effective use of MRA in clinical diagnosis.

#### **10.2.1 IDEAL SIGNAL INTENSITY WHICH CAN BE EXPECTED FROM THE ROTATING DRUM PHANTOM**

Normal signal intensity for the angiographic imaging depends on the inflow of fresh spins into the imaged volume (see chapter 3). In the case of the rotating drum, the percentage of fresh spins will be greater the larger the radius of the drum, and the greater the speed of rotation of the gel. To obtain the ideal signal which would be expected from the flowing gel- i.e. the signal dependent only on the number of flipped spins flowing through unit volume in unit time, the gel can conveniently be considered to be a set of concentric annuli of thickness 1cm. The signal then depends on the volume of gel contained in each of these annuli. This can be calculated along the principal diameter of the drum, when the gel and hence spin flow is perpendicular to the slice, and it is found that the signal will increase linearly with radius from the centre of rotation, and the rate of increase will depend on the rate of rotation of the drum.

In imaging terms the tangential velocity is not the most useful spin velocity parameter. It is only for the central axis slice that the flow is perpendicular to the imaged slice. For all the other slices, the flow is tangential to the circle of rotation, and it can thus be resolved into a horizontal component of velocity in the plane of the

slice, and a vertical component of velocity perpendicular to the plane of the slice. This distinction is vital since any signal losses are due to motion of the spins in the encoding gradients, and these are themselves perpendicular and parallel to the plane of the reconstructed slices (Figure 10.1a) and b)). Calculation shows that the vertical component of velocity of spins at the same distance from a common vertical axis through the drum is the same, no matter how far the slice is from the central diameter of the drum. It depends only on the rate of rotation of the drum. (figure 10.2). Similarly the horizontal component of velocity is a constant for all reconstructed slices. The ideal signal from all reconstructed slices would thus be expected to be the same, and any deviations from the ideal value must be due to signal loss in that slice due to either of the two mechanisms of saturation or velocity dephasing.

### **10.2.2 ENCODING GRADIENTS AND VELOCITY DEPHASING IN THE ROTATING DRUM PHANTOM SCANS**

Chapter 3 has described in detail the changes in phase of the transverse magnetisation of the spins when they move parallel to an applied encoding gradient. In the case of the rotating drum, the proton spins move in circles, and their velocity at any instant is along the tangent to the circle of motion. The images are however obtained as a stack of parallel planes. The spin velocity vector is thus inclined to the scan plane, and it can be resolved into two components, parallel and perpendicular to the plane.

The encoding gradients are applied along the orthogonal axes, two of which coincide with the reconstructed image plane (Fig.10.1a). For FISP 3D imaging, the motion of the spin thus has components parallel

to two of the encoding axes. There is no component parallel to the frequency encoding (read axis), and so these phantom scans cannot evaluate the dephasing effect of this gradient. Motion does occur relative to the slab select/phase encoding direction, and also relative to the phase encoding direction, and it is the dephasing effect of these two gradients which will affect the detected spin signal and hence the reconstructed image intensity. A compensating gradient (GMR) is applied relative to the slab select gradient, but not relative to the two phase encoding gradients. For the FISP 3D sequence, however, the condition that steady state free precession is achieved in the transverse plane means that a series of rewinder phase encoding pulses are applied along the phase encoding only axis, whereas they are not applied along the slab select/phase encoding direction. This is described in detail in chapter 4.

In the case of FLASH 2D imaging, a slice select rather than a slab select gradient is used, and there is no phase encoding along this axis (Fig.10.1b). Neither is there any rephasing gradient applied along the phase encoding axis itself. Velocity dephasing effects due to the frequency encoding gradient have not been studied for these sequences either, since there is no component of spin velocity parallel to this gradient.

### **10.2.3 POSITIVE DETECTION OF MOVING SPINS BY THE PULSE SEQUENCE**

Criteria have to be established and applied to the measured signal intensity from the phantom scan slices so that decisions can be made about the range of velocities which the pulse sequence will image. The qualitative observation that the scanned slices of the rotating phantom give a signal intensity at all the imaged velocities is not

sufficient. One of the values of imaging an identical static drum adjacent to the rotating drum is that the signal from the second can be normalised against that from the first. If the signal intensity from the rotating drum is greater than that from the static drum, the sequence is giving a positive detection response to the flowing spins. If the signal intensity from the rotating drum is less than that from the static drum, then there is some property of the moving spins which is destroying the detected signal intensity. These regions of shortfall in signal intensity are one of the main areas of interest of this study, since it is the inability of the pulse sequences to image spins under all conditions of flow, resulting in signal voids and ambiguous losses of image intensity, which have the potential to make MRA diagnostically unreliable.

#### 10.2.4 OBSERVER EVALUATION OF IMAGES

It is generally accepted that for a signal to be detectable, the signal to noise ratio must be in the range 3 to 5 (Halmshaw, 1981). This criterion has been applied to the following scan images. (The static drum signal intensity has been used since it is unaffected by movement of spins and hence provides a figure for comparison of sequence performance regardless of the spin velocity response of the sequence).

Static field = 1T

Sequence = FISP 3D, FA = 40°, TR = 36msec, TE = 10msec

Effective signal to noise ratio for the slice = Mean signal for the rotating drum image : mean background noise

= 515.6 : 65.2 = 7.9

Static field = 1T

Static field = 1T

Sequence = REPHASE-DEPHASE FISP 3D, FA = 15<sup>0</sup>, TR = 50msec, TE = 14/14msec

Effective signal to noise ratio for the slice = mean rotating drum  
signal : mean background noise  
= 517.8 : 500.9 = 1.03

Since the mean signal for the rotating drum slice is a measure of the ability of the sequence to respond to spins at the range of velocities imaged, these imaged spins then being viewed by the observer against a background of screen noise, the calculations show that the FISP 3D scan with flip angle 40<sup>0</sup>, will give a signal of sufficient intensity to be detectable to the unaided eye. The REPHASE-DEPHASE scan, however, with a signal to noise ratio of 1.03, does not produce sufficient intensity when imaging flowing spins for reliable vessel detection when tested against the accepted criteria for signal to noise ratio.

Static field = 1.5T

FISP 3D, FA = 15<sup>0</sup>, TR = 36msec, TE = 6msec.

A signal intensity profile for a rotating drum slice imaged with this sequence is presented graphically (Fig.10.3). The background signal to noise level is included for comparison, and the signal noise level to give a SNR greater than 3 is also shown. It is clear from this presentation that the peripheral slices of this scan (e.g. slice 1) have a SNR ~1, and will not be detectable. Across the intensity profile of a slice central to the image volume, e.g. slice 32, the SNR falls below 3 at the periphery, and a region of ambiguity of detection will then result.

Further definition of acceptable signal to background noise ratio is needed if these evaluations are to be meaningful in the clinical imaging context. Arterial flow is imaged against static tissue rather than against screen noise in in vivo clinical images, and the ratio of flowing blood spin image intensity to static tissue intensity might provide a better guide to the clinical validity of the pulse sequence at a given spin velocity. No work has yet been done in this field, and the nature of the construction of the rotating drum phantom is such that it cannot be attempted in the terms of this study.

### **10.3 SIGNAL INTENSITY OBTAINED FROM FISP 3D SCANS.**

Four FISP sequences have been used in this study:

1. Drum rotating at 114rpm,  $FA = 40^{\circ}$ ,  $TR = 36\text{msec}$ ,  $TE = 10\text{msec}$ , static field = 1T.
2. Drum rotating at 114rpm,  $FA = 20^{\circ}$ ,  $TR = 36\text{msec}$ ,  $TE = 10\text{msec}$ , static field = 1T.
3. Drum rotating at 67rpm,  $FA = 15^{\circ}$ ,  $TR = 50\text{msec}$ ,  $TE = 14/14\text{msec}$ , static field = 1T.
4. Drum rotating at 64rpm,  $FA = 15^{\circ}$ ,  $TR = 36\text{msec}$ ,  $TE = 6\text{msec}$ , static field = 1.5T.

#### **10.3.1. IMAGING CAPABILITY OF MRA PULSE SEQUENCES**

The detailed statistical data obtained on a slice by slice basis for the six image volumes scanned in this study is now examined in detail. The purpose is to establish what the ideal signal from the rotating volume of gel in the drum phantom would be if it were not marred by velocity related scan artefacts. The velocities for which such shortfalls do occur can then be quantitatively established, and

the reasons for these shortfalls deduced. Predictions can then be made about the applicability of the sequences for in vivo imaging. If the longitudinal flow rate which it will image is known from the phantom scans, then the body vessels for which it can be used can be established, by reference to the normal flow rates established in chapter 5.

The sequence considered first is

FISP3D\_10rb108.ufa      TR = 36msec, TE = 10msec, FA = 20<sup>0</sup>.

Recommended for velocities 45 - 115cmsec<sup>-1</sup>.

Drum rotation rate = 114rpm.

Velocity range simulated by rotating drum = 10 - 110cmsec<sup>-1</sup>.

### 10.3.2. DISCREPANCIES OBSERVED BETWEEN THE IDEAL SIGNAL LINE AND THE EXPERIMENTAL SIGNAL LINE FOR EACH OF THE IMAGED SLICES

Paragraph 10.1 shows that the ideal signal from the rotating drum increases linearly with the distance from the centre of the drum, and depends on the rate of rotation of the drum. In real time imaging, the slope of the ideal signal line depends on the specific gradients applied by the pulse sequence under test to the spins, and thus it is not an absolute value but is pulse sequence dependent. It can be established by inspection of the 2D image intensity profiles of consecutive slices for any one scan. The signal is sufficiently uniform from slice to slice to establish a straight line trend of intensity from the centre to the periphery of the rotating drum, which is applicable to all the slices of the scan. When this ideal signal intensity is represented on each 2D intensity profile, deviations from it at that exact location in the image volume can be noted and investigated.

The following points arise from a comparison of ideal and actual signals for this FISP 3D sequence. The points are illustrated in Fig.10.4 which graphs typical normalised image intensity profiles from four adjacent slices in the scan volume. The remaining profiles for the other reconstructed slices of this scan are included in Appendix 2.

i) The signal intensity is not symmetrical with the rotational axis of the drum. The direction of motion of the spins through the slice affects the detected signal.

ii) Near to the axis there is reduced signal intensity on many of the slices. This is the region in which the spins are moving relatively slowly, and it may be supposed that reduced signal intensity is due to saturation effects. The range of velocities for which the effect is noted depends on the depth of the slice in the imaged volume.

iii) there is also a shortfall in signal intensity at the edge of the slices, where the gel is rotating at its highest velocities. The expected mechanism for loss in intensity here is velocity dephasing due to motion in the applied gradients. It is found that the extent of this effect also depends on the depth of the imaged slice in the scanned volume.

### **10.3.3 SATURATION EFFECTS ON THE DRUM GEL SPINS**

The imaged volume is less than the total volume of the drum so that the rotating gel moves into and out of the volume during the scan. The degree of saturation of the spins will depend on the time that they spend in the encoding gradients as compared with the time they are moving in free space and able to undergo relaxation.

Fig 10.5 shows that there is a region close to the axis of the drum where the spins are contained in the imaged volume for the whole of the scan. It would therefore be expected that these spins would be fully saturated and that the signal intensity would be reduced as a result. As the distance from the centre of the drum increases, the gel spends correspondingly less time in the encoding gradients. From the known rate of rotation of the drum, and the known pulse sequence repetition time, it is possible to predict the pattern of pulses received by the gel spins at a particular radius. The gel can be divided into bands in which the same stimulus is received by all the spins it contains, by inspection of the geometry of the drum, as shown in Fig. 10.6. The number of pulses applied to each region of the gel is extracted and presented in the table below.

**Table 10.1**  
**PREDICTION OF SATURATION EFFECTS IN FISP 3D SEQUENCE**

BAND	PATTERN OF PULSES APPLIED PER BAND	MEAN RADIUS FOR BAND
A	15.6 consecutive RF pulses	1cm
B	12.6RF, 3relax	2.3cm
C	5RF, 6relax, 6RF, 3relax	2.85cm
D	4RF, 1relax, 4RF, 5relax	3.2cm
E	3RF, 3relax, 4RF, 5relax	3.5cm
F	3RF, 4relax, 3RF, 5relax	4.5cm
G	2RF, 5relax, 3RF, 5relax	6.1cm
H	2RF, 5relax, 2RF, 6relax	7.2cm
J	1RF, 7relax, 1RF, 6relax	8.5cm

The spins contained in gel at less than 1cm would be expected to be fully saturated; this is found to be the case within the radius of the perspex axle of the drum and the spins do not image. At 2.3cm

and less, there are 12.6 consecutive pulse sequence applications to the gel, and it then relaxes for the duration of three pulse sequences before re-entering the imaged volume. Since relaxation time is T1 and T2 dependent, and both these (T1 = 1100msec, T2 = 400msec at 1.5T for the gel) are very much greater than the pulse sequence repetition time of 40msec, relaxation effects are expected to be small compared to the saturation effects built up by subsequent pulses. It is in this region that maximum saturation effects are to be expected. It has already been shown (chapter3) that the number of pulses it takes to achieve total spin saturation is about 15 if the flip angle is 15° and 20° if the flip angle is 30°. In this sequence, where the flip angle is 20°, saturation would be expected at about 18 pulses, and would thus be complete after two revolutions of the drum. Balance between time for which RF stimulation is received and time for relaxation of spins is fairly equal over the radius 2.85-3.5cm. Some saturation might be expected in this region. However beyond this radius, the figures above indicate that the drum gel does not receive sufficient consecutive RF pulses for the spins to achieve saturation.

These expected saturation effects are superimposed on the diagram showing experimentally measured deviations from the ideal signal (Fig.10.5). The agreement between expected and actual signal loss due to this cause supports the theory that saturation of spins at this flip angle will only occur for 15 consecutive pulse applications or above.

Whether or not these saturation effects are present because the drum is rotating, and whether they are equally likely to be present if

the imaged volume were a slab of in vivo tissue containing vessels showing longitudinal flow, must be considered. Theory predicts that saturation effects only occur with this sequence if the spins receive a total of 15 consecutive RF pulses or more. The minimum slab thickness for which this can occur depends on the velocity of the spins and can be evaluated from the phantom. Spins at radii less than 2.3cm are fully saturated. The distance travelled by these spins during one rotation of the drum is 14cm, and the spin velocity is  $12\text{cmsec}^{-1}$ . If spins at this velocity travel a greater distance, they will also be totally saturated. Thus saturation effects detected with the rotating drum phantom, while not exactly mimicked by longitudinal in vivo flow, can make accurate predictions for saturation effects in clinical imaging.

#### 10.3.4 SIGNAL DEGRADATION DUE TO VELOCITY DEPHASING EFFECTS.

It is clear from Fig.10.6 above that there are regions in the scanned image slices where the signal falls below the ideal value, and which also lie outside the region where saturation effects can be responsible for this. This is where velocity dephasing effects come into play, and their effect on the signal from the moving spins can be described for one rotation of the drum as follows.

The spins enter the lower edge of the imaged slab, moving clockwise. Immediately there is a depression of the signal at the periphery of the drum, where the spins are moving at velocities of  $100\text{cmsec}^{-1}$  and above. As the spins move further into the drum, the region at the edge of the drum where there is this shortfall in intensity gradually broadens, until at the far edge of the slice, it occupies nearly the whole width of the slice.

The conclusion must be that these experimental results indicate that there is a time dependent effect in velocity dephasing, as well as a factor which is dependent on the absolute magnitude of the velocity. Spins moving at high velocity receive a massive change of phase as they enter the encoding gradients, due to the relatively large distance that they move in the gradients. This immediately leads to partial volume effects because of the incoherent summation of adjacent phases. By comparison, in this region of the scan volume, the phase change of slower spins is not sufficient to give rise to partial volume effects in the voxel, and hence there is no significant loss in signal intensity. However the longer these spins remain in the encoding gradients, the greater the phase change they accumulate, until, in this case, by the time even the slowest spins have travelled a distance of 48mm in the encoding gradients, the spin angle differentials in each reconstructed voxel are sufficient to give rise to image intensity loss. It can be assumed that if the maximum slab thickness of 80mm had been used, increased loss in signal intensity, due to spin dephasing, would have accumulated across the slab, for all imaged velocities. In clinical terms this means that the blood signal from vessels would be severely affected for the whole of the length of the imaged vessel at velocities greater than  $110\text{cmsec}^{-1}$ , whereas for slow flow at around  $15\text{cmsec}^{-1}$ , signal loss along the vessel length only becomes significant at depths of more than 44mm into the imaged slab. In its clinical application it is clear that this sequence cannot be used to image the arteries of the thorax, or the common carotid arteries, since the longitudinal flow rates in these vessels are too great. In other vessels with lower flow rates, some positive detection is likely. However the clarity of vessels will not be uniform but will

deteriorate along their length because of spin dephasing effects. The sequence can be applied to the arteries of the head, and to the extremities, provided that the slab thickness is not greater than 48mm. Although the system is capable of imaging slabs of greater thickness, diagnostic clarity would be greatly impaired, and better results would be obtained by adopting multi-slab techniques.

#### **10.4 VALIDATION OF THE DISCUSSION OF SPIN DEPHASING EFFECTS USING HAHN'S EQUATIONS.**

It is important to establish whether the pattern of signal loss due to velocity dephasing described in 10.3 is unique to this FISP sequence (3D acquisition, FA = 20<sup>0</sup>, TR = 36msec, TE = 10msec), or whether it is generally applicable to FISP sequences. It is not clear what factors are responsible for the observed effects. The same reductions in intensity may occur with a 2D acquisition; on the other hand they may be a unique feature of a 3D acquisition. They may occur when a FLASH sequence is used, but there is also the possibility that they are a product of FISP sequence imaging.

Theoretical work which has been developed to describe the response of moving spins to magnetic gradients has been presented in detail in chapter 3. The conclusions of this work are now matched to the observed behaviour of flowing spins under experimental conditions.

Hahn proposed that the behaviour of spins which dephased due to their motion in the applied gradients could be described by the equation

$$\phi = \frac{\gamma G v t^2}{2}$$

which indicates that relative dephasing of adjacent spins depends linearly on their velocity, and also in proportion to the square of the time they spend in the applied gradients. Here, the existence of spin dephasing effects in the phantom images is assumed to be present if the signal intensity falls, in a systematic way, below the ideal signal, and if it can also be shown that this cannot be the result of spin saturation effects.

Thus the phantom scans reveal a graphed picture of cumulative dephasing effects. These can be compared to the change in intensity profile predicted from Hahn's equation.

a) The spin dephasing will increase linearly with velocity as indicated by the straight line graph.

b) the spin dephasing will increase quadratically with time as shown by the curve. The 32 time units (32 slices making up a slab of 48mm) have been considered in groups of 4 for convenience, and the observed result that spin dephasing occurs at all velocities at a depth of 48mm, so that at  $t = 32$  the whole width of the slab is affected, has been assumed. The width of the slab affected for shorter times has been scaled accordingly.

c) A semi-quantitative prediction of signal loss in the slab can now be obtained by combining the two graphs. The result of doing this is shown in Fig.10.7.

d) Comparison between this prediction and the curves obtained during the FISP scan of the phantom show some correlation. The curve which demarcates the region of shortfall in signal intensity due to

velocity dephasing corresponds very closely to that drawn to represent the time squared effects of velocity dephasing. The offset to these values which would be imparted if the velocity only effects were a contributing factor is not present.

Gradient motion refocussing (GMR) is applied along the slab select direction and it seems from these results that this gradient has exactly compensated for spin dephasing resulting simply from the magnitude of the spin velocity relative to this gradient. This GMR however is inadequate to compensate for the accumulation of change in transverse phase which arises because of the time for which the spins are travelling in the spin-warp gradient. This is a revealing limitation of GMR techniques in current practice, and such experimental evidence for the clinical effects of ineffectual GMR has not been presented before.

## **10.5 IMAGING POTENTIAL OF OTHER FISP 3D SEQUENCES**

The deleterious effects of saturation and spin dephasing on flowing spins imaged with a FISP 3D sequence (FA = 20<sup>0</sup>, TR = 36msec, TE = 10msec) have now been fully established. Subsequently the same analysis is applied to the three other FISP sequences which have been used in this study .

### **10.5.1 FISP SEQUENCE DESIGNED FOR USE WITH VELOCITIES UP TO 180cmsec<sup>-1</sup>.**

TR = 36msec, TE = 10msec, FA = 40<sup>0</sup>, static field = 1T.

Matrix = 256 x 256.

The slices images reconstructed from this scan show a marked zebra stripe pattern. This has been described very thoroughly in 9.2.1.2 and it has been proved that the regular bands of intensity which appear on these slices are in no way artefacts arising from the use of a rotating drum, but are the inevitable result of imaging flowing spins using a SSFP, and in particular, a FISP sequence. They are numerous and close together, and the measured mean pixel intensity obtained at 1cm intervals in sampling the images to get the slice intensity profiles is thus a reasonable approximation to the true signal intensity.

An ideal signal line can be drawn in on all the 2D slice profiles obtained from this scan by inspection of all the profiles. Saturation effects are much more important when this sequence is used, because the flip angle is larger. The procedure previously adopted to find out what volume of the gel will be affected by spin saturation because of repeated application of RF pulses to the gel has been used again with these slice profiles. The same drum rotation rate and the same pulse repetition time was used (Figure 10.9). These regions of heavy and light saturation have been delineated on Fig.10.8 so that direct comparison can be made between calculated and observed regions where saturation effects reduce image intensity.

The shape of the individual slice profiles, as compared with the ideal signal, show that saturation effects occur at higher velocities when this sequence is used. Spins detected to be saturated are shown in Fig. 10.8, and the effect is appreciable up

to velocities of  $70\text{cmsec}^{-1}$  whereas when a flip angle of  $20^\circ$  was used, saturation ceased above  $20\text{cmsec}^{-1}$ .

Typical 2D slice image intensity profiles for this scan are shown in Fig.10.10. The signal starts to deteriorate at high velocities at the periphery of the drum due to velocity dephasing effects. These follow a pattern similar to those investigated in 10.3.2, in that they appear not only as a result of high velocity, but also as the result of the time the spins have spent in the gradients. Thus eventually they start to appear at lower velocities as the distance travelled through the slab increases (Fig.10.8). It is also apparent that velocity dephasing is not as significant when this sequence is used as when the drum is imaged under the same conditions of rotation, but using a flip angle of  $20^\circ$  (Fig.10.5).

For all gel velocities, there is a time delay before the spins begin to show signal loss because of velocity dephasing when a flip angle of  $40^\circ$  rather than  $20^\circ$  is used. The linear dependence of this effect on velocity and its quadratic dependence on time are less marked in this use of the FISP sequence. (Fig. 10.11). It appears that there is an inverse relationship between the onset of velocity dephasing, and the size of the flip angle applied to the spins. More phantom scans using a wider range of flip angle values and a wider range of drum velocities would be valuable in establishing whether or not this is generally true.

This sequence has been recommended by the manufacturer for the imaging of the aorta where the flow rate is  $140 \pm 40 \text{ cmsec}^{-1}$ . Thus it should be capable of imaging flow rates up to  $180 \text{ cmsec}^{-1}$ . It has not been possible to test it beyond  $110 \text{ cmsec}^{-1}$  because the air pressure available to drive the phantom motor could not produce rotation rates above this. A gear system would have to be incorporated into the phantom to allow higher rotation rates to be scanned. The scans which were obtained show saturation effects up to velocities of  $70 \text{ cmsec}^{-1}$ . These would also be present in clinical images of longitudinal flow, because they are not cumulative as the drum rotates. In an imaged slab of thickness 48mm, arteries sustaining blood flow rates above  $70 \text{ cmsec}^{-1}$  would darken in appearance along their length, and signal voids can occur because of this saturation effect.

At the tested flow rates, spin dephasing effects reduce the signal above velocities of  $90 \text{ cmsec}^{-1}$ . Flow rates in the normal imaging region of  $70\text{-}90 \text{ cmsec}^{-1}$  are those of the carotid arteries of the head, but not those of the neck and thorax, where higher velocities occur. It encompasses the basilar artery, the arteries of the extremities and the arteries of the abdomen, including the renal and hepatic arteries. The normalised signal intensity, whilst less regular in trend with velocity than that when the sequence is used with a flip angle of  $20^\circ$ , is also slightly reduced on average.

This sequence appears to have some clinical value for imaging the arteries listed here. The over-riding factor, however, is that all these vessels will show zebra stripe periodicity of intensity, and this will complicate the detection of any anatomical abnormality

(Figure 9.8). This sequence cannot be recommended for clinical imaging for this reason.

#### 10.5.2 REPHASE-DEPHASE FISP 3D SEQUENCE DESIGNED FOR VELOCITIES IN THE RANGE 30-70cmsec<sup>-1</sup>

Static field = 1T, Matrix = 256 x 256. TR = 50msec, TE = 14/14msec, FA = 15°

Within the pulse sequence, repeated at 50msec intervals, two FISP acquisitions are obtained, both with an echo time of 14msec. The first is velocity compensated by the use of additional encoding gradients, to ensure that the flowing spins image at maximum intensity. The second has no compensating gradients, and the signal from the flowing spins is destroyed. Stationary tissue response is the same in both cases, and is eliminated when the two sets of signals are subtracted, leaving only that of the flowing spins (4.3).

The unique feature of the graphed intensities from these slices is that there is no regular change in intensity either within each slice, or between the slices when they are stacked together. Some random fluctuation in signal intensity is shown, the minimum signal being 0.79 and the maximum 1.2. This sequence has been designed to give a response which is uniform at all velocities. Interpretation of this aim for imaging the rotating gel would in fact mean that the detected signal would increase along the length of the image slice, as the volume of the gel, and hence the percentage of fresh spins flowing into the image volume, increases with radius. The constant signal intensity noted across each imaged slice thus indicates that the rephase-dephase sequence is giving a poorer

response to the faster moving spins. Either the rephase-dephase procedure with the velocity compensating and uncompensating gradients is inadequate, or the FISP sequence itself is not one which is suitable for use in this context. The images do not show signal loss at low velocities due to saturation, which is the result of the use of a low flip angle (8.5).

In chapter 8 the effect of changing the sequence parameters, notably FA and TE, for FISP sequences was calculated, and the conclusion reached there was that for a rephase-dephase sequence, where the echo time is necessarily long, a higher flip angle was essential. A possible extension of the work presented in this study would be to use the same rotating phantom with this same rephase-dephase sequence, and keeping TE constant at 14msec, but to increase the value of the flip angle between the scans, so that signal intensity dependence could be monitored.

Some discussion of the efficacy of the rephase-dephase sequence has already been given in 9.3.13, 9.4.5 and 10.2.2.. Its failure in terms of its inability to give an adequate signal to noise ratio to ensure detail detection was described there. The fact that it gives a normalised signal response of about 1 at all velocities has been expanded on here, and it is now clear that this sequence is unreliable since it will image spins moving at lower velocities with better response than those at higher velocities, if the flow is purely longitudinal. The drum phantom images indicate that if this sequence is used clinically, the detected signal intensity may be expected to fall from acceptable, at  $0\text{cmsec}^{-1}$ , in a linear manner with increasing velocity.

### 10.5.3 FISP 3D SEQUENCE DESIGNED TO IMAGE SLOW FLOW AT 1.5T.

TR = 36msec, TE = 6msec, FA =  $15^{\circ}$ . Matrix = 160 x 256.

This sequence uses a low flip angle of  $15^{\circ}$  and a reduced echo time of 6msec. The calculated values of FISP sequence intensity (see chapter 8) show that this should result in a signal equal to that from the FISP sequence which uses a flip angle of  $20^{\circ}$  and an echo time of 10msec. This is the sequence described in detail in 10.4. It is clear, however, from inspection of the slice image intensity profiles, that although these two sequences may show this equality of response for the slow velocities imaged near to the axis of the rotating drum, there is marked discrepancy for velocities above  $35\text{cmsec}^{-1}$ .

For this FISP sequence (FA =  $15^{\circ}$ , TR = 36msec, TE = 6msec) the normalised signal intensity rises in a linear fashion as would be expected if it were following the ideal signal increase, up to flow rates of  $35\text{cmsec}^{-1}$  (Fig.10.12). There is no indication that saturation effects are causing any signal reduction at low velocities, and this is the result of the use of a low flip angle. However the decrease in normalised signal intensity above  $35\text{cmsec}^{-1}$  is very dramatic, the end result being that at velocities of  $60\text{cmsec}^{-1}$  and above, the normalised signal has the same intensity as the background noise of the phantom scan for all the slices of the image volume. For the peripheral slices, signal loss is marked all the way across the slice. Such a signal loss is not matched in any of the other FISP scans.

There appear to be three possible causes of signal degradation as observed with this sequence. The first is that velocity dephasing effects may be greater for the same spin longitudinal flow rate if the flip angle is small. Thus velocity dephasing effects may be observed at lower flow velocities when a flip angle of  $15^\circ$  is used, instead of  $20^\circ$  or  $40^\circ$ . Evidence presented in the image intensity profiles for the two sequences tested at static field = 1T can be used to evaluate this statement. For both these sequences, the drum rotation rate was 114rpm, and TR = 36msec, TE = 10msec. Thus the only variable is the flip angle. Signal shortfalls due to velocity dephasing effects occur above  $60 \text{ cmsec}^{-1}$  for the larger flip angle, but above  $80 \text{ cmsec}^{-1}$  for the smaller flip angle. It must thus be concluded that a lower flip angle will result in reduced velocity dephasing under otherwise identical conditions, and that this factor cannot be responsible for enhanced signal loss observed with the use of this sequence.

Secondly the echo time recommended for use with this sequence is unusually small. This may have an effect on the detected signal, and the procedure devised in this thesis for evaluating the imaging potential of MRA pulse sequences could further be used with this sequence, applied at a chosen range of echo times. This is a recommendation made in the conclusion to this study.

Thirdly partial volume effects are much greater in the reconstructed images of these slices because a matrix of  $160 \times 256$  has been used, instead of a matrix of  $256 \times 256$ . This latter theory could be tested simply by repeating the scans using a finer reconstruction matrix.

This sequence can be recommended only for clinical imaging of the lower extremities. It is only effective for velocities up to  $35\text{cmsec}^{-1}$ , and data presented in chapter 5 indicate that flow rates of  $60\text{cmsec}^{-1}$  occur in the popliteal arteries in the knee, and about  $75\text{cmsec}^{-1}$  in the arteries of the forearm. Only the body regions which have slower arterial flow rates than these can be imaged. In the intra-cranial circulation, flow rates of  $35\text{cmsec}^{-1}$  and below are encountered. However this sequence cannot be recommended to image this anatomical region because these flow rates are always accompanied by velocities of up to  $70\text{cmsec}^{-1}$  in adjacent vessels. Simultaneous imaging of all these flow rates is required in this region, and signal voids will inevitably result if this sequence is used.

#### **10.6 DETECTED FISP SIGNAL APPROXIMATES TO A FLASH SIGNAL FOR MOVING SPINS**

There are some features of the divergence between the ideal signal and the experimentally detected signal which cannot be explained by any of the velocity related mechanisms used so far. They are not zebra stripes, nor the result of saturation, nor of spin dephasing. They are noticeable on the peripheral slices of the image volume scanned as FISP3D,  $\text{FA} = 40^\circ$ ,  $\text{TR} = 36\text{msec}$ ,  $\text{TE} = 10\text{msec}$  (figure 10.13). They are a feature of these slices which does not appear on those obtained with the same FISP sequence used with a flip angle of  $20^\circ$ . These peripheral slices do not show the expected signal increase with drum radius, as has been derived for the rotating drum gel. Instead the signal is constant for all the velocities imaged. It is shown most markedly on the first four reconstructed slices where the freshest spins which have undergone the maximum permitted

relaxation re-enter the image volume at P. It is shown to a lesser extent after the spins have achieved a lower degree of relaxation in the further half of the drum and re-enter the image volume at Q.

This imaged behaviour of the spins has to be considered carefully alongside the fact that the FISP sequence is designed to maintain a constant transverse magnetisation. This is not the effect which is being demonstrated in the phantom scans. If transverse magnetisation were maintained at a constant level, the signal intensity should rise across the slice as the volume of gel intersecting the image slab increases with increased velocity of rotation. Some response is being shown by the FISP sequence which is actually decreasing with spin velocity, so that increased inflow of fresh spins with increasing drum radius and velocity counteracts it, and produces the observed constant signal intensity.

It seems that the true FISP sequence ability to detect a signal from flowing spins is very poor, and deteriorates the faster the spins are moving. This can be explained by considering the effect of the unique refocussing gradients used to maintain free precession in the steady state. Spin dephasing occurs when the 256 steps of the phase encoding gradient are applied prior to the detection of the echo. To ensure steady state of transverse magnetisation, the 256 steps are repeated after the echo, with the purpose of refocussing the spins. They are applied in the reverse order, so the desired effect, that spin phase changes in the transverse plane are reversed, is achieved if the spins are stationary. However, for flowing spins, the magnitude of the gradient at the point of rephasing is not the same as that at the point of dephasing, because the spins are

constantly moving in the applied fields. These second stepped gradient lobes will therefore provide a further complex dephasing mechanism, and will tend to further destroy or spoil transverse magnetisation, rather than maintain it at a constant level.

In the peripheral image volume normalised slice intensities shown in Fig.10.13 the signal intensities from this FISP scan show two types of response. As they enter the fields, signal response is poor because of the unique FISP rewinder gradient effects on the flowing spins. With increased depth into the image slab, and greater dephasing effect of these gradients, transverse magnetisation is spoiled altogether between the detection of one echo and the application of the next RF pulse, and the FISP sequence now effectively behaves as a FLASH sequence. Signal intensities now increase with distance across the imaged slice, behaviour which is shown in the true FLASH scans.

This transition in imaging response from FISP to FLASH is shown by the FISP sequence using  $FA = 40^\circ$  but not that using  $FA = 20^\circ$ . The component of transverse magnetisation is initially larger for spins flipped through the bigger angle, and the transition takes longer to become apparent when the sequence gradients are applied. For the FISP sequence imaged at  $FA = 20^\circ$ , all the slice signal intensities correspond to detection of a FLASH signal rather than detection of a FISP signal.

The shortfall in FISP sequence response even when it is producing this FLASH-type detected signal are revealed by comparison of signal intensities obtained in this study for FLASH scans and FISP

scans of the drum under identical conditions. These show that normalised FLASH intensities are of the order of 2.5, whereas FISP intensities are at most 1.5. Thus the gradients used to detect a FISP response give a poorer FLASH type signal from moving spins than do the gradients purposely set up to achieve a FLASH scan, because the gradient timing and duration is different.

The important and direct clinical implication of these observations is that poorer results will always be achieved if a FISP sequence is used to image flowing spins rather than a FLASH sequence. One previous author has commented on this effect. In 1990, Haacke evaluated the contrast of flowing blood spins as compared to stationary tissue spins which could be achieved with a range of imaging parameters using FISP, FLASH and ROAST sequences. ROAST is a derivative sequence of FISP, for which refocussing gradients are applied in the phase encoding, but not the read or slab select directions. Haacke notes in the context of this work that "the motion of the blood has led to a natural type of spoiling acting to reduce the effective T<sub>2</sub>, making blood appear as if it has a FLASH contrast even in ROAST imaging". In his consideration of the clinical effect of this deduction, he concludes that if FLASH and ROAST sequences show equivalent signals, then FISP and FLASH will do so. These observations are in agreement with the conclusions drawn from the experimental work of this study. However the use of the rotating phantom has made possible more precise and quantitative definition of FISP sequence behaviour.

There is further validation for the discussion of moving spin behaviour in FISP gradients given here. As described above, the

rephase-dephase FISP sequence with  $FA = 15^\circ$  gives phantom slice intensities of the same steady value as those of the peripheral slices for the  $FA = 40^\circ$  FISP scan. Without the velocity compensating gradients used in the rephase-dephase sequence, the behaviour of a FISP scan with  $FA = 15^\circ$  would be the same as that for  $FA = 20^\circ$ , in that it would always show FLASH response behaviour. That it maintains its FISP response throughout the image volume must be due to the presence of the velocity compensating-uncompensating gradients.

## 10.7 FLASH 2D SEQUENCES

It would be expected that there will be different saturation effects and velocity dephasing effects when the image data acquisition is a stacked set of 2D sequential slices rather than a 3D volume acquisition. The proportion of total scan time for which the spins remain in the encoding gradients is different for the two acquisitions. For the 3D volume, all the spins are subject to  $256 \times 256 \times (\text{no. of partitions})$  encoding gradients for as long as they remain in the volume. For a 2D acquisition, the spins will only receive more than one set of 256 encoding pulses if they are moving at a speed such that they remain in the image volume whilst further slices are being encoded.

### 10.7.1 FLASH 2D SEQUENCE DESIGNED TO IMAGE FLOW IN THE RANGE 30-45cmsec<sup>-1</sup>.

TR = 40msec, TE = 10msec, FA =  $35^\circ$ .

Static field = 1T. Matrix = 256 x 256

The slice images obtained with this sequence do not show the pronounced signal minima which have been described as occurring with

the FLASH sequence in its application to faster flow rates. It has been proved in chapter 9 that these dark bars are the result of incomplete relaxation of the spins between pulse sequence applications. For the slower rate of rotation of the drum used here, the time for one complete revolution of the drum is 895msec. This compares with the T1 relaxation time for the spins of 1000msec, and is close enough for the assumption to be made that the spins will have reverted to their non-flipped state during one rotation. Also the flip angle of the spins is  $35^{\circ}$ , and the value of T1 is quoted for 63% relaxation of spins which have been flipped through  $90^{\circ}$ . This substantiates the above assumption.

Though 256 applications of the encoding gradients are made to the region defined as the first slice of the 2D stack, the rotation of the gel means that fresh spins are constantly entering this volume. The region of the scan volume where such effects could be expected is shown in Fig. 10.14. With the comparative timings calculated above, saturation effects are not expected either for the rotating gel, or for fresh blood spins moving longitudinally into a defined image slab. Inspection of the graphed signal intensities slice by slice, shows that there is little depression from the ideal signal at low velocities (Fig.10.15). Calculations presented in chapter 8 indicate that for a flip angle of  $35^{\circ}$ , about 80% maximum longitudinal magnetisation is regained after a TR of 40msec. The phantom test scans indicate that this is not significant in signal intensity terms, and this immediately presents itself as one advantage of using FLASH 2D in the clinical scanning of moving fluid spins.

The discrepancies between the expected ideal signal and the measured signal for the complete scan volume are indicated in Fig.10.16. Some velocity dephasing effects occur. Since the scan volume was not centrally placed in the drum, the spin relaxation times in the two halves of the drum are not identical, and spin dephasing is hence greater in one half than the other. This is an artefact created by the scan technique, and it would not occur if longitudinal flow for which the spins passed once only through the imaging volume were undertaken. The scan results thus reliably indicate that the sequence will image velocities up to  $55\text{cmsec}^{-1}$  without spin dephasing effects or saturation effects. It is proved that the sequence is reliable for use in the extremities, as recommended by the manufacturer. It can encode slow intra-cranial flow, defined as up to  $45\text{cmsec}^{-1}$ , but some signal loss will occur with fast intra-cranial flow, defined as  $45\text{-}70\text{cmsec}^{-1}$ . As these flow rates are encountered in adjacent vessels in the ICV, it is essential that the imaging sequence can encode the entire range, for diagnostic efficacy, and some doubt thus exists about the suitability of this sequence for ICV, for which it is recommended by the manufacturer.

The normalised signal intensity never falls below 2, which compares very favourably with the minimum signal intensity from the FISP scans of 0.79.

#### 10.7.2 FLASH 2D SEQUENCE DESIGNED TO IMAGE FLOW IN THE RANGE $60\text{-}180\text{cmsec}^{-1}$ .

TR = 39msec, TE = 10msec, FA =  $40^{\circ}$ .

Static field = 1T. Matrix = 256 x256

The reason for the appearance of the dark bars on these scans has already been described in detail in 9.1.2.1, and is not repeated here. The bars have been proved to be artefacts of the rotating phantom, and it has been shown that they will not occur in clinical images of longitudinal flow at equivalent flow rates. The method of sampling the image intensities for these scans was necessarily different, as has also been described, and because intensities were taken at irregular locations along each slice, it has not been possible to graph the intensities using standard software.

The graphed data (Fig. 10.16) shows not only the dark minima, but a pronounced region of signal intensity loss at the centre of each slice, which remains fairly constant in width from slice to slice. The reason for this is again cumulative saturation of the gel on consecutive pulse application, which arises for the same reasons as those responsible for the dark bars. It can be viewed as a region for which the density of the bars is so great that the overall intensity is reduced to 75% of its true value. Again, these effects would not be present in clinical scans.

True indication of the response of the sequence to flowing spins can be seen by looking at the trend in image intensity values graphed from scan intensities at locations between the dark bars. For nearly all the slices, the signal continues to rise with the velocity of the gel, showing at least that it will image velocities up to  $110\text{cmsec}^{-1}$  consistently. The intensity is good, hardly falling below a normalised value of 3. Extrapolation from the measured intensities to those which would be expected at lower velocities, shows that the normalised signal would never fall below 2.5. This

increase in signal as compared to that for slower rotation does not arise because a larger flip angle is used. It is due to the higher number of fresh spins entering unit image volume in unit time, because of the faster rotation of the drum. The same effects would occur at fast longitudinal flow rates, ensuring bright blood signals for the velocity range  $10\text{-}110\text{cmsec}^{-1}$  in clinical images.

## 10.8 CONCLUSION

It has been the purpose of this thesis to comment on the imaging capability of six pulse sequences commercially available for use in magnetic resonance angiography, and this chapter must therefore conclude with a comparison of the performance of the sequences which will be valuable in clinical terms.

The sequence FLASH2D\_10rb78.ufa used with  $FA = 40^{\circ}$ ,  $TR = 39\text{msec}$  and  $TE = 10\text{msec}$  has the best signal response across the range of velocities  $11\text{-}110\text{cmsec}^{-1}$ . There is very little discrepancy between the ideal and the experimentally observed signal, and the only problem is that there may be a small reduction in image intensity for vessels carrying flowing spins above  $100\text{cmsec}^{-1}$ . This sequence can confidently be recommended for use with all body vessels except the aorta, and the carotid arteries. Further tests with higher drum rotation rates would have to be carried out before the same degree of certainty could be applied to its use with these vessels. There are no systematic artefacts which would appear in scans of flowing spins when this sequence is used.

The same sequence used with a flip angle of  $35^{\circ}$  and  $TR = 40\text{msec}$  only gives a good response up to velocities of  $55\text{cmsec}^{-1}$ , and hence cannot be recommended for general use.

Both these FLASH sequences are, however, more reliable than any of the FISP 3D sequences tested. These latter sequences all have inbuilt zebra stripe artefacts which are hardly noticeable at a flip angle of  $15^{\circ}$ , but mar images of flowing spins with increasing severity as the flip angle is increased. At  $FA = 40^{\circ}$  the resulting gradations in signal intensity are large enough and prominent enough to cause significant errors in the detection of the dimensions of signal voids due to stenoses, should these also be present.

All the FISP sequences show some deficiency in gradient motion refocussing, although that at  $FA = 40^{\circ}$  has less than that at  $20^{\circ}$ . With the sequence used at the lower flip angle, some signal loss along the length of vessels containing flowing spins with velocities greater than  $80\text{cmsec}^{-1}$  would be unavoidable, and at lower velocities, the same degree of signal loss would be observed at all velocities if the imaging slab thickness were greater than 48mm.

When the FISP sequence is used at higher flip angles to overcome this intensity loss resulting from spin dephasing, saturation effects start to be more prominent, and as a result the sequence cannot be used for blood velocities lower than  $70\text{cmsec}^{-1}$  without there being the possibility that signal voids due to saturation will occur. This makes it unreliable at these velocities for clinical use, because diagnostic ambiguities may arise.

The rewriter gradients which are a unique feature of the FISP sequence have been shown to make it unreliable for imaging flowing spins, and indeed to be the cause of both zebra stripes and the poor response at high velocities. It is probable that the FISP sequence has been used to date for blood flow imaging not because of its specific gradient properties, but simply because it is a fast imaging sequence. It has been thought that the reduction in patient motion usually associated with fast sequences and low acquisition times will provide sufficient benefit in imaging terms, and the detailed response of the sequence to different flow rates has not been quantitatively considered before.

It has also been shown that the signal obtained from the FISP sequence when it is used to image flowing spins changes significantly, depending on the flip angle used and the time the spins spend in the encoding gradients. The best signal obtained using the FISP sequence is observed when conditions are such that the rewriter gradients are totally ineffective, and the signal response is identical in form to that obtained with a FLASH sequence. Even so, a true FLASH sequence will give a stronger signal than a FISP sequence used to scan the same velocity range, by a factor of 1.5-2.

The rephase-dephase sequence based on 3D FISP and using a flip angle of  $15^{\circ}$  results in a signal which hardly rises above background noise, and which will show a decreasing intensity with increasing spin velocity for longitudinal flow. This type of sequence is still being developed by the manufacturer and cannot be recommended for clinical imaging of any sort in its present form.

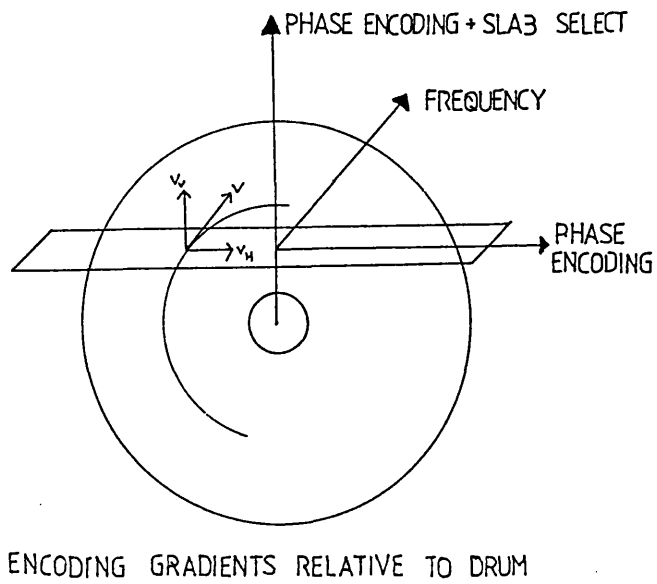


FIG.10.1a) Gradients applied during FISP pulse sequences for both stationary and moving spins. Gradient motion rephasing is applied in the frequency(read) and slice select directions. The unique feature of this sequence is the rewinder pulse which ensures that the transverse magnetisation is maintained in a steady state.

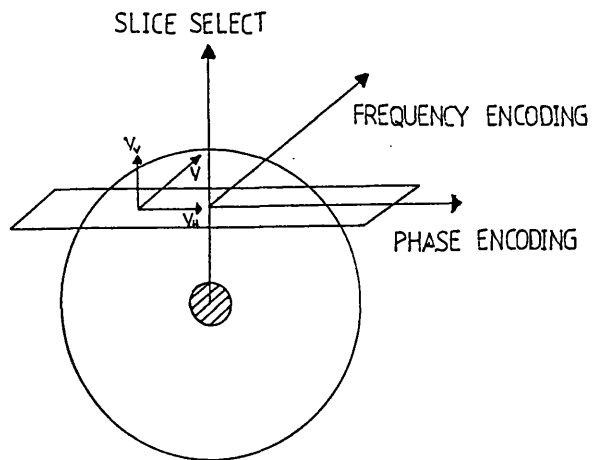


FIG.10.1b) Gradients applied during FLASH pulse sequence for both stationary and moving spins. Gradient motion refocussing (rephasing) is applied in the frequency(read) and slice select directions. The unique feature of the sequence is the spoiler pulse applied after the echo.

FIG.10.2 VERTICAL COMPONENT OF VELOCITY ACROSS IMAGED SLICE. VECTORS ARE INDEPENDENT OF SLICE POSITION AND DEPEND ON RATE OF DRUM ROTATION.

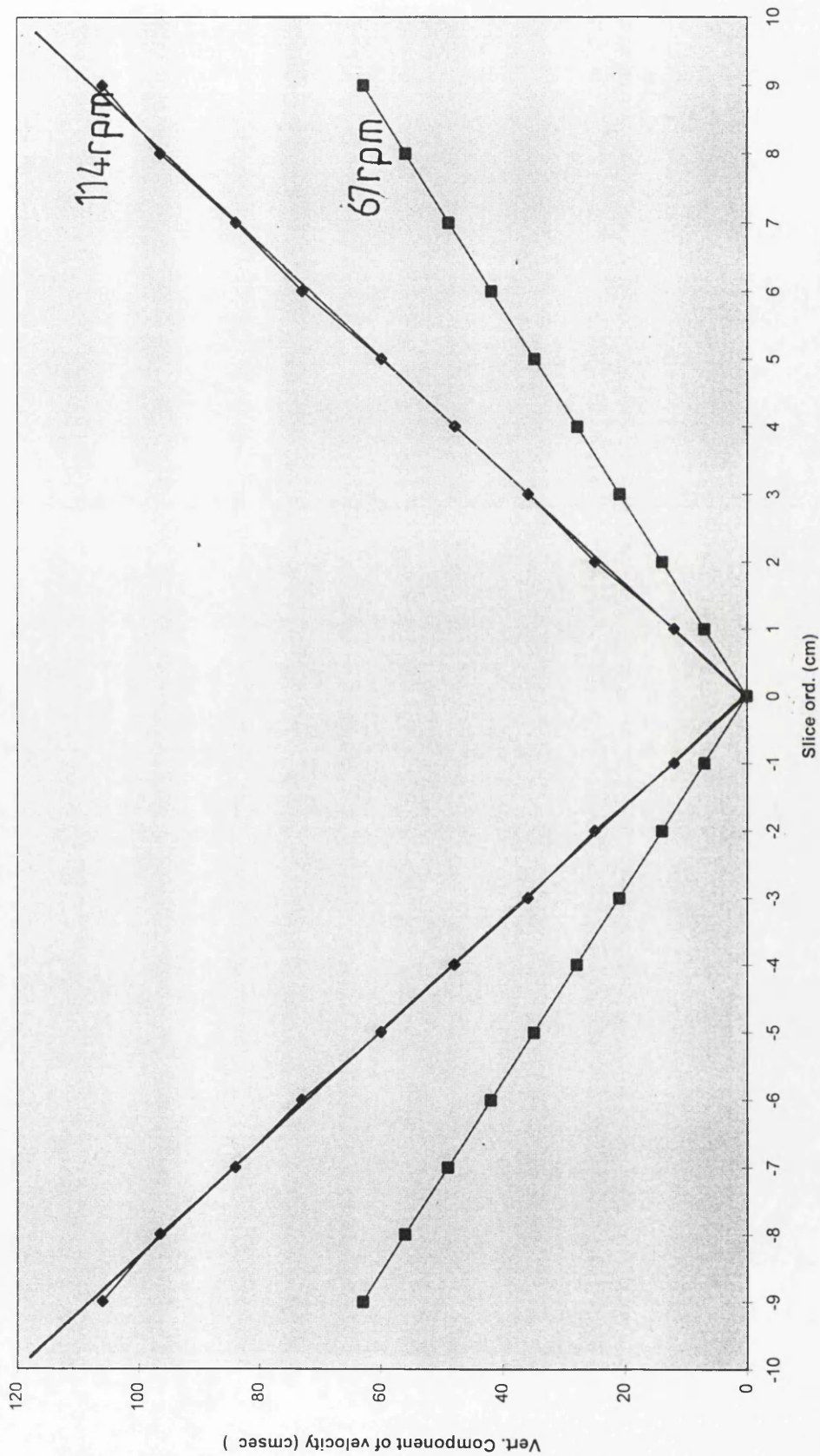


FIG.10.3 Signal to noise ratio in console images. The pixel intensity across the central slice of the image volume, obtained with the sequence FISP 3D, FA = 15°, TR = 36msec, TE = 10msec has been graphed. The noise level has been measured across this same region, and is also graphed for comparison. The signal intensity equivalent to 3 x noise has been shown, since it is for signal intensities above this that image contrast will be adequate for detection of clinical detail..

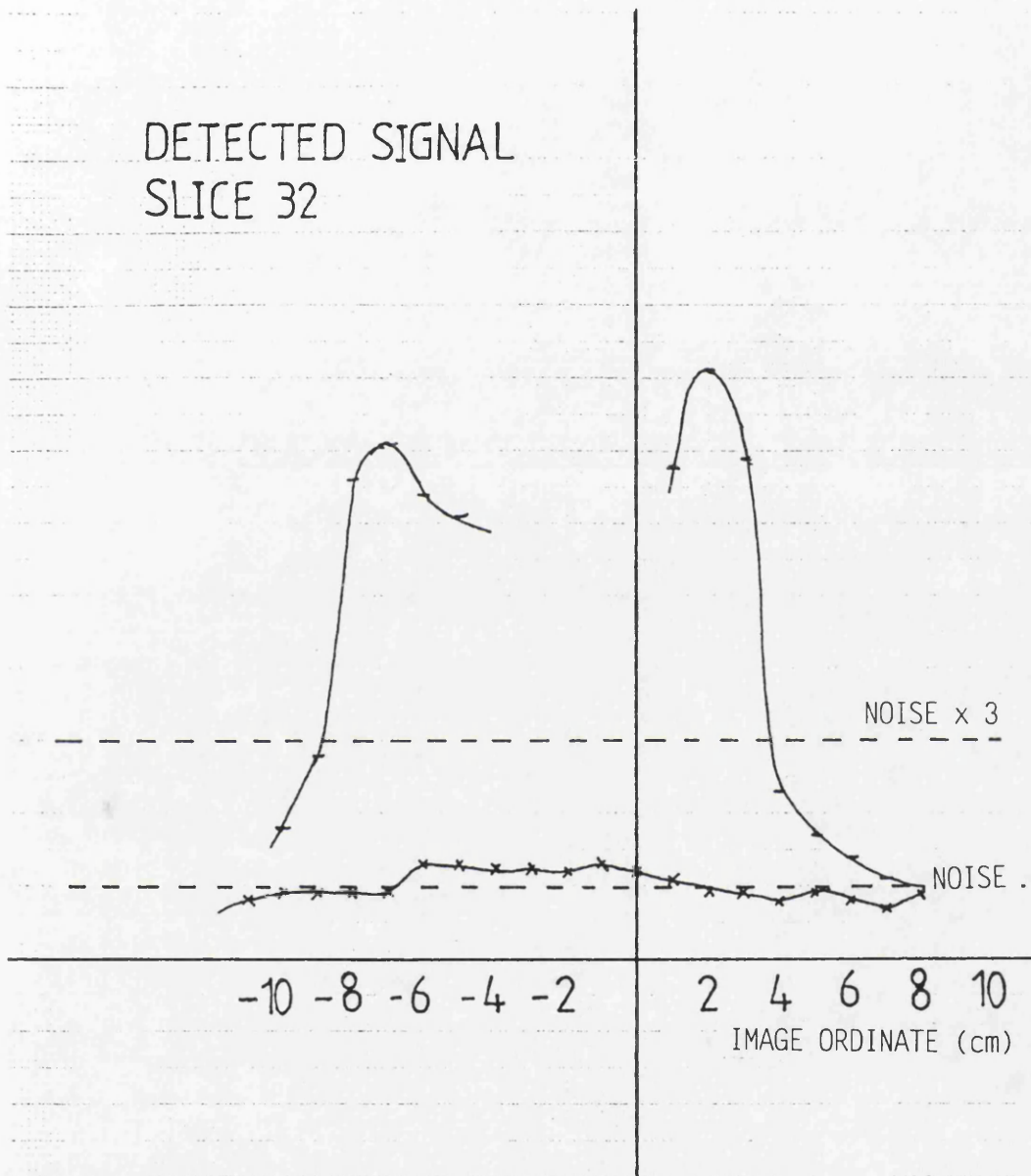


FIG.10.4

# SLICES 17-20

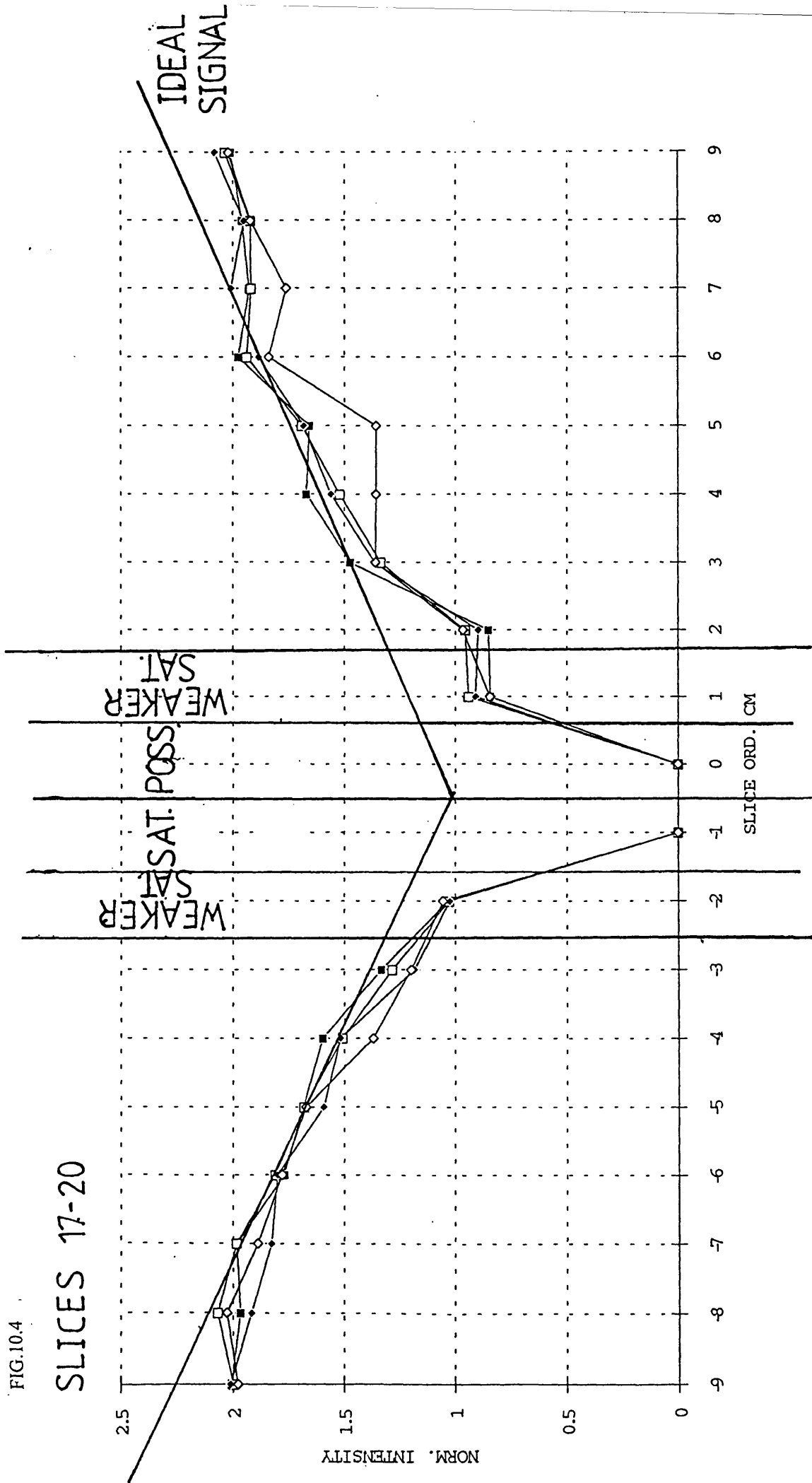


FIG.10.5 Saturation effects which can be expected with the scans obtained using the sequence FISP 3D, FA = 20°, TR = 36msec, TE = 10msec. The saturation effects observed when the rotating drum phantom is used are very sensitive to the exact positioning of the scan volume.

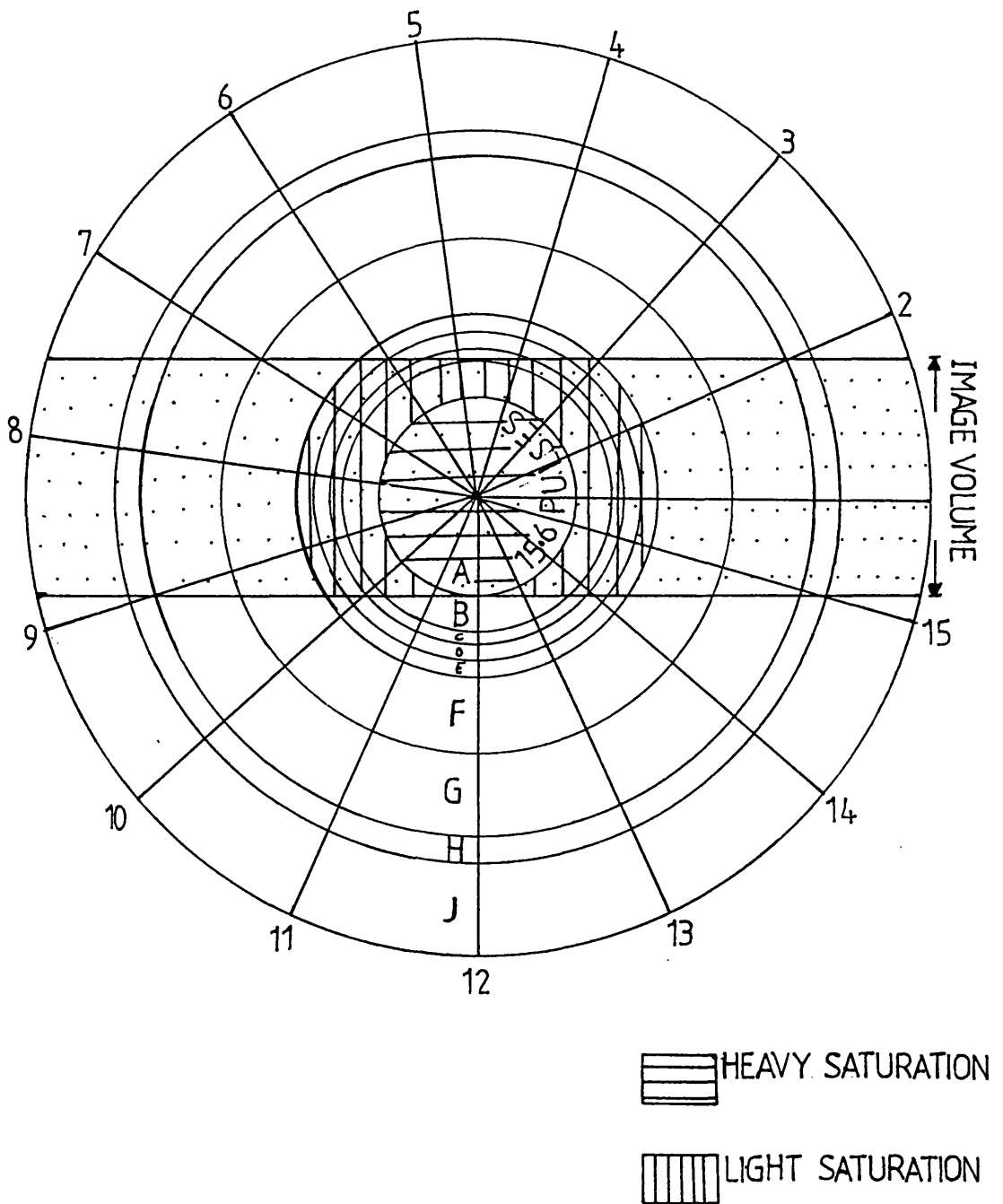
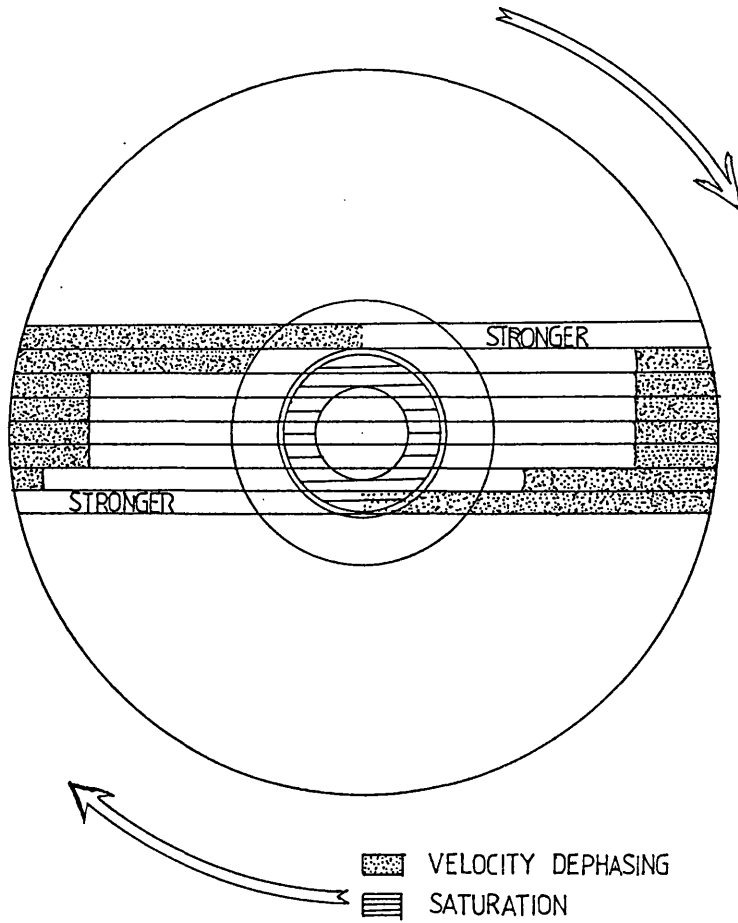


FIG.10.6

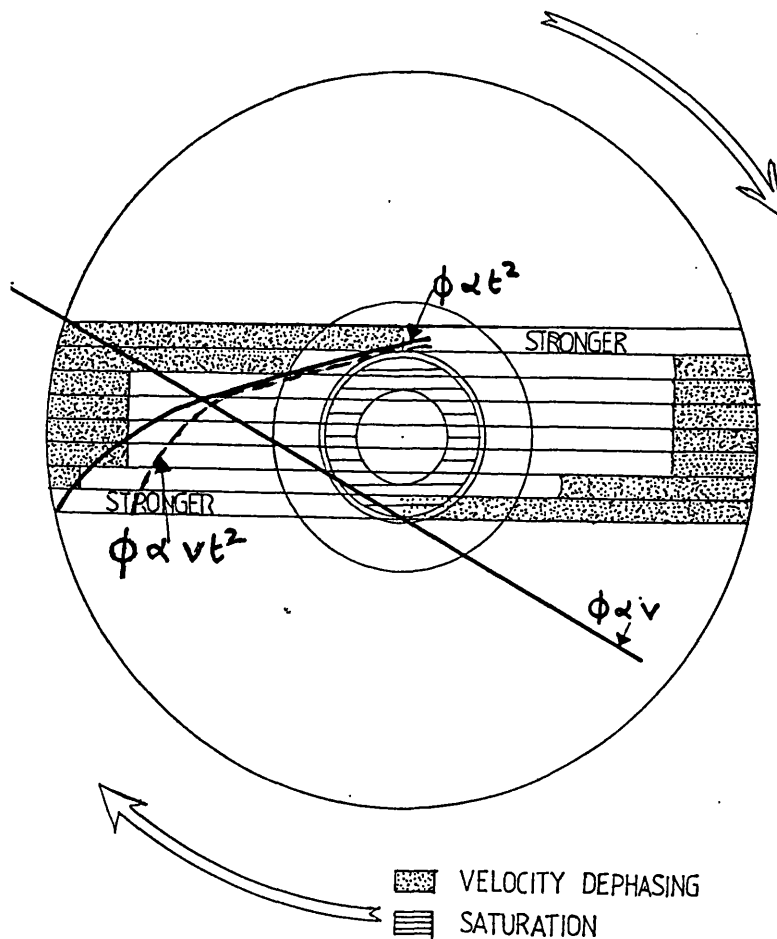
Detected signal intensity across the whole of the image volume for the scan at FISP3D, FA =  $20^\circ$ , TR = 36msec., TE = 10msec. Shaded regions show where spin dephasing and saturation effects are responsible for reductions in signal intensity below the expected ideal.



FA =  $20^\circ$

FIG.10.7 The effects of gradient motion refocussing in the sequence FISP3D, FA=20°, TR=36msec, TE=10msec. This is applied to overcome spin dephasing due to motion.

The increase in phase change due to spin velocity alone, a linear effect, is shown. The quadratic dependence of spin phase on time is also shown. These two effects are combined ( $\phi=vt^2$ ) and the resultant theoretical effect on signal intensity can then be compared with that experimentally observed. Were the gradient motion refocussing lobes applied completely effective, there would be no observable loss of signal due to velocity dephasing.



$$FA=20^\circ$$

FIG.10.8

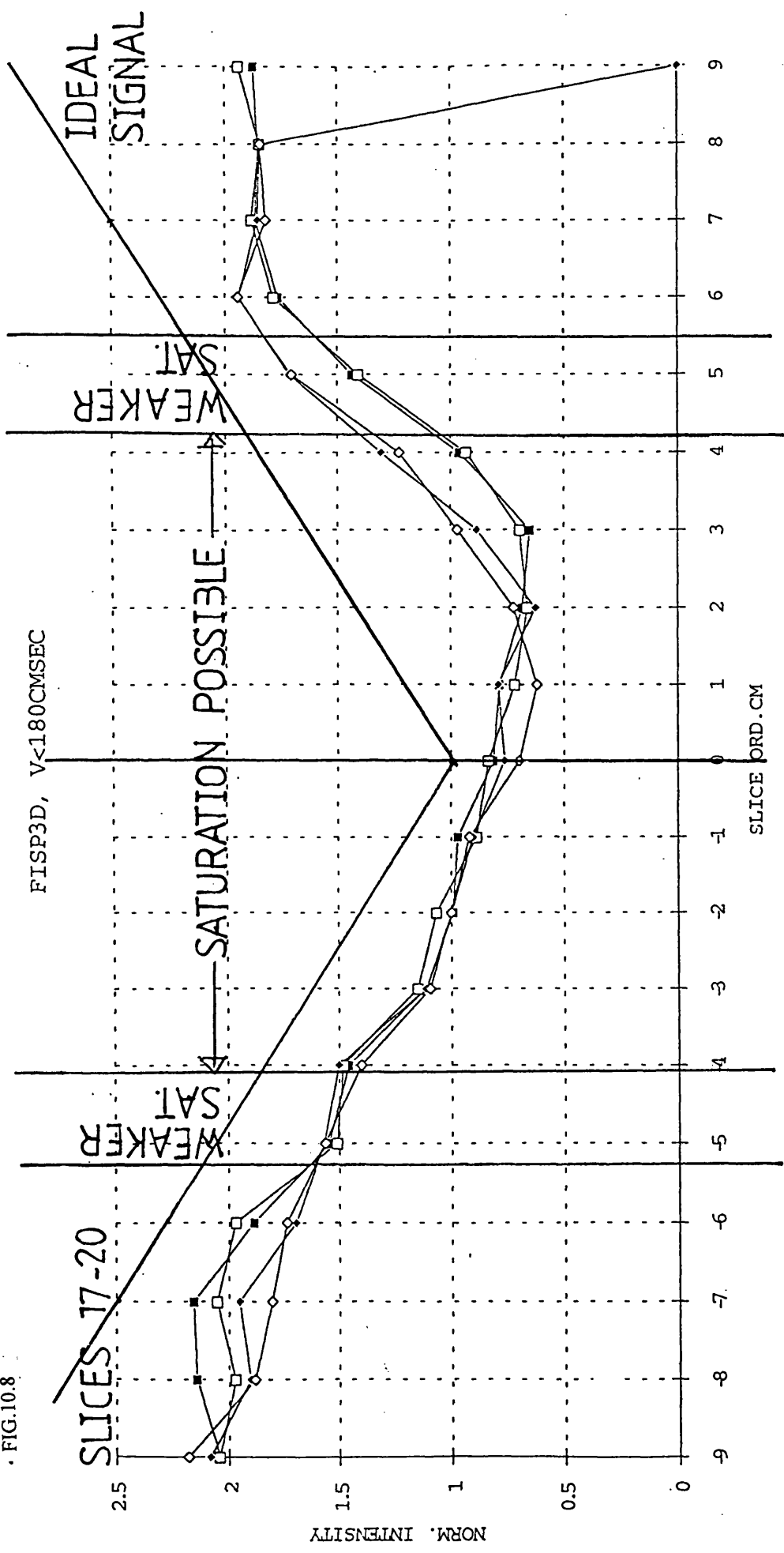


FIG.10.9 Saturation effects in the rotating drum phantom when the sequence FISP 3D,  $FA = 40^\circ$ ,  $TR = 36\text{msec.}$ ,  $TE = 10\text{msec.}$  is applied.

The degree of saturation of the gel depends on how many consecutive RF pulses it receives, and for how long comparatively it can relax between applications of the pulse sequence. This in turn depends on the location of the image slab in the rotating drum, the rate of rotation of the drum compared with the pulse sequence repetition time.

This diagram shows the maximum number of consecutive RF pulses the gel receives in different annular regions, as the gel passes through the image volume. It also shows the equivalent number of pulse sequence repetition times for which the gel relaxes as it rotates out of the image volume.

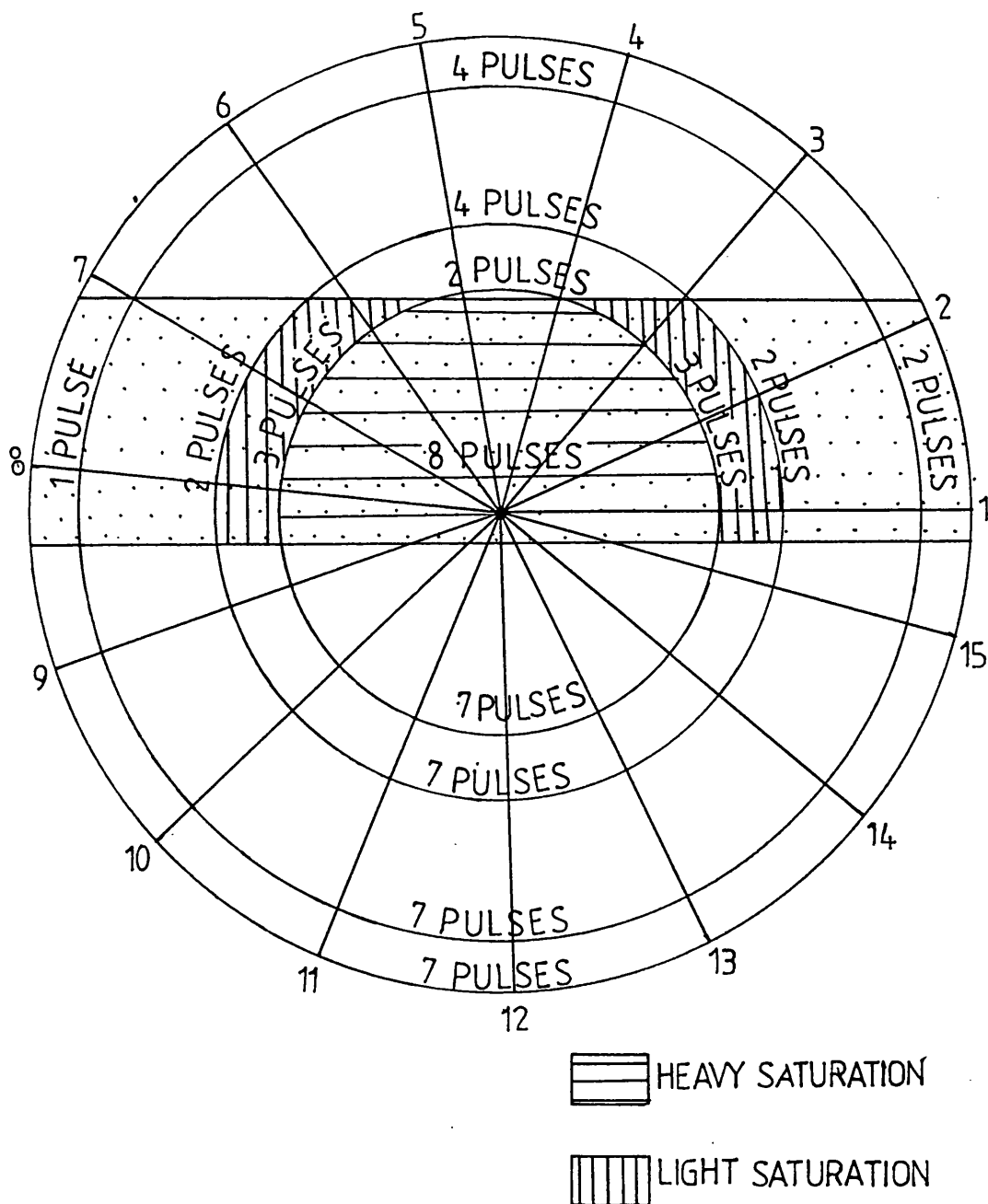


FIG.10.10 Detected signal intensity across the whole of the image volume for the scan at FISP3D, FA = 40°, TR = 36msec., TE = 10msec. Shaded regions show where spin dephasing and saturation effects are responsible for reductions in signal intensity below the expected ideal.

The diagram also shows how the response of the pulse sequence gradually changes from FISP type signal detection to FLASH type signal detection as the spins penetrate the image volume.

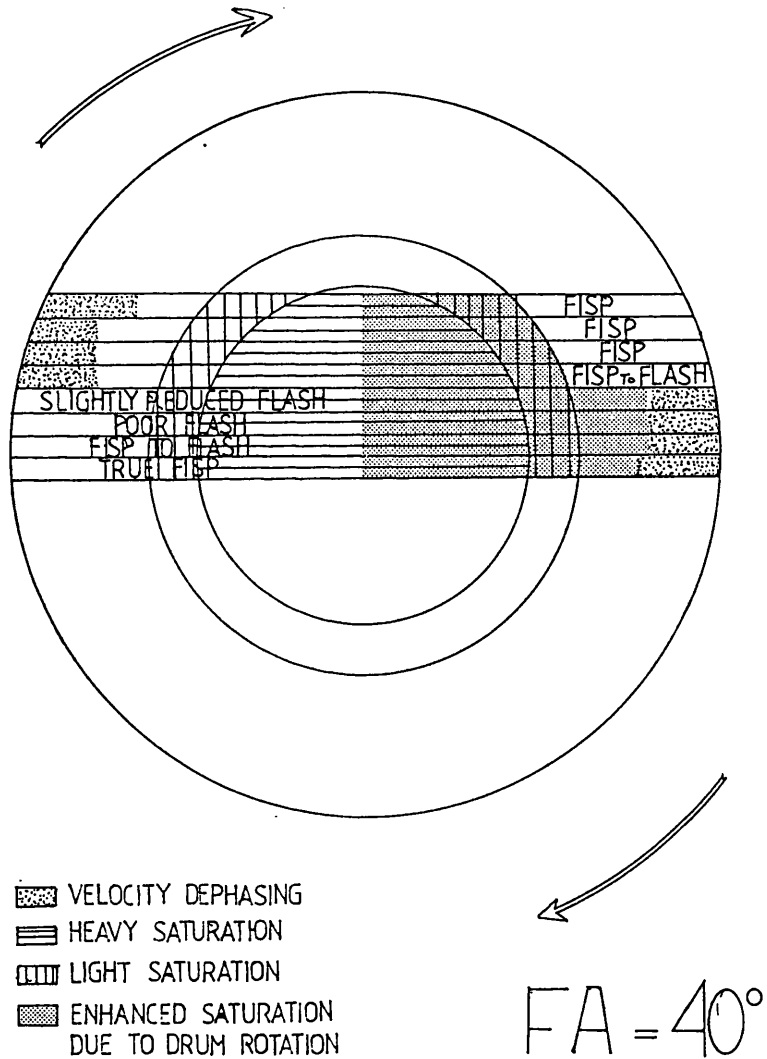


FIG.10.11 The effects of gradient motion refocussing in the sequence FISP3D, FA = 40°, TR = 36msec., TE = 10msec. This is applied to overcome spin dephasing due to motion.

The increase in phase change to spin velocity alone, a linear effect, is shown. The quadratic dependence of spin phase on time is also shown. These two effects are combined ( $\phi \propto vt^2$ ) and the resultant theoretical effect on signal intensity can then be compared with that experimentally observed. Were the gradient motion refocussing lobes applied completely effective, there would be no observable loss of signal due to velocity dephasing.

There is noticeably less dephasing due to velocity with this sequence compared to that at FA = 20°, when the same spin velocities are considered. This is probably because the spin flip angle is larger, and dephasing in the transverse plane is relatively smaller.

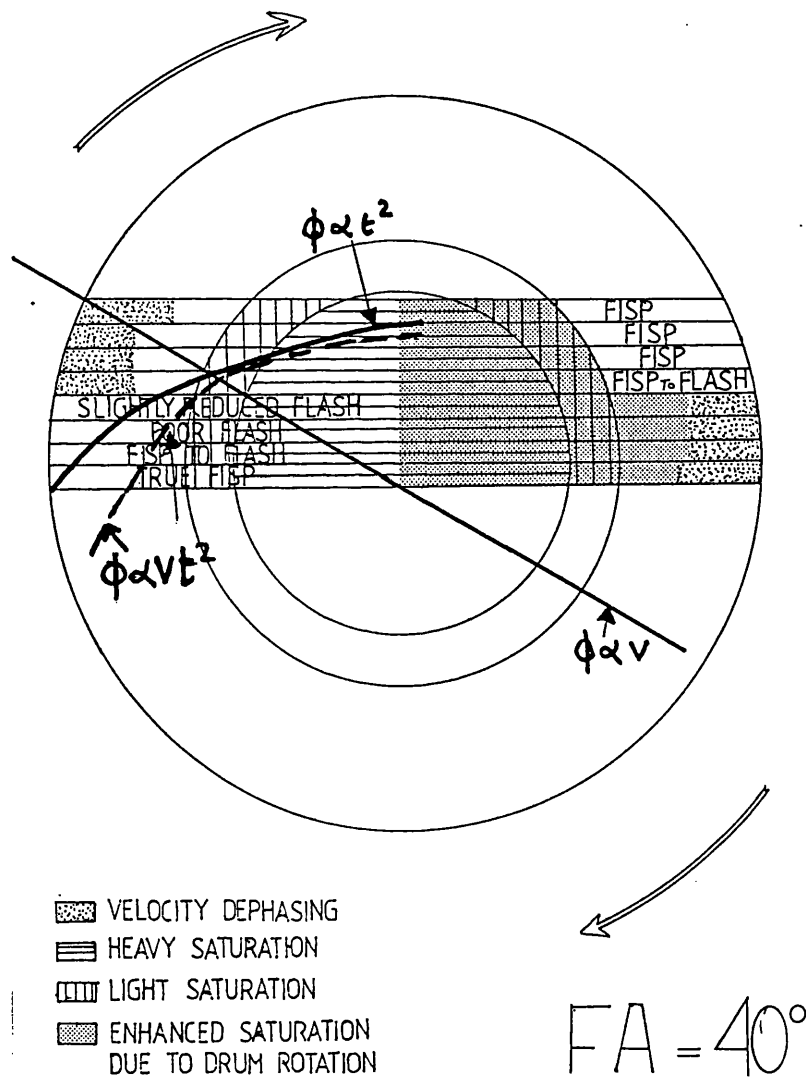
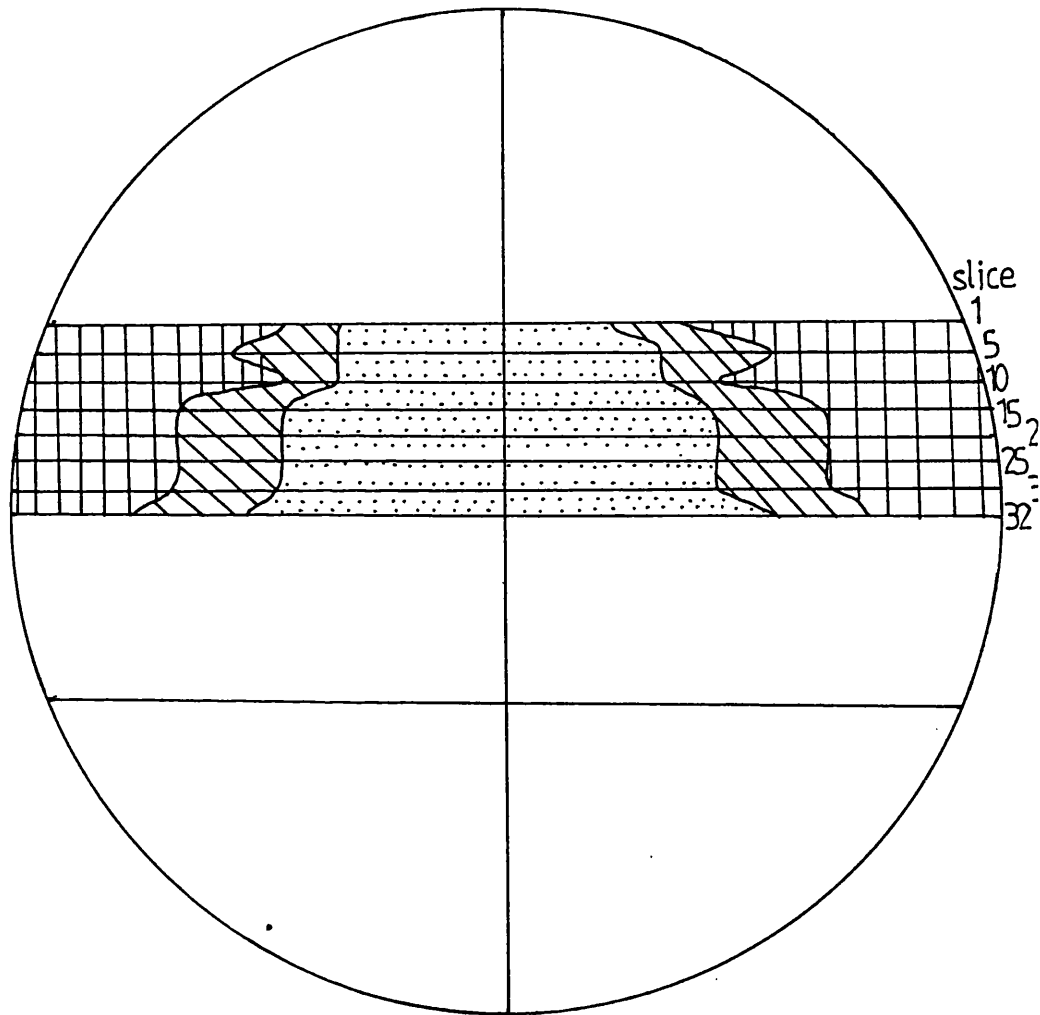


FIG.10.12 OBSERVED SIGNAL LOSS IN FISP 3D SCAN AT 1.5T, WITH  
 FA=15°, TR = 36MSEC, TE=6MSEC.



SIGNAL INCREASING WITH INCREASE IN GEL VOLUME  
 PER UNIT SLICE AREA



SIGNAL RAPIDLY DECREASING



SIGNAL COMPARABLE TO CONSOLE SCREEN NOISE

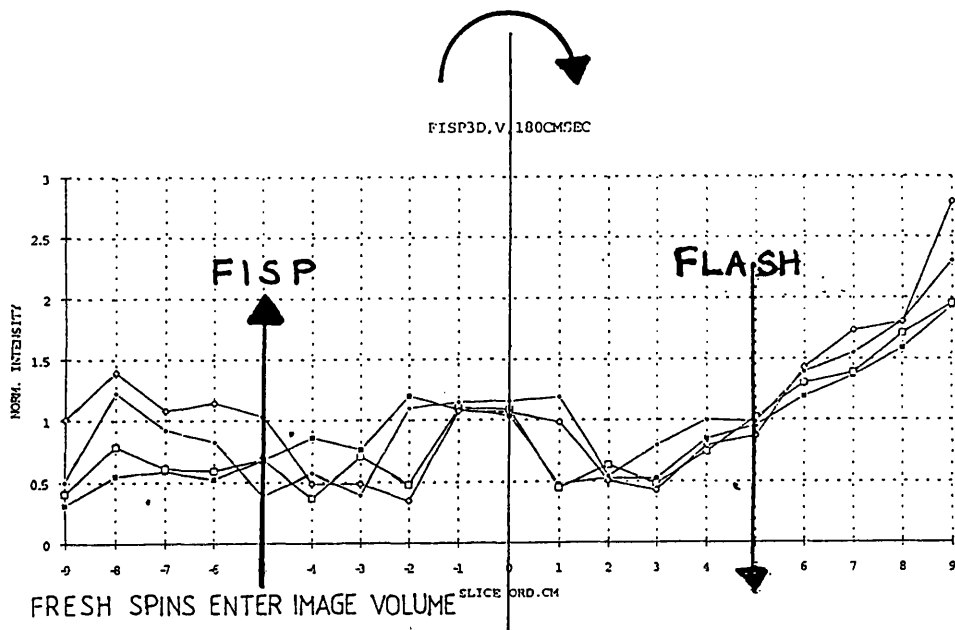


FIG.10.13 Image intensity profiles of peripheral slices scanned using the sequence FISP 3D FA =  $40^\circ$ , TR = 36msec, TE = 10msec show how the spins respond with a FISP signal as they first enter the image volume. By the time they have been encoded through the gradients of the whole image volume, spin dephasing effects are such that the detected signal resembles that expected from a FLASH sequence rather than a FISP sequence.

FIG 10.14 POTENTIAL SATURATION EFFECTS WITH THE SLOWER ROTATION RATE OF THE DRUM USED WHEN THE FLASH 2D SEQUENCE WITH  $FA = 35^\circ$  IS USED FOR SCANNING.

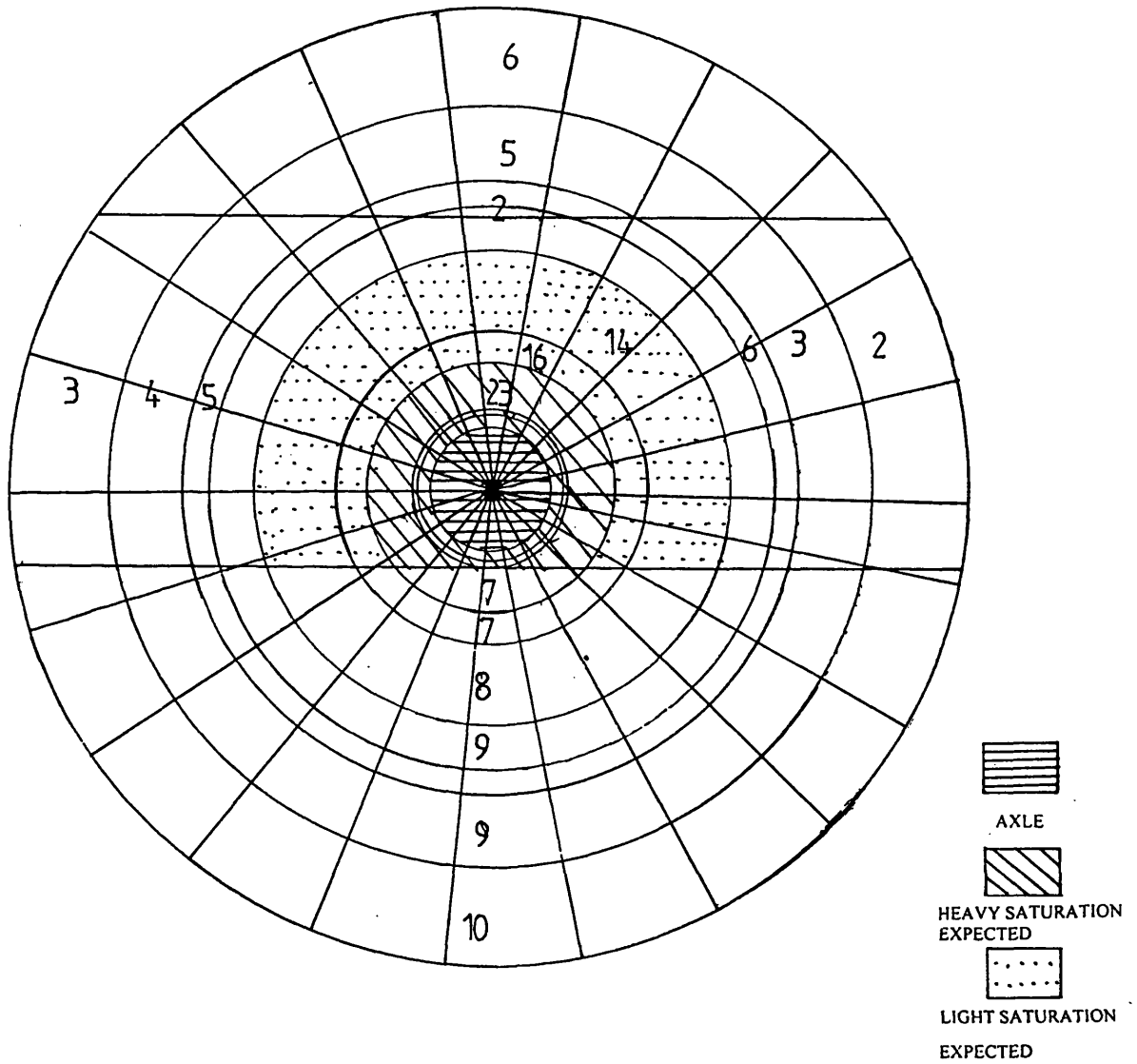
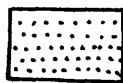
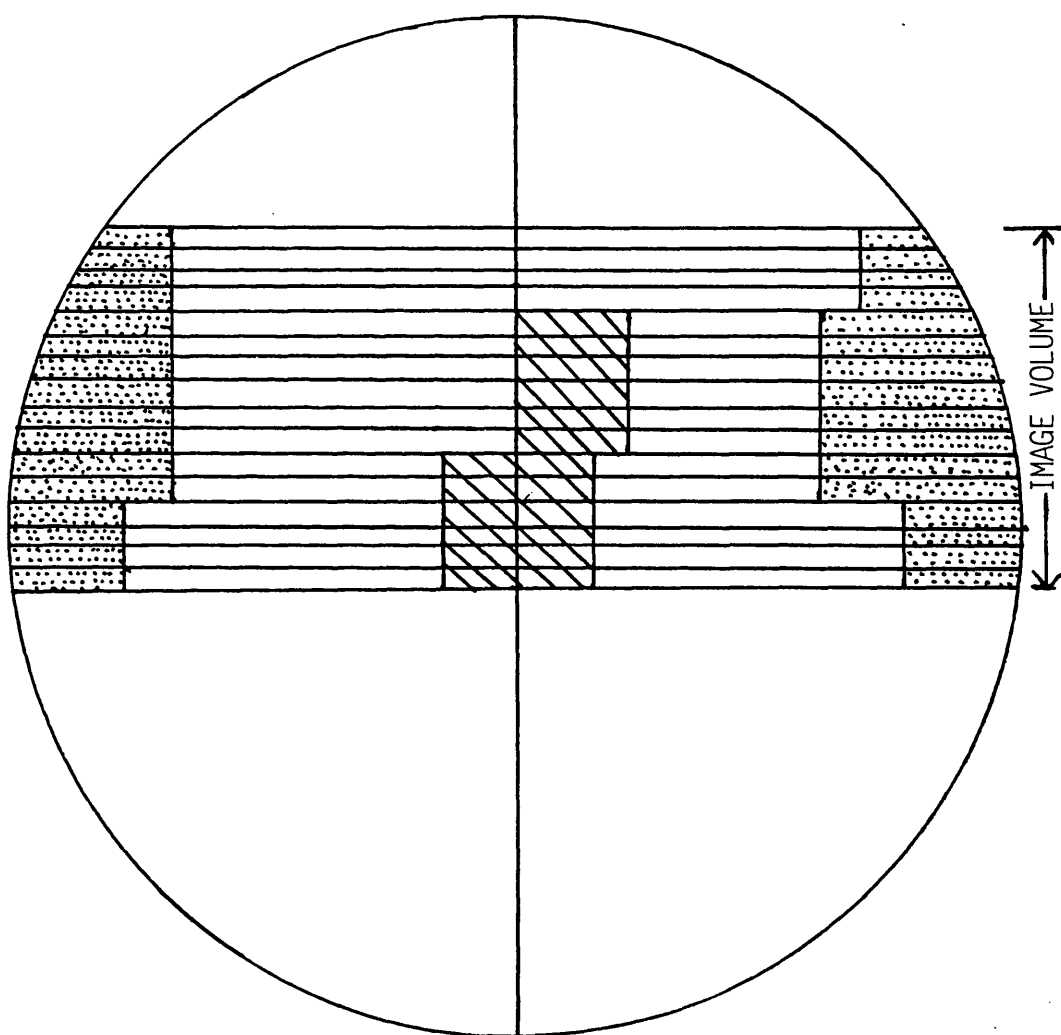


FIG.10.15

OBSERVED SIGNAL LOSS IN FLASH 2D SCAN WITH  $FA = 35^\circ$ ,  
 $TR = 40\text{MSEC}$ ,  $TE = 10\text{MSEC}$ .



VELOCITY DEPHASING EFFECTS

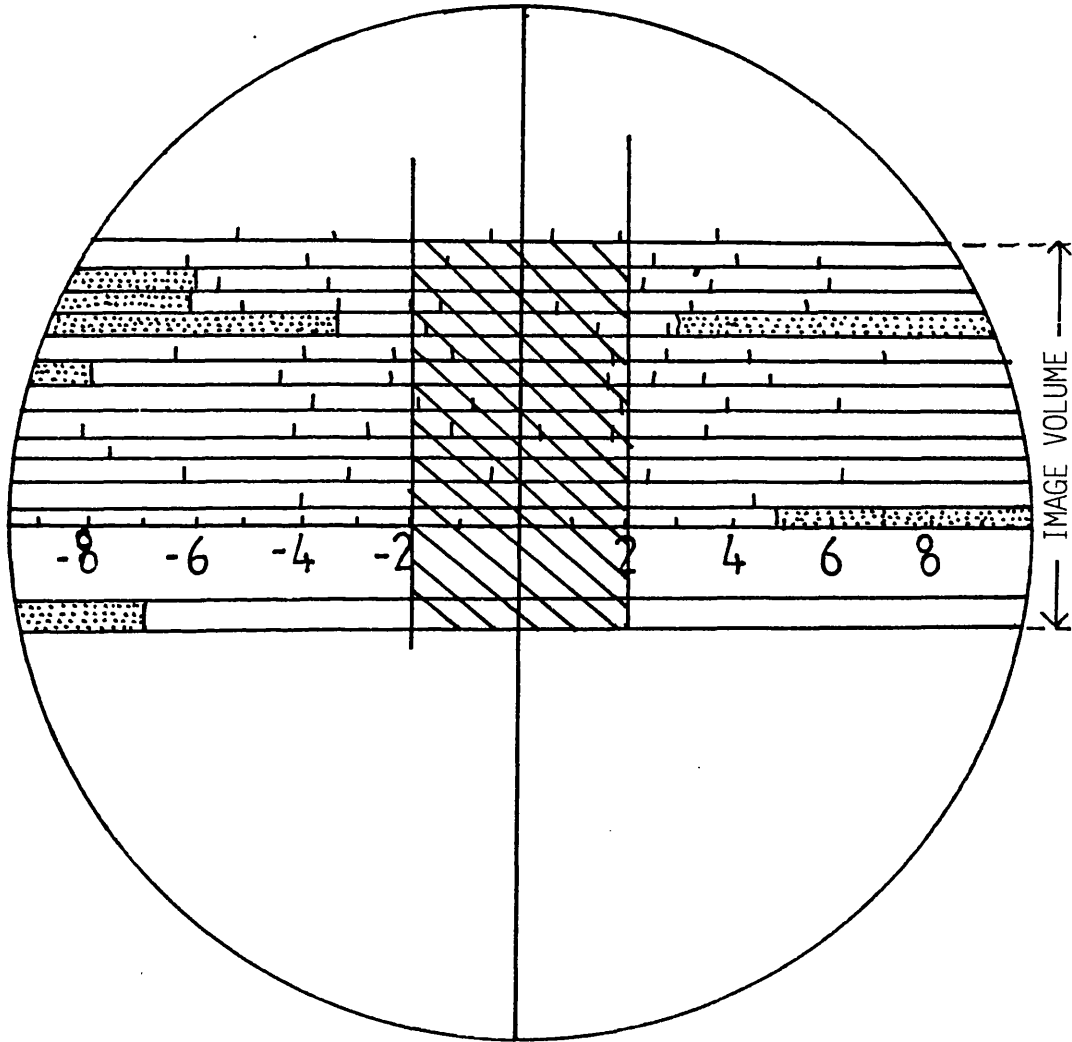


SATURATION EFFECTS

FIG.10.16

OBSERVED SIGNAL LOSS IN FLASH 2D SCAN WITH  $FA=40^{\circ}$ ,  
 $TR = 39\text{MSEC}$ ,  $TE = 10\text{MSEC}$ .

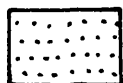
Saturation effects occurring when this sequence is used are fully discussed in chapter 9.



EXPERIMENTALLY OBSERVED SIGNAL MINIMA



SATURATION EFFECTS



VELOCITY DEPHASING EFFECTS

## **CHAPTER 11 : APPLICATION OF PHANTOM SCAN RESULTS TO PROBLEM AREAS OF DIAGNOSTIC IMAGING**

The detailed evaluation of pulse sequence scan images presented in chapters 9 and 10 has led to clear statements about the imaging capabilities of the six tested sequences, and about their applicability for imaging longitudinal flow in the major body arteries. It has been the contention throughout this study that it is essential that the pulse sequence selected in clinical imaging shall be known to be capable of imaging all the longitudinal flow rates which will be encountered in the vessel under scrutiny. In addition to this, the clinician expects that the sequence will be capable of imaging the tortuosities which are an expected part of arterial geometry, and the anatomical abnormalities which he is hoping to diagnose. These are usually present as aneurysms and stenoses.

This chapter draws together aspects of these more complex imaging problems on which the results obtained in this study can throw some light. This study was not designed to study the specific problems of the imaging of stenotic flow, or variable tissue contrast and flow rates through the body of an aneurysm, but its results are to some degree applicable to these imaging challenges. The chapter also looks at the problems of imaging flow through tortuosities.

### **11.1.PROBLEMS OF IMAGING STENOTIC FLOW.**

In clinical MRA, a stenosis can be detected by the appearance of signal void in the length of an otherwise well defined vessel. From the dimensions of the signal void, the degree of stenosis in the

vessel may be calculated (Kilner 1991). Problems arise because the degree of turbulence which exists in the bloodstream immediately after the stenosis can cause ambiguity in the image. Over or under diagnosis of the degree of stenosis are well documented (Bowen, 1994). It appears that the pulse sequence cannot always encode the range of blood spin phases and velocities which are encountered in the post-stenotic region, and this causes clinical misdiagnosis.

Any distortion of the blood vessel lumen, including physiological bifurcations and bendings, may produce local disturbances of blood flow (Azuma (1976), Caro (1992)). This in itself is problematic for MRA, in that there may be deviation from the model of longitudinal flow with a laminar flow profile adopted for use in this study. Flow can influence the morphology, endocytosis and metabolism of endothelium and the dimensions of blood vessels, because of the abnormal haemodynamic forces associated with disturbed flow patterns. Thus a feedback mechanism can occur by which anatomical distortions and associated local flow abnormalities lead to the development of clinical abnormalities which then cause greater flow disturbances.

In some cases, a local effect is the result of distant flow irregularities. For example, Stebbens (1961) suggested that atherosclerotic plaques at intracranial bifurcations might be caused by turbulence in the cerebrovascular system.

Azuma (1976) has undertaken extensive experimental work to investigate probable flow patterns occurring in the region of in vivo stenoses. He used cylindrical tubes made of glass or

metacrylate resin. Axisymmetric constrictions of varying degrees were added to these to provide models of stenotic blood vessels. For steady flow through the tubes, he defined the following regions of interest for the flow:

- i) The boundary layer. Under some flow conditions, this separates from the tube wall.
- ii) The velocity profile across the tube lumen.
- iii) Flow past a hemispherical bulge.
- iv) Flow in the region of axisymmetric constrictions.

He photographed the flow patterns developed and graphically analysed these. He makes it clear that vortical and turbulent flow arises once the flow medium has separated from the vessel wall. Thus presence of abnormal flow proximal to an in vivo stenosis is a complex interaction between the blood velocity and viscosity within the precise dimensions of the length and cross-sectional area of the stenotic region.

All attempts to image stenoses have to take these complex flow factors into consideration. The effects have to be considered in three dimensions. Turbulent flow may be defined as the breakdown of streamlined flow, and its replacement by a region of random spin movement, where all angular phases in the transverse plane can occur. The range of velocities is poorly defined, but will be wider than that encountered in laminar flow in the associated vessel.

The imaging capabilities of MRA sequences have been tested using tube flow phantoms containing constrictions, whose dimensions are such as to give rise to turbulent flow regions which mimic those of anatomical stenoses. (Sondergaard, 1992, Stahlberg, 1990, Cronqvist

1994, Heisermann, 1992). Such phantoms have been commented on in chapter 6. It is also the case that to date, stenosis detection has been commonly used in the clinical evaluation of MR angiography sequences (Masaryk, 1989, Ruggieri, 1989). The imaging capabilities of different sequences are evaluated on their ability to detect stenosis in the same anatomical circumstances. The stenosis is thus used as a test object.

A new approach to the evaluation of pulse sequence response in the presence of stenoses is possible using the rotating phantom. The problem of imaging stenoses can be broken into two components, firstly the ability of sequence to collect a flowing spin signal at the stenosis, and secondly the ability of the reconstruction software to handle the partial volume effects which arise because of the random nature of the phases of spins at the stenosis.

The rotating drum phantom has a unique feature in that it presents a continuous range of velocities from the axle at the centre of the drum to the periphery. This may be treated in another way: along a circle of constant velocity, the drum demonstrates all the phases of flow possible for a spin travelling at that velocity, from 0-360° (figure 11.1). Thus if the sequence images longitudinal flow without signal void along the whole circle of rotation, it is likely that it will be able to respond to all phases occurring in turbulent flow. If the signal intensity is mapped across the entire circular face of the drum, it represents the instantaneous response of that

sequence to spins at all the flow rates covered by the motion of the drum, and at all phases from  $0 - 360^{\circ}$ . If the signal intensity is constant across the whole of this map, then the sequence must be able to image stenotic flow at these flow rates. If only phases from  $0-270^{\circ}$  will image, then the sequence will give a lower image intensity at the stenosis.

The imaging problem is then one of reconstruction: is the intra-voxel dephasing effect such that a low signal arises in the region of turbulence when the image is reconstructed? The advantage of this approach using the rotating phantom is that the known condition of signal loss due to turbulence can be studied in its component parts, that of data collection and that of image reconstruction, separately. This is not possible using tube phantoms where the flow conditions at the false stenosis are not known.

For each of the six sequences used in this study mapping of the circular face of the drum phantom to reveal normalised signal response has been undertaken (Appendix 2). The data from these scans is incomplete since in all cases only a portion of the drum has been scanned. In five cases the image slab is 48mm thick, and in one case 80mm thick, as compared to a total drum diameter of 186mm. Multiple slabs of image data would have to be obtained by repeated scanning of the drum phantom, to map its whole volume, so that comment on the potential applicability of the sequence to stenotic flow imaging could follow.

To ensure quality imaging under conditions of stenotic flow, the effect of the frequency or read gradient on flowing spins would have to be quantified in the manner already used in this study for phase encoding and slice/slab gradients. The possibility of doing such work has been discussed in chapter 6. The fact that flow rates in the region of stenoses can be almost double those found in the normal vessel has already been mentioned in chapter 5. It would be necessary to increase the rotation rate of the drum significantly to be able to simulate these velocities, to obtain the complete phase response data of the sequence under all possible velocity rates encountered at the stenotic site.

The scan data already obtained (Appendix 2) for a restricted range of phases and velocities for the six tested pulse sequences indicates that the FLASH 2D sequences give image data which is almost independent of phase angle and velocity. The FISP 3D scans on the other hand present a more fragmented response for both velocity and phase detection.

## **11.2 PROBLEMS ASSOCIATED WITH THE IMAGING OF ANEURYSMS**

The second main vascular abnormality of interest in clinical terms is the aneurysm. This is a widening of the artery due to local deposits of thrombus, and there is associated clinical risk that the aneurysm may rupture, the degree of risk depending on the aneurysm size.

The gold standard for aneurysm imaging at present is conventional angiography (Meyer 1993), which has the radiation and procedural risks described in chapter 1 associated with it. MRA is now being

used in aneurysm diagnosis. The imaging problems involved are very different from those encountered with stenoses, since the volume of the aneurysm contains both flowing blood and thrombus (Nadel 1990). The clotting of blood and the alteration of regional blood velocity may occur simultaneously, and so cannot be distinguished by images separated in time. Relaxation time changes caused by blood clot degradation can profoundly affect the intensity of magnitude images, and the diagnostic problem is then to distinguish between the signal due to thrombotic material, and the signal due to flowing blood. The cells in thrombotic material vary in oxygen content and in the degree to which they remain intact, and this affects their relaxation times (Gomori,1987). The signal from such cells may be indistinguishable from that due to the flowing blood spins moving through the unrestricted portion of the aneurysm, and this causes problems of interpretation in clinical images.

For surgical purposes, the important information is the size of the aneurysm, the size of the neck of the aneurysm, and the surgical orientation of the aneurysm and its parent arteries. The flow patterns associated with this complex vessel geometry have not yet been defined, but the premise of this study, that no reliable imaging can be undertaken if the pulse sequence does not positively detect spins flowing at velocities normally associated with the vessel of interest, must first be fulfilled if any value is to be obtained from scans involving aneurysms.

One technique which has been devised to overcome the problems of ambiguity is that of reconstructing phase images rather than modulus images from the scan data. This is an option on both the Siemens

scanners used in this study. The image data is then based solely on the phase of the spin vectors in the transverse plane. Moving spins have an additional phase component in this plane because of the spin dephasing effect, and hence they will be reconstructed as brighter intensity than the thrombic material which is stationary. Thus the two can be differentiated.

The value of the results of the rotating phantom study is that they can define a pulse sequence for use at the range of velocities tested which will give an optimal detected signal without loss due to spin dephasing effects. A sequence which shows reduced image intensity at high velocities due to spin dephasing will not provide the differentiation of brightness between thrombic material and flowing blood required for diagnostically viable imaging of aneurysms.

It is possible that magnitude contrast techniques such as that of the rephase-dephase sequence tested in this study could be used to image aneurysms, since stationary thrombic tissue would be eliminated in the subtractive process. Again the caveat of reliable pulse sequence response at the expected flow rates must be applied. The phase contrast technique (Dumoulin, 1989) uses the magnitude contrast effect along all the imaging axes, and again may be useful in this context. The use of contrast agents which will be preferentially absorbed in the thrombic material has not yet been reported.

### 11.3 PROBLEMS OF IMAGING TORTUOUS FLOW

The imaging of tortuous flow has been shown by several authors (Beach (1992), Caro(1992), Kerber (1992)) to be more complex than simply that of imaging the flow of blood round bends.

Kerber (1992) has developed an elastic, transparent, life-sized model of the cranial vessels which allowed the direct visualisation of carotid artery flows. Flow was simulated by pumping an isotonic saline through silicone tubing modelled on vessel structure from 12 adult cadavers. Pulsatile flow was simulated, flow velocities were calculated by introducing small polyvinyl alcohol particles into the flow stream. the streamlines of flow were made visible by the introduction of isobaric food dyes.

This novel approach showed that in the approximately linear internal carotid artery, a helical flow pattern of irregular pitch is set up. It is not clear whether this has a laminar cross sectional profile or not.

A similar procedure has also been used for models of the left cervical and petrous internal carotid arteries. These show a more open but also twisting flow pattern round the more angular vessel geometry found in these regions.

Caro (1992) has concluded that flow is primarily laminar but that longitudinal flow patterns may be complicated by the presence of secondary flow effects. He reconstructed phase images obtained for cross-sections of a tube phantom, and showed that these do not all

have a concentric decrease in intensity from a central maximum to a boundary minimum. The phase-velocity maps are more consistent with the existence of spiral or helical flow in the tube.

Kilner (1992) has also used the phase image reconstruction technique to show the existence of spiral rather than longitudinal flow in models of the aortic arch.

It thus appears that the problems of imaging tortuous vessels are those of simultaneous detection of all spin phases in three dimensions, at a wider range of velocities than that encountered in the linear portions of the vessel, because of accelerated flow at the tortuosity. The effectiveness of pulse sequences under these conditions can therefore be judged on the same criteria and by the same methods as have been described for use with stenotic flow.

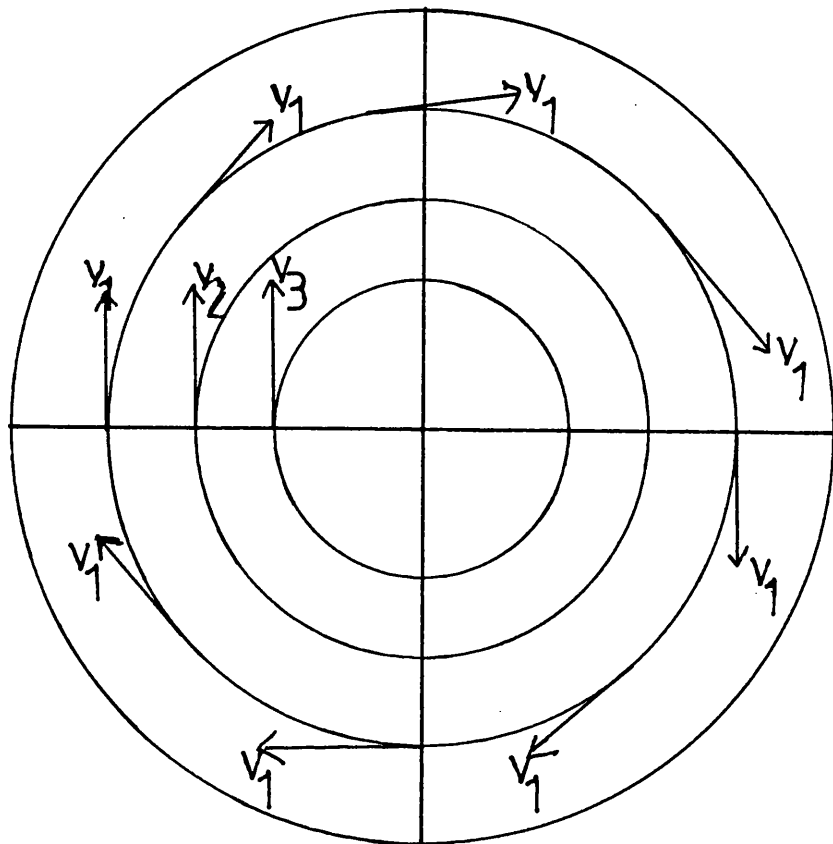
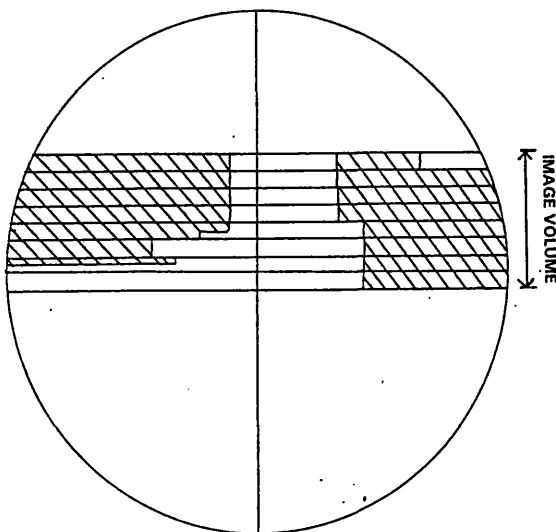


FIG.11.1 Instantaneous image of drum face shows all tangential components at the range of velocities imaged. Velocity phase angles range from  $0-360^\circ$ . Hence signal intensities obtained for a scan of the whole volume of the drum would indicate how the sequence will respond to the imaged range of velocities over the complete phase range.

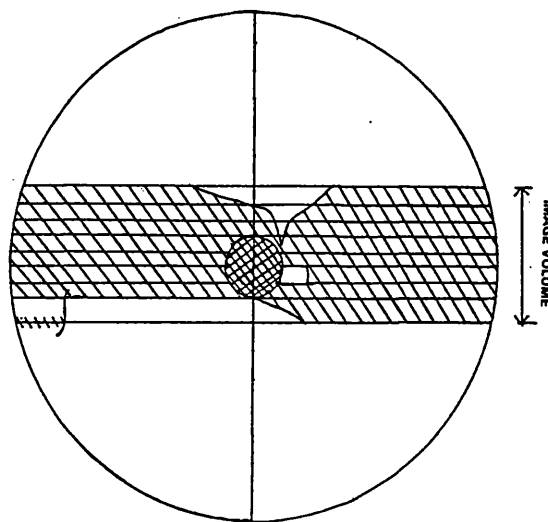
FIG.11.2 COMPARATIVE DRUM VOLUME TESTED FOR VELOCITY RESPONSE OF PULSE SEQUENCES USED IN THIS STUDY

FISP3D\_10rb108.ufa

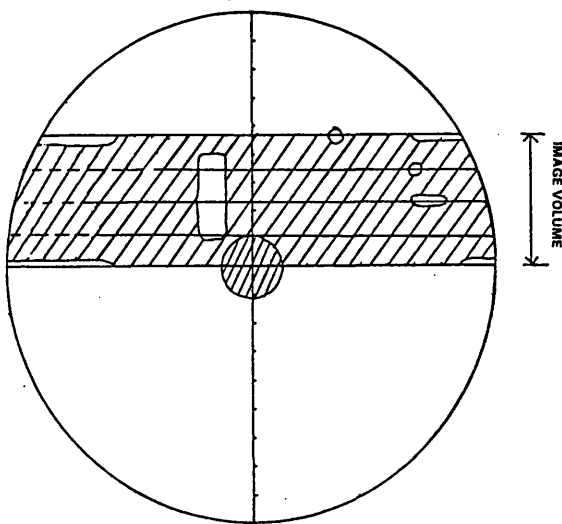
FA = 40°  
TR = 36msec  
TE = 10msec



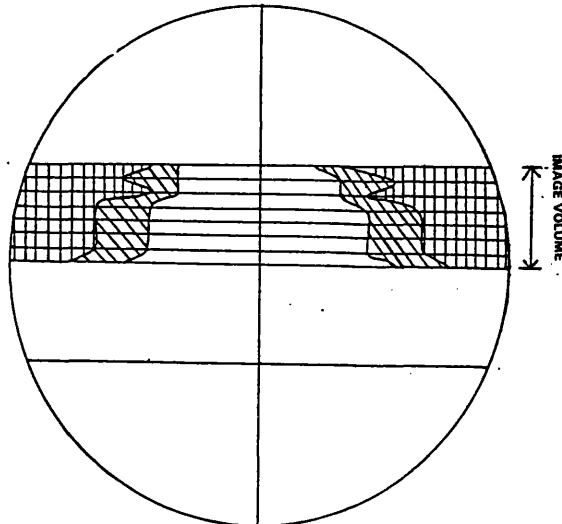
FISP 3D for velocities 35-180cmsec<sup>-1</sup>  
FA = 20°, TR = 36msec, TE = 10msec.



REPHASE-DEPHASE sequence for velocities of 30-45cmsec<sup>-1</sup>  
FA = 15°, TR = 50msec, TE = 14msec.

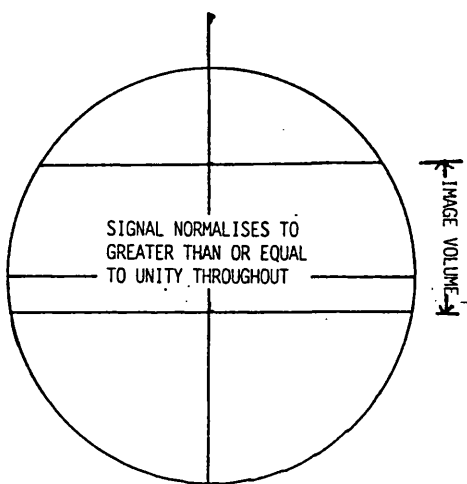


FISP 3D sequence for use at 1.5T, for velocities 30-70cmsec<sup>-1</sup>.  
FA = 15°, TR = 36msec, TE = 6msec.



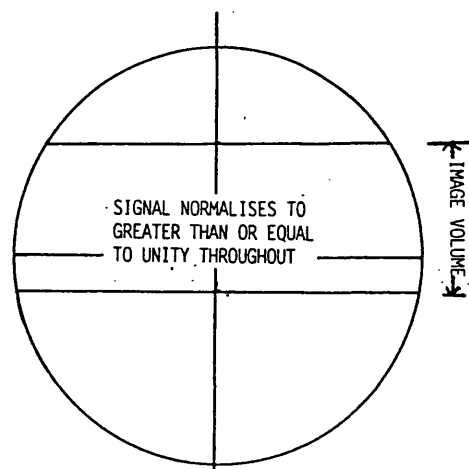
FLASH2D\_s\_10rb78.ufa

FA = 35°  
TR=40msec  
TE=10msec  
STATIC FIELD = 1.0T



FLASH2D\_s\_10rb78.ufa

FA = 40°  
TR = 39msec  
TE = 10msec  
STATIC FIELD = 1.0T



SIGNAL NORMALISES TO  
GREATER THAN OR EQUAL  
TO UNITY THROUGHOUT

SIGNAL NORMALISES TO  
GREATER THAN OR EQUAL  
TO UNITY THROUGHOUT

## CHAPTER 12 : ASSESSMENT OF THE VALUE OF THIS STUDY

Several new initiatives have been developed in this work, and the study concludes with an appraisal of these.

Firstly, the use of a rotating drum phantom in the evaluation of the imaging potential of MR pulse sequences has been thoroughly investigated. The advantages of using a rotating drum phantom over a tube phantom have been listed, and the novel aspect of this phantom which is the use of a static drum in close spatial proximity to the rotating drum has been described. The essential function of the static drum signal in normalising the rotating drum signal, to remove static field artefacts and to eliminate errors arising from discrepancies in gel and in vivo blood relaxation times, has been described.

No other literature exists which describes in detail the artefacts which arise in images because the flow being investigated is circular rather than longitudinal. The detailed evaluation presented here of artefacts arising when FLASH and FISP sequences are used to scan the rotating gel can be regarded as a reference for future studies of this kind.

The importance of using a gel whose magnetic properties match those of in vivo blood has been thoroughly investigated. This has not been done by other authors and the degree to which the results of their experimental studies are invalidated in clinical application is not clear. This study presents detailed calculations to show how differences between relaxation times for gel and in vivo blood will affect the application of the rotating drum phantom study results to diagnostic imaging. The reasons for the discrepancies between the

relaxation times for the gel used here, and the values for in vivo blood, are explained. At the same time the claim can be made for this gel that it has T1 and T2 values closer to those of flowing blood than those used by other authors to date.

The survey of blood flow rates in the major arteries presented in chapter 5 is a critical appraisal of state of the art in in vivo flow measurement. It highlights the fact that there are only a limited number of recent studies which give an extensive range of reliable values. It indicates that the new imaging modalities, which require a knowledge of blood flow rates before imaging if they are to be effective, themselves present new techniques by which such values can be obtained.

The chief purpose of this study has been to evaluate the imaging potential of six commercially available pulse sequences specified for use in magnetic resonance angiography. Several features of evaluation of the pulse sequences are unique to this study.

i) To the author's knowledge no attempt has previously been made to calculate blood spin properties under a range of scan parameters using mathematical expressions for FISP and FLASH signal intensity. These equations were derived for stationary spins, so discrepancies between calculated and experimental values reveal differences in behaviour of flowing and stationary spins, and validate explanations for observed signal loss in the image slices.

ii) The computed graphical technique for presenting the image intensity profile in 3D surface form is a novel presentation of the

pulse sequence response to the imaging of flowing spins. The advantages of this as a mode of presentation are fully discussed.

iii) Saturation effects and spin dephasing effects on the image intensities obtained for all sequences have been quantitatively evaluated. Saturation effects are well understood, and the value of the work in this area presented in this study is that it establishes for what velocities signal degradation occurs with each sequence because of it. The work on spin dephasing is a new and comprehensive combination of theoretical work already derived in this field, and experimental data which shows the magnitude of the effect at different flow rates. Comparison of theoretical and experimentally observed effects shows that there are limitations in the existing understanding of the behaviour of moving spins in encoding gradients, and that the refocussing techniques used to date are restricted in effectiveness as a result.

iv) The differences between the response of the FISP pulse sequence gradients and the FLASH pulse sequence gradients to the detection of the signal from moving spins have been evaluated. It has been shown that there are inevitable image artefacts when the FISP sequence is used in flow studies, which do not arise in FLASH imaging. Evidence has been presented to indicate that the SSFP mechanism imparted in the FISP sequence is not appropriate when flowing spins are imaged, and that the FISP sequence loses this signal component under these conditions, responding as if it were a FLASH rather than a FISP sequence. The advantages of 2D over 3D acquisitions in the reduction of spin dephasing and saturation effects have also been delineated.

v) A quantitative and reliable evaluation has been made of the longitudinal flow rates which each pulse sequence can effectively image. Clinical application of these results has been made in definition of the major body arteries which each sequence can therefore reliably be expected to image.

The study has not been able to fully establish the response of the tested sequences to clinical situations in which imaging problems can be expected to arise, such as aneurysms and stenoses. However it has clearly established that the clinician cannot expect diagnostically viable images if the velocity response of the sequence used is not fully understood. This is the most valuable contribution made by the work presented in this study to clinical imaging.

## GLOSSARY OF TERMS USED IN THIS STUDY

**ASCENDING ACQUISITION** This is a 2D image data acquisition technique for which the data is acquired for consecutive slices 1,2,3...etc.

**DISTANCE FACTOR** It can be arranged that collected image data for 2D acquisitions is obtained in overlapping units. The degree to which these superimpose is decided by the distance factor.

**ECHO TIME (TE)** Time that elapses between the application of the RF pulse and the detection of the echo or signal from the precessing spins.

**FLIP ANGLE (FA)** The angle of inclination of the proton spin to the direction of the static field, on application of the RF pulse.

**FREE INDUCTION DECAY (FID)** This is the rise and fall in magnitude of the transverse magnetisation induced in the proton spin because of repeated applications of the RF pulse.

**FREQUENCY ENCODING GRADIENT** This linearly increasing gradient is applied along one of the imaging axes the spatially encode the spins along that axis.

**GRADIENT ECHO SEQUENCE** This type of pulse sequence uses a gradient lobe to produce a detectable signal from the precessing proton spins.

**GRADIENT MOTION REFOCUSING (GMR)** Additional gradient lobes can be applied to overcome transverse plane dephasing effects due to spin velocity and acceleration.

**INFLOW TECHNIQUE** This is the same as time-of-flight imaging.

**INTERLEAVED ACQUISITION** This is a 2D image data acquisition technique for which the data is acquired for slices 1,3,5 ...etc followed by the data for slices 2,4,6...etc.

**MAGNITUDE CONTRAST IMAGE** This type of image is possible when two sets of data are collected. One of these must contain image information which is different from that of the second. This criterion applies to only one of the scan axes. Subtraction of the two sets of data eliminates image information which is common to both scans, and leaves only the difference data. It is a technique applied to image bloodflow, when the static tissue image data is the same for both scans, and can be eliminated. leaving only the image of the blood vessels.

**MATRIX** This is the grid on which the image is reconstructed for the console screen.

**MAXIMUM INTENSITY PROJECTION (MIP)** A ray tracing procedure which selects the brightest pixel along an imaginary ray passing through the image volume, and reconstructs only this pixel in the image. MIP's are 3D images.

**MODULUS IMAGE** A reconstructed image whose brightness depends on the strength of the signal detected from individual proton spins.

**MULTIPLE PROJECTION RECONSTRUCTION(MPR)** It is customary to reconstruct several MIP's from one set of image data, using a range of start points for the observer.

**PHASE CONTRAST IMAGE** The magnitude contrast technique is used along all three imaging axes. Subtraction of image data is then done three times to give the final difference image.

**PHASE ENCODING GRADIENT** A linearly increasing gradient applied in 256 stepped inclinations. This discriminates it from the frequency encoding gradient, and allows a second unique spatial co-ordinate to be allocated to each proton spin.

**PHASE IMAGE** A reconstructed image whose brightness depends on the phase angle of the detected signal. This is defined by the ratio of the imaginary and real parts of the detected signal. It should not be confused with the flip angle.

**PULSE SEQUENCE REPETITION TIME (TR)** Time that elapses between consecutive applications of the RF pulse, followed by the encoding gradients.

**PULSE SEQUENCE** The group of RF pulses and encoding gradients which is applied to produce one unit of image data from the tissue.

**READ GRADIENT** The same as the frequency encoding gradient.

**REPHASE-DEPHASE IMAGE** The same as a magnitude contrast image.

**RF PULSE** An alternating magnetic field at radio frequencies applied at right angles to the static field usually for microseconds. It has a finite bandwidth, but its maximum amplitude is at resonant frequency of the protons of interest in the tissue. Its purpose is to flip the spins from their alignment with the static field to some required inclination between  $0^{\circ}$  and  $90^{\circ}$ .

**SATURATION** The normal state of imaged stationary spins. Repeated applications of the pulse sequence result in an equilibrium inclination of the spins to the direction of the static field. After one RF pulse is applied, they relax somewhat, but the next RF pulse returns them to their equilibrium state.

**SPIN DEPHASING** This is also known as velocity dephasing. Moving spins dephase faster in the transverse plane because they travel through the encoding gradients, and this term describes the effect.

**SPIN ECHO SEQUENCE** This type of pulse sequence uses a second RF pulse to produce a detectable signal from the precessing proton spins.

**SPIN WARP** This technique was devised to select a slice or slab of interest for scanning. It involves the use of a slice or slab select gradient and an RF pulse simultaneously.

**SPIN-LATTICE RELAXATION** Interaction between adjacent proton spins is responsible for the rate at which longitudinal relaxation of the spins occurs.

**SPIN-SPIN RELAXATION** Longer range interaction between the proton spins, and between the spins and the applied gradients, controls the rate of spin relaxation in the transverse plane.

**STATIC FIELD** This is the resistive or superconducting magnetic field used in the scanner to align all the proton spins before the imaging gradients are applied.

**STEADY STATE FREE PRECESSION (SSFP)** This condition is achieved when sufficient pulse sequence gradients are applied to ensure that the magnitude of the component of transverse magnetisation does not change during the pulse sequence.

**T1** The longitudinal relaxation time for the proton spin. It is the time that elapses between the application of the RF pulse, and the return of the spin to 63% of its initial longitudinal magnetisation.

**T2** The transverse relaxation time for the flipped proton spins. When the RF pulse is applied the spins are in phase in the transverse plane. Gradually they dephase, and T2 is the time taken for transverse magnetisation to fall to 37% of its maximum value.

**T2\*** The effective transverse relaxation time for the proton spins. Local inhomogeneities in the imaging system give a unique value to the time for transverse magnetisation to fall to 37% of its maximum value.

**TIME-OF-FLIGHT(TOF)IMAGING** This technique is used to image flowing spins. It is based on the fact that flowing spins have an enhanced contrast in comparison to the stationary spins in the image volume.

## APPENDIX ONE: GRADIENT LOBE STRUCTURE OF ALL PULSE SEQUENCES MENTIONED IN THIS STUDY

The gradient lobe structure of each of the pulse sequences mentioned in this thesis is shown here in schematic form. The duration of the pulses, the rise and fall times and the strength of the gradients is not available. The sequences are presented in the temporal order in which they were developed. Thus they can be compared to see how their different functions have necessitated the inclusion of new gradients. The  $180^{\circ}$  pulse was replaced by a gradient echo lobe when gradient echo sequences followed spin echo sequences. Compensatory gradients were introduced to overcome the dephasing effects of each of the encoding gradients. Finally gradient motion refocusing was included in sequences used to image flowing spins. Each inclusion of new gradients is likely to increase the pulse sequence repetition time.

The exact shape and timing of the gradients incorporated into a sequence depends on the use for which the sequence was designed, and on the range of sequence parameters which the manufacturer specifies as appropriate for the sequence. A FISP 3D sequence which has TR allowed in the range 100-1000msec, and a second FISP 3D sequence which has TR allowed in the range 10-100msec, will not respond in identical fashion if TR=30msec is used in both cases, and if all other imaging parameters are identical.

The sequences listed here are

**FOR THE IMAGING OF STATIONARY SPINS ONLY:**

SPIN ECHO  
GRADIENT ECHO

**FOR THE IMAGING OF FLOWING SPINS IN STATIONARY TISSUE:**

SPIN ECHO WITH GRADIENT MOTION REFOCUSING  
GRADIENT ECHO WITH GRADIENT MOTION REFOCUSING

**FAST IMAGING SEQUENCES WHICH CAN USE GRADIENT MOTION  
REFOCUSING:**

FLASH  
FISP

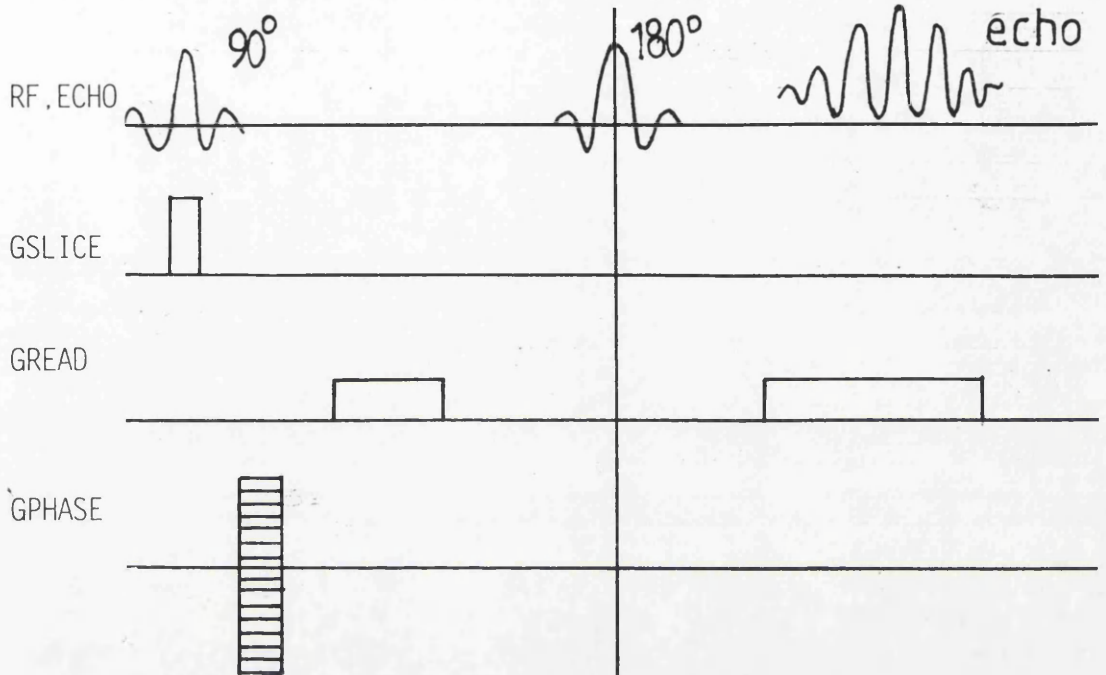
**MAGNITUDE CONTRAST SEQUENCES FOR DIFFERENCE IMAGES, USING  
INTERLEAVED SEQUENCES**

CISS  
REPHASE-DEPHASE

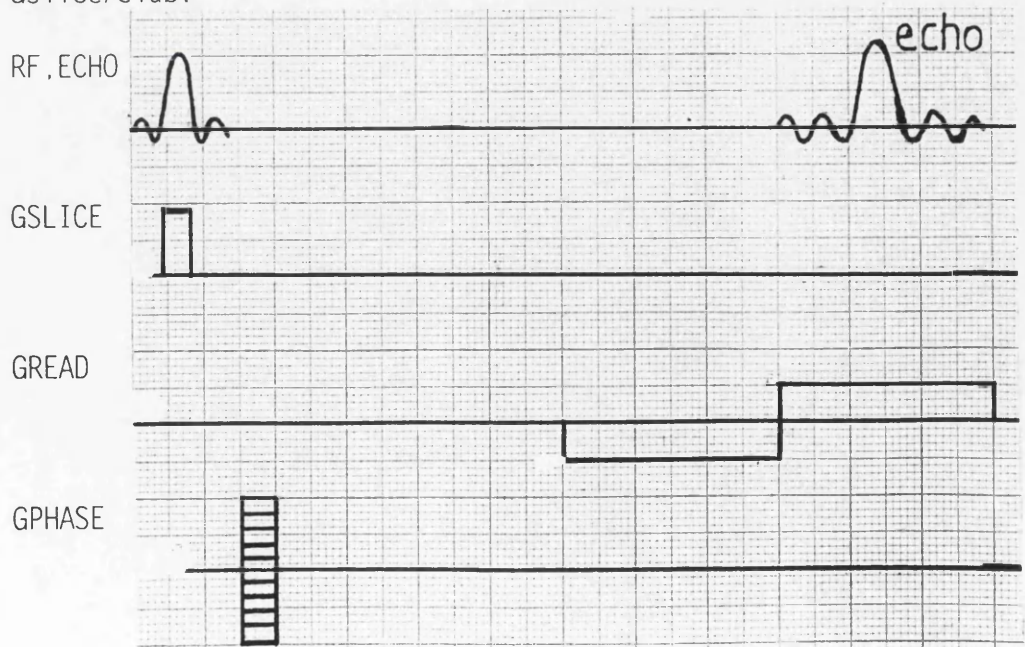
Graphs compiled from Ross(1989), Laub(1988), Haase(1986), Oppelt(1986),  
Casselman(1993), Stahlberg(1989), Axel(1987).

# IMAGING STATIONARY SPINS; SPIN ECHO AND GRADIENT ECHO SEQUENCES

Spin echo sequence for stationary spins. The sequence is shown as applied for 2D imaging. A second set of phase encoding lobes is used along Gslice/slab for 3D imaging.

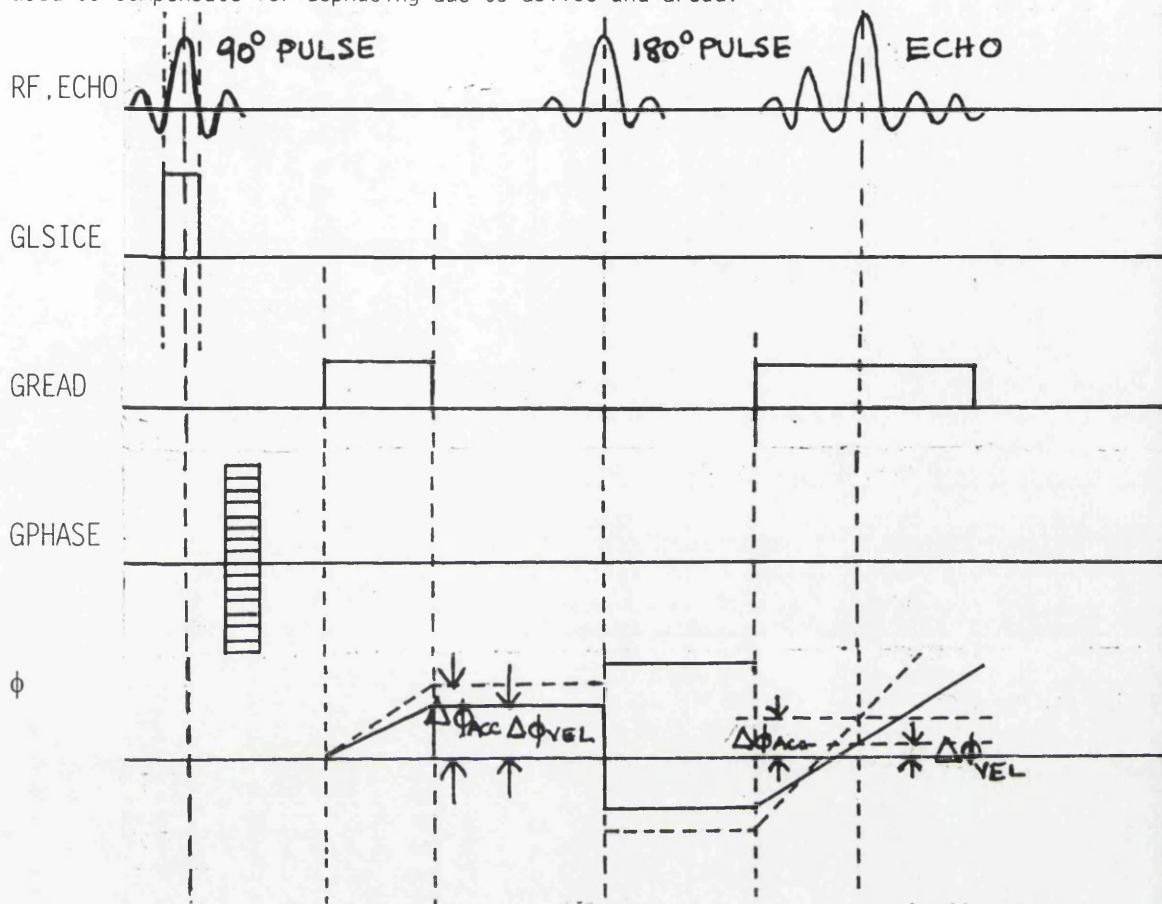


Gradient echo sequence for 2D imaging of stationary spins. The refocussing of spins prior to echo is done by a reverse polarity gradient. The TR is lower than that for a comparable spin echo sequence because complete longitudinal relaxation of the spins is not necessary before they can be refocussed. For 3D imaging an additional phase encoding lobe is used along Gslice/slab.

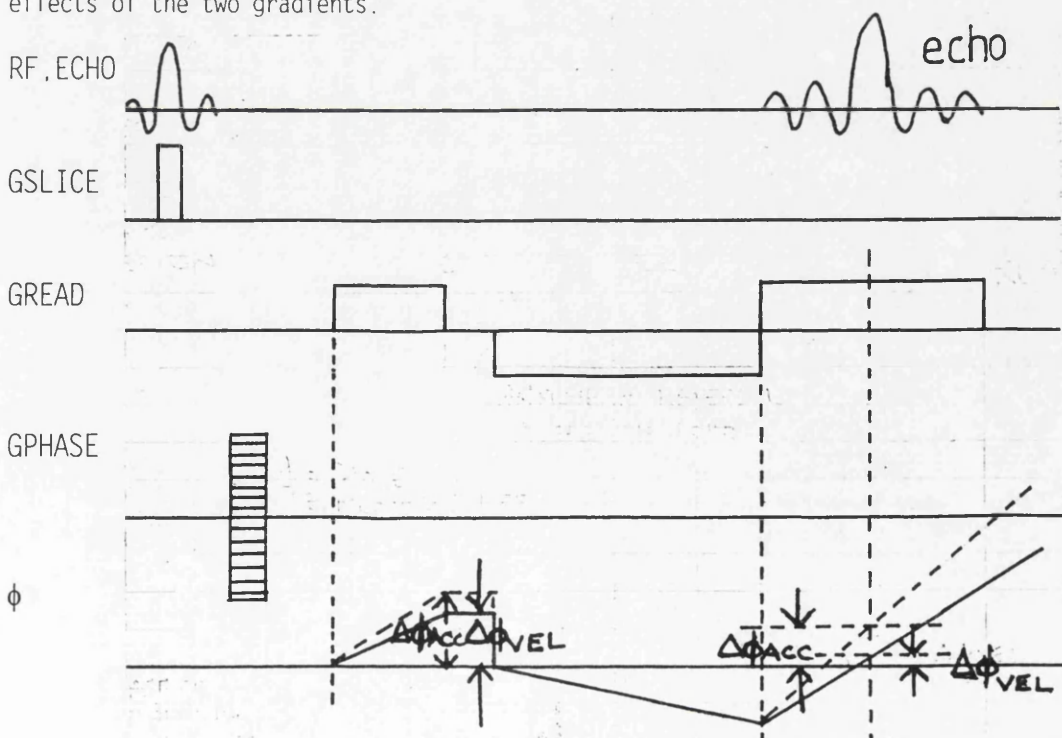


# FLOW COMPENSATION IN SPIN ECHO AND GRADIENT ECHO IMAGING

Spin echo sequence used for flowing spins in 2D imaging. GMR lobes are used to compensate for dephasing due to  $G_{slice}$  and  $G_{read}$ .



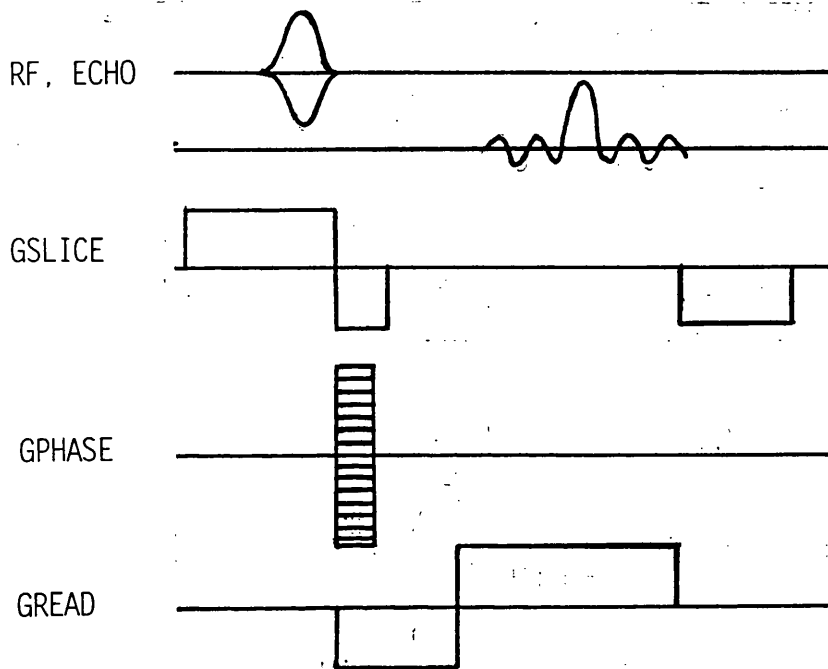
Gradient echo sequence used to image flowing spins. Additional Gmr lobes have been used along  $G_{slice/slab}$  and  $G_{read}$  to compensate for the dephasing effects of the two gradients.



## Fast imaging sequences for stationary and flowing spins.

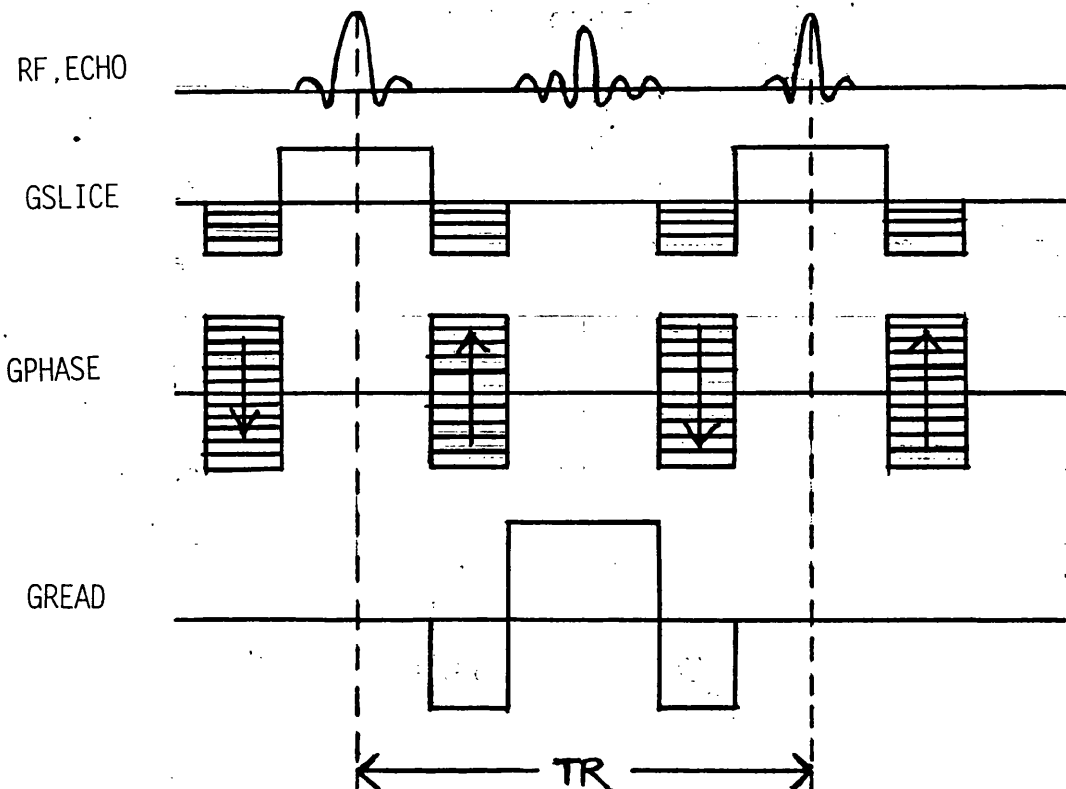
The FLASH sequence is shown for 2D imaging. For 3D imaging additional Gphase gradient lobes are used along Gslice. The number and type of gradient lobes used is that of a gradient echo sequence. The difference is that the choice of RF pulse ensures that a limited flip angle is applied to the spins. An additional spoiler pulse, which may be either a second RF pulse or another gradient, is applied immediately after the echo and before the pulse sequence is repeated. This is the unique feature of a FLASH sequence.

If the sequence is used to image flowing spins, GMR may be applied along Gslice/slab and Gread.



FISP 2D sequence. For 3D imaging the Gphase gradients are repeated along Gslice. The unique feature of FISP is the use of the rewinder gradients along Gphase. These are identical to the phase encoding gradients, but are only used for refocussing purposes.

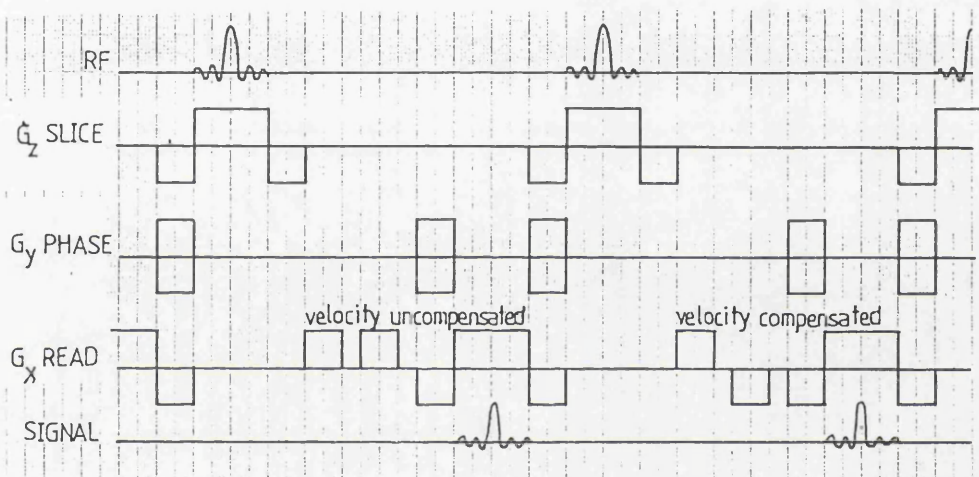
If the sequence is used to image flowing spins, GMR is normally applied along Gslice/slab and Gread. It is only rarely applied along Gphase.



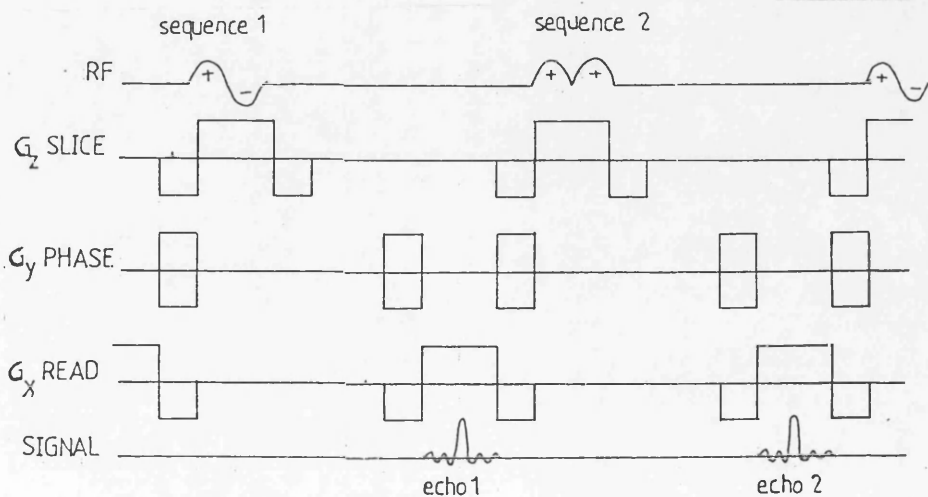
## AN INTERLEAVED SEQUENCE FOR IMAGING FLOWING SPINS

MAGNITUDE CONTRAST SEQUENCES. These eliminate stationary tissue, and image flowing spins as bright.

Magnitude contrast uses an intensity subtraction technique based on an interleaved sequence data collection procedure. In REPHASE-DEPHASE imaging, the sequence has velocity compensating lobes on its first application, and velocity un-compensating lobes on its second application. In CONSTRUCTIVE INTERFERENCE IN THE STEADY STATE (CISS) imaging, the interleaved sequences use a positive RF pulse on the first application, and a negative RF pulse on the second application. No additional gradients are then needed.



## REPHASE-DEPHASE SEQUENCE USING COMPENSATING GRADIENTS



## CISS SEQUENCE USING ALTERNATING AND NON-ALTERNATING RF PULSES

## APPENDIX 2: NORMALISED IMAGE INTENSITY PROFILES PRESENTED IN 2D GRAPHICAL FORM FOR EACH OF THE SIX PULSE SEQUENCE SCAN VOLUMES.

The FISP3D scans were each reconstructed as 32 2D slices, representing 1.5mm thickness of tissue.

The FLASH2D scans were each reconstructed as 16 2D slices, representing 3mm thickness of tissue.

## 2D IMAGE SLICE INTENSITY PROFILES FOR THE SEQUENCE

FISP3D\_10rb108.ufa

$$FA = 20^{\circ}$$

$$TR = 36\text{msec.}$$

$$TE = 10\text{msec.}$$

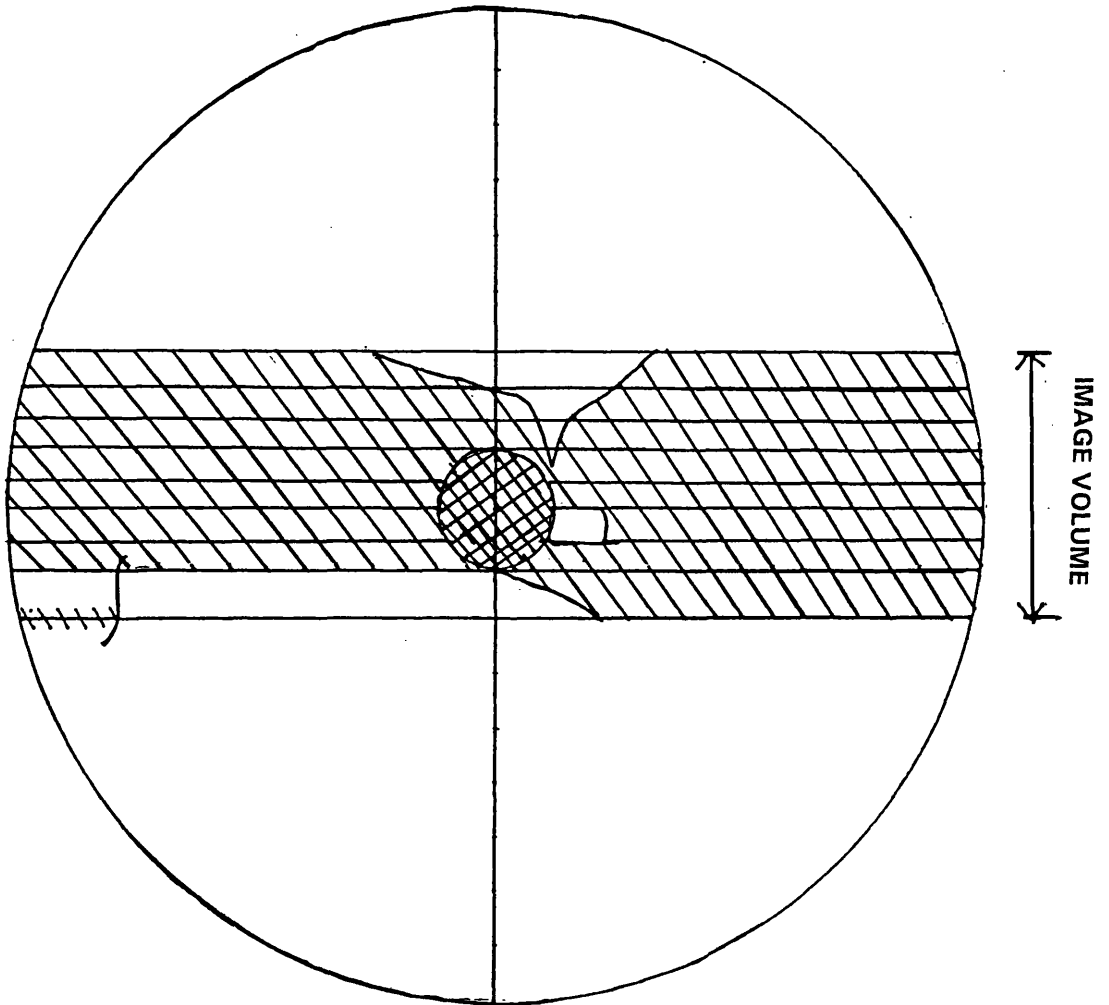
The location of the scan volume relative to the complete volume of the drum is shown in Graph 1. The normalised image intensity has been obtained for each of the 32 slices of the reconstructed image of the scanned volume, using the method detailed in Chapter 9. These image intensity profiles are presented here in groups of four, in the order in which they were reconstructed.

It has been established in chapter 6 that the ideal signal response of the rotating drum phantom for all of the reconstructed slice profiles is a linear increase in intensity with radius, with zero intensity at the centre of the drum. The gradient of the profile is independent of the distance of the slice from the centre of the drum, and depends only on the rate of rotation of the drum.

The ideal signal response of this FISP 3D scan has been estimated by scrutiny of all the profiles, and has been drawn in as a signal intensity reference line on all the sets of graphs. Any discrepancies between this ideal signal and the experimentally measured signal is the result of signal degradation because of spin movement.

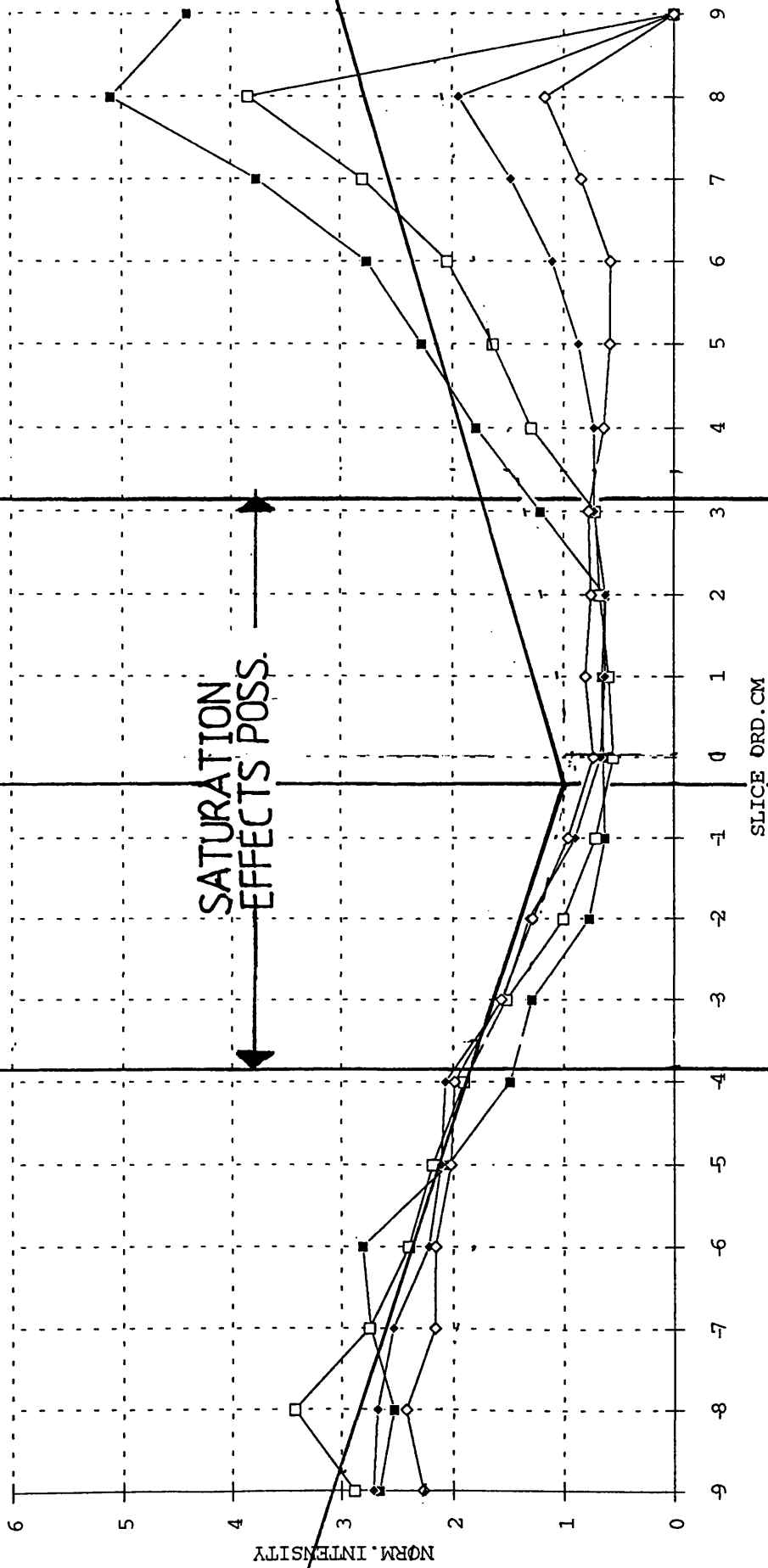
The two processes by which moving spins produce a less than ideal signal are saturation at low velocities, and spin dephasing at high velocities (see chapter 3). All these profiles have been scrutinised for signal loss, and the velocities at which it occurs have been obtained accurately. The collated data on signal loss is presented in Chapter 10, and in this chapter a detailed discussion of the effects of spin saturation and spin dephasing on the image intensity is given.

FISP 3D for velocities  $35-180\text{cmsec}^{-1}$   
FA =  $20^\circ$ , TR = 36msec, TE = 10msec.



Shaded area shows the region of the imaged volume where the normalised signal intensity is greater than or equal to unity.

SLICES 1-4



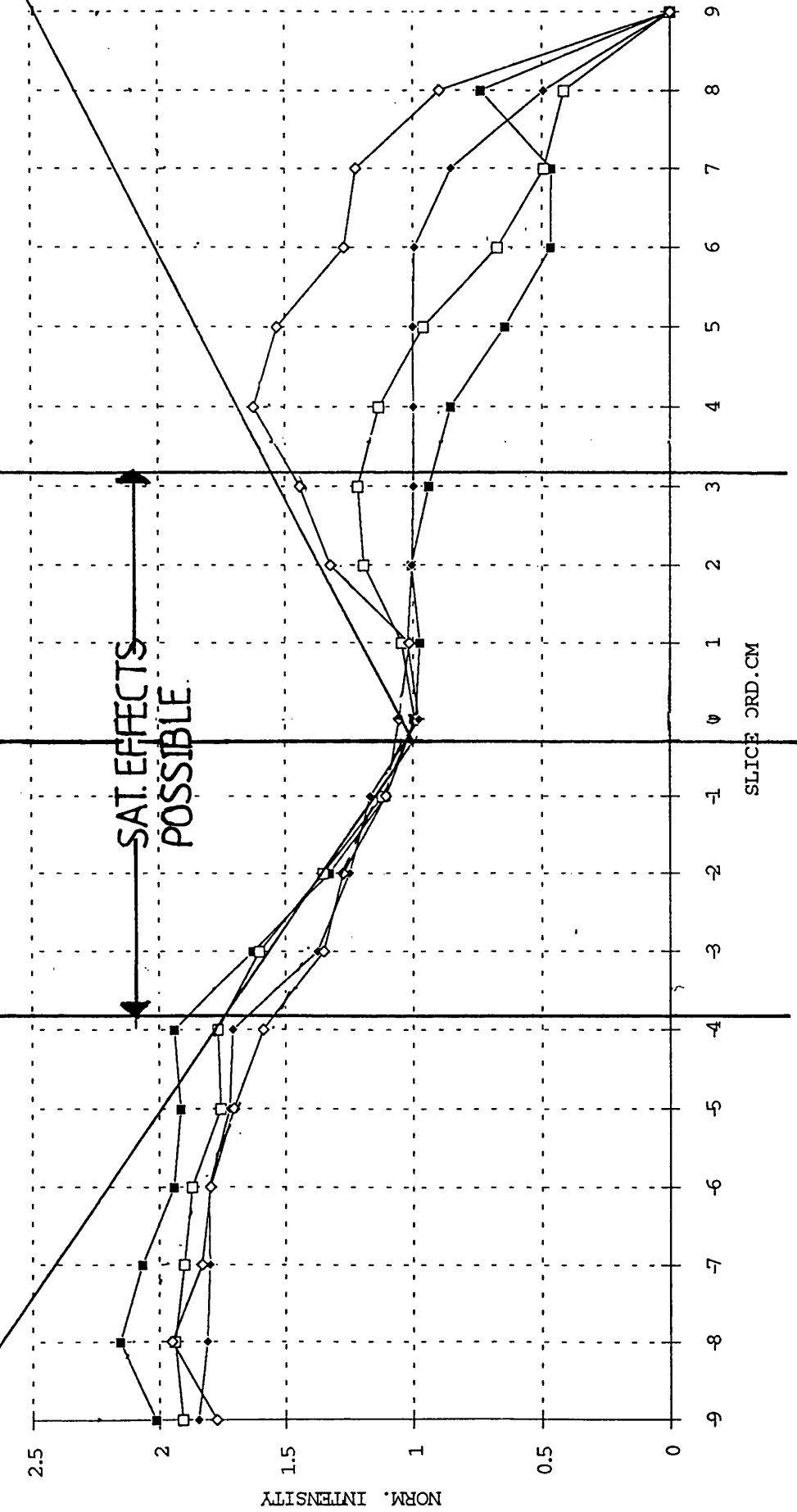
IDEAL  
SIGNAL

SATURATION  
EFFECTS POSS.

NORM. INTENSITY

SLICE ORD. CM

SLICES 5-8



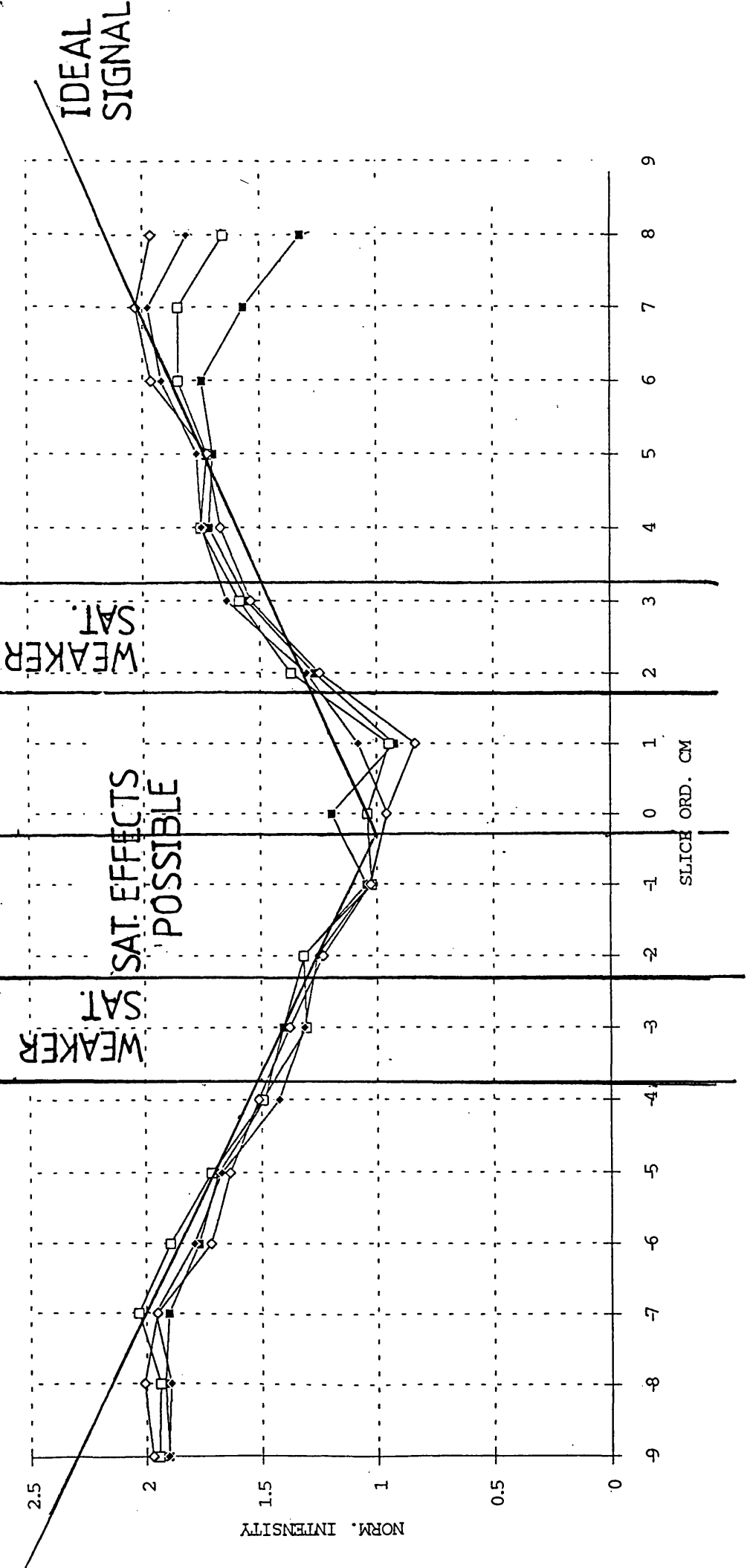
IDEAL SIGNAL

SAT. EFFECTS POSSIBLE

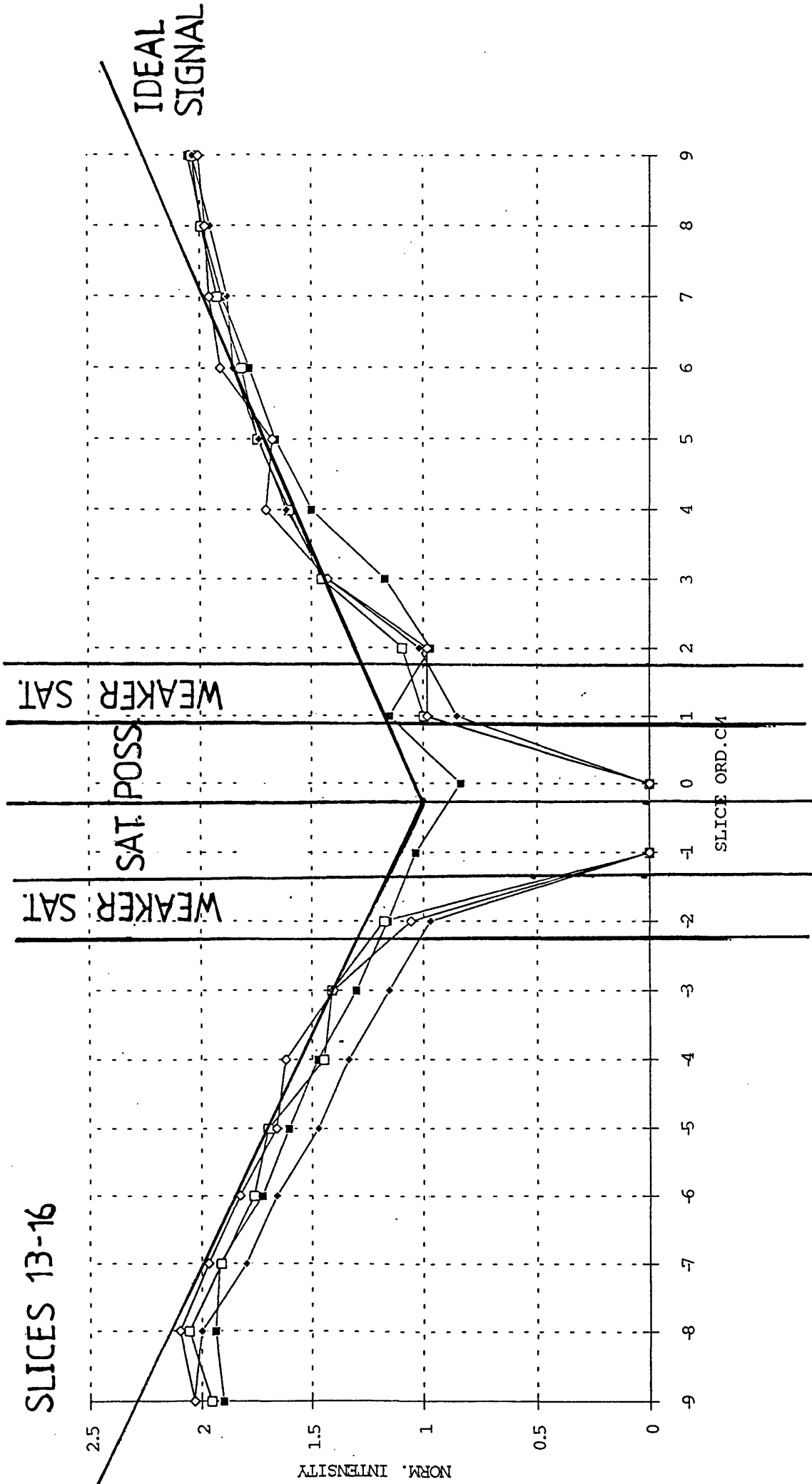
NORM. INTENSITY

SLICE ORD. CM

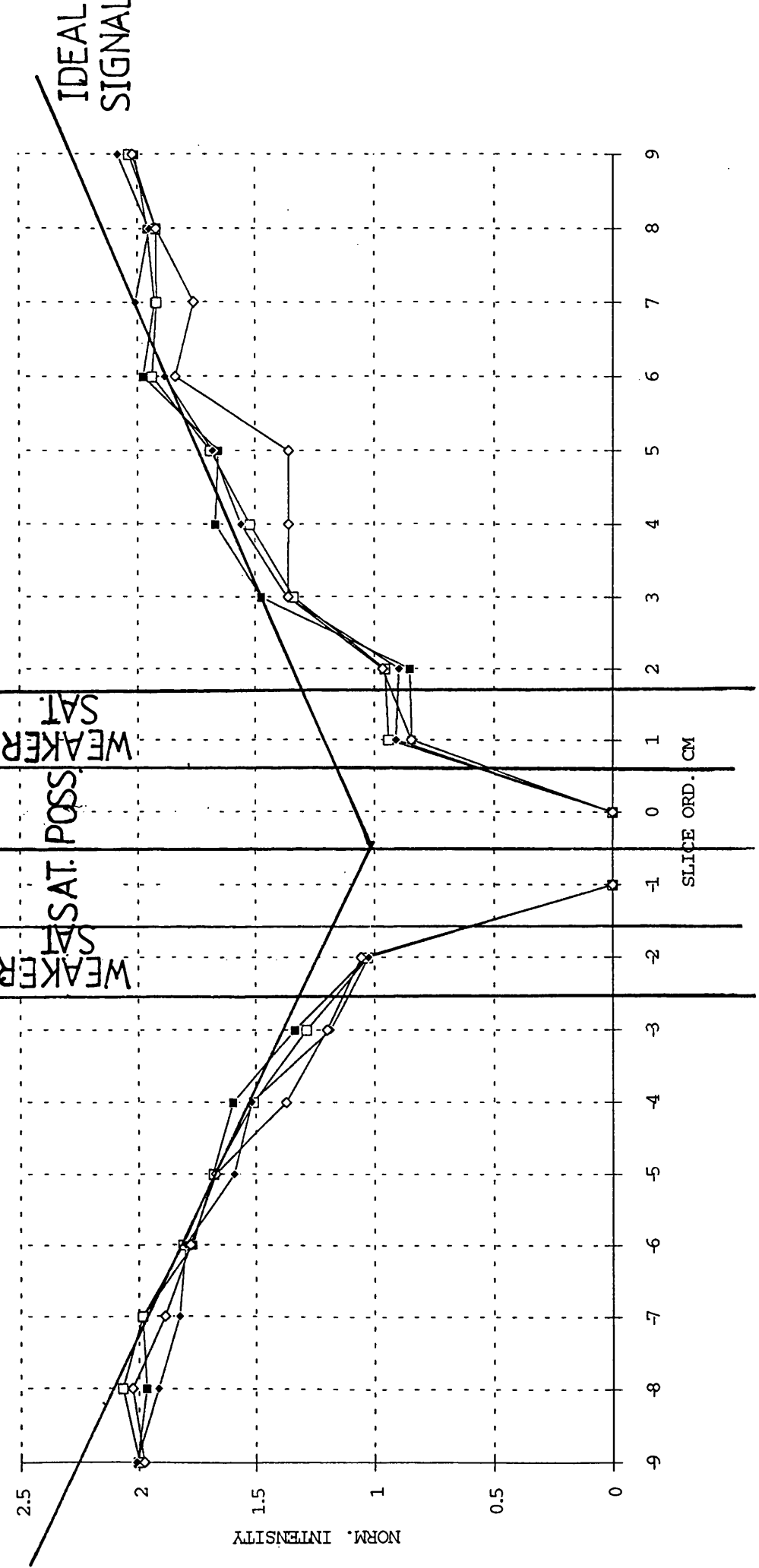
# SLICES 9-12



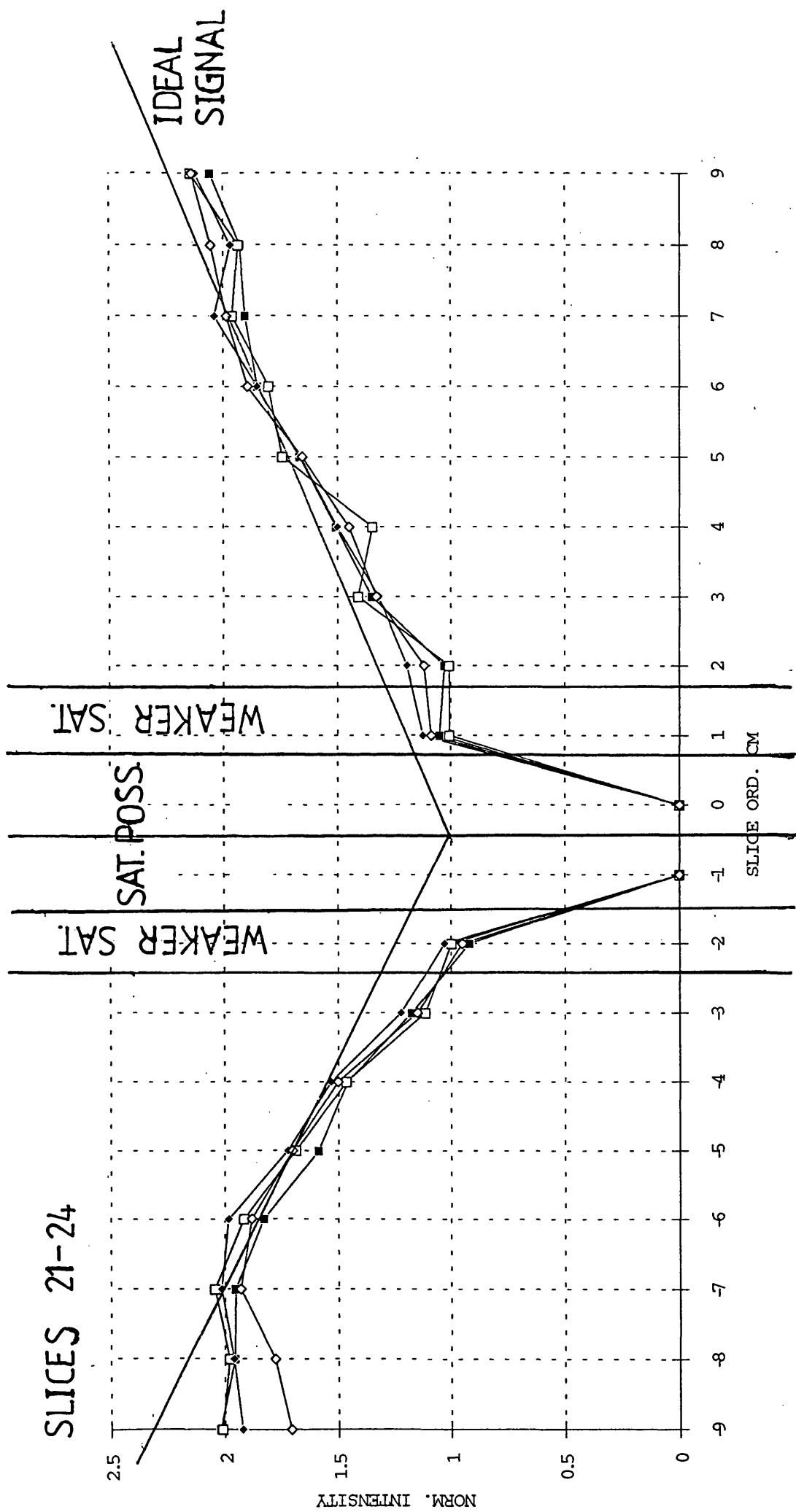
# SLICES 13-16



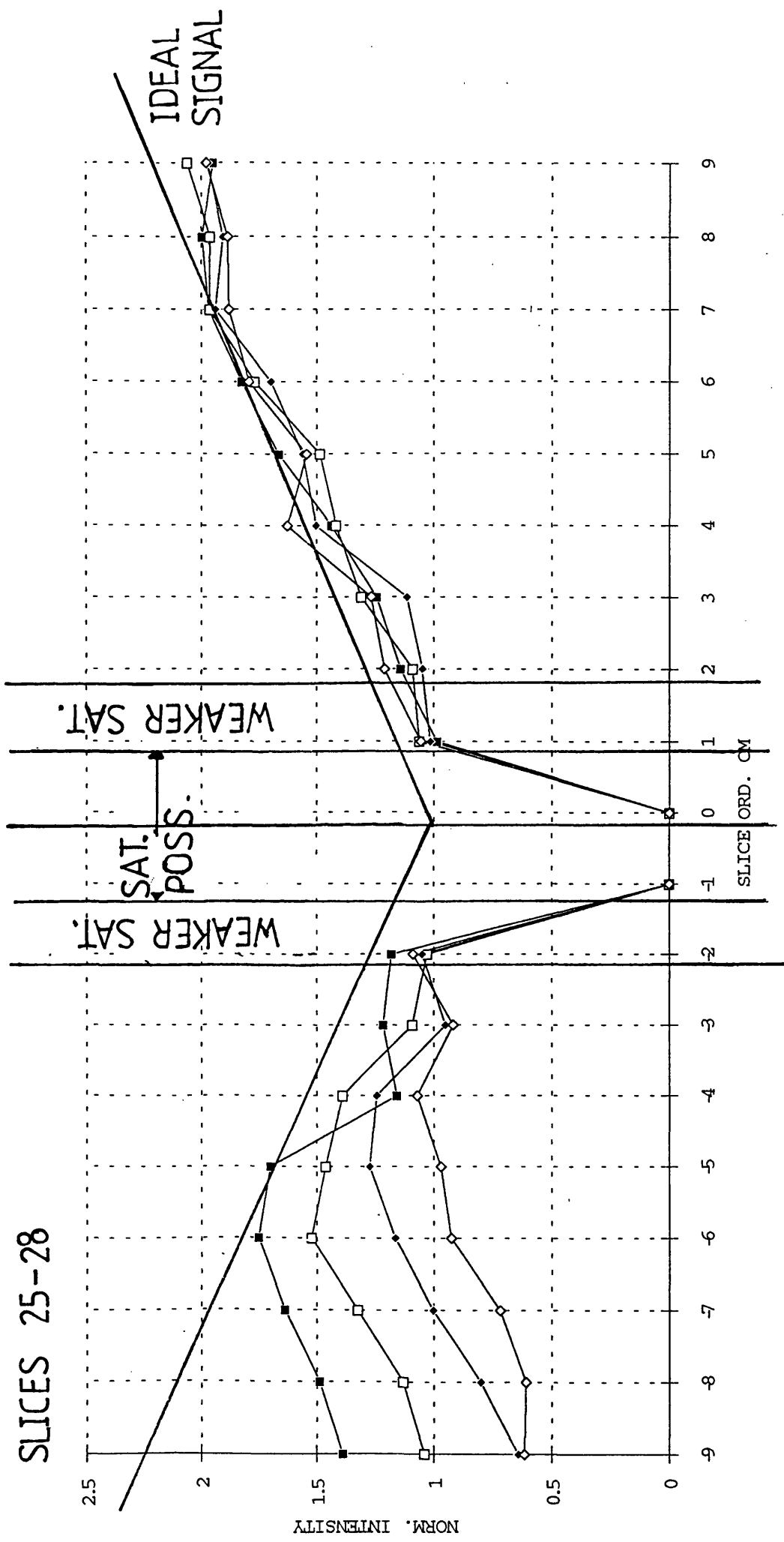
# SLICES 17-20



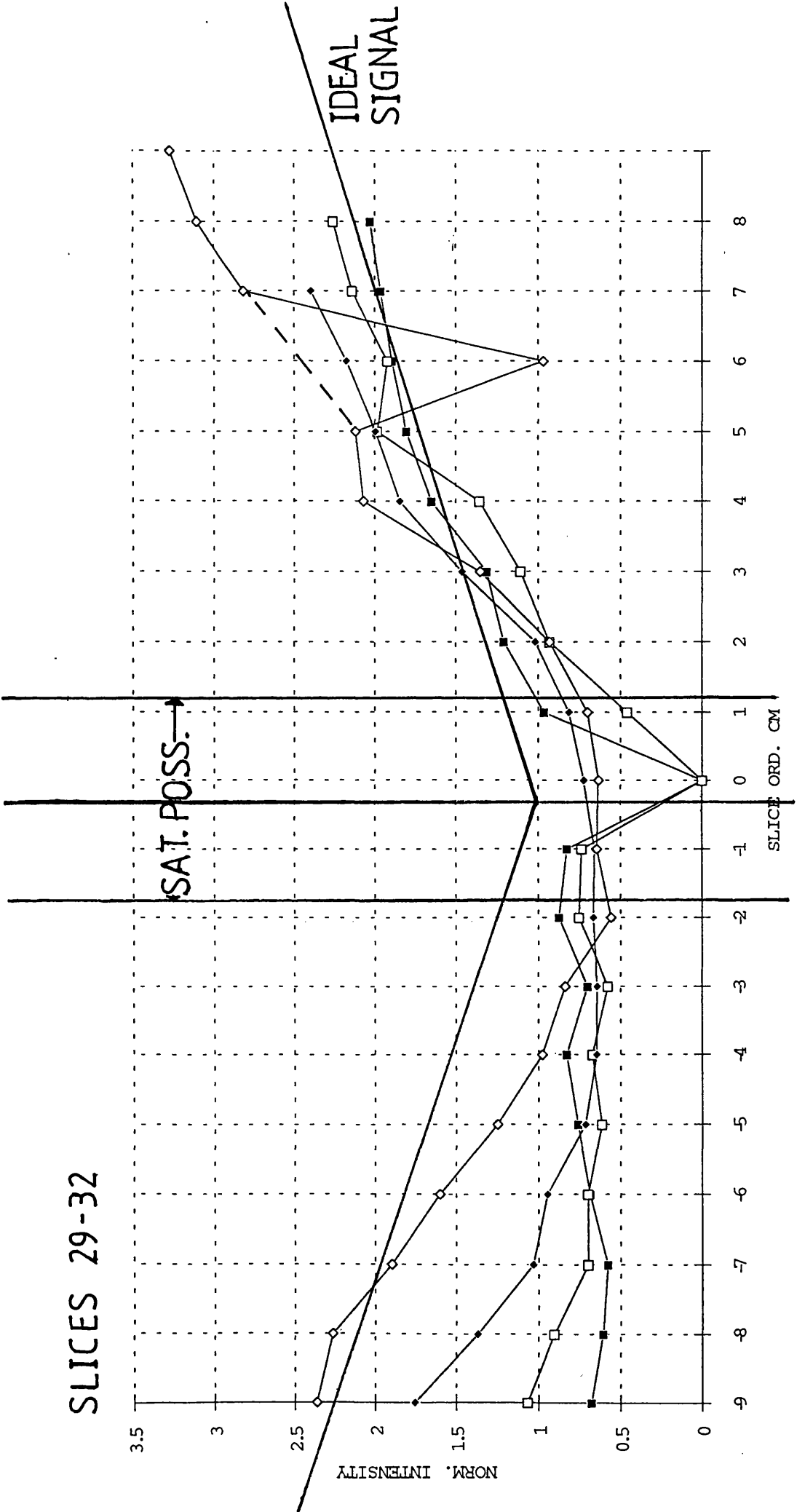
# SLICES 21-24



# SLICES 25-28



# SLICES 29-32



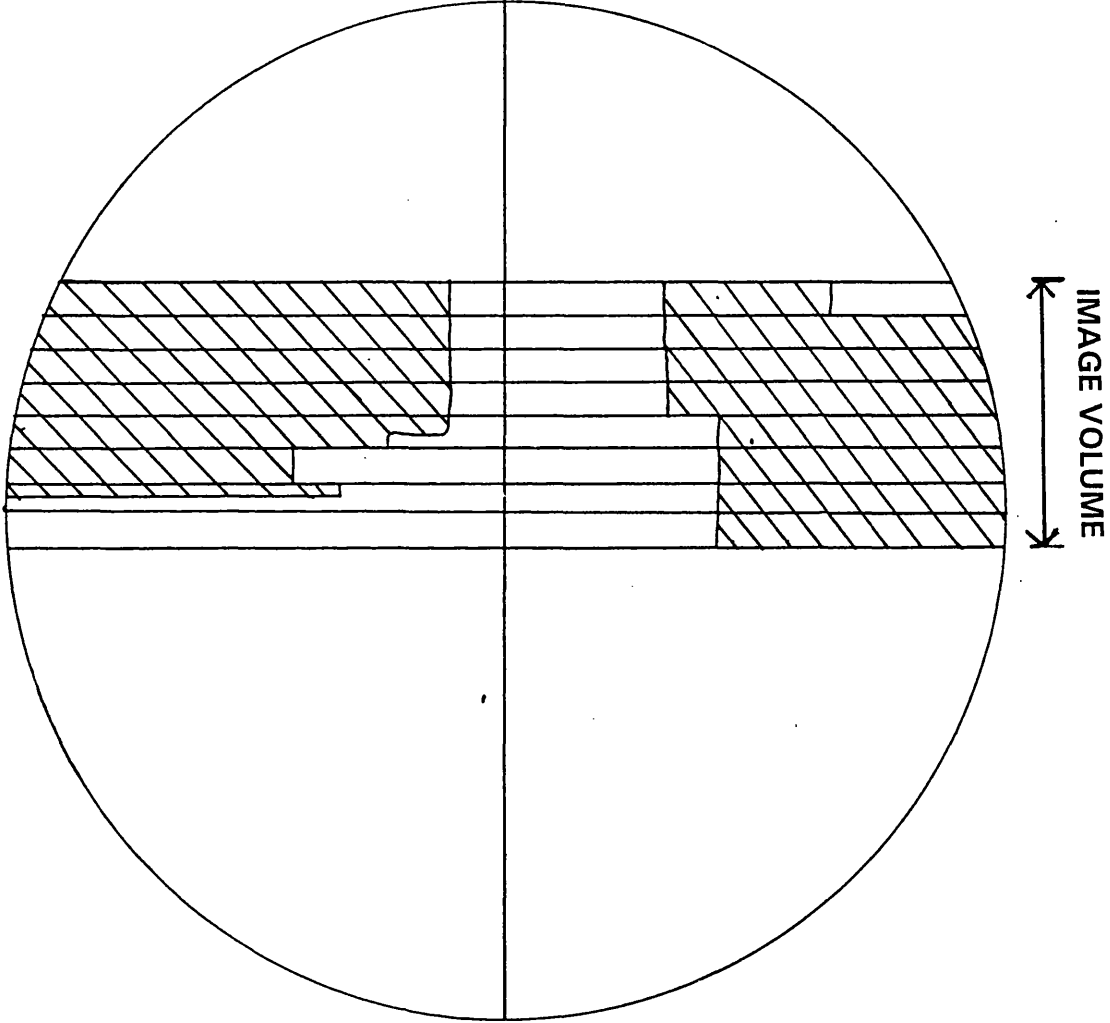
2D IMAGE SLICE INTENSITY PROFILES FOR THE SEQUENCE

FISP3D\_10rb108.ufa

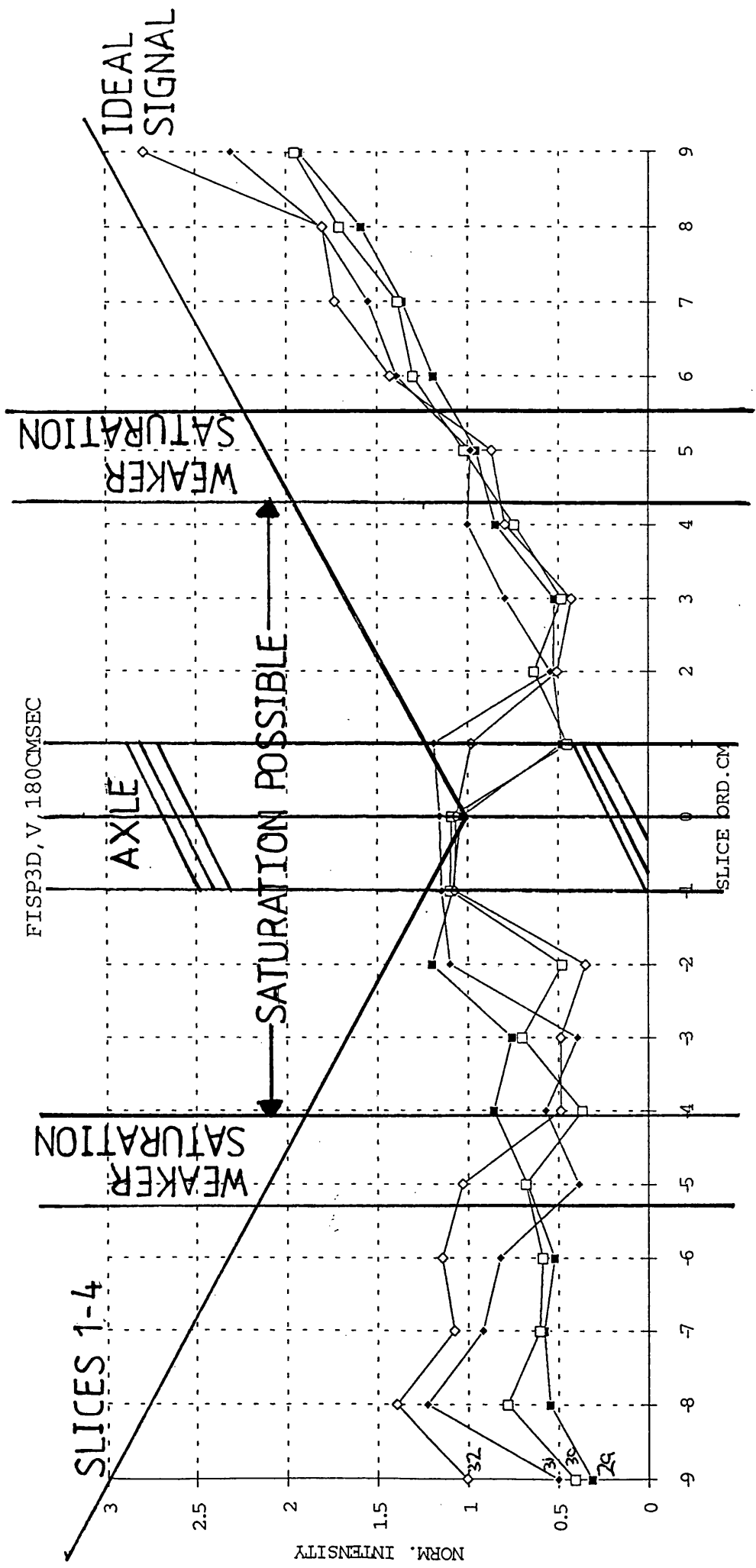
FA =  $40^{\circ}$   
TR=36msec  
TE=10msec

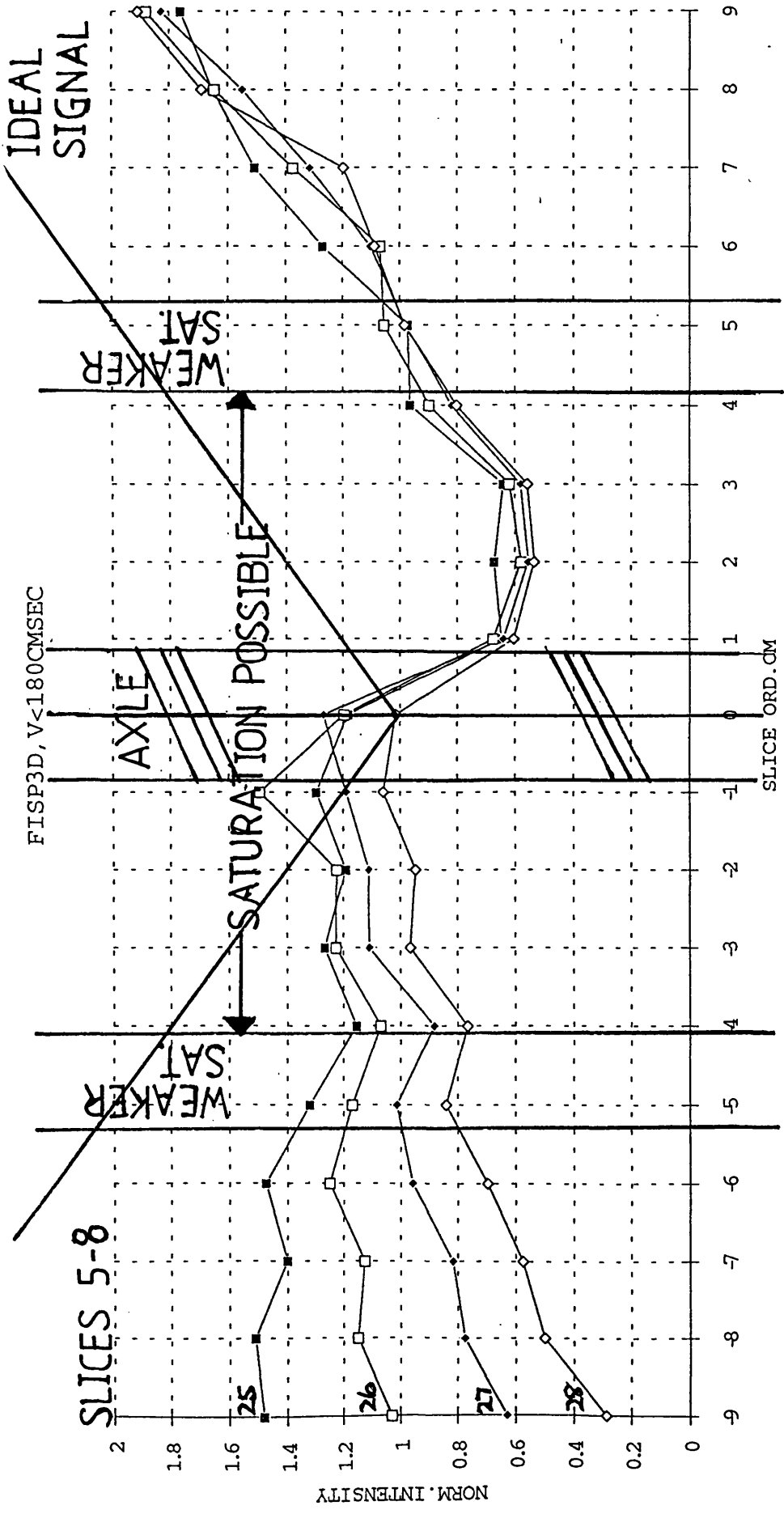
2D IMAGE SLICE PROFILES FOR THE SEQUENCE  
FISP3D\_10rb108.ufa

FA = 40°  
TR = 36msec  
TE = 10msec

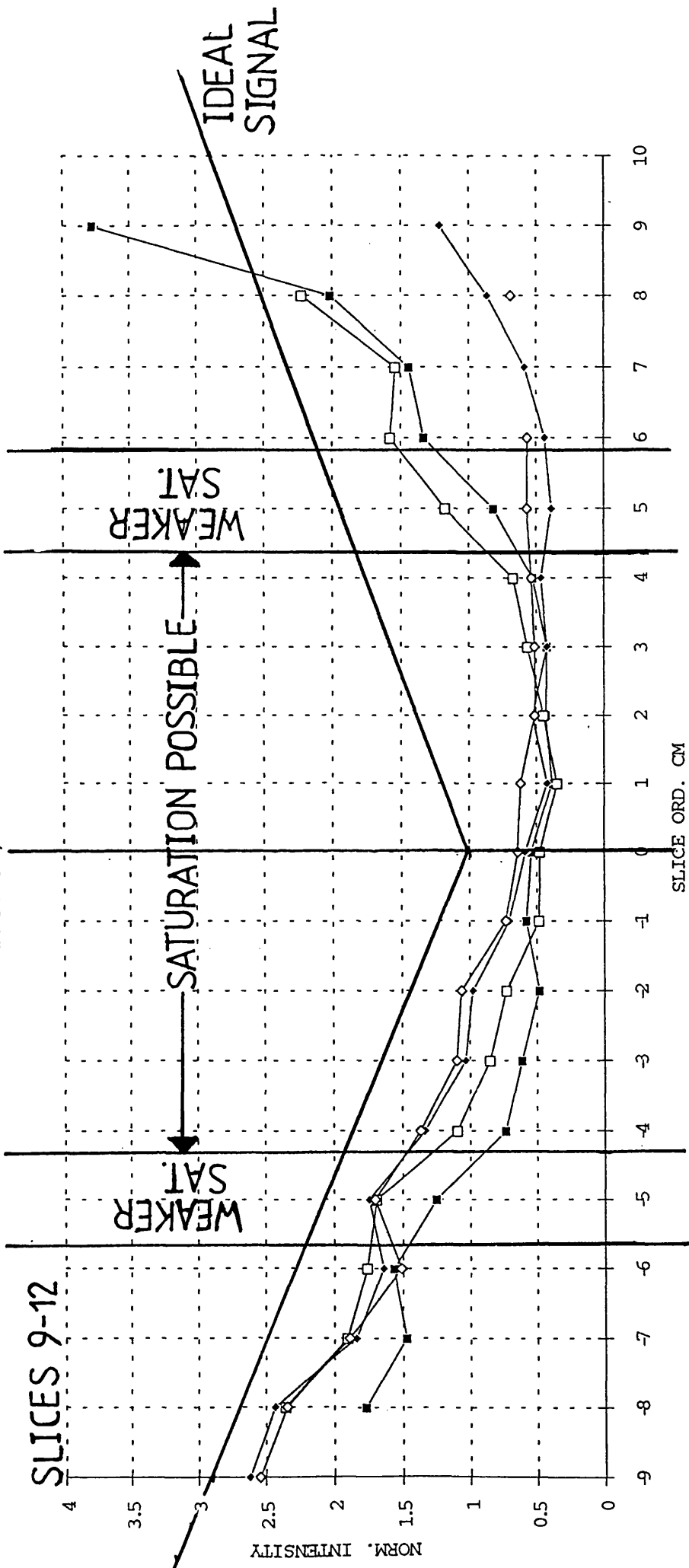


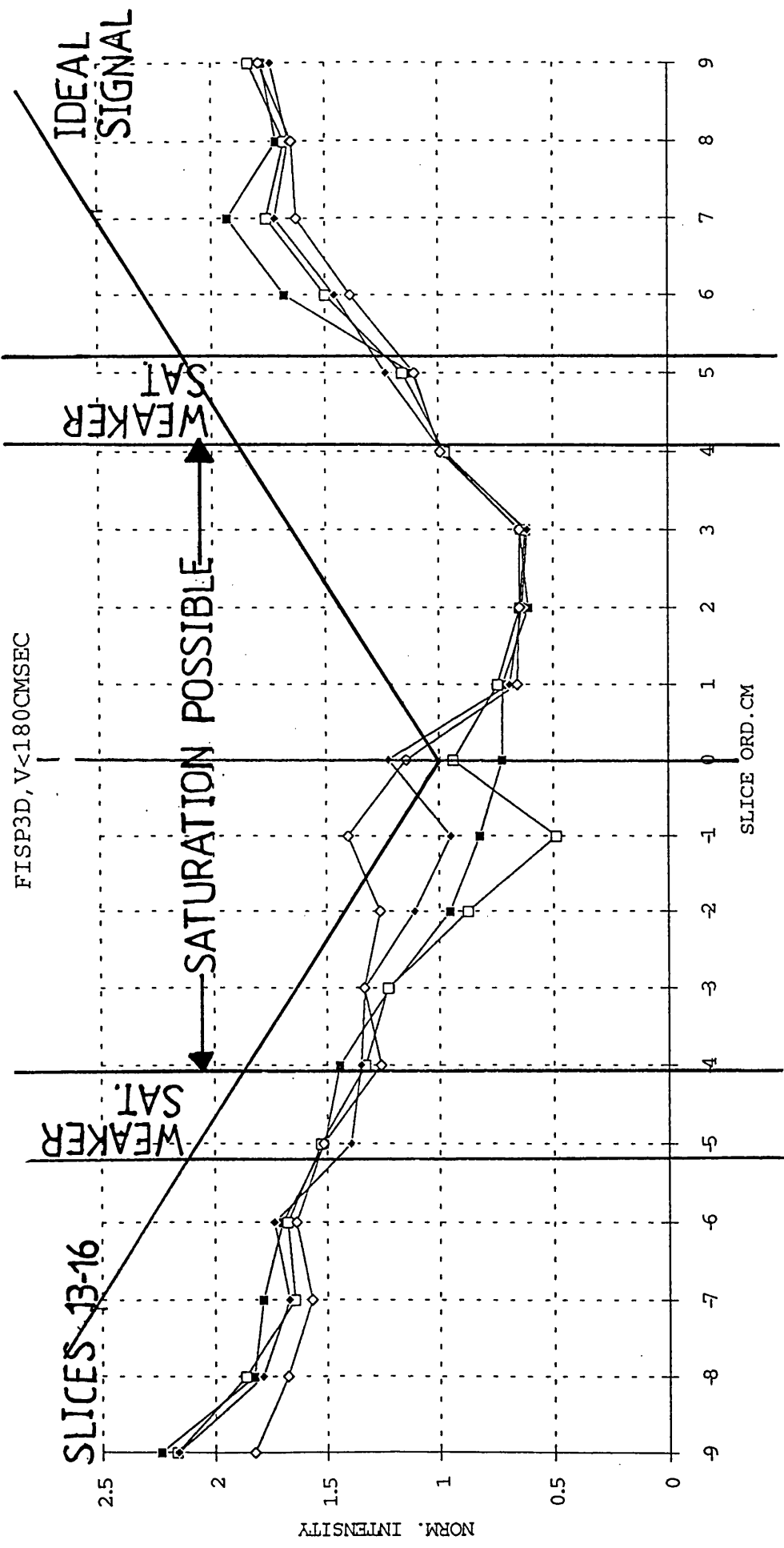
Regions of the image volume where the signal normalises to greater than or equal to unity are shown shaded.

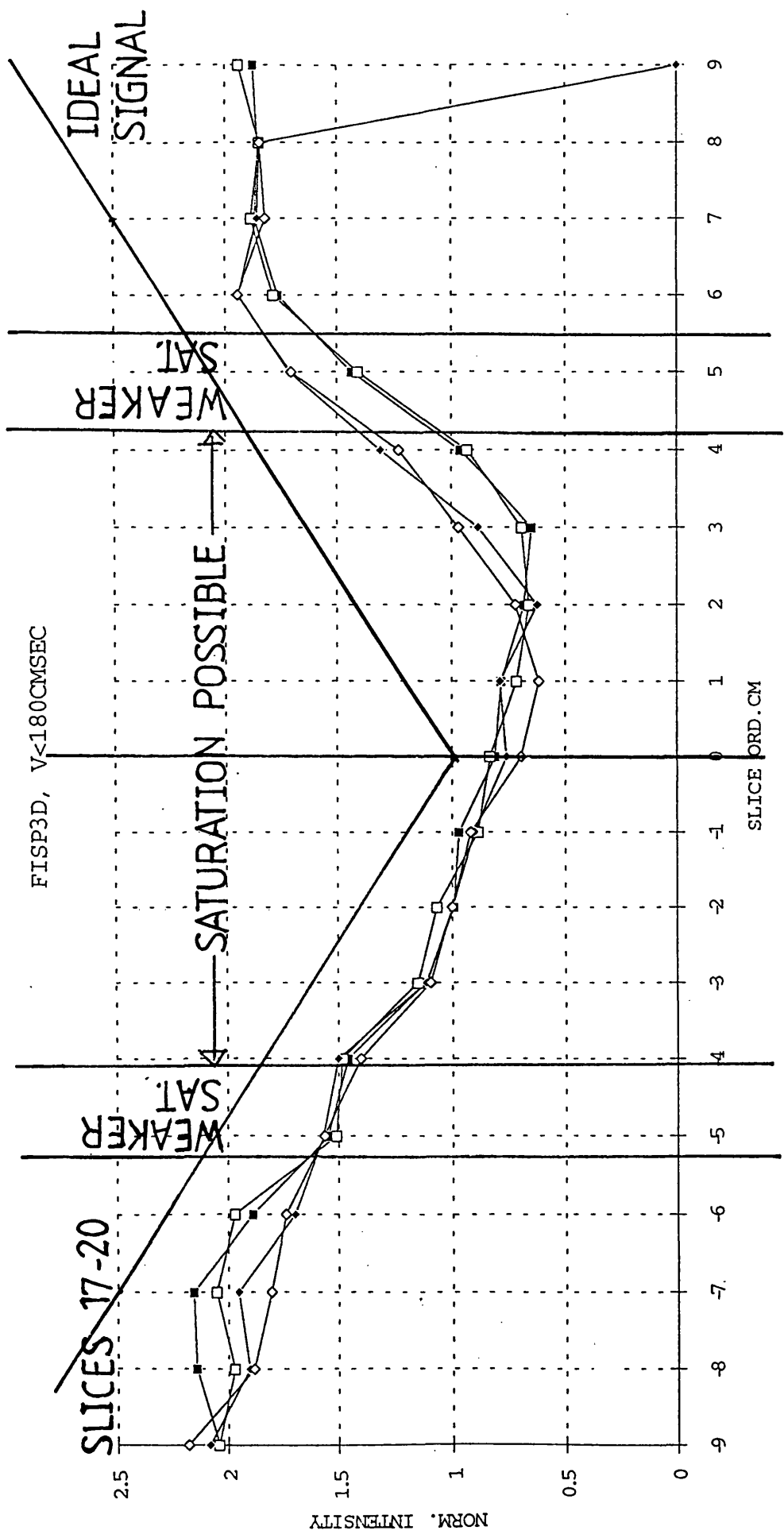


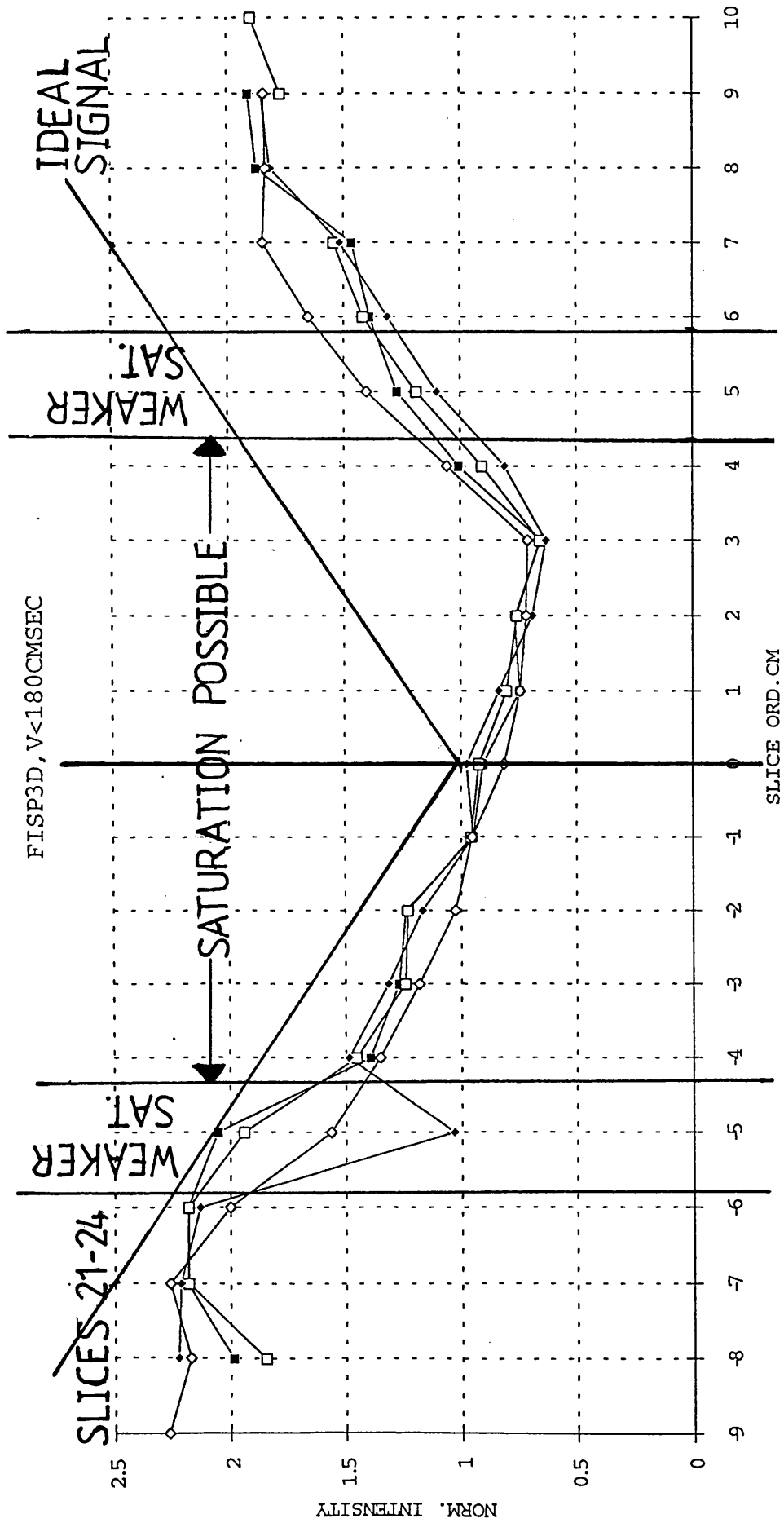


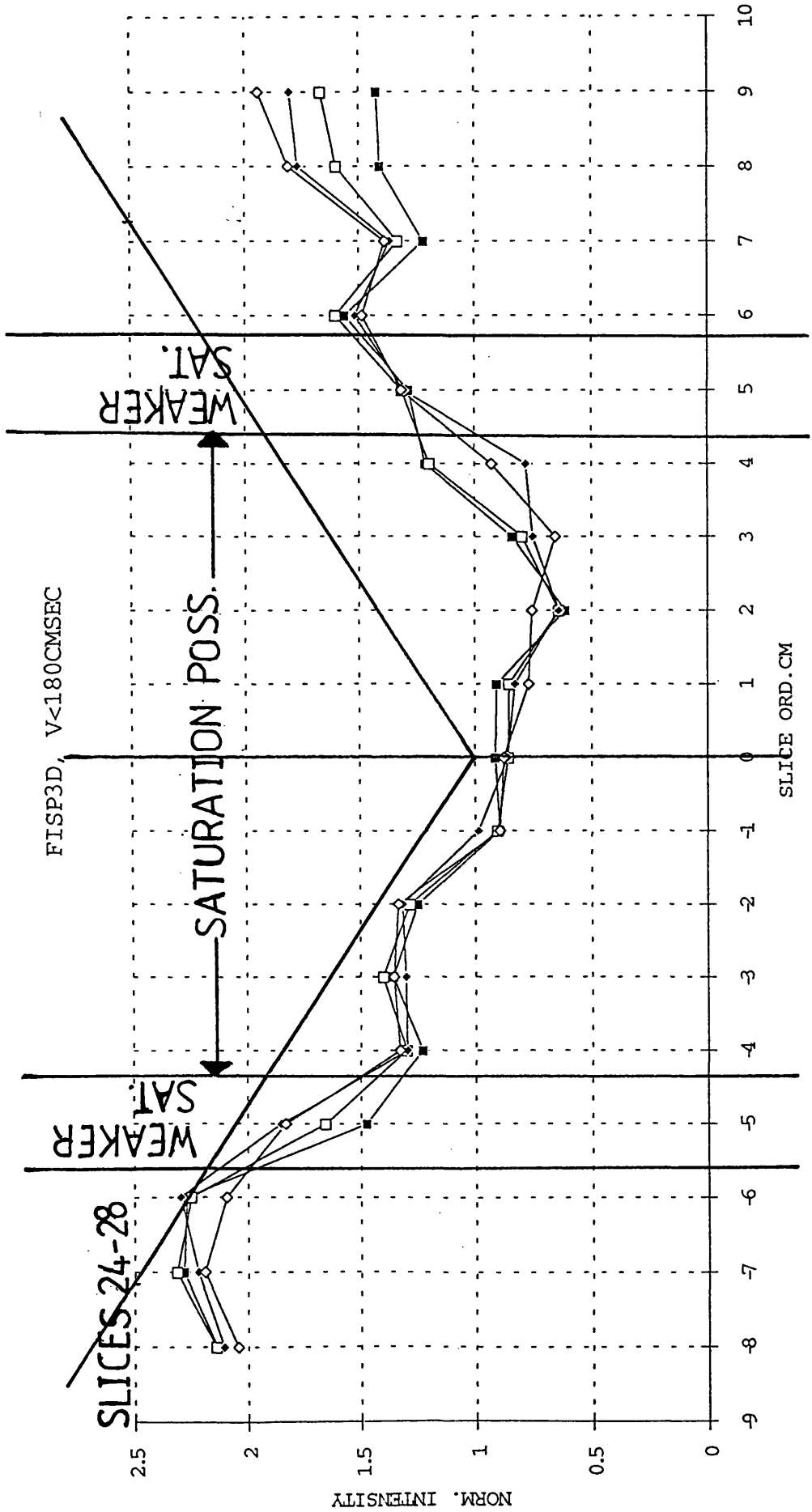
FISP 3D, V<180CMSEC

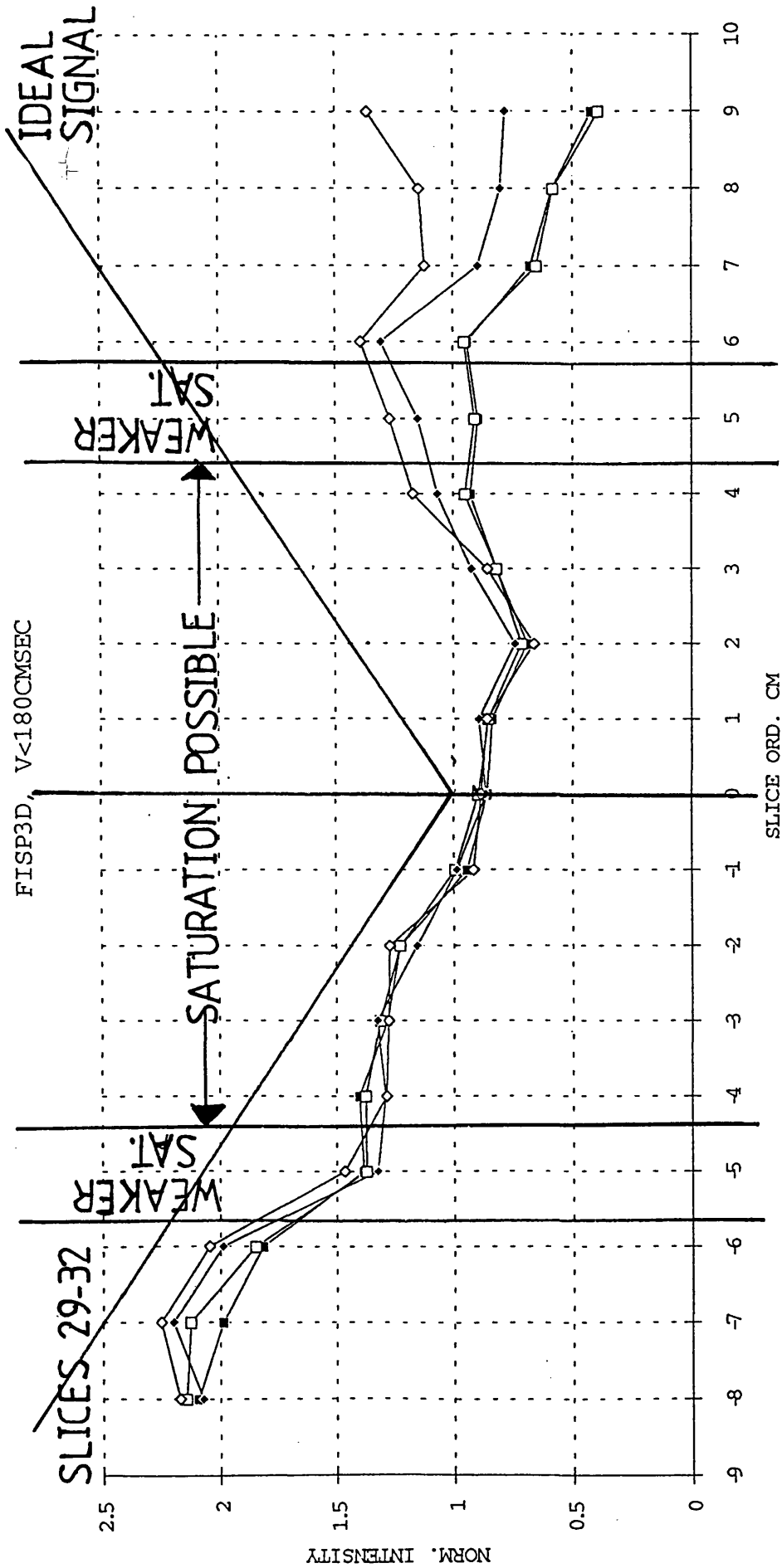












2D IMAGE SLICE INTENSITY PROFILES FOR THE SEQUENCE

FISP3D\_64\_6rb195.ufa

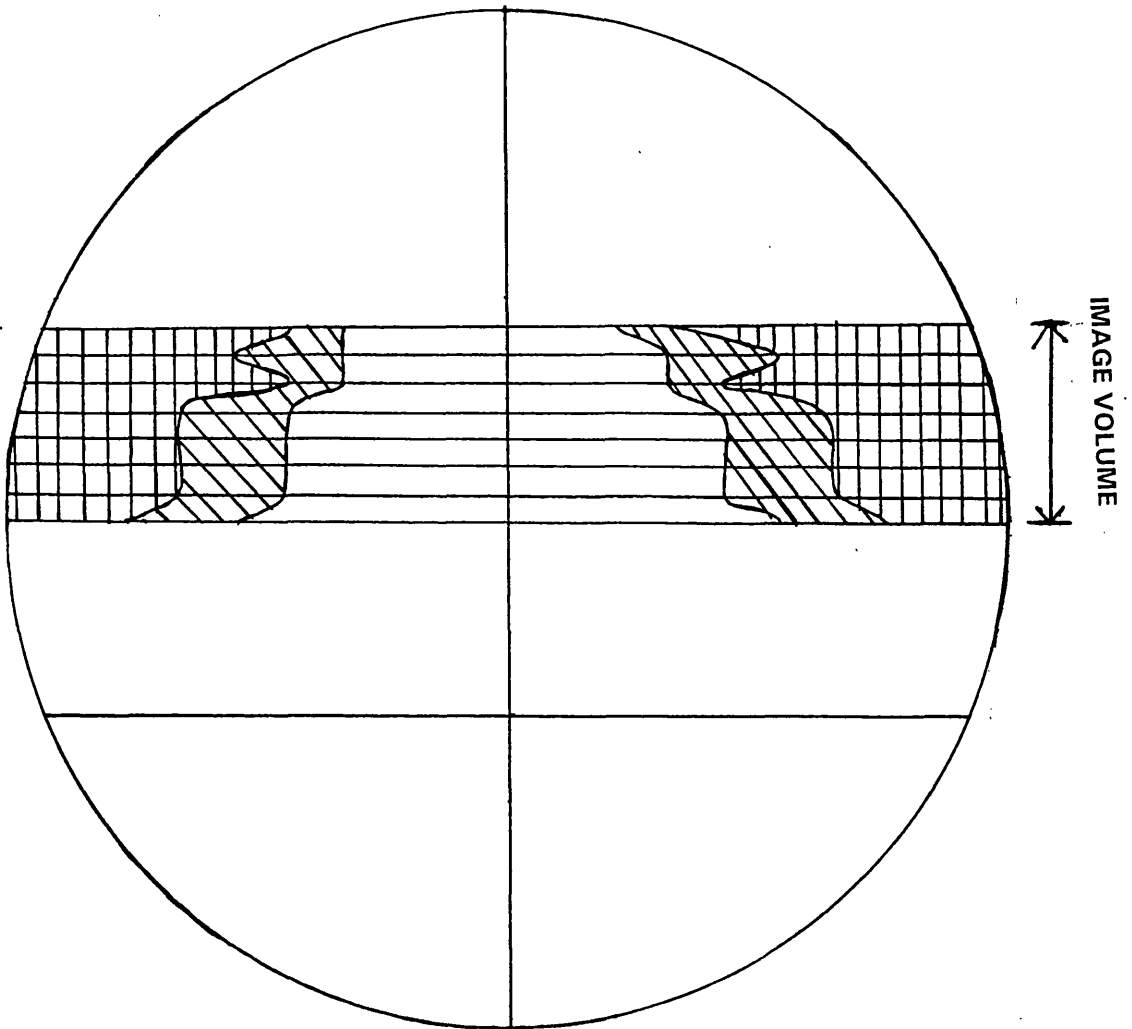
FA =  $15^{\circ}$

TR=36msec

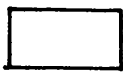
TE=6msec

STATIC FIELD = 1.5T

FISP 3D sequence for use at 1.5T, for velocities 30-70cmsec<sup>-1</sup>.  
FA = 15°, TR = 36msec, TE = 6msec.



The normalised signal for the whole of the scanned volume, illustrated here, shows



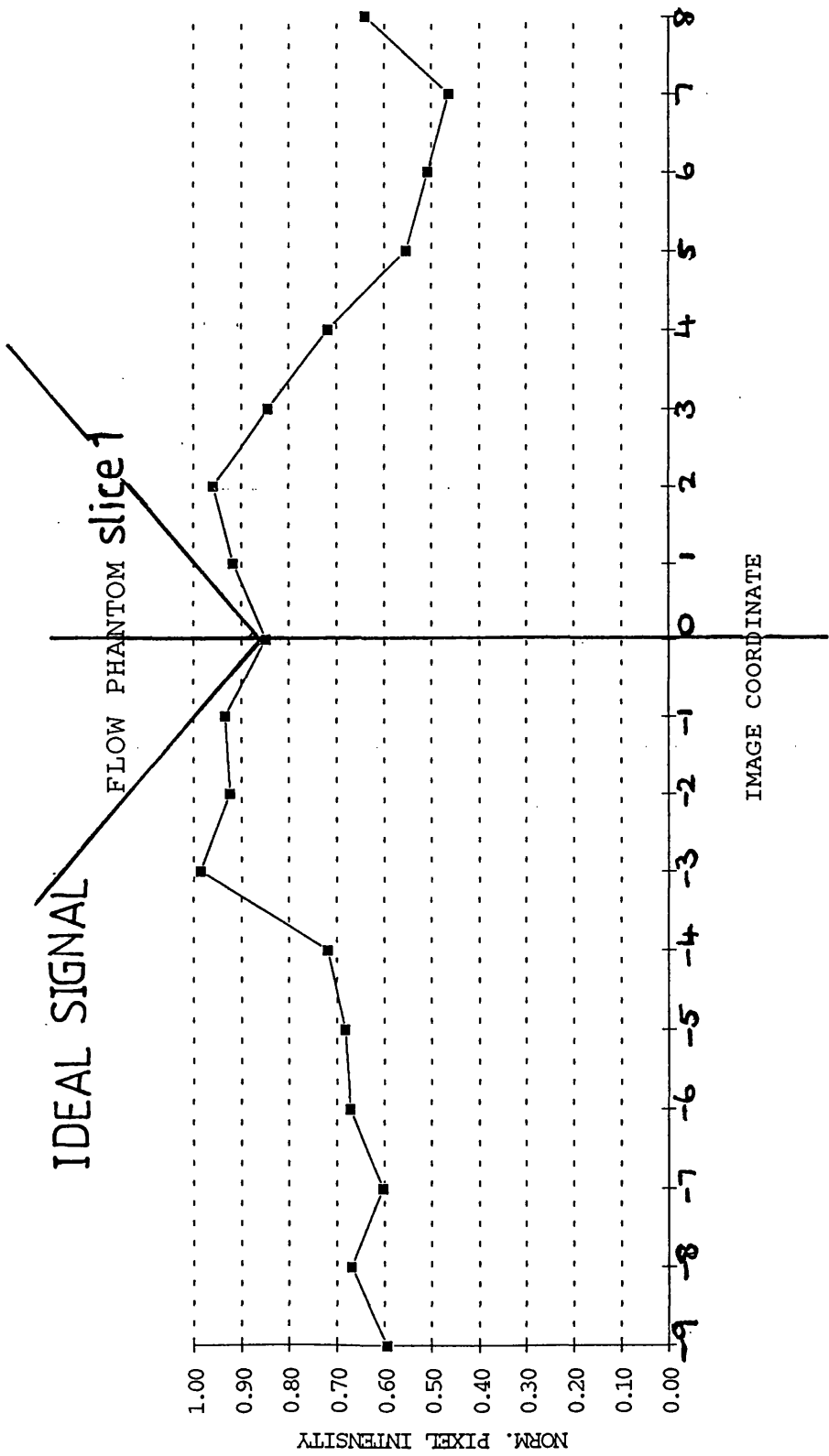
Signal is increasing with increase in imaged gel volume per unit slice area.

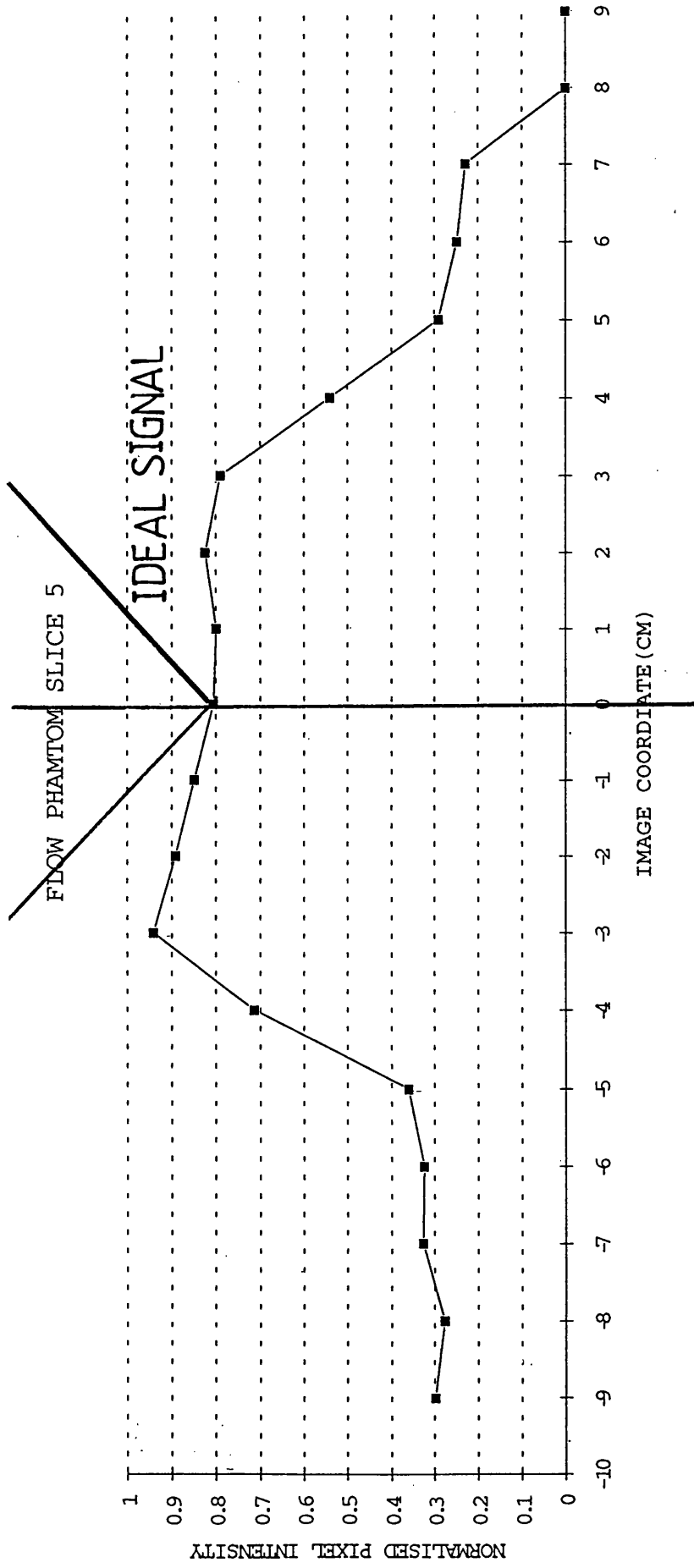


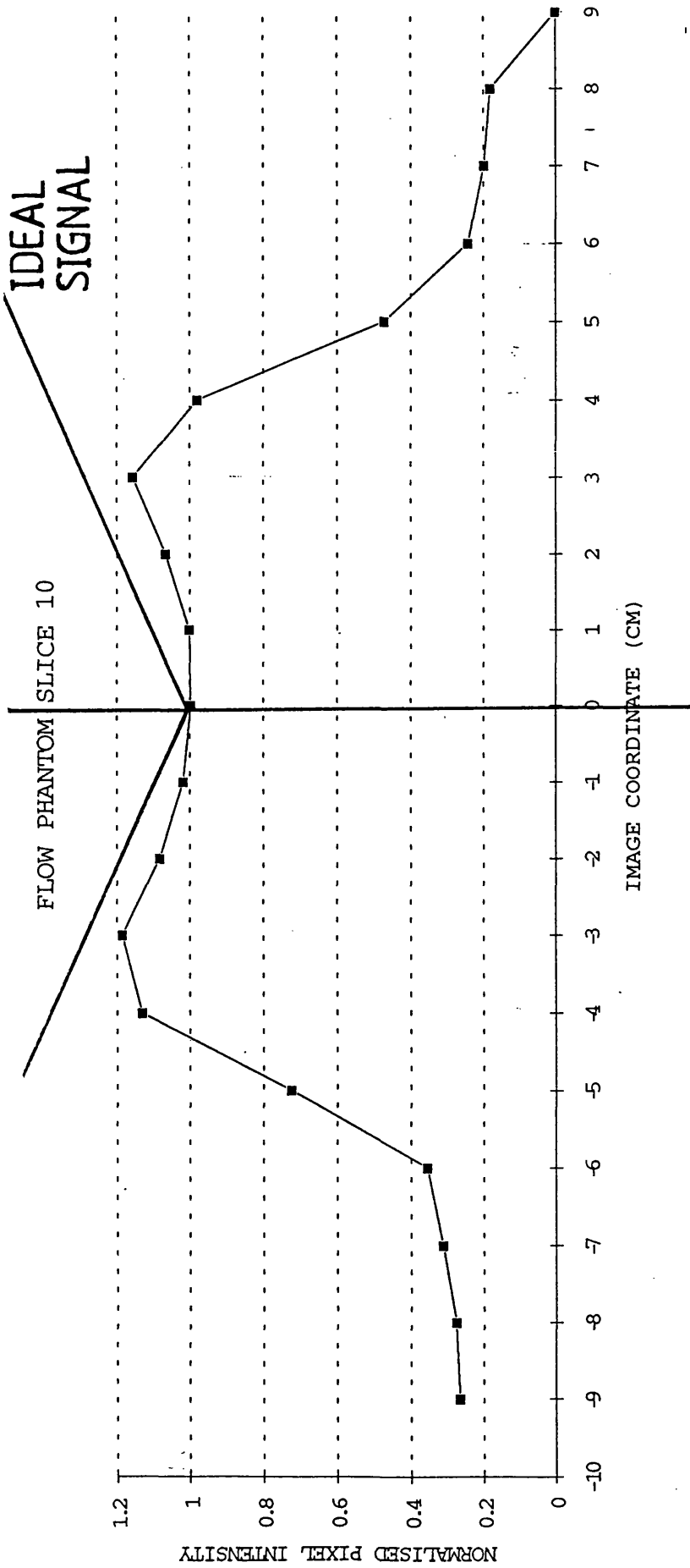
Signal is decreasing rapidly.

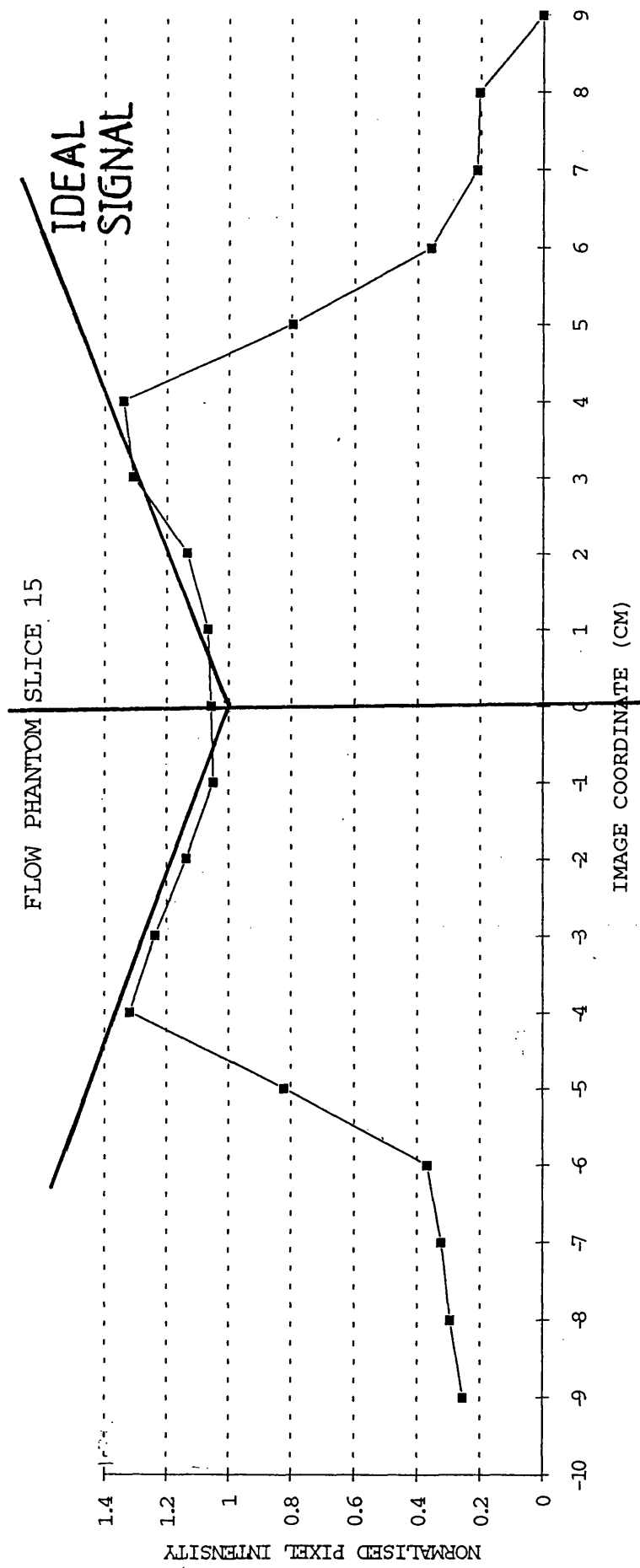


Signal approximates to background noise.

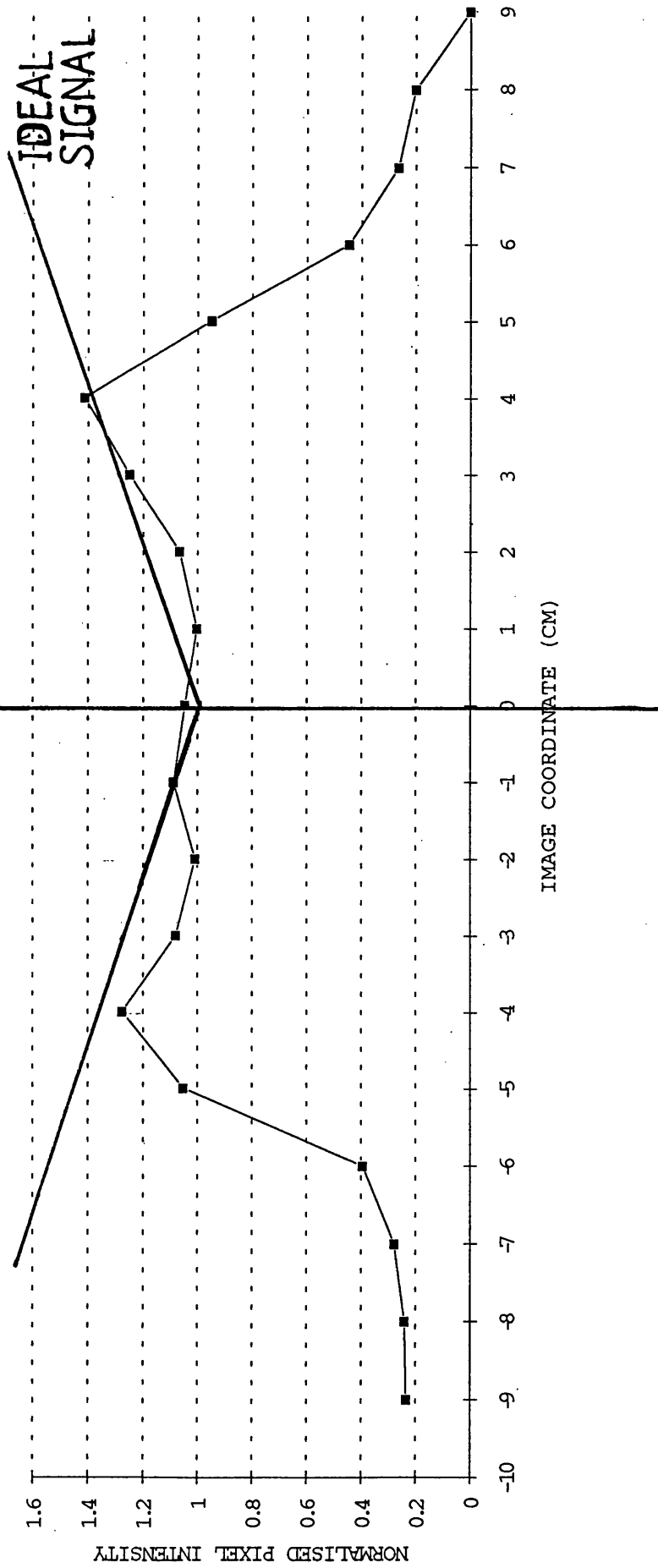




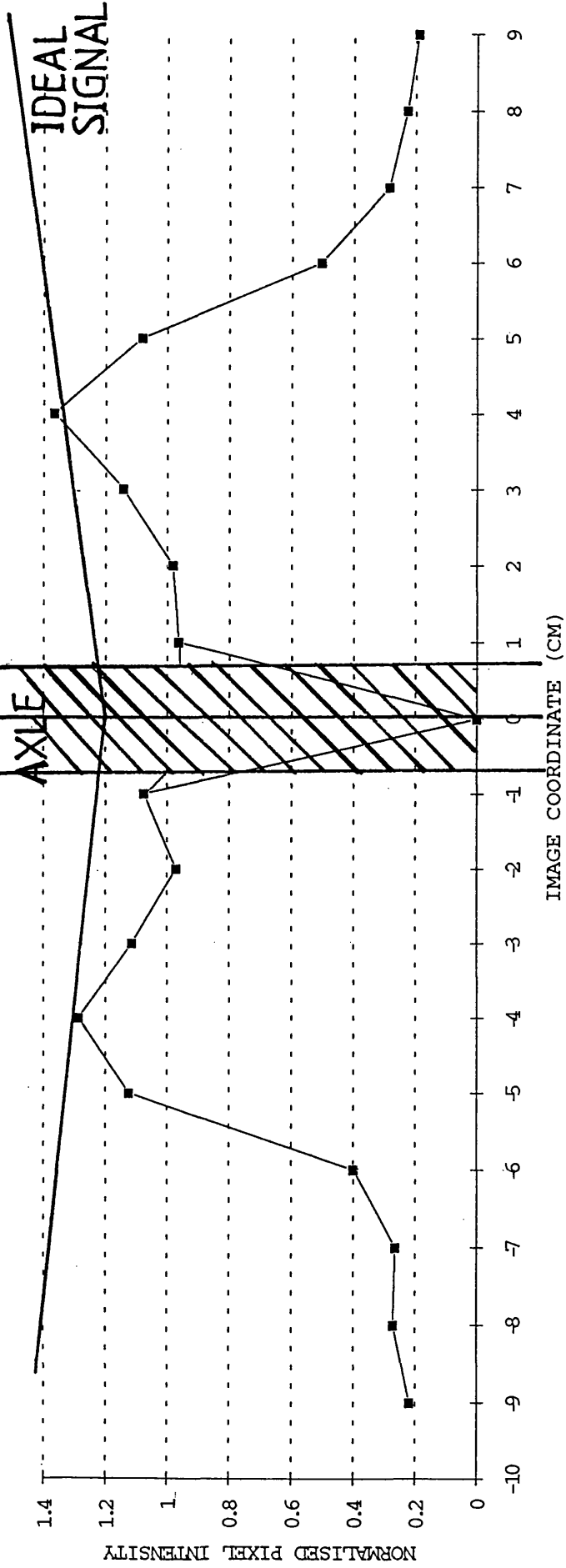


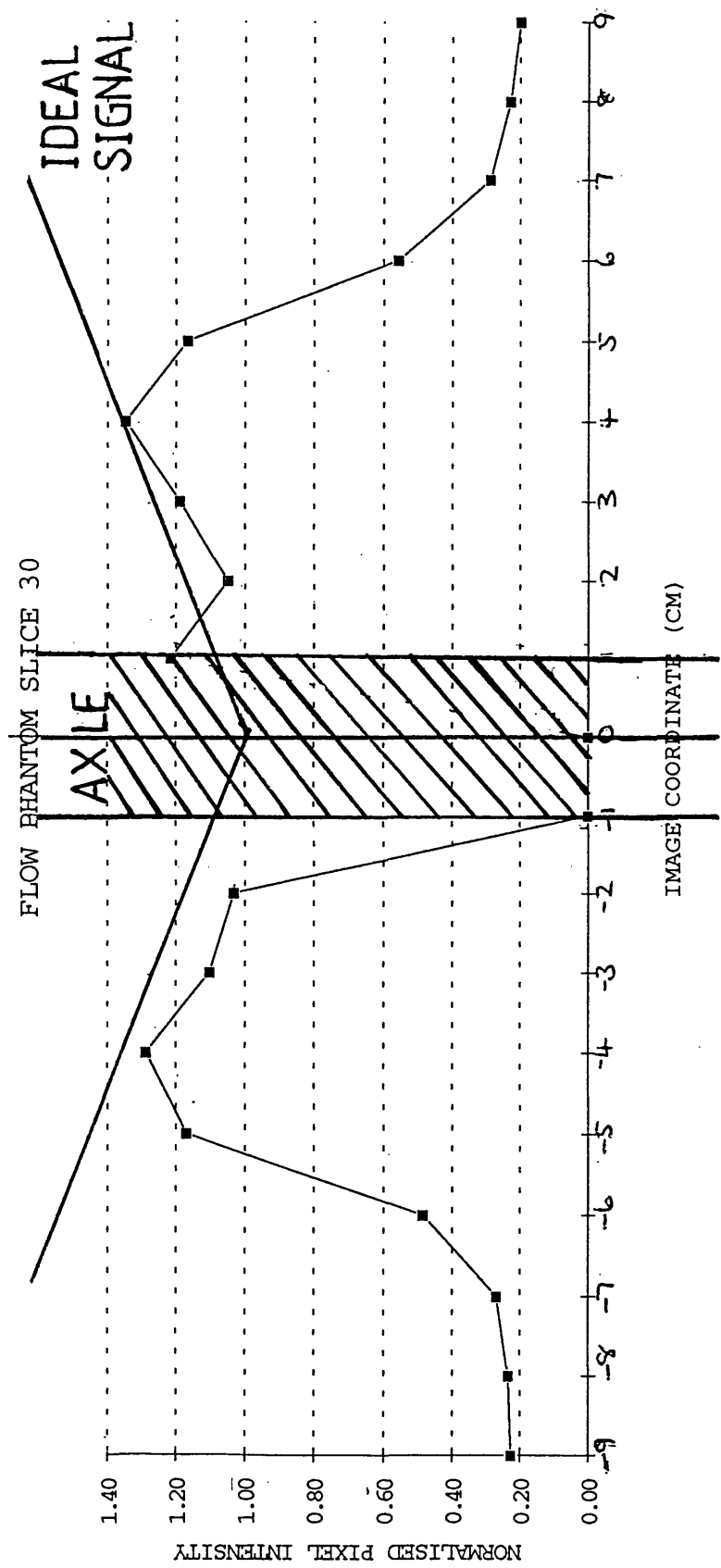


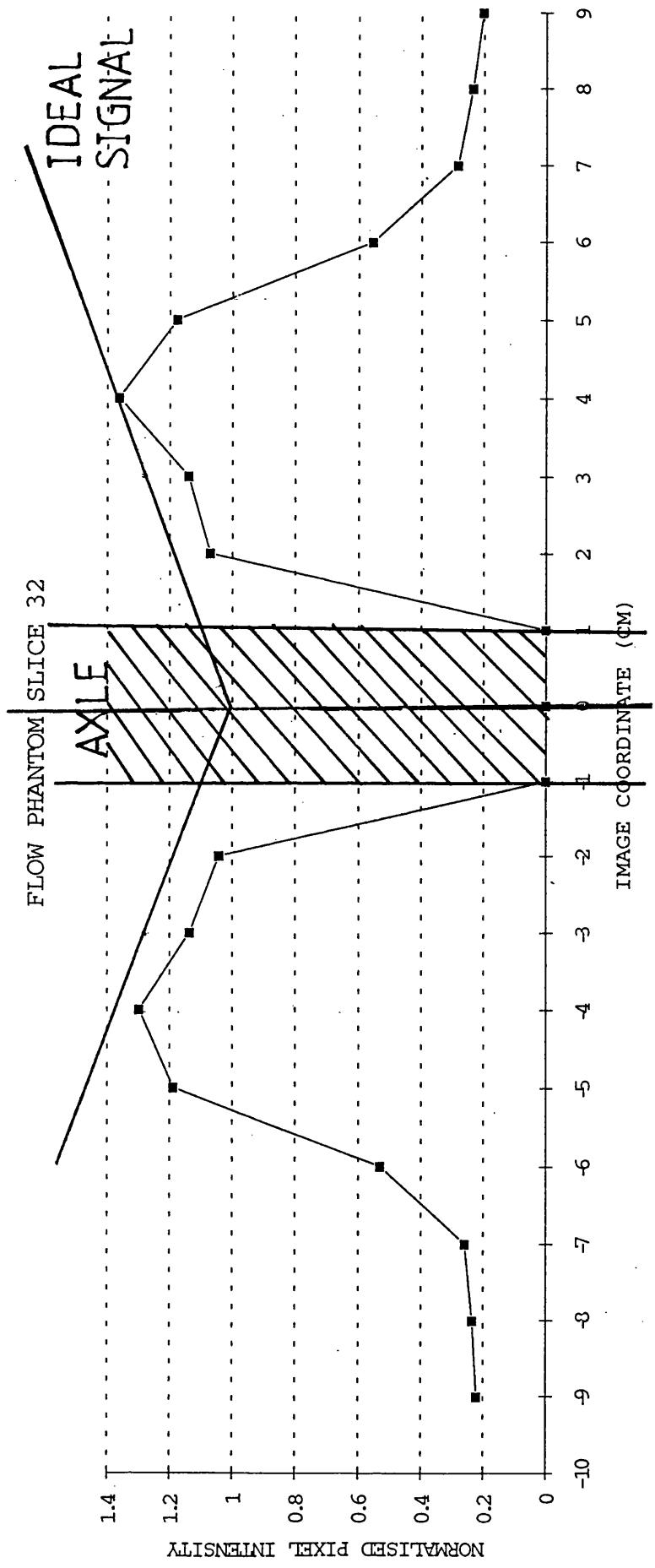
FLOW PHANTOM SLICE 20



FLOW PHANTOM SLICE 25





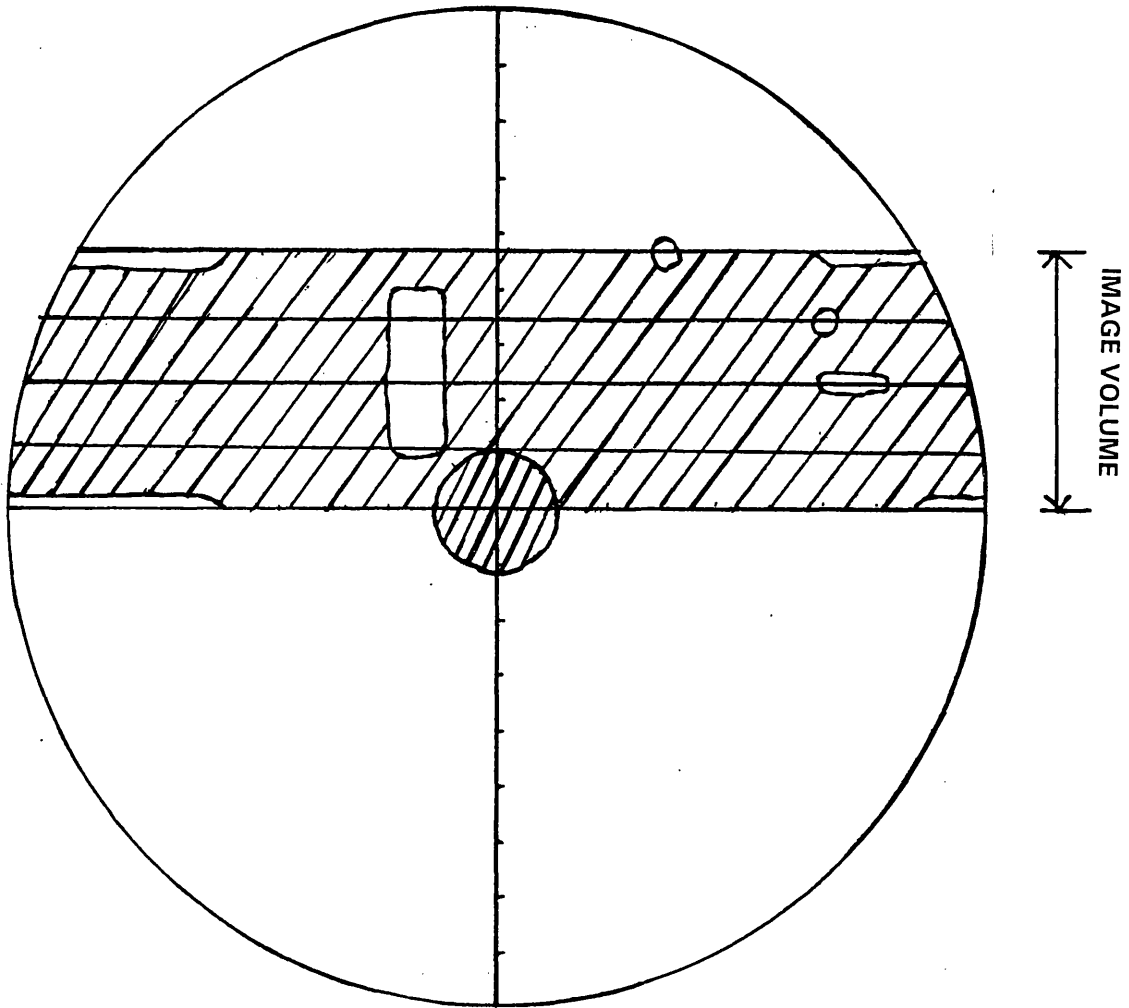


2D IMAGE SLICE INTENSITY PROFILES FOR THE SEQUENCE

REPHASE-DEPHASE FISP3D\_14rdb108.wfa

FA =  $15^{\circ}$   
TR=50msec  
TE=14/14msec

REPHASE-DEPHASE sequence for velocities of  $30\text{-}45\text{cmsec}^{-1}$   
FA =  $15^\circ$ , TR = 50msec, TE = 14msec.

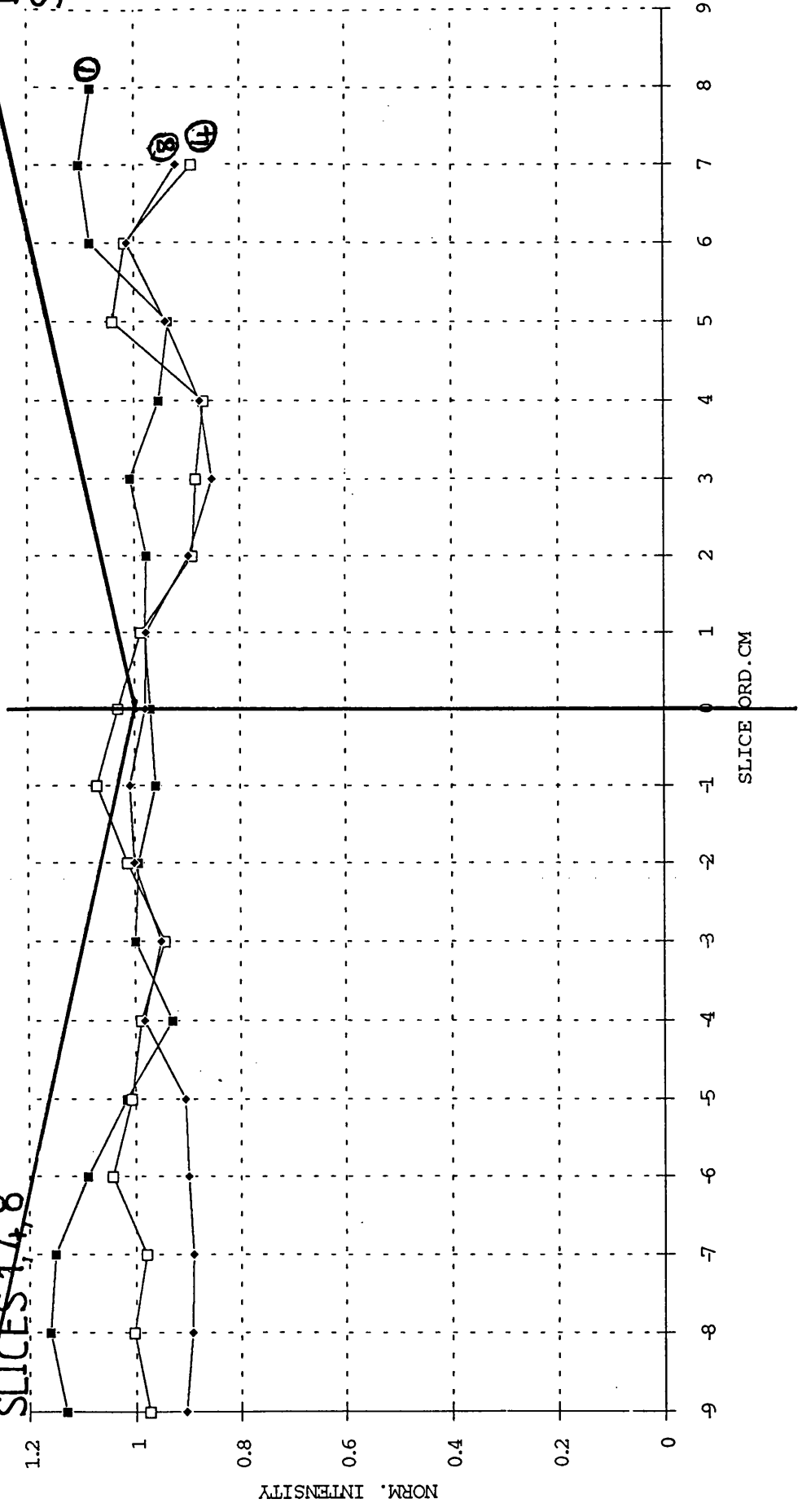


Regions of the total scanned image volume where the signal normalises to values greater than or equal to unity is shown shaded.

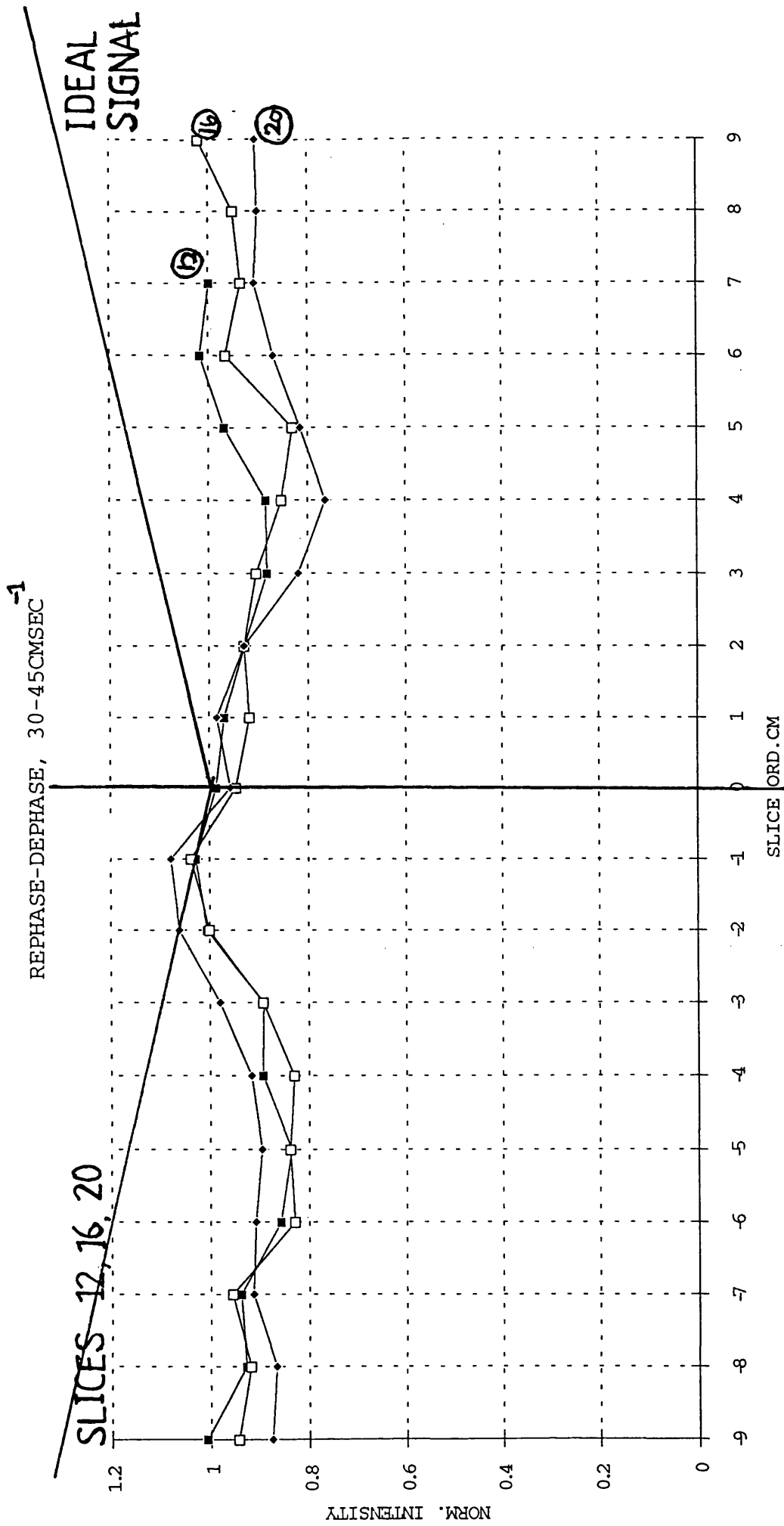
REPHASE-DEPHASE, 30-45CMSEC<sup>-1</sup>

IDEAL SIGNAL

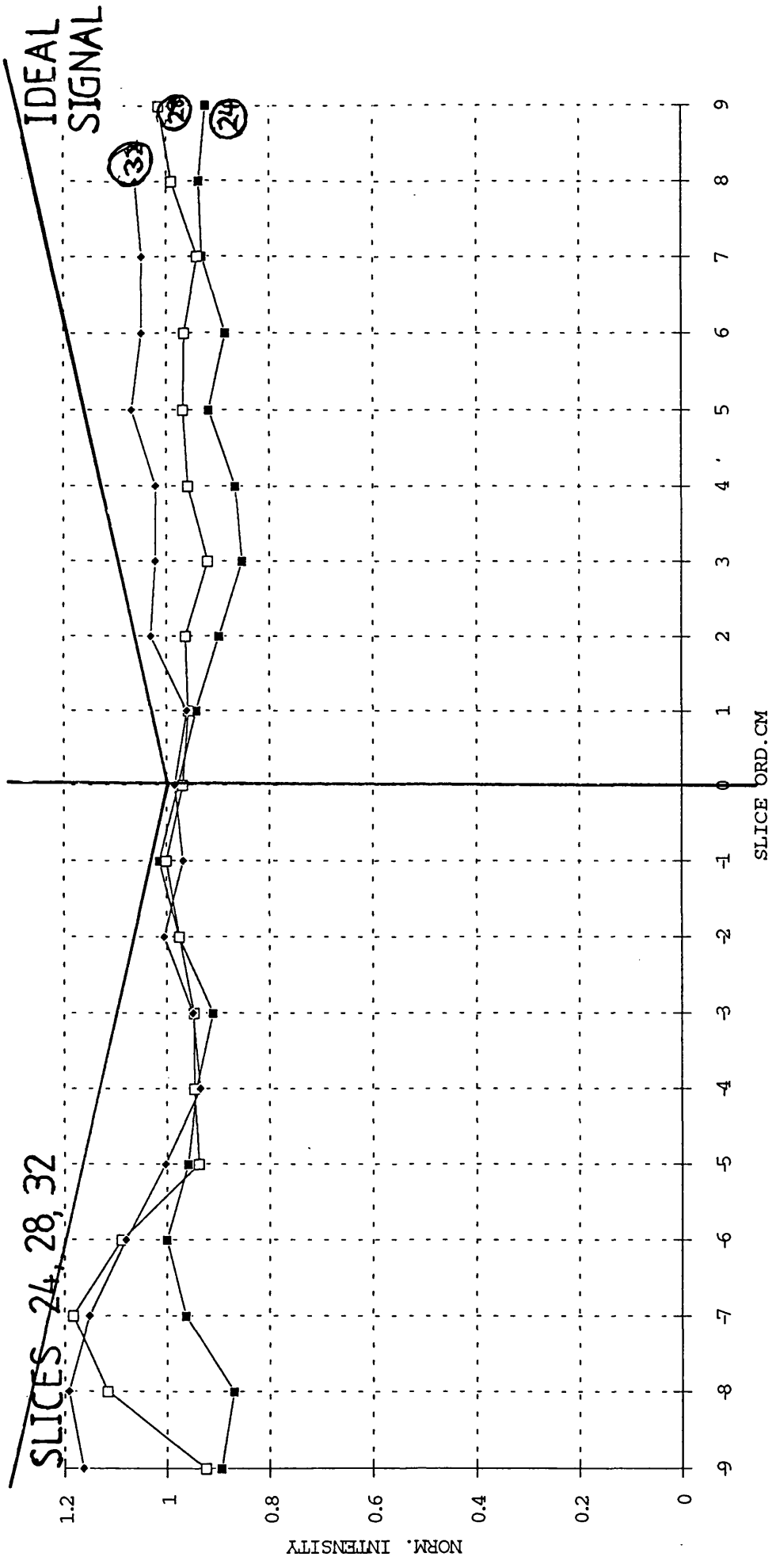
~~SLICES 1, 4, 8~~



①  
③  
④



REPHASE-DEPHASE, 30-45CMSEC<sup>-1</sup>



SLICES 24, 28, 32

IDEAL SIGNAL

## 2D IMAGE SLICE INTENSITY PROFILES FOR THE SEQUENCE

FLASH2D\_s\_10rb78.ufa

FA = 40°

TR=39msec

TE=10msec

STATIC FIELD = 1.0T

These image slice intensity profiles have been obtained by manually sampling the pixel intensity at an operator selected range of intervals across the slice, each approximately three pixels wide. Since the location of the minima is specific, and since the change in intensity at the minima is rapid, without graduation through shades of grey, they can be mapped accurately. The narrowness of the sampling area also ensures that measurement in the bright areas is not reduced by averaging bright pixels with dark pixels.

This has enabled the trend in pixel intensities from the centre of the drum to be established. The intensity at the dark bars which produce signal minima at fairly well defined locations along the length of the slice can be found by the same method. The graphed data presented here shows the trend in intensity which slowly increases from the centre of the drum is shown for all slices, and also the magnitude and location of the intensity minima.

A detailed explanation is presented in chapter 9 for the presence of the dark bar artefacts seen in these profiles.

2D IMAGE SLICE INTENSITY PROFILES FOR THE SEQUENCE

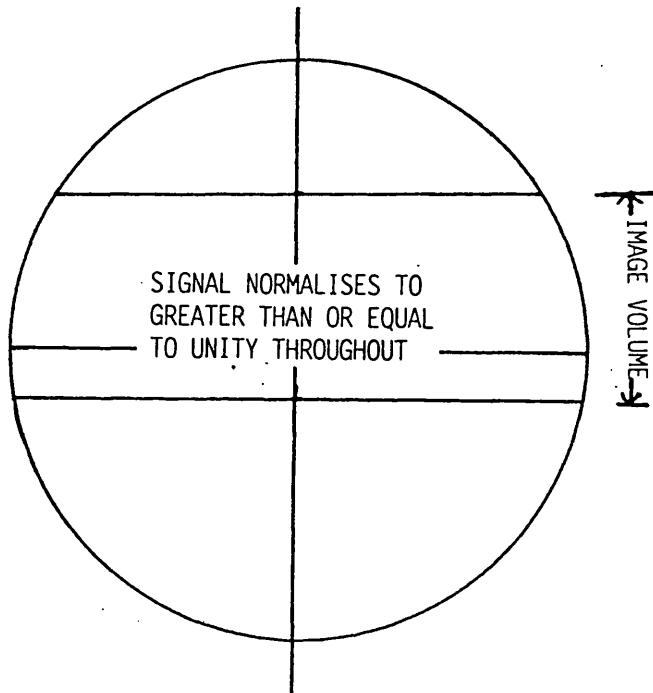
FLASH2D\_s\_10rb78.ufa

FA =  $40^{\circ}$

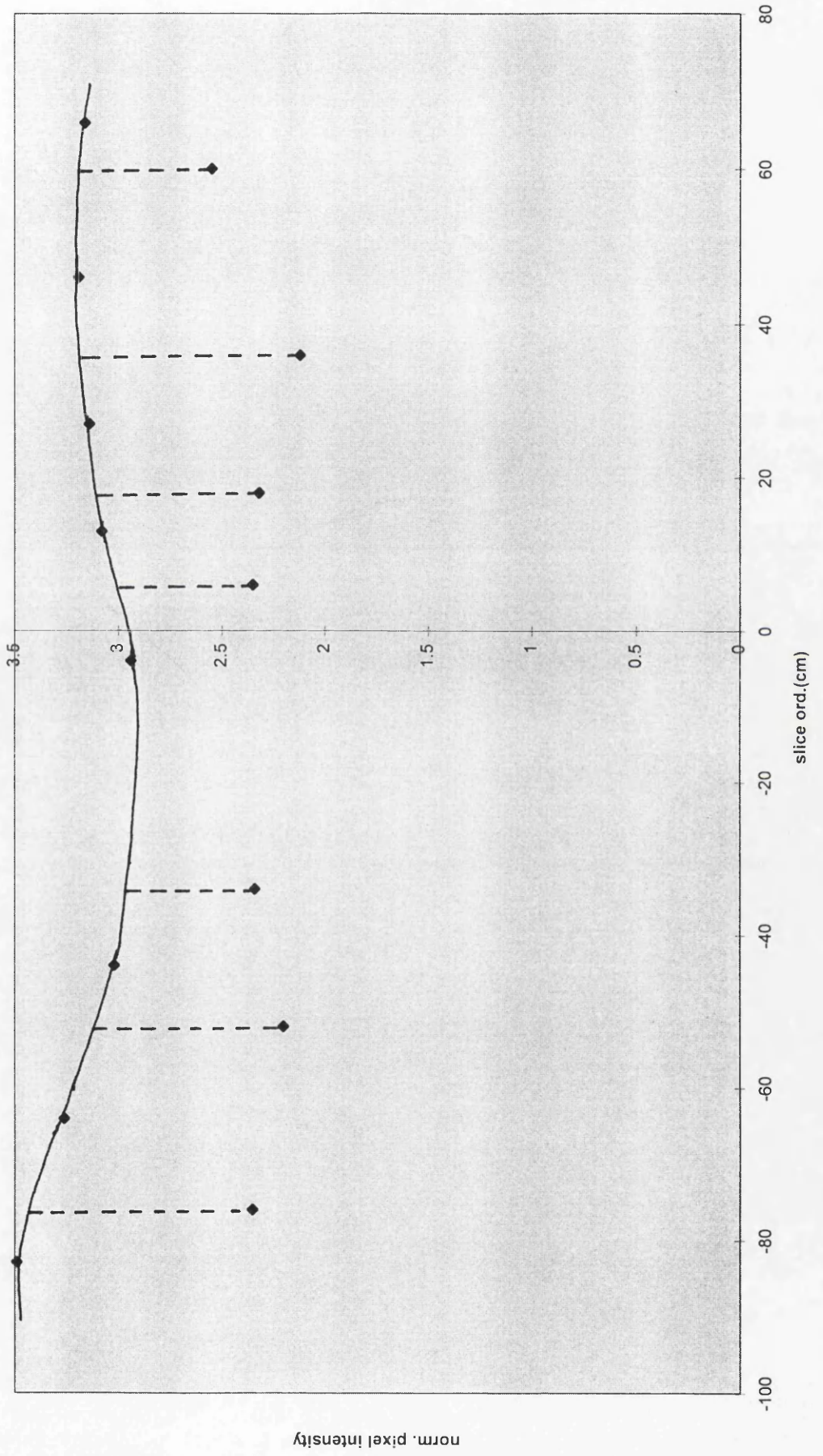
TR = 39msec

TE = 10msec

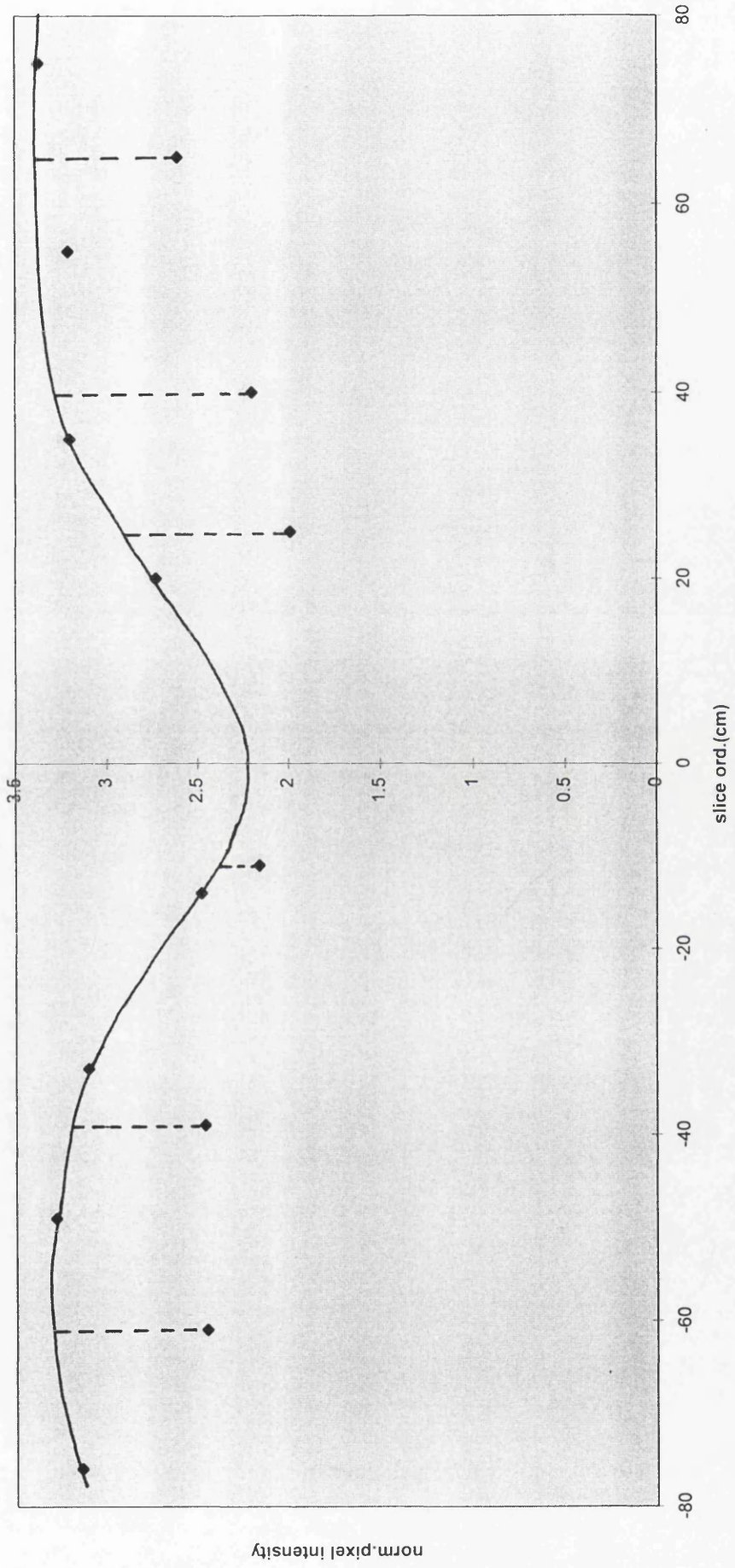
STATIC FIELD = 1.0T



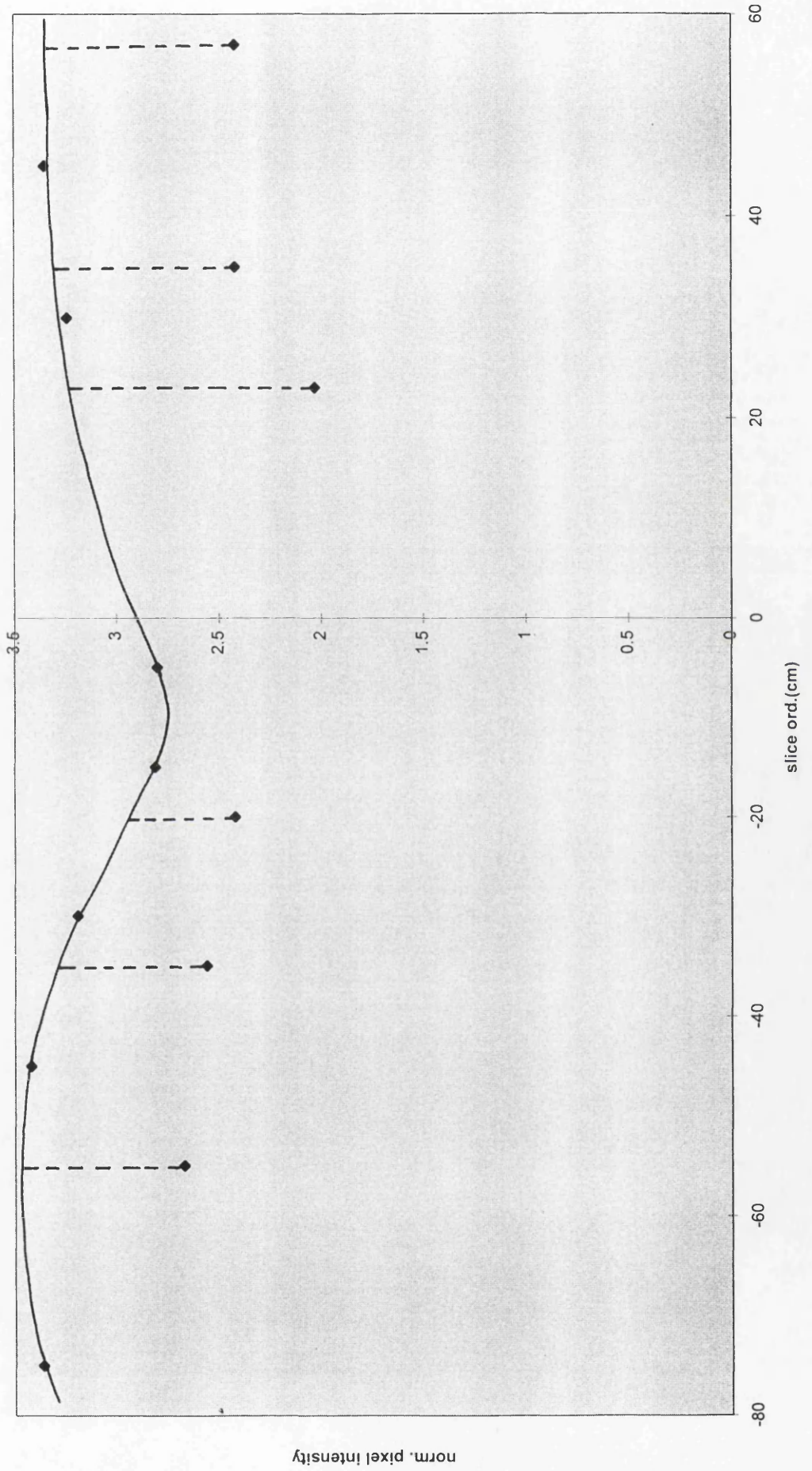
FLASH2d, v=60-180cmsec, slice1



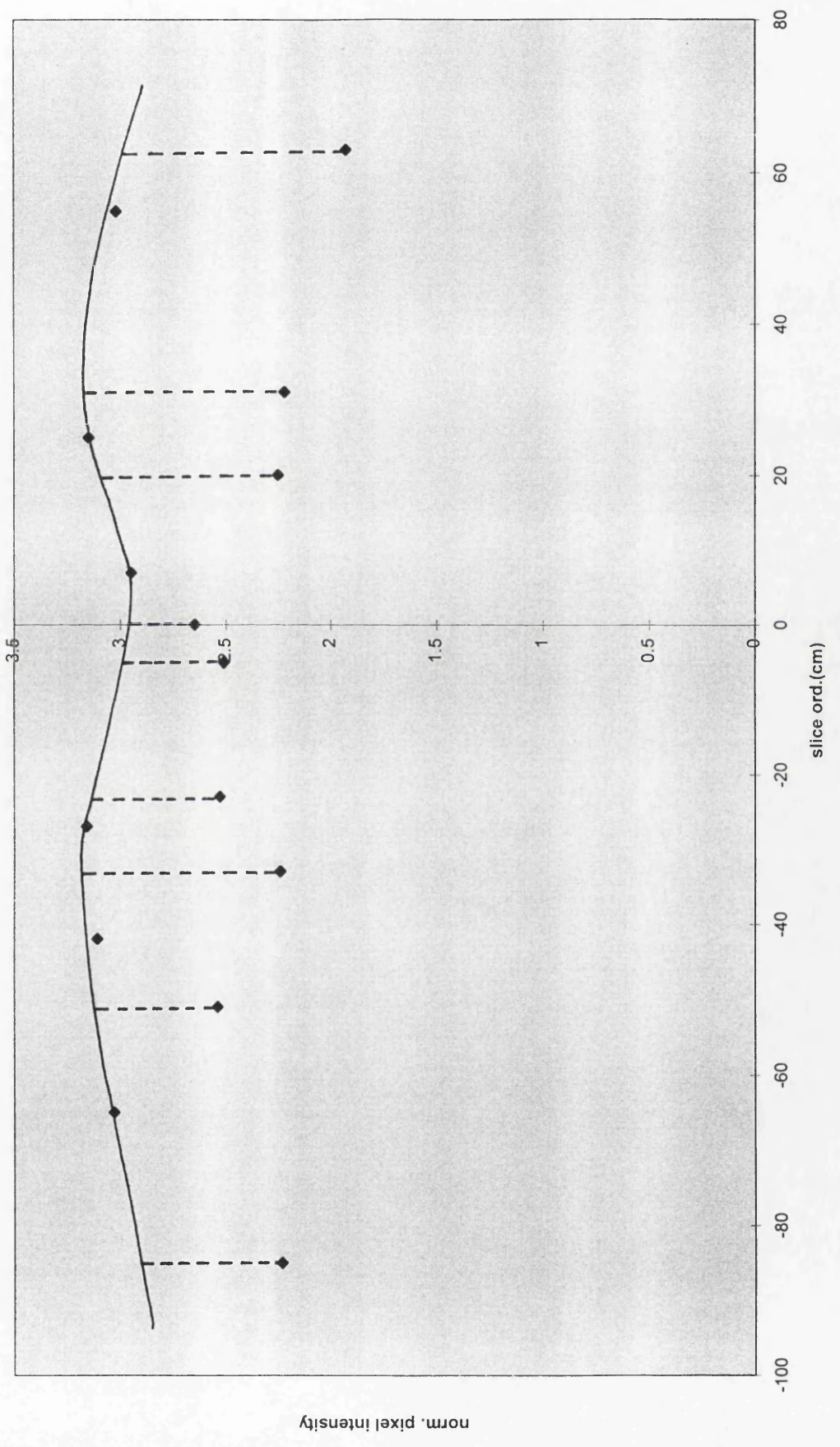
FLASH2d, v=60-180cmsec, slice2



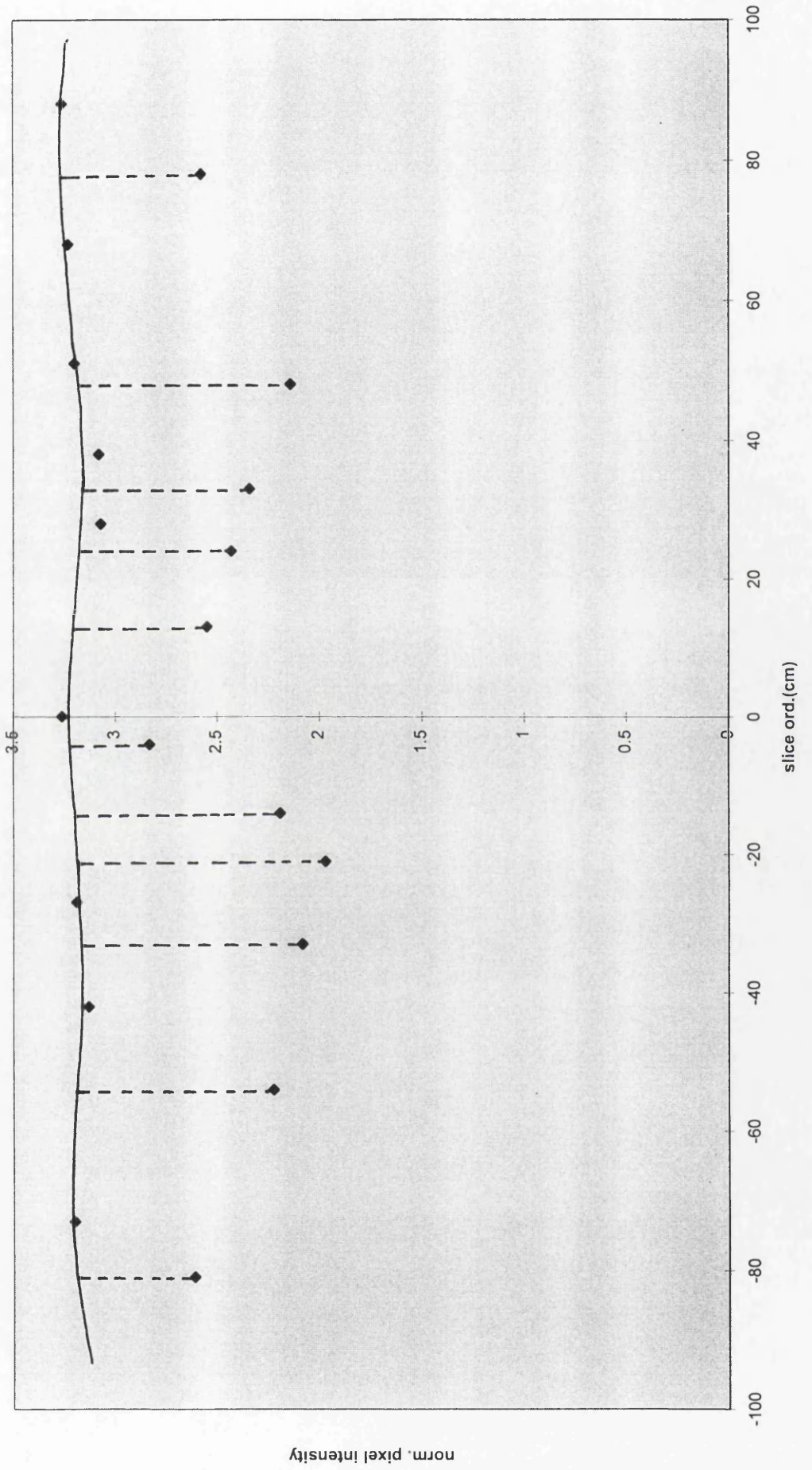
FLASH2D, v=60-180cmsec, slice3



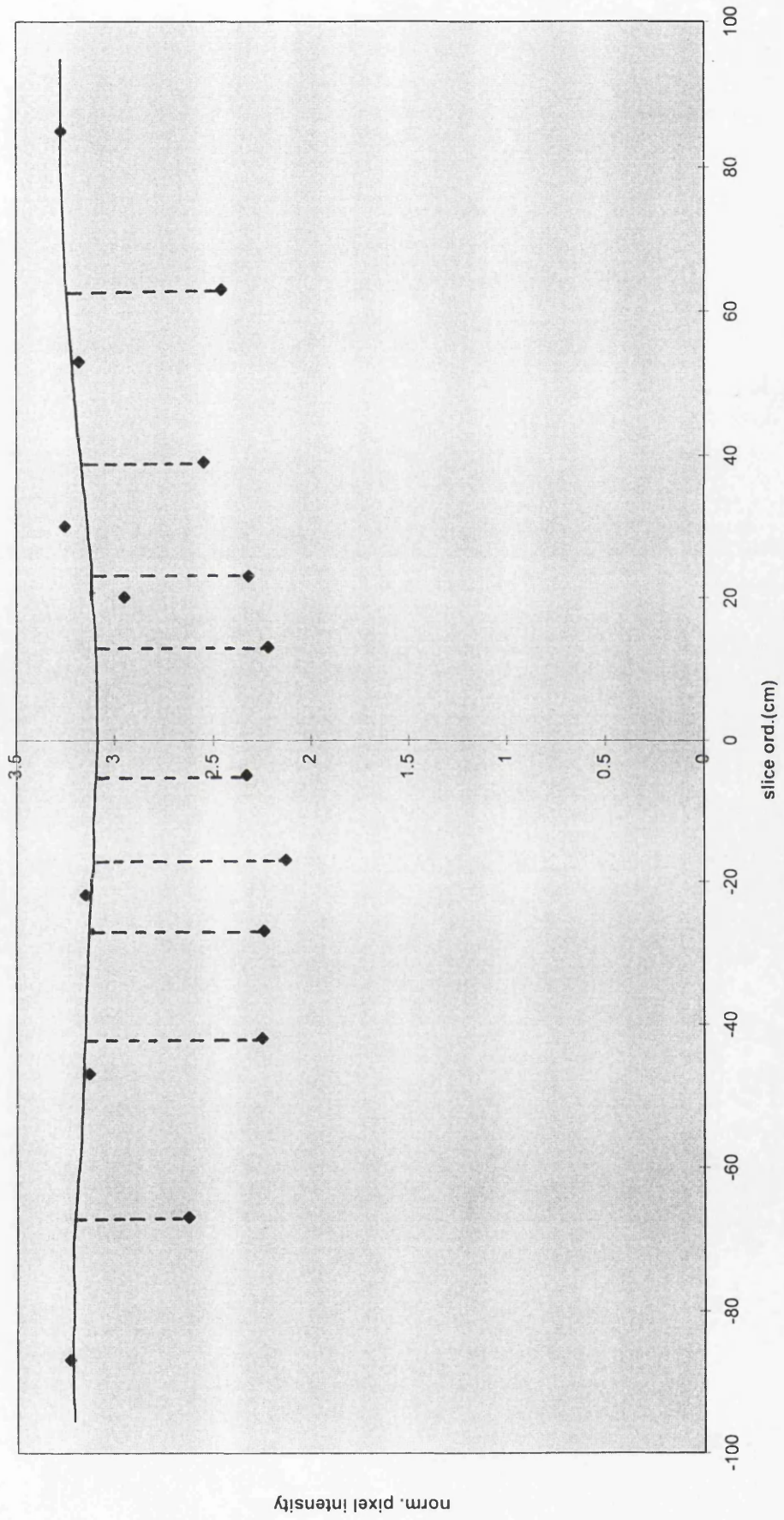
FLASH2d, v=60-180cmsec, slice4



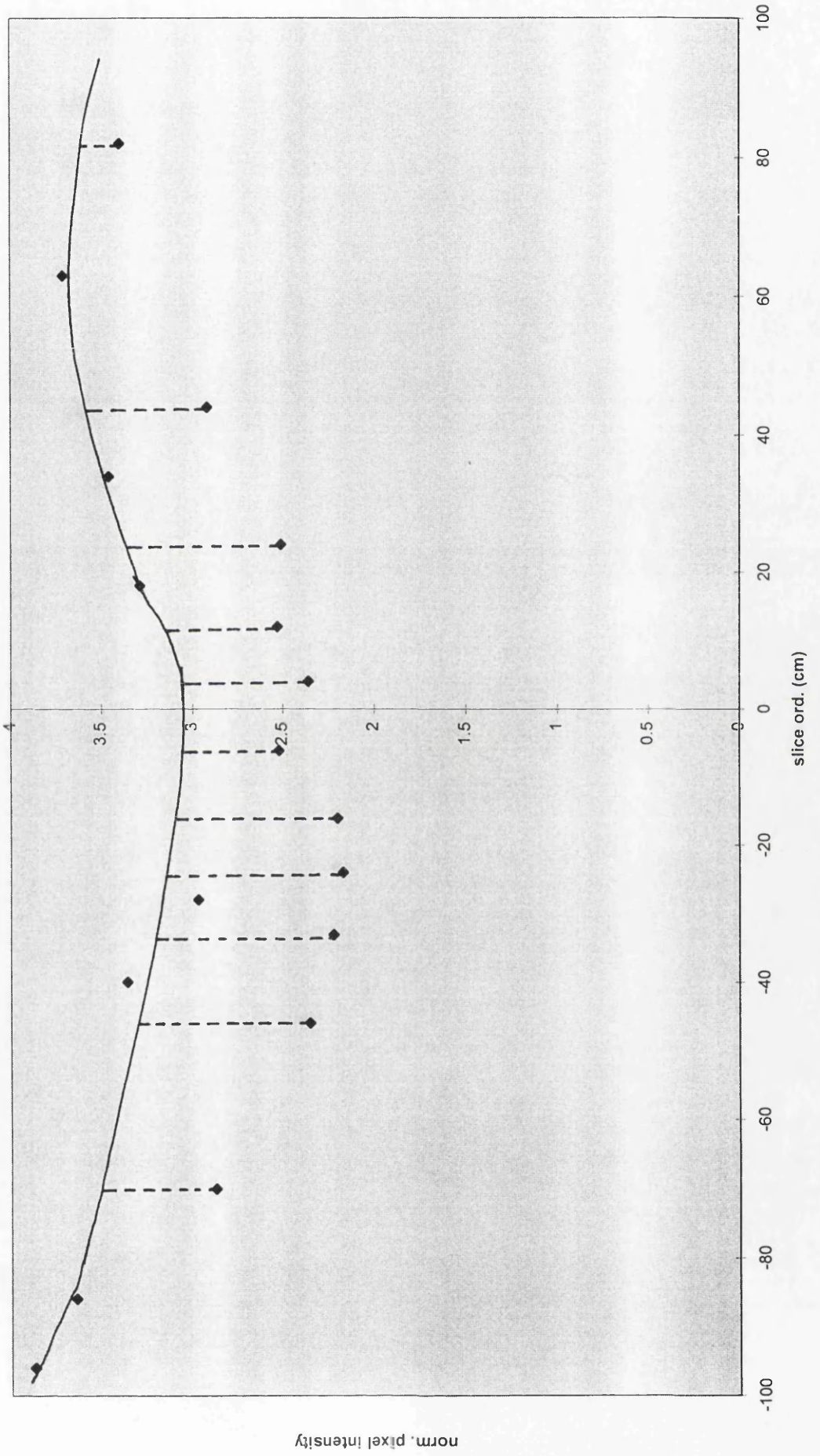
FLASH2D, v=60-180cmsec, slice5



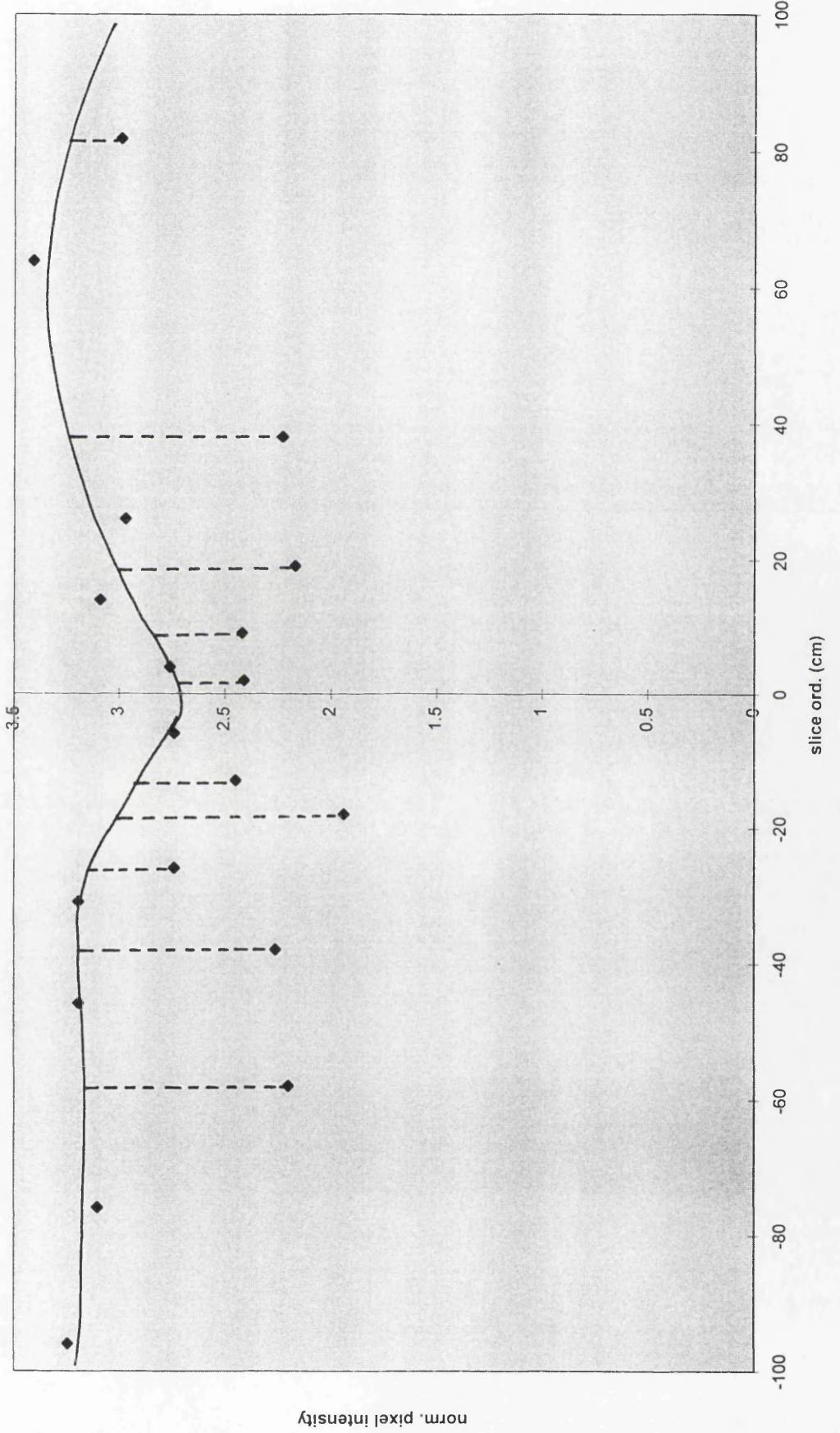
FLASH2d, v= 60-180cmsec, slice6



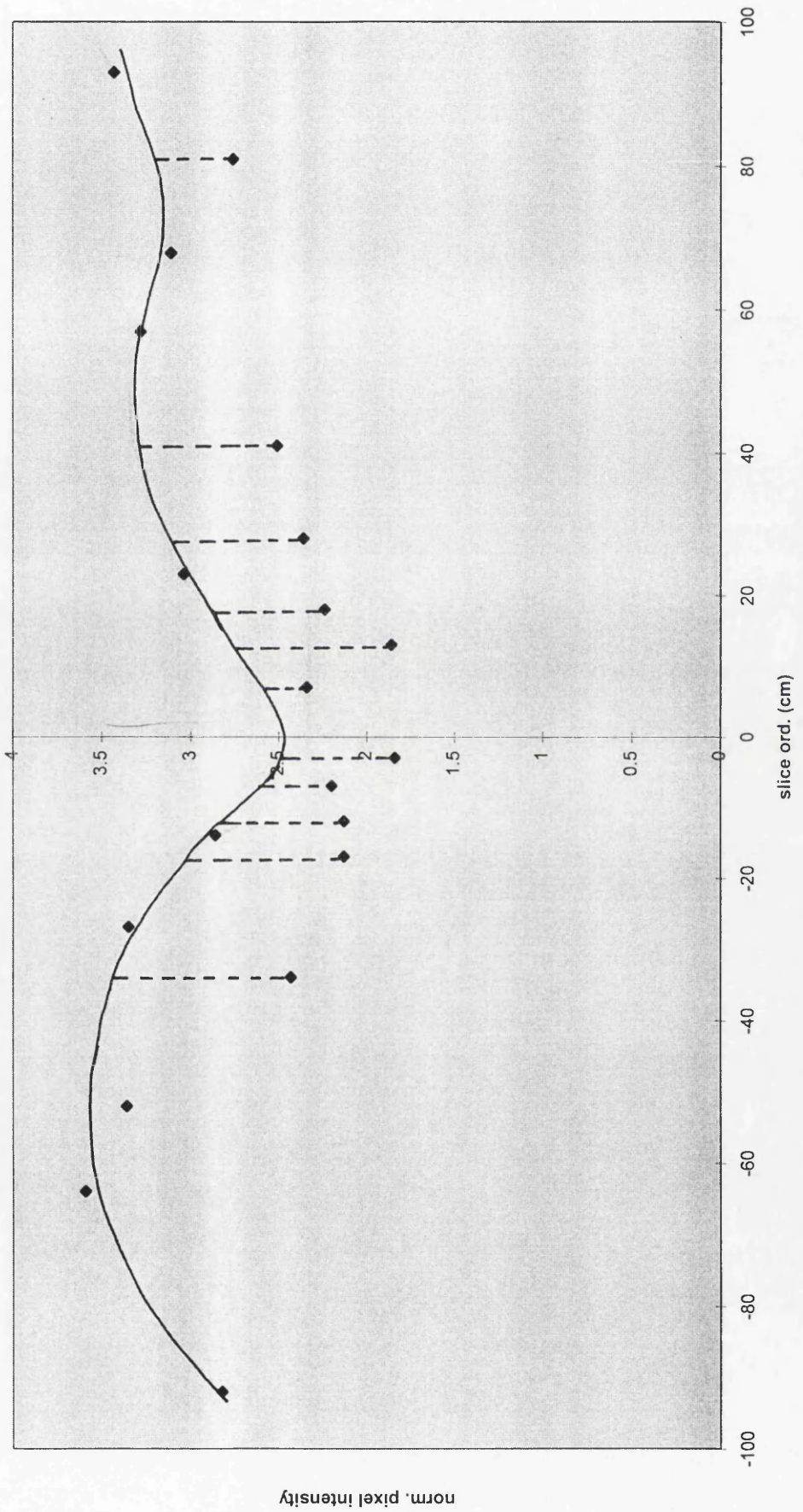
FLASH2d, v=60-180cmsec, slice7



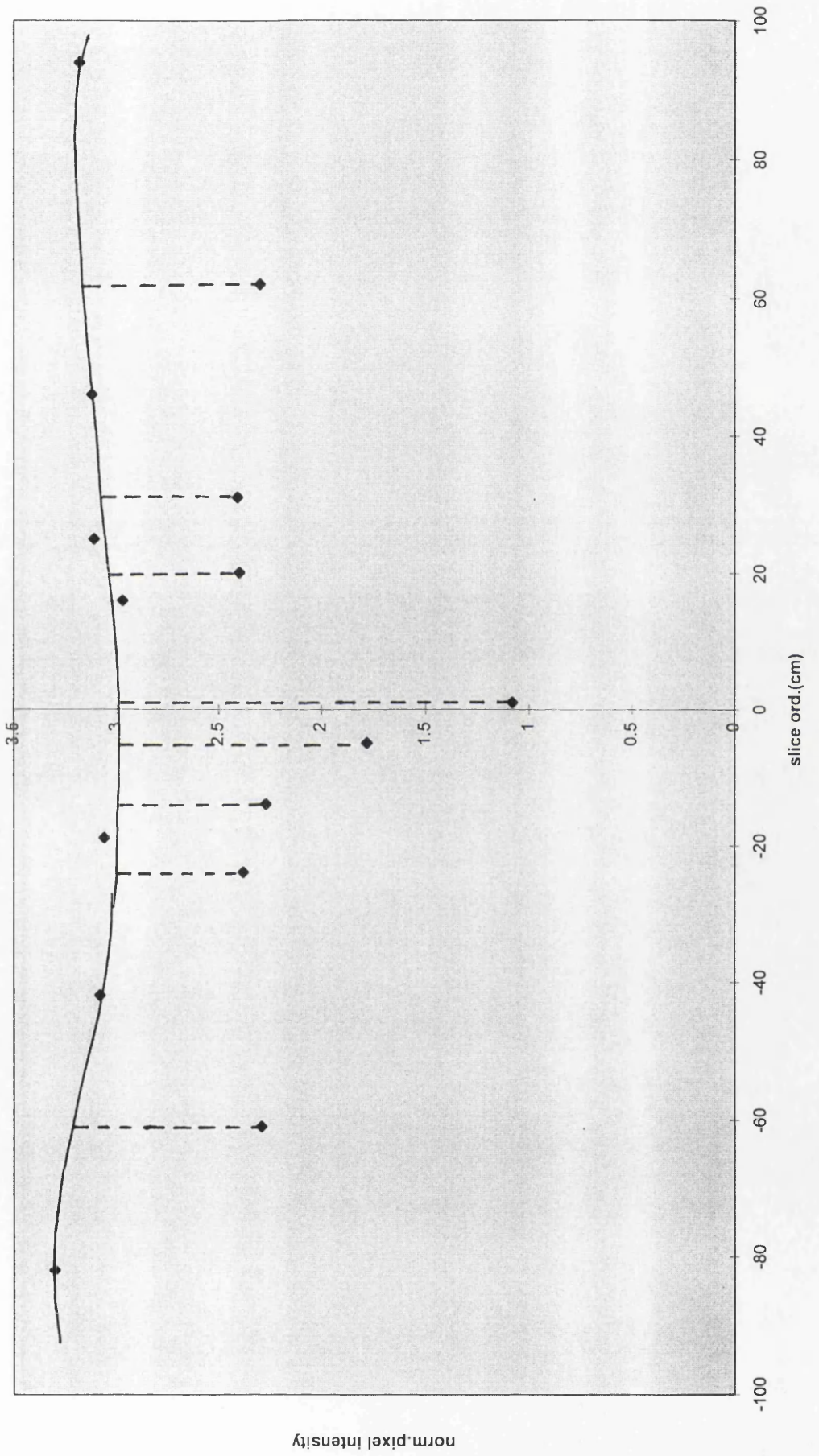
FLASH2D, V=60-180cmsec, slice8



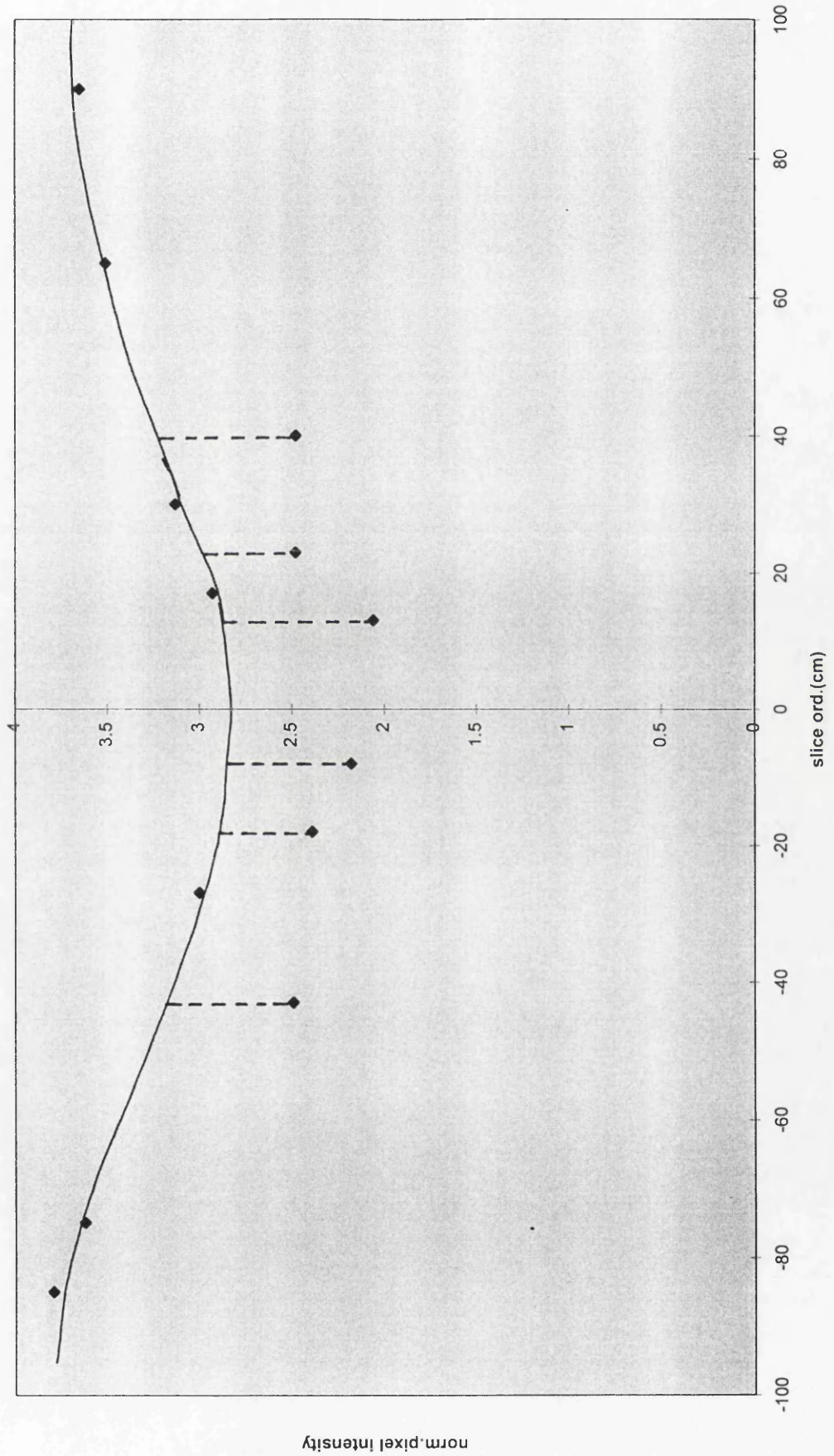
FLASH2d, v=60-180cmsec, slice9



FLASH2d, v=60-180cmsec, slice10



FLASH2D, v=60-180cmsec, slice11



2D IMAGE SLICE INTENSITY PROFILES FOR THE SEQUENCE

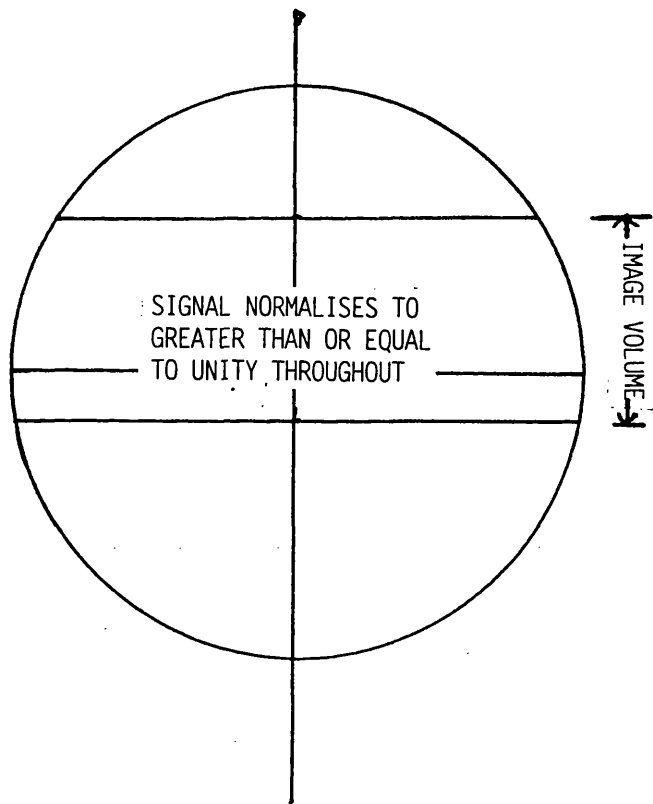
FLASH2D\_s\_10rb78.ufa

FA =  $35^{\circ}$

TR=40msec

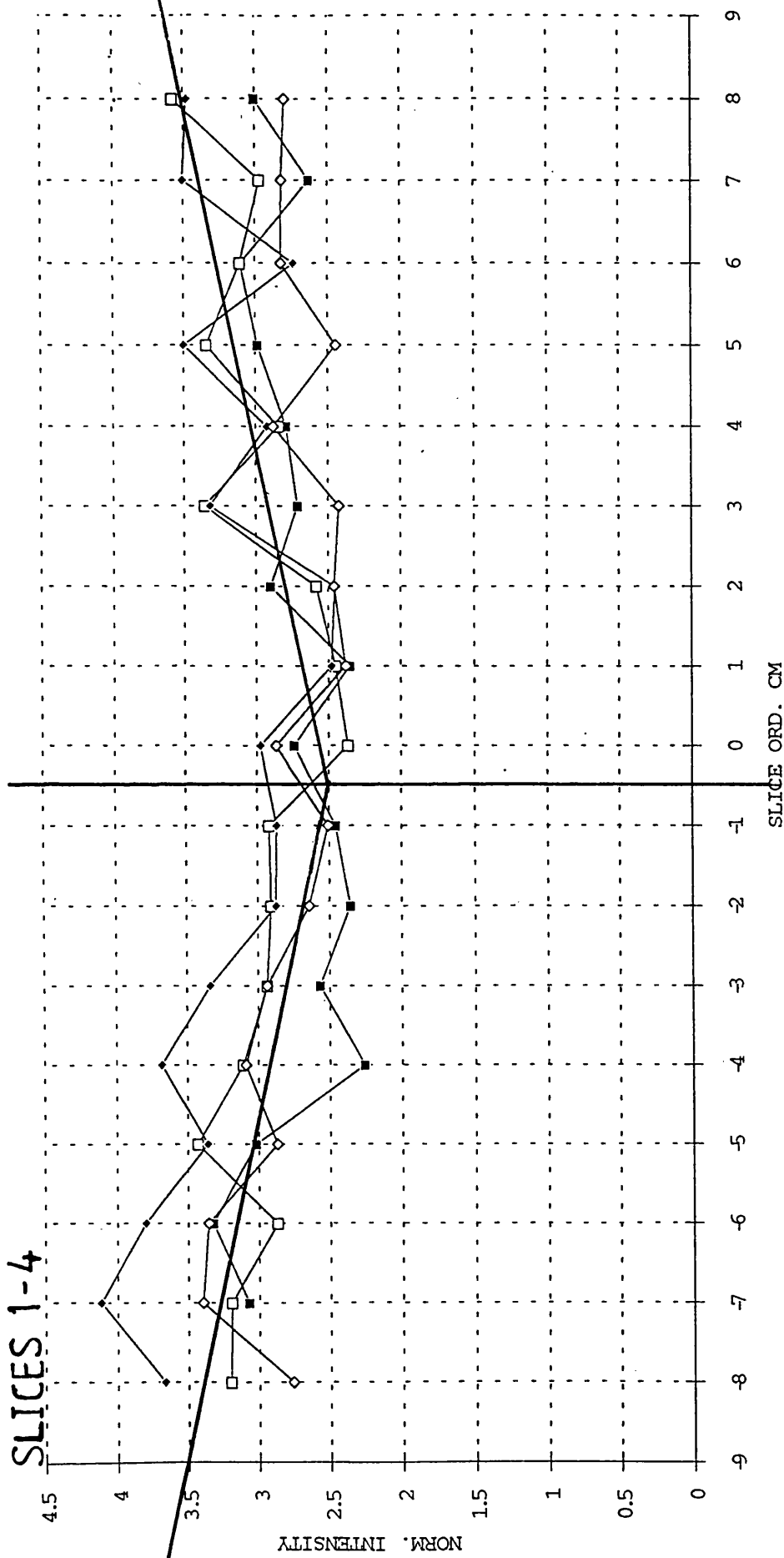
TE=10msec

STATIC FIELD = 1.0T



FLASH2D, 30-45CMSEC

SLICES 1-4

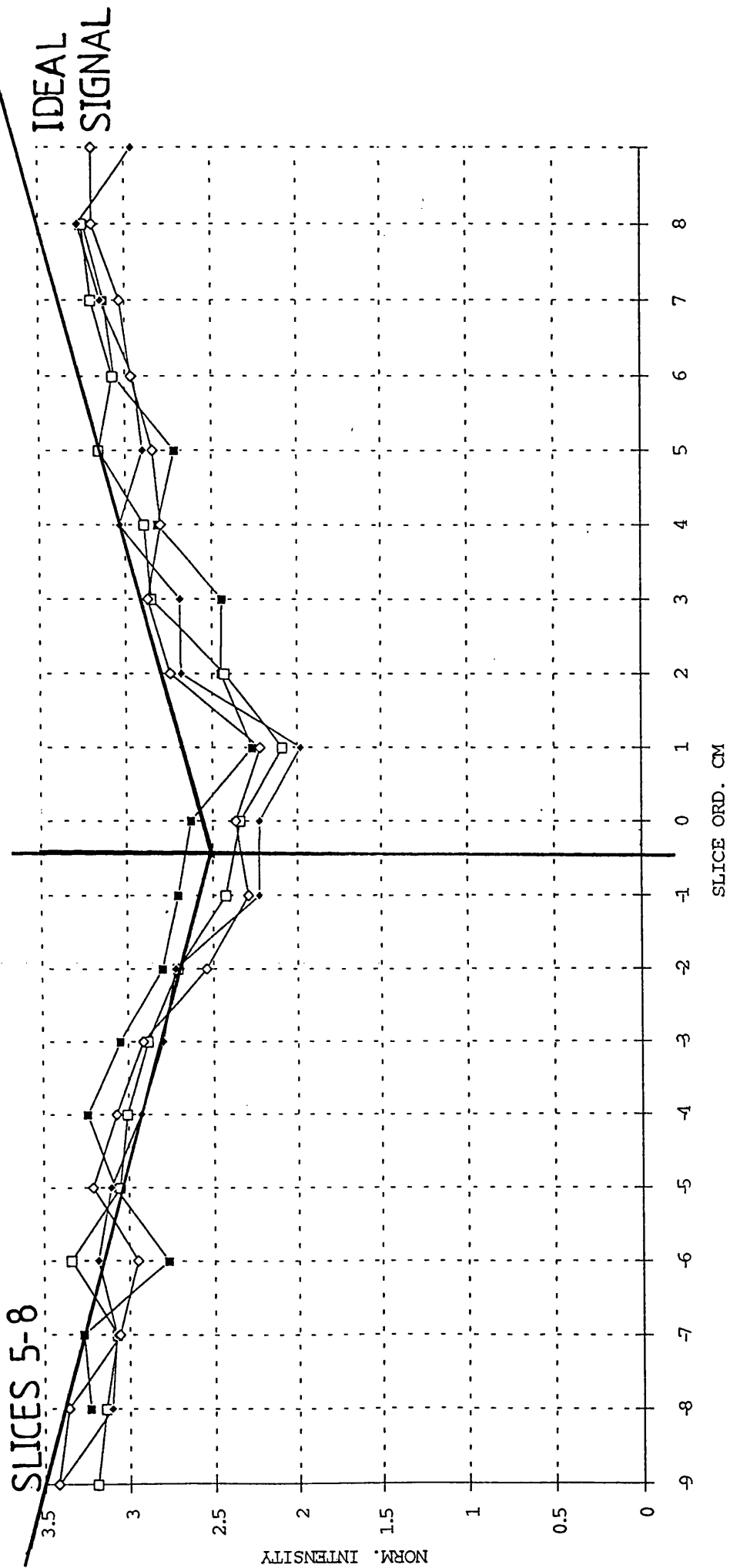


IDEAL  
SIGNAL

NORM. INTENSITY

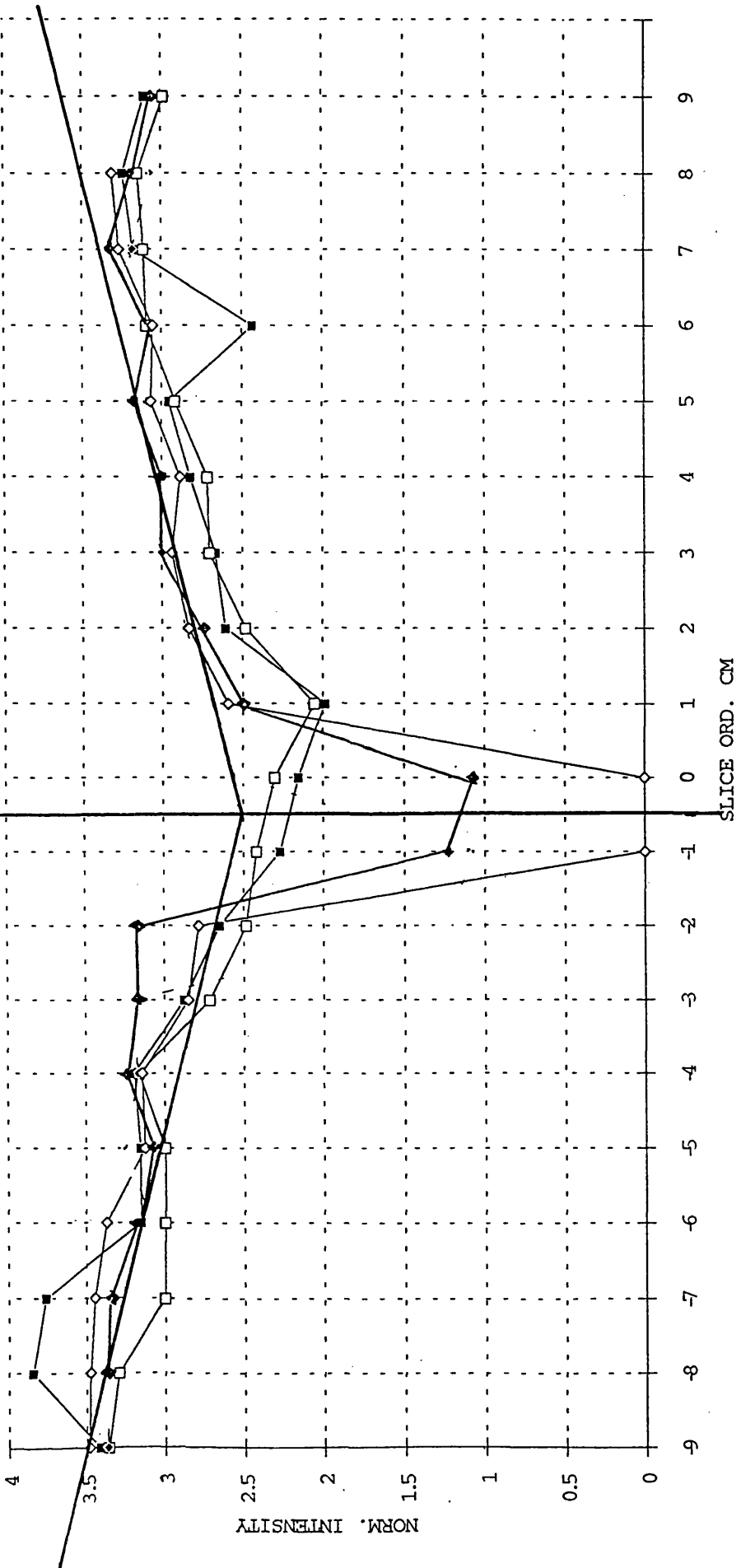
SLICE ORD. CM

FLASH2D, 30-45CMSEC



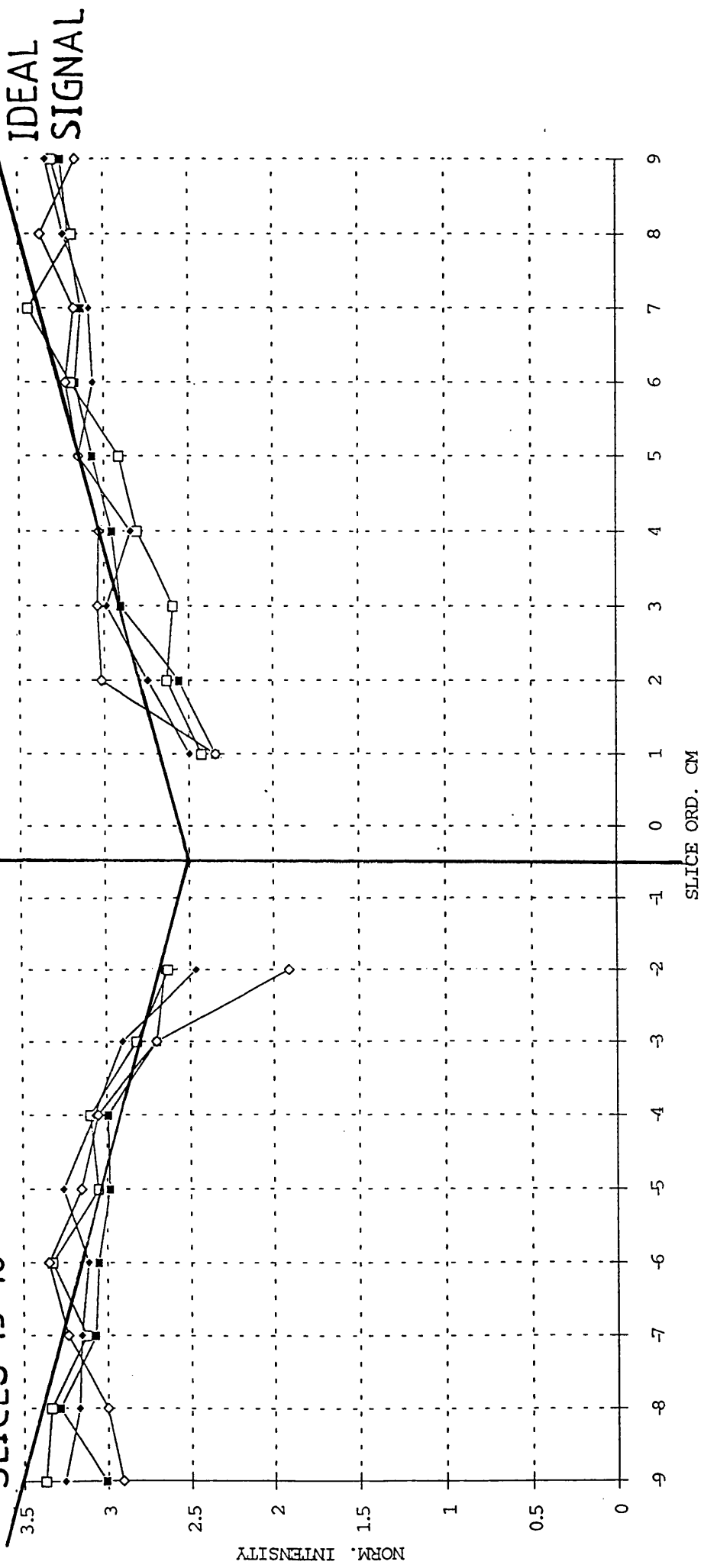
FLASH2D, 30-45CMSEC

SLICES 9-12



FLASH2D, 30-45CMSEC

SLICES 13-16



## BIBLIOGRAPHY

- Alexandrov A., Bladin C., Maggisano R., Norris J. (1993) Measuring carotid stenosis; time for reappraisal. *Stroke* vol. 24, 9, 1292-1296.
- Anderson C., Haacke E. (1992) Approaches to diagnostic magnetic resonance carotid angiography. *Sem. US, CT and MRI* vol. 13, 4, 246-255.
- Arlat I., Guhl L., Edelman R. (1992) Magnetic resonance angiography of the abdominal aorta. *Clin. Gastroenterol.* 14(3), 268-273.
- Asai H., Shimamoto K., Ishigaki T., Baldelli V. (1992) Influence of vessel size, matrix shape, vascular diameter, flow velocity and course of vessels on MR angiography. *Radiation Medicine* vol.10, 4, 145-153.
- Axel L., Morton D. (1987) MR flow imaging by velocity compensated/uncompensated difference images. *J.Comm.Ass.Tom.* 11(1), 31-34.
- Azuma T., Fukushima T. (1976) Flow patterns in stenotic blood vessel models. *Biorheology* 13, 337-355.
- Baum R. (1995) MRA surpasses angio in peripheral vessels. *Diagnostic Imaging International*, 45-48.
- Beall P.T., Amtey S.R., Kasturi S.R. (1984) NMR data handbook for biomedical applications. *Pergamon Press, New York*.
- Beach K. (1992) 1975-2000 ; a quarter of a century of ultrasound technology. *Ultrasound in Med. and Biol.*, Vol. 18, No.4, 377-82.
- Boecherschnarz H.G., Ungersboeck K., Ulrich P., Fries G., Wild A., Perneczky A. (1994) Transcranial Doppler diagnosis of cerebral vasospasm following sub-arachnoid haemorrhage: correlation and analysis of the results in relation to the age of the patients. *Acta Neurochir.* 27(1-2), 32-36.
- Bosmans H., Marchal G., van Hecke P., van Hoenacker P. (1992) MRA review. *Clin. Im.*, 16, 152-167.
- Bottomley P., Foster T., Argersinger R., Pfeiffer L. (1984) A review of normal tissue hydrogen NMR relaxation times and relaxation mechanisms from 1-100Mhz: dependence on tissue type, NMR frequency, temperature, species, excision, age. *Med.Phys.*, 11(4), 425-448.

Bowen B.C., Quencer R.M., Margosian P., Pattany P.M. (1984) MR angiography of occlusive disease of the arteries in the head and neck: current concepts. *AJR*, **162**, 9-18.

Bradley W. (1988) Flow phenomena. In ed. Stark D., Bradley V. *Magnetic resonance imaging*. C.V. Mosby Co., USA.

Brant-Zawadski M., Gillan G. (1992) Extra-cranial magnetic resonance angiography. *Cardiovasc. Intervent. Radiol.*, **15**, 82-90.

Breger R., Rimm A., Fischer M., Paplee R., Haughton V. (1989) T1 and T2 measurements on a 1.5T commercial scanner. *Radiol.*, **171**, 273-276.

Brockstedt S., Thomsen C., Wirestam R., de Poorter J., Olsson M. (1994) Development of a diffusion-sensitive pulse sequence using an enhanced whole body gradient system. *Abstract SMRM*, 1035.

Carr H.Y. (1958) Steady state free precession in nuclear magnetic resonance. *Phys.Rev.*, **112(5)**, 1963-1701.

Carr H., Purcell E. (1954) Effect of diffusion in free precession in nuclear magnetic resonance experiments. *Phys.Rev.*, **94**, 630-638.

Casselmann J.W., Kuhneide R., Deimling M., Ampe W., Dehaeme I., Meeus L. (1993) Constructive interference in steady-state 3DFT MR imaging of the inner ear and cerebellar angle. *AJNR*, **14**, 47-57.

Chahed N., Perroneau P., Delouche A., Diebold D. (1991) Velocity profiles and streamlines of a revolution post-stenotic flow. *Biorheology*, **28**, 383-400.

Condon B.R., Patterson J., Jenkins A., Wyper D., Hadley D., Grant R. (1987) MR relaxation times of cerebrospinal fluid. *J.Comm.Ass.Tom.*, **11(2)**, 203-207.

Condon B., Patterson J., Wyper D., Hadley D., Jenkins A., Lawrence A. (1986) Comparison of calculated relaxation times between an MR imager and spectrometer operating at similar frequencies. *Mag. Res. Im.*, **4**, 449-454.

Condon B., Patterson J., Wyper D., Hadley D., Teasdale G., Grant R. (1986) A quantitative index of ventricular and extraventricular intracranial CSF volumes using MR imaging. *J. Com.Ass.Tom.*, **10(5)**, 784-792.

Coulden R.A., Readman L.P. (1993) Coronary angiography: an analysis of radiographic practice in the UK. *BJR*, **66**, 327-331.

Cronqvist M., Stahlberg F., Larsson E.M., Holtas H. (1994) Phantom evaluation of TOF and PC MRA sequences in stenotic flow fields at 1T-influence of imaging parameters on examination quality. *Abstract SMRM*, 984.

Deimling M., Mueller E., Lenz G., Barth K., Fritshy P., Seiderer M. (1986) Description of flow phenomena in magnetic resonance imaging. *Diag. Im. Clin. Med.*, **55(1-2)**, 37-51.

Dewitt L.D., Wechsler L. (1988) Transcranial Doppler. *Stroke*, **19(7)**, 915-921.

Duerk J., Pattany P. (1988) In-plane flow velocity quantification along the phase-encoding axis in MRI. *Mag.Res.Im.*, **6**, 3421-3433.

Duerk J.L., Pattany P.M. (1986) Analysis of imaging axis significance in motion artefact suppression (MAST<sup>TM</sup>); MRI of turbulent flow. *Radiol.*, **161(3)**, 717-720.

Duerk J.L., Simonetti O., Hurst G., Motta A. (1990) Multi-echo multi-moment refocussing of motion in magnetic resonance imaging: MEM-MOR-RE. *Mag.Res.Im.*, **21(2)**, 535-541.

Dumoulin C., Souza S., Walker P., Wagle W. Three-dimensional phase contrast angiography. *Mag.Res.Med.*, **9**, 139

Edelman R. (1992) Basic principles of magnetic resonance angiography. *Cardiovasc.Intervent.Radiol.*, **15**, 3-13.

Edelman R., Ahn S., Chien D., Li W., Goldmann A., Mantello M. (1992) Improved time of flight MR angiography of the brain with magnetisation transfer contrast. *Radiol.*, **184**, 395-399.

Edelman R., Mattle H., Kleefield J., Silver M. (1989) Quantification of blood flow with dynamic MR imaging and presaturation bolus tracking technique. *Radiol.*, **171**, 551-556.

Edelman R., Siewert B., Adamis M., Gaa J., Laub G., Wielopolski P. (1994) Signal targeting with alternating radio-frequency (STAR) sequences: application to MR angiography. *Mag.Res.Med.*, **31**, 233-238.

Edelstein W.A., Hutchison J.M.S., Johnson G., Redpath T. (1980) Spin-warp NMR imaging and applications to whole body imaging. *Phys.Med.Biol.*, 751-756.

Frahm J., Haase A., Matthaei D. (1986) Rapid NMR of dynamic processes using the FLASH technique. *Mag.Res.Med.*, **3**, 321-327.

Freiherr G. (1994) Conventional X-ray still tops in vascular imaging. *Diag. Im. Internat.*, 16-20.

Ganong W.F.(1989) Review of medical physiology (14th ed<sup>n</sup>.) *Appleton and Lange, Prentice Hall International, Connecticut USA.*

Gatenby J.C., McCauley T.R., Core J.C. (1993) Mechanism of signal loss in magnetic resonance imaging of stenoses. *Mag.Phys.*, **20(4)**, 1049-1057.

Gloger S., Gloger A., Vogt H., Kretschmann H.-J. (1994) Computer-assisted 3D reconstruction of the terminal branches of the cerebral arteries: III Posterior cerebral artery and the Circle of Willis. *Neuroradiol.*, **36**, 251-257.

Gomori J., Grossman R., Yu-I P.C., Asakura T.(1987) NMR relaxation times of blood: dependence on field strength, oxidation state and cell integrity. *J.Comm.Ass.Tom.*, **11(4)**, 684-690.

Gouliamos A., Gotsis E., Vlahos L., Samara C., Kapsalaki E., Rologis D.(1992) Magnetic resonance angiography compared to intra-arterial digital subtraction angiography in patients with sub-arachnoid haemorrhage. *Neuroradiol.*, **35**, 46-49.

de Graaf R., Groen J. (1992) MR angiography with pulsatile flow. *Mag.Res.Im.*, **10**, 25-34.

Gomori J., Grossman R., Yu-IP C., Asakura T. (1987) NMR relaxation times of blood : Dependence on field strength, oxidation state and cell integrity. *J. Comm. Ass. Tom.*, Vol. 11, No. 4., 684-690.

Government Statistical Service (1992) Report to the Registrar General of Scotland

Guinness M. (1995) Hopes of MRA replacing the invasive angiogram. *RAD*, **Jan.**, 30.

Haacke E., Lenz G. (1987) Improving MR image quality in the presence of motion by using MR rephasing gradients. *Am.J.Radiol.*, **148**, 1251-1258.

Haacke E.M., Masaryk T.J., Wielopolski P.A., Zypman F.R., Tkach J., Arnatur S. (1990) Optimising blood vessel contrast in fast three dimensional MRI. *Mag.Res.Med.*, **14**, 202-221.

Haase A., Frahm D., Matthaei D., Honicke W., Merboldt K. (!986) FLASH imaging-rapid NMR using low flip angle pulses. *J.Mag.Res.Im.*, **67**, 258-266.

- Hahn E. (1960) Detection of sea water motion by nuclear precession. *J. Geophys. Res.*, **67**, 258-266.
- Halmshaw R. (1981) Formation of images. *Aspects of medical imaging*, ed. Moores B.M., Parker R.P., Pullan B.R., *John Wiley*.
- Hankey G.J., Warlow C.P., Sellar R.J. (1990) Cerebral angiographic risk in mild cerebrovascular disease. *Stroke*, **21(2)**, 209-222.
- Hatsukami T., Primozich J., Zierler R., Strandness D. (1992) Colour Doppler characteristics in normal lower extremity arteries. *US. Med. Biol.*, **18(2)**, 161-171.
- Hendrick R.E., Raff U. (1992) Image contrast and noise in eds. Stark D., Bradley V., *Magnetic Resonance Imaging*, C.V. Mosby Co., USA, 109-144.
- Heiserman J.E., Drayer B., Keller P., Fram E. (1992) Intracranial vascular stenosis and occlusion: evaluation with three dimensional time-of-flight MR angiography. *Radiol.*, **185**, 667-673.
- Huston J., Lewis B., Weibers D., Meyer F., Riederer S., Weaver A. (1993) Carotid artery: prospective blinded comparison of two dimensional time of flight MR angiography with conventional angiography and Duplex US. *Radiol.*, **186**, 339-344.
- Huston J., Rufenacht D., Ehman R., Wiebers D. (1991) Intracranial aneurysms and vascular malformations: comparison of time-of-flight and phase contrast MR angiography. *Radiol.*, **181**, 721-730.
- Ikawa F., Kiya K., Uozumi T., Kurisi K., Arita K., Satoh H. (1994) Diagnostic value of MR angiography in the cerebral aneurysms - statistical correlation and surgical benefit of 3D TOF MRA. *Abstract SMRM*, 952.
- Jones-Bey H. (1994) MRA and CTA take aim at X-ray angiography. *Diag. Im. Int.*, **Mar/Apr.**, 25-28.
- Keele C.A., Neil E., Joels N. (eds) (1982) *Samson Wright's Applied Physiology*. Oxford University Press.
- Keller P., Dayer B., Fram E., Williams K. (1989) MR angiography with two dimensional acquisition and three dimensional display. *Radiol.*, **173**, 527-532.

Kerber C., Heilman C. (1992) Flow dynamics in the human carotid artery : 1.Preliminary observations using a transparent elastic model.*AJNR.*,13, 173-180.

Kilner P., Firmin D., Rees S., Pennell D., Dumoulin C., Souza S.(1991) Valve and great vessel stenosis: assessment with velocity jet mapping. *Radiol.*,178, 229-235.

Koivula A., Suominen K., Timonen T., Kiviniitty K.( 1982) The spin-lattice relaxation time in the blood of healthy subjects and patients with malignant blood disease. *Phys.Med.Biol.*,27, 937.

Kraft K., Fatouros P., Fei D., Rittgero S., Kishore P. (1989) MR imaging of model fluid velocity profiles. *Mag.Res.Im.*,7,69-77.

Lacy C.M. (1993) Software phantoms of 3D imaging. *Project report, University of Aberdeen.*

Laub G., Kaiser W. (198 ) MR angiography with gradient motion refocussing. *J.Com.Ass.Tom.*, 12(3), 377-382.

Lauterbur P.C. (1973) Image formation by induced local interactions: examples employing nuclear magnetic resonance. *Nature*, 242, 190-191.

Lee J., Riederer S., Pelc N. (1989) Flow compensated limited flip angle MR angiography. *Mag. Res. Med.*, 12, 1-13.

Lenz G., Haacke E., Masaryk T., Laub G. (1988) In-plane vascular imaging: pulse sequence design and strategy. *Radiol.*, 166, 875-882.

Lustgarten J., Solomon R., Quest D., Khanji A., Mohr J. (1994) Carotid endarterectomy after non-invasive evaluation by duplex ultrasonography and magnetic resonance angiography. *Neurosurgery*, 34(4),612-618.

Maier S., Meier D., Boesiger P., Moser U., Vieli A. (1989) Human abdominal aorta: comparative measurements of blood flow with MR imaging and multi-gated Doppler US. *Radiol.*, 171, 487-492.

Maier S., Morocz I., Jolesz F.(1994) Estimation of average flow of velocities in 3D angiograms. *Abstract SMRM*, 988.

Manning W., Li W., Edelman R. (1993) A preliminary report comparing magnetic resonance carotid angiography with conventional angiography. *New. Eng. J.Med.*, 328(12), 828-832.

- Martin P., Evans D., Naylor A., Bell P. (1993) Transcranial colour-coded sonography as an aid to measurement of blood flow velocities in the basal cerebral arteries. *US.Med.Biol.*, **19(9)**, 711-716.
- Masaryk T., Modic M., Ross J., Ruggieri P., Laub G., Lenz G. (1989) Intracranial circulation: preliminary clinical results with three dimensional volume MR angiography. *Radiol.*, **171**, 793-799.
- Matthaei D., Haase A., Merboldt D., Hanicke W., Deimling M.(1987) ECG triggered arterial flash-MR flow measurements using an external standard. *Mag.Res.Im.*, **5(5)**, 325-330.
- Mattle H., Wentz K. (1992) Selective magnetic resonance imaging of the head. *Cardiovasc. Intervent. Radiol.*, **15**, 65-70.
- Meier D., Maier S., Bosiger P. (1988) Quantitative flow measurements in phantoms and on blood vessels with MR. *Mag.Res.Med.*, **8**, 25-34.
- Mogelvang J., Lindvig K., Stahlberg F., Thomsen C. (1989) Evaluation of in vivo blood flow by MRI at 1.5T. *Abstract SMRM*, 201.
- Moran P.(1982) A flow zeugmatographic interface for NMR imaging in humans. *Mag.Res.Im.*, **1**, 197-203.
- Morse O., Singer J. (1970) Blood velocity measurements in intact subjects. *Science*, **170**, 440.
- Nadel L., Braum I., Kraft K., Fatouros P., Laine F. (1990) Intracranial vascular abnormalities: value of MR phase imaging to distinguish thrombus from flowing blood. *Am. J. Mag.Res.*, **11.**, 1133-1140.
- Nordell H.,Dullerud D., Amthor R. (1993) Grading stenoses of the internal carotid artery by estimation of blood velocity with pulsed Doppler ultrasound. *Eur. Neurol.*, **33(1)**, 38-43.
- Nordell B., Stahlberg F., Bergstrand G., Ericsson A., Greitz T. (1986) Quantification of CSF velocities in the cerebral aqueduct using phase information in MR imaging. *Abstract SMRM*, 131-2.
- Nordell B., Stahlberg F., Ericsson A. (1987) A novel phantom for the study of flow effects in NMR imaging. *Abstract SMRM*, 55.
- Nordell B., Stahlberg F., Ericsson A., Ranta C. (1988) A rotating phantom for the study of MR imaging. *Mag.Res.Im.*, **6**, 695-705.

NRPB (1990) Risks associated with ionising radiations. *Annals of ICRP*, Pergamon Press.

Oppelt A., Graumann R. (1986) FISP- a new MRI sequence. *Electromedica*, **54(1)**, 15-18.

Paschal C., Haacke E.M., Adler L., Finelli D. (1992) Magnetic resonance coronary artery imaging. *Cardiovasc. Intervent. Radiol.*, **15**, 23-31.

Patruş B., Laissy J., Jouini S., Kawiecki N., Coty P., Thiebot J. (1994) Magnetic resonance angiography (MRA) of the Circle of Willis: a prospective blinded comparison with conventional angiography in 54 subjects. *Neuroradiol.*, **36**, 193-7.

Patz S. (1988) Some factors that influence the steady state in steady state free precession. *Mag.Res.Im.*, **1**, 405-413.

Pykett L., Newhouse J., Buonanno F., Brady T. (1982) Principles of nuclear magnetic resonance. *Radiol.*, **143**, 157-168.

Riles T., Eidelman E., Litt A., Perito R. (1992) Comparison of magnetic resonance angiography, conventional angiography and Duplex scanning. *Stroke*, **23(3)**, 341-6.

Rindt C., Steenhoven A., Janssen J., Reneman R., Segal A. (1990) A numerical analysis of steady flow in a three dimensional model of the carotid artery bifurcation. *J.Biomech.*, **23(5)**, 341-346.

Rindt C., Vosse F., Steenhoven A., Janssen J. (1987) A numerical and experimental analysis of the flow field in a two dimensional model of the human carotid artery bifurcation. *J. Biomech.*, **20(5)**, 499-509.

Ross J., Masaryk T., Modic M., Harik S., Wiznitzer M., Selman W. (1989) Magnetic resonance angiography of the extra-cranial carotid arteries and intra-cranial vessels: a review. *Neurology*, **39**, 1396-1376.

Ruggieri P., Laub G., Masaryk T., Modic M. (1989) Intracranial circulation: pulse sequence considerations in three dimensional (volume) MR angiography. *Radiol.*, **171**, 785-791.

Ruggieri P., Masaryk T., Ross J., Modic M. (1992) Intracranial magnetic resonance angiography. *Cardiovasc. Intervent. Radiol.*, **15**, 71-81.

Saloner D. (1989) Intensity dependence of flow signal in slice selective velocity measurements. *Mag.Res.Im.*, **7**, 61-67.

Schultess G.K., Higgins C.B. (1985) Blood flow imaging with MR: spin phase phenomena. *Radiol.*, **157**, 687-695.

Siebert J., Pernicone J., Potchen J. (1992) Physical principles and applications of magnetic resonance angiography. *Sem. US, CT and MRI*, **13(4)**, 227-245.

Siemens (1992) Magnetom SP angiography applications guide.

Siemens (1993) Magnetom Impact angiography applications guide.

Siemens (1993b) Magnetom Impact applications guide.

Shimizu K., Matsuda T., Sakurai T., Fujita A., Ohara H., Okamura S. (1986) Visualisation of moving fluid: quantitative analysis of blood flow velocity using MR imaging. *Radiol.*, **159**, 195-199.

Singer J.R. (1959) Blood flow measurements by nuclear magnetic resonance measurements. *Science*, **130**, 1652.

Singer J., Crooks L. (1983) Nuclear magnetic resonance blood flow measurements in the human brain. *Science*, **221**, 654.

Sitzer M., Furst G., Fisher H., Siebler M., Fehlings T., Kleinschmidt A. (1993) Between method correlation in quantifying internal carotid stenosis. *Stroke*, **24**, 1513-1518.

Smith F.W. (1982) Clinical applications of NMR tomographic imaging. *Proceedings of the international symposium on NMR imaging*, ed. Witcofski A.L., Karstaedt K., Partain C.L., *Bowman Gray School of Medicine, Winston-Salem NC*, 125-132.

Smith F.W. (1983) The value of NMR imaging in paediatric practice: a preliminary report. *Paediatr. Radiol.*, **13**, 141.

Smith F., Mallard J., Reid A., Hutchison J. (1981) Nuclear magnetic resonance tomographic imaging: imaging in liver disease. *Lancet*, **1**, 963.

Smith F., Reid A., Hutchison J., Mallard J. (1982) Nuclear magnetic imaging of the pancreas. *Radiol.*, **142**, 667.

Smith F., Reid A., Mallard J., Hutchison J. (1982) Nuclear magnetic resonance tomographic imaging in liver disease. *Diag. Im.*, **51**, 209-213.

Sondergaard L., Stahlberg F., Gyomose E., Malmgren L., Thomsen C., Mueller E. (1992) Comparison between ECG triggering and retrospective gating in MR velocity mapping. *Abstract SMRM*, 2901.

Sonderberg L., Stahlberg F., Stensgaard A., Thomsen C., Henricksen O. (1992) The cross-sectional area of the orifice in stenosis quantified by magnetic resonance imaging. *Abstract SMRM*, 2529.

Spritzer C.E., Pelc N.J., Lee J.N., Evans A.J., Sostman A.D., Riederer S.J. (1990) Rapid MR imaging of blood flow with phase-sensitive, limited flip angle, gradient recalled pulse sequence: preliminary experience. *Radiol.*, **176**, 255-262.

Stadelmann H., Muller E., Geibel K. (1991) Relaxation times for venous blood as a function of field strength. *Electromedica*, **59**, 82-88.

Stahlberg F., Ericsson A., Nordell B., Bergstrand G. (1986) Method for quantification of low flow velocities by magnetic resonance phase imaging. *Acta Radiol. Diag. Suppl.*, **386**, 486-489.

Stahlberg F., Ericsson A., Nordell B., Thomsen C., Henriksen O., Persson B.R.R. (1992) MR imaging, flow and motion. *Acta Radiol.*, **33(3)**, 179-200.

Stahlberg F., Henricksen O., Thomsen C., Stubgaard M., Persson B. (1987) Determination of flow velocities from magnetic resonance multiple spin echo images. *Acta Radiol.*, **28(5)**, 643-648.

Stahlberg F., Mogelvang J., Thomsen C., Nordell B., Stubgaard M., Ericsson A. (1989) A method for MR quantification of blood flow velocities and CSF using interleaved gradient pulse echo sequences. *Mag.Res.Im.*, **7**, 655-667.

Stahlberg F., Nordell B., Ericsson A. (1986) Quantitative study of flow dependence in NMR images at low flow velocities. *J.Comm.Ass.Tom.*, **10(6)**, 1006-1015.

Stahlberg F., Sondergaard L., Peng Q., Mogelvang J., Stubgaard M. (1990) Phase information in the presence of turbulent flow: a study of parameters influencing linearity breakdown. *Abstract SMRM*, 714.

Stahlberg F., Sondergaard L., Thomsen C., Henricksen O. (1992) Quantification of complex flow using MR phase imaging- a study of parameters influencing the phase-velocity relationship. *Mag.Res.Im.*, **110**, 13-23.

Stahlberg F., Thomsen C., Mogelvang J., Nordell B., Ericsson A., Stubgaard M. (1989) Further development of a flow phase imaging technique for oblique plane and in-plane motion quantification. *Abstract SMRM*, 883.

Stahlberg F., Thomsen C., Nordell B., Mogelvang J., Greitz D., Ericsson A. (1988) A general interleaved pulse sequence for rapid quantification of CSF and blood flow velocities. *Abstract SMRM*, 587.

Steele H., Templeton D. (1993) Patient doses received during digital subtraction angiography. *BJR*, **66**, 452-456.

Summers P., Taylor M., Padayachee T. (1994) Role of imaging parameters in phase mapping flow measurement. *Abstract, 1st Nottingham symposium on magnetic resonance in medicine*, 18.

Tarnawski M., Porter D., Graves M., Smith M. (1989) Flow determination in small diameter vessels by magnetic resonance imaging. *Abstract SMRM*, 896.

Tarnawski M., Taylor G., Smith M. (1988) The calibration of MR velocity images. *Abstract, 2nd European Congress of NMR in medicine and biology, Berlin*, 132.

Taylor C., Macaulay T. (1992) Magnetic resonance imaging in the evaluation of the portal venous system. *J. Clin. Gastroenterol.*, **14(3)**, 268-273.

Thomsen C., Saloner D., Stahlberg F., Nordell B. (1992) Improved sensitivity of low velocity phase mapping using reversed polarity flow encoding gradients. *Abstract SMRM*, 2924.

Tyen R., Saloner D., Jou L., Berger S. (1994) MR imaging of flow through tortuous vessels: a numerical situation. *Mag. Res. Med.*, **31**, 184-195.

Valk P., Hale J., Crooks L., Kaufman L., Roos M., Ortendahl D. (1986) MRI of blood flow: correlation of image appearance with spin echo phase shift and signal intensity. *Am. J. Radiol.*, **146**, 931-939.

Walker P., Lerski R., Mathur-de-Vre (1988) Preparation of agarose gels as reference substances for NMR relaxation time measurements. *Mag. Res. Im.*, **6**, 215-222.

Waugh J.S. (1970) Sensitivity in fourier transform NMR spectroscopy of slowly relaxing systems. *J. Mol. Spectrosc.*, **35**, 298-305.

Wedeen V., Rosen B., Chesler D., Brady T. (1985) MR velocity imaging by phase display. *J.Comm.Ass.Tom.*, **9(3)**, 530-536.

Wehrli F., McFall J., Axel L., Shutts D., Glover G., Herfkens R. (1984) Approaches to in-plane and out-of-plane flow imaging. *Non-inv. Med.Im.*, **1(2)**, 127-136.

Wehrli F.W., Shimakawa A., McFall J., Axel L., Perman W. (1985) MR imaging of venous and arterial flow by a selective saturation recovery spin echo (SSRSE) method. *J.Comm.Ass.Tom.*, **9(3)**, 537-545.

Williams P., Warwick R., Dyson M., Bannister L. eds. (1989) Gray's Anatomy. *Churchill Livingstone (37th ed<sup>n</sup>.) Edinburgh.*

Wirestam R., Salford L., Thomsen C., Brockstedt S., Lilja A., Persson B. (1994) CSF flow and intracranial dynamics in patients with supratentorial tumours. *Abstract SMRM*, 520.

Wood M. (1992) Fourier Imaging in eds. Stark D., Bradley V., *Magnetic Resonance Imaging, C.V. Mosby Co., USA, 21-66.*

Yucel E. (1992) Magnetic resonance angiography of the lower extremity and renal arteries. *Sem. US, CT and MRI*, **13(4)**, 291-302.

der Zwan A., Hillen B., Tulleken C., Dujorny M. (1993) A quantitative investigation of the variability of major arterial territories. *Stroke*, **24(12)**, 1951-1959.

